Mathematical Modelling of Surfactant Adsorption Structures at Interfaces

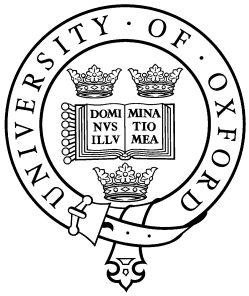

Cara Morgan

St. Anne's College

University of Oxford

A thesis submitted for the degree of

Doctor of Philosophy

Trinity Term 2012

To Grandad.

Abstract

In this thesis we derive and solve mathematical models for surfactant systems with differing adsorption structures at interfaces. The first part of this thesis considers two dynamic experimental set-ups for which we derive the associated mathematical surfactant–fluid description. Firstly we consider the behaviour of a weakly interacting polymer–surfactant solution under the influence of a steady straining flow. We reduce the model using asymptotic methods to predict the regimes under which we observe phase transitions of the species in the system and show how the bulk dynamics couple to the surfactant adsorption. Secondly we model an experiment to observe the desorption kinetics of a surfactant monolayer, designed to emulate the 'rinse mechanism' used for the removal of surfactant-containing products using water. Through the comparison of our model with experimental data we derive a semi-empirical relationship that describes the variation in depth of a near-surface diffusive boundary layer with the reduced Péclet number. We then employ a combination of asymptotic and numerical techniques that validate this result.

The second part of this thesis is concerned with surfactant systems that exhibit more pronounced adsorption at the interface due to the surfactant monomers no longer arranging themselves in a single layer, as is typically the case, but rather in multiple layers. Such self-assembled structures are commonly referred to as multilayers. We derive a simplified model that describes the rearrangement of surfactant within the multilayer structure and draw comparisons between the features of our model and experimental observations. We consider an extension of the theory to the situation of multilayer formation between two adsorbing interfaces, which is governed by an implicit free-boundary problem. We also consider incorporation of bulk solution effects, such as the addition of an electrolyte. Finally, we draw our conclusions and suggest further theoretical and experimental work related to the models presented in this thesis.

Acknowledgements

I would like to thank my supervisors Dr. Christopher Breward, Dr. Ian Griffiths, and Dr. Peter Howell for their patience, direction, help, and guidance throughout the last four years. I would also like to thank my Mathematics CASE collaborators Prof. Jeff Penfold and Dr. Robert Thomas, whose experience and knowledge of surfactant systems have been invaluable, and Dr. Ian Tucker for his assistance in the experimental work detailed on Chapter 3. I gratefully acknowledge the financial support of the Engineering and Physical Sciences Research Council.

I would like to thank my colleagues at OCIAM for many useful mathematical discussions, coffee and cake, and friendship over the last four years. In particular, I am grateful to the invaluable advice and guidance from Mohit Dalwadi, Gemma Fay, David Hewett, Anthony Lock, Sarah Munday, Alex Shabala, Michele Taroni, and Yichao Zhu. I would like to thank Maria Donovan, Holly Driver, Miriam Jones, Joseph Meehan, Claire Pearce, and Adam Still for helping with the proof reading of this thesis.

Finally, I would like to thank my family, especially my parents, for their continual support throughout the last four years, which made the completion of this thesis possible.

Contents

1 Introduction **1**

1.1 Overview . . . 3

1.2 Review of surfactant and polymer–surfactant systems . . . 4

1.2.1 Surfactant systems . . . 5

1.2.1.1 Self-assembled structures at interfaces . . . 7

1.2.2 Polymer–surfactant systems . . . 8

1.2.2.1 Weakly interacting systems . . . 9

1.3 Terminology and basic concepts for modelling surfactants . . . 10

1.3.1 A review of static surfactant and polymer–surfactant modelling 10

1.3.2 Adsorption and surface tension . . . 15

1.3.3 Coupled surfactant–fluid models . . . 18

1.4 Typical parameter scales . . . 19

1.4.1 Typical lengthscales of surfactant systems . . . 19

1.4.2 Typical concentrations of surfactant and polymer . . . 20

1.4.3 Estimating diffusivities . . . 20

1.4.4 Other relevant physical parameters . . . 21

1.5 Neutron reflectometry . . . 21

1.6 Statement of originality . . . 25

2 Straining flow of a weakly interacting polymer–surfactant solution 27
2.1 Review of the overflowing cylinder experiment 28
2.1.1 Experimental observations 29
2.1.2 Review of mathematical models of the OFC 30
2.2 Derivation of the model 31
2.2.1 Nondimensionalisation 33
2.2.2 Modelling the flow 34
2.2.3 The equilibrium limit 36
2.3 Case 1: Diffusion coefficients for all phases equal 37
2.3.1 Large-aggregation-number limit 41
2.3.1.1 Leading-order solutions 42
2.3.1.2 Asymptotic solutions to $O(\epsilon)$ 48
2.3.1.3 Inner solutions 49
2.4 Case 2: Diffusion coefficients for polymer and polymer–micelle aggregate phases equal 55
2.4.1 Numerical results 56
2.4.2 Large aggregation-number limit 58
2.4.2.1 Leading-order solutions 58
2.4.2.2 Asymptotic solutions to $O(\epsilon)$ 63
2.4.2.3 Inner solutions 66
2.5 Summary 69

3 Kinetic adsorption–desorption of a monolayer at the air–liquid interface 71
3.1 Introduction . . . 71
3.2 The kinetic monolayer dilution experiment . . . 72
3.2.1 The flow cell . . . 72
3.2.2 Experiment details . . . 73
3.2.3 Results of the experiment . . . 74
3.3 Diffusion-limited model . . . 77
3.3.1 Governing equations . . . 78
3.3.1.1 Boundary and initial conditions . . . 79
3.3.1.2 Typical parameter values . . . 81
3.3.1.3 Nondimensionalisation . . . 82
3.3.2 Analysis of the model . . . 83
3.3.2.1 Model reduction via the equilibrium limit and the rapid-surface-reaction limit . . . 84
3.3.2.2 Numerical results . . . 85
3.3.2.3 The large-aggregation-number limit . . . 88
3.4 Mathematical model to estimate the thickness of the dilution layer . . 91
3.4.1 Governing equations . . . 92
3.4.1.1 Boundary and initial conditions . . . 93
3.4.1.2 Typical parameter values . . . 95
3.4.1.3 Nondimensionalisation . . . 96
3.4.2 Numerical simulations . . . 99
3.5 Summary and discussion . . . 109
3.5.1 Suggested experimental extensions of this work . . . 110

4 A mathematical model for self-assembly at interfaces 111
4.1 Introduction . . . 111
4.1.1 Typical parameter scales . . . 112
4.2 Mesoscopic model . . . 112
4.2.1 Model formulation . . . 112
4.2.2 Nondimensionalisation . . . 118
4.2.3 Steady-state solutions . . . 119
4.2.4 Numerical solutions to mesoscopic model . . . 121
4.3 Macroscopic model . . . 126
4.3.1 Derivation of macroscopic model . . . 126
4.3.2 Boundary conditions . . . 128
4.3.2.1 Boundary conditions on the adsorbing surface . . . 129
4.3.2.2 Boundary condition for time-dependent surfactant concentration on the adsorbing surface . . . 131
4.3.2.3 Boundary condition at depth . . . 131
4.3.2.4 Conservation of Mass . . . 132
4.3.3 Steady-state solution . . . 133
4.3.4 Linear stability analysis . . . 134
4.3.5 Numerical solutions . . . 137
4.3.5.1 Constant surfactant concentration on the adsorbing surface . . . 137
4.3.5.2 Time-dependent surfactant concentration on the adsorbing surface . . . 140
4.3.6 A similarity solution . . . 142
4.4 Model for self-assembly between two adsorbing surfaces . . . 144
4.4.1 Mesoscopic model . . . 144
4.4.1.1 Steady-state solutions . . . 146
4.4.1.2 Numerical solutions . . . 151
4.4.2 Macroscopic model . . . 157
4.4.2.1 Steady-state solution . . . 160
4.4.2.2 Numerical solutions . . . 162
4.4.2.3 Small-time analysis for the formation of ‘sharp troughs’ 166
4.5 Summary . . . 168

5 Electrolytic self-assembly at interfaces 171
5.1 Experimental observations . . . 172
5.1.1 Penfold *et al.* 2007 [30] . . . 172
5.1.2 Tucker *et al.* 2011 [39] . . . 173
5.1.3 Kinetic multilayer formation for LAS-6/$CaCl_2$ . . . 174
5.1.4 Petkov *et al.* 2010 [31] . . . 177
5.1.5 Summary of experimental observations . . . 178
5.2 Free-surfactant model . . . 179
5.2.1 Governing equations . . . 180
5.2.1.1 Parameter estimates . . . 182
5.2.2 Steady-state solutions . . . 184
5.3 Free-surfactant and free-electrolyte model . . . 186
5.3.1 Governing equations . . . 187
5.3.2 Steady-state solutions . . . 188
5.4 Summary . . . 189
5.4.1 Comparison of the two models . . . 189
5.4.2 A note on microscopic reversibility . . . 190
5.4.3 Future work . . . 192

6 Conclusions 193
6.1 Summary . . . 193
6.2 Future work . . . 195
6.3 Discussion . . . 197

A Experimental data for the kinetic monolayer dilution experiment 199

B Implementation of the kinetic monolayer dilution experiment using COMSOL Multiphysics 201
B.1 Implementation in COMSOL . . . 203

C Numerical methods for the model of self-assembly at interfaces 205
C.1 One-adsorbing-surface problem . . . 205
C.2 Two-adsorbing-surfaces problem . . . 206
C.2.1 Numerical scheme that solves for the free boundary . . . 207
C.2.2 Numerical scheme for the regularized problem . . . 208

D Derivation of models presented in Chapter 5 **211**
D.1 Free-surfactant model 211
D.1.1 Nondimensionalisation 214
D.1.2 Derivation of macroscopic model 216
D.1.2.1 Dimensional model 220
D.2 Free calcium-surfactant model 221

Bibliography **223**

List of Figures

1.1 A surfactant molecule. 4
1.2 Schematic of a surfactant-only system. 5
1.3 Sketch of surface tension, γ, versus bulk surfactant concentration, S_b. 6
1.4 Schematic of a surfactant multilayer structure. 7
1.5 Schematic of a weakly interacting polymer–surfactant system. 9
1.6 Plots showing the concentrations of surfactant monomers, micelles, polymer, and polymer–micelle aggregates as the bulk concentration varies. 14
1.7 Schematic of an adsorbing interface between two bulk phases. 15
1.8 Schematic of a NR experiment set-up. 22
1.9 Typical reflectivity plots. 24

2.1 Image of the overflowing cylinder experiment. 28
2.2 Schematic of the overflowing cylinder experiment. 29
2.3 Graphs of the solutions for monomer, micelle, polymer, and polymer–micelle aggregate concentrations in Case 1. 40
2.4 Graphs that compare the exact solutions to the leading-order asymptotic solutions for monomer, micelle, polymer, and polymer–micelle aggregate concentrations in Case 1. 44
2.5 Graphs that compare the exact solutions to the leading-order asymptotic solutions with the parameters S^* and P^* varying in Case 1. . . . 46
2.6 Graphs that compare the exact solutions to the leading-order asymptotic solutions with the parameters N and M varying in Case 1. . . . 47
2.7 Graphs of the outer, inner, and composite asymptotic solutions via matching at the left against the exact solution for the monomer concentration near $z = z_1$ in Case 1. 51
2.8 Graphs of the outer, inner, and composite asymptotic solutions via matching at the right against the exact solution for the monomer concentration near $z = z_1$ in Case 1. 52

2.9 Graphs that compare the exact solutions to the order ϵ asymptotic solutions in Case 1. 54
2.10 Graphs of the numerical solutions for the concentrations of monomer, micelles, polymer, and polymer–micelle aggregates in Case 2. 56
2.11 Graphs of the numerical solutions for Case 2 with the diffusion coefficients D and D_1 varying. 57
2.12 Graphs that compare the numerical solutions to the leading-order asymptotic solutions in Case 2. 63
2.13 Graph that compares the numerical solution to the order ϵ asymptotic solution for monomer concentration in Case 2. 69

3.1 Experimental set-up of the flow cell and syringe pump. 72
3.2 Schematic of Lamgmuir trough and flow-cell weir. 73
3.3 Results of the dilution Experiments 1–6. 76
3.4 Schematic of the initial conditions for the diffusion-limited model. . . 77
3.5 Plots of $\Gamma(t)$ for the fitted numerical solution to the diffusion-limited model against the experimental data. 86
3.6 Plots of (a) H_c/H_f versus $Pe = UL/D_s$ and (b) H_c/H_f versus $Pe^* = \epsilon^2$. 87
3.7 Plots of the leading-order analytical solutions to the diffusion-limited model in the limit $K, N \to \infty$ and $\lambda_D \to 0$. 90
3.8 Comparison of the fully analytic solution to the diffusion-limited model with the experimental data. 91
3.9 Schematic of the flow cell. 92
3.10 Plots of the monomer concentration profile, S, at the mid-point of the dilution phase. 101
3.11 Plots of the monomer concentration profile, S, at the mid-point of the dilution phase. 102
3.12 Plots of the monomer concentration profile, S, at the end of the dilution phase. 103
3.13 Plots of the monomer concentration profile, S, at the end of the dilution phase. 104
3.15 Plots of the surface velocity at different times during the dilution phase. 106
3.16 Schematic phase-diagram for the development of Marangoni-convection-like roll waves. 107

3.17 Plots of the monomer concentration at the end of the dilution phase as a function of depth evaluated at the mid-point of the trough for different values of Pe^*. 108

4.1 Schematic of a surfactant multilayer structure. 113
4.2 Schematic of bilayer interfaces in a multilayer structure. 115
4.3 Plots of the steady-state solutions to the mesoscopic model. 120
4.4 Plots of the difference between the solutions to equations (4.21b) and (4.22) for Γ. 121
4.5 Plots of the numerical solutions to the system of ODEs (4.16) subject to the initial conditions (4.24). 123
4.6 Plots of the numerical solutions to the system of ODEs (4.16) for random initial data. 124
4.7 Plots of the numerical solutions to the system of ODEs (4.16) for uniform initial data. 125
4.8 Evolution of surface concentration, Γ, with time given implicitly by (4.42). 132
4.9 Comparison of the steady-state solutions of the mesoscopic and macroscopic models. 134
4.10 Linear growth rate λ versus effective domain size k for the eigenvalue problem (4.54). 135
4.11 Plots of the numerical solution to (4.63). 139
4.12 Comparison of the mesoscopic and macroscopic models. 139
4.13 Plots of the numerical solutions to the mesoscopic and macroscopic models for the time-dependent surfactant concentration at the adsorbing surface. 141
4.14 Comparison of the numerical solution to (4.67) with the similarity solution given by (4.70). 144
4.15 Schematic of multilayer compartments for the two-adsorbing-surfaces problem. 145
4.16 Schematic of steady-state set up for the two-adsorbing-surfaces problem. 148
4.17 Plots of the steady-state solution to the two-adsorbing-surfaces problem for the adsorbed concentration, Γ_{L}. 150
4.18 Plots of the numerical solutions to the system of ODEs (4.74) subject to the initial conditions (4.98). 153

4.19 Plots of the numerical solutions to the system of ODEs (4.74) subject to the initial conditions given by the steady-state solution (4.21). . . 154
4.20 Plots of the numerical solutions to the system of ODEs (4.74) subject to random initial conditions. 155
4.21 Plots of the numerical solutions to the system of ODEs (4.74) subject to initial conditions (4.99). 156
4.22 Schematic of $B(i\epsilon, t)$ near $i = n$. 158
4.23 Plots of the steady-state solution to the macroscopic model for the two-adsorbing-surfaces problem. 162
4.24 Plots of the numerical solution to the macroscopic model for the two-adsorbing-surfaces problem with symmetric initial and boundary conditions. 162
4.25 Plots of the numerical solution to the macroscopic model for the two-adsorbing-surfaces problem by mapping to a fixed domain. 165
4.26 Plots of the numerical solution to the macroscopic model for the two-adsorbing-surfaces problem by regularising the problem. 165
4.27 Plots of the moving boundary for the two-adsorbing-surfaces problem by regularising the problem. 166
4.28 Plot of the leading-order similarity solution in the small t analysis. . . 167

5.1 Reflectivity plots of the NR data for Experiment 1. 176
5.2 Reflectivity plots of the NR data for Experiment 2. 176
5.3 Plots of the number of bilayers in the multilayer structure against bulk surfactant concentration for different parameter values. 185
5.4 Schematic of the forward and backward reactions (5.25) and (5.26). . 191

List of Tables

3.1 Trough dimensions for the kinetic monolayer dilution experiment. . . 73
3.2 Summary of kinetic dilution experiments. 74
3.3 Typical dimensional parameters for the diffusion-limited model. . . . 81
3.4 Definitions of the dimensionless parameters and typical values for the diffusion-limited model. 83
3.5 Parameters used to fit the diffusion-limited model to the experimental data and the fitted values of h and H_c. 85
3.6 Typical dimensional parameters for the kinetic monolayer dilution Experiment 2. 95
3.7 Definitions of the relevant dimensionless parameters and corresponding typical values for the kinetic monolayer dilution Experiment 2. 97

4.1 Typical lengthscales for the surfactant/electrolyte systems (i) SDBS/Ca^{2+} and (ii) SLES/Al^{3+}. 112

5.1 Key model parameters for the analysis of LAS/$C_{12}EO_8$ surface adsorption in $CaCl_2$ reproduced from [30]. 173
5.2 Key model parameters for the analysis of surface adsorption of a $2\,\mathrm{mol\,m^{-3}}$ LAS-6/LAS-4 mixture in $1\,\mathrm{mol\,m^{-3}}$ $CaCl_2$ reproduced from [39]. . . . 174
5.3 Experimental data for multilayer formation. 175
5.4 Experimental data for multilayer formation for SLES/$AlCl_3$/NaCl. . . 178
5.5 Dimensional parameters of the free-surfactant model for self-assembly. 182
5.6 Dimensionless parameters of the free-surfactant model for self-assembly. 184
5.7 The change in the number of molecules in different states per unit time for the forward and backward reactions (5.25) and (5.26). 191

A.1 Experiment 1 data. 199
A.2 Experiment 2 data. 199
A.3 Experiment 3 data. 200
A.4 Experiment 4 data. 200
A.5 Experiment 5 data. 200

A.6 Experiment 6 data. 200

B.1 Definitions of the relevant dimensionless parameters and corresponding typical values for the kinetic monolayer dilution Experiment 2. 203

Chapter 1

Introduction

This thesis is concerned with the dynamics of surfactant and polymer–surfactant mixtures and the structures that they form at interfaces. Our work focuses on the dynamics of surfactant solutions governed by diffusion, advection and bulk aggregation processes. We couple these dynamic processes to the formation of surfactant structures at interfaces to gain a better understanding of the process of *self-assembly* that such surfactant systems exhibit.

The work in this thesis is motivated by the wide range of industrial, chemical and biological applications of surfactant and polymer–surfactant mixtures. One of the most common uses of surfactant is as a cleaning agent in detergents and shampoo. The addition of polymer to a surfactant mixture helps to control the rheology of the solution and, for example, is used in emulsions such as creams and lotions and detergent based products such as fabric softeners and hair conditioners. In current detergent formulations, the most important features in determining the functionality of the product are how the formulation behaves under dynamic conditions such as fluid motion and the formulation's ability to exploit surfactant accumulation at an interface and hence remove unwanted substances, *e.g.* fats, oils, dirt. The kinetics of surfactant adsorption are important in determining the foamability (the ability to form foams and lathers) and stability of foams for different detergent formulations, thus, a better understanding of the dynamic processes and surface properties of such systems is important in improving the design and efficiency of these products. In addition, many large manufacturing companies now have sustainability programmes to reduce surfactant and water usage, such as, Unilever who aims to reduce water usage in their product production and life cycles by 65 % [40]. Consequently, a better understanding of adsorption–desorption dynamics will aid in optimising the rinsing mechanisms and so reduce water usage associated with their products.

The formation of self-assembled structures at interfaces are increasingly being observed experimentally in systems that include surfactants, lipids, polyelectrolyte, polymer–surfactant mixtures and electrolyte–surfactant mixtures, [14, 20, 21, 30, 31, 36, 39]. For example, pulmonary surfactants, which coat human and animal lungs, and aid in the absorption of oxygen into the bloodstream exhibit self-assembly *in vitro* [14]. In medical applications exogenous lung surfactants are already used in treatments for infant respiratory distress syndrome that premature babies commonly suffer [35]. Craster and Matar [12] considered surfactant transport on mucus films lining the pulmonary airways, which are comprised of a non-Newtonian fluid layer with insoluble surfactant adsorbed onto the surface in a bilayer system. However, their analysis did not consider the lipid multilayer formation that has been observed in pulmonary surfactants [14]. Other clinical areas in which the study of surfactants arises include the development and delivery of anti-inflammatory drugs, the treatment of asthma and other hypersensitivity disorders, and treatments for persistent pulmonary hypertension (see the review paper [13]). Thus, a theoretical framework for the dynamics of surfactant multilayers would be of significant benefit to medical applications. Furthermore, the mechanisms that govern the formation of self-assembled structures at interfaces are also key to understanding bio-lubrication [44]. However, the features which control or determine the formation of such structures are either poorly understood or have yet to be systematically investigated.

In this thesis we study two different coupled surfactant–fluid problems. In the first of these problems we investigate the straining flow of a weakly interacting polymer–surfactant solution. In the second problem we investigate, both experimentally and mathematically, an idealised rinsing mechanism, which reduces the concentration of surfactant adsorbed at a surface. Although this problem is oversimplified it provides a good starting point from which to develop a deeper understanding of rinsing mechanisms for surfactant products. In the latter part of this thesis we present a novel model for the rearrangement and reorganisation of a self-assembled surfactant structure at an interface. We show how the model can be extended to include bulk solution effects and also electrolyte, which is typically present in systems that exhibit self-assembly.

1.1 Overview

In the remainder of this chapter we review the key features of surfactant and polymer–surfactant systems. In §1.3 we summarise the fundamental mathematical models for surfactant and polymer–surfactant systems that this thesis is focused upon. Typical parameter scales for the surfactant systems of interest are given in §1.4. Finally, in §1.5 we briefly discuss the use of neutron scattering techniques to determine the composition of surfactant structures at interfaces.

In Chapter 2 we model mathematically the behaviour of a weakly interacting polymer–surfactant solution under the influence of a steady straining flow with an adsorbed surfactant monolayer present at the air–water interface. The model describes the variation in the concentration of the surfactant monomers, free polymers, micelles and polymer–micelle aggregates with depth. We apply numerical and asymptotic techniques to solve the governing equations and through these approaches we are able to determine distinct regions in the fluid that are characterised by the presence or absence of species in the system. In the large-aggregation-number limit the leading-order analysis identifies the boundaries of these regions which depend on the physical properties of the surfactant and polymer used. The next-order asymptotics suggests that the boundaries determined at leading order are in fact layers wherein phase transition of the species occurs. The sizes of these layers can be determined and shown to depend on the physical parameters of the model.

In Chapter 3 we focus our attention on the kinetic desorption experiment that is presented in [25]. The experiment investigates the dissolution of a surfactant monolayer following a dilution of the bulk solution with water using a specially designed flow cell. We summarise the experimental observations and develop a diffusion-limited model to describe the desorption process. The results of the model are compared with experimental data. We then extend this model to incorporate the fluid dynamics of the experiment and present numerical solutions to this model.

Chapters 4 and 5 are concerned with dynamic multilayer structures at an interface. We first develop a theoretical model for a surfactant-only multilayer structure by considering the microscopic dynamics within the multilayer, which we then extend to the meso- and macroscopic scale. The resulting macroscopic model is in the form of a novel third-order partial differential equation (PDE) that, to our knowledge, has not been systematically derived before. The rest of this chapter is concerned with analysis of the PDE and the corresponding numerical solutions. In Chapter 5 we extend the

multilayer model developed in Chapter 4 to a more physically realistic scenario that includes free surfactant monomer and electrolyte. We investigate the dependence of the multilayer structure on the bulk surfactant and electrolyte concentrations and on the adsorption rate parameters.

Finally, in Chapter 6 we draw conclusions from the models presented in Chapters 2, 3, 4, and 5 and discuss future extensions to this work.

1.2 Review of surfactant and polymer–surfactant systems

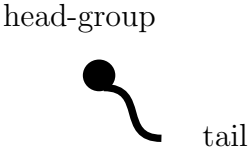

Figure 1.1: A surfactant molecule.

A surfactant is an amphiphilic molecule comprised of a hydrophobic long-chain hydrocarbon tail and a hydrophilic ionic head-group. Therefore, surfactants contain both a water-soluble (oil-insoluble) component and a water-insoluble (oil-soluble) component. The name surfactant, meaning 'surface active agent', refers to the molecule's ability to adsorb at a gas–liquid or solid–liquid interface due to its amphiphilic properties. In applications, surfactant and polymer–surfactant systems are usually aqueous solutions containing relatively low concentrations of surfactant and polymer. In certain polymer–surfactant systems the surfactant molecules form complexes with the polymer molecules and these too may become surface active [37]. The accumulation of surfactant and polymer near an interface is a desirable property and is exploited in the many applications of these systems. For example, in commercial and industrial detergents, the high concentration of surfactant at an interface improves the performance of the cleaning product.

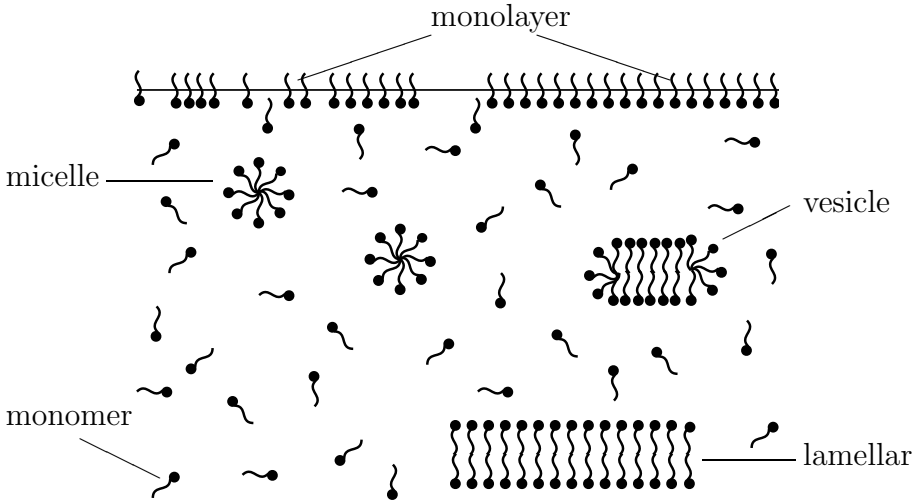

Figure 1.2: Schematic of a surfactant-only system.

1.2.1 Surfactant systems

A single surfactant molecule is commonly referred to as a *monomer*. Typically, monomers may have one or two hydrocarbon tails and in the latter case they are referred to as di-chain surfactants. Surfactants are usually categorised according to the polar head group. If the net charge for the head group is neutral, negative or positive the surfactant is referred to as non-ionic, anionic or cationic respectively. If the head group for a surfactant contains two oppositely charged groups it is referred to as zwitterionic.

When in aqueous solution, monomers just beneath the air–water interface arrange themselves so as to shield their hydrophobic tails from the water molecules whilst their heads remain within the aqueous solution as shown in Figure 1.2. This process is known as *adsorption*, and the single layer of surfactant monomers that adsorb at the air–water interface is referred to as an orientated monomolecular layer or *monolayer*. Surfactant molecules in the monolayer disrupt the hydrogen bonds between the water molecules at the surface and thus lower the surface tension. It is this property of lowering the surface tension at the air–liquid interface that has resulted in the extensive use of surfactants in industrial and domestic applications.

Another way in which surfactants shield their hydrophobic tails when in aqueous solution is to form aggregates in the bulk known as *micelles* and *vesicles*. Micelles are usually spherical in shape and typically consist of between 20 and 200 monomers, whereas vesicles, in general, are more sausage-like in shape, contain more monomers, and form at higher concentrations of surfactant. If the surfactant concentration is

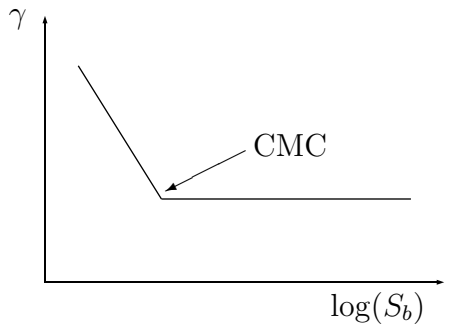

Figure 1.3: Sketch of surface tension, γ, versus bulk surfactant concentration, S_b.

sufficiently high then more planar structures or *lamellae* will form [29]. A schematic diagram of micelles, vesicles and lamellae/lamellar fragments is shown in Figure 1.2.

We note that formation of aggregates only occurs if the surfactant concentration is sufficiently high so that it becomes energetically favourable [1]. The surfactant concentration at which micelles start to form in the bulk is referred to as the critical micelle concentration (CMC). One way to think about the CMC is to consider the effect upon surface tension of variations in the total bulk concentration of surfactant. At low bulk concentration, the surface tension reduces with increasing surfactant concentration as the surfactant monomers adsorb at the interface. When the surfactant concentration reaches the CMC it then becomes more energetically favourable for monomers to form micelles in the bulk rather than to adsorb at the surface. Therefore, further increases in the bulk surfactant concentration have little effect in reducing the surface tension. A typical sketch of surface tension, γ, versus bulk surfactant concentration, S_b, is shown in Figure 1.3. Mathematical models that relate the surfactant concentration to surface tension are discussed in §1.3.2.

Commercial and industrial surfactant-based products often contain blends of different surfactants. The components are often selected in order to achieve desired rheological or cleaning properties. In recent years, such systems have been studied from the experimental viewpoint, for example see [22, 29, 30, 41]. Mixtures that contain ionic/non-ionic surfactants or cationic/anionic surfactants exhibit greater surface activity at the air–water interface [19, 30]. We discuss this further in §1.2.1.1.

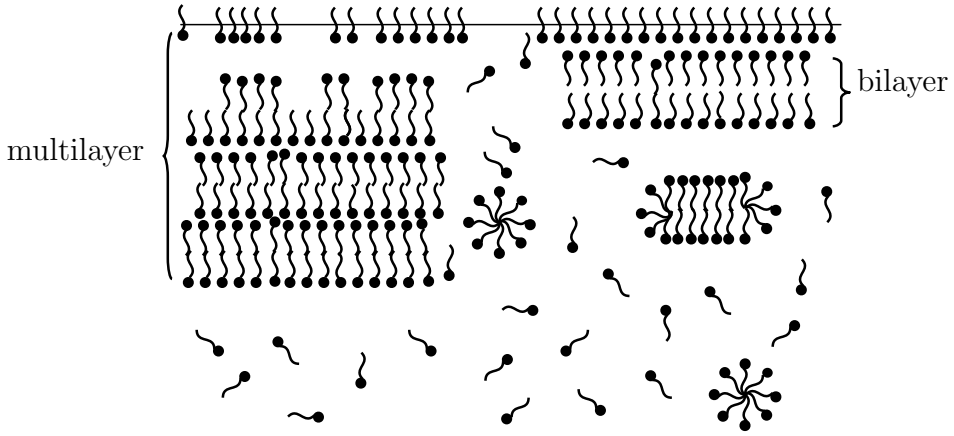

Figure 1.4: Schematic of a surfactant multilayer structure.

1.2.1.1 Self-assembled structures at interfaces

Surfactant systems can also undergo self-assembly at interfaces, see [14, 18, 30, 31]. These experiments show that the higher concentration of surfactant observed at the interface is in the form of a multilayer, in which the monomers no longer arrange themselves in a single layer but instead do so in multiple layers. In general, the ordering of surfactant in the layer is not well understood and proposed structures are shown in Figure 1.4. Self-assembled structures we refer to in this thesis are:

a *monolayer* – a single layer of surfactant;

a *bilayer* – a layer of surfactant that has depth equal to the length of two monomers;

a *trilayer* – a monolayer with a bilayer beneath it;

a *multilayer* – a monolayer with more than one bilayer beneath it.

Self-assembly of surfactant at interfaces is vital to understanding the mechanism by which detergent formulations work and more importantly in biological applications such as lipid multilayer formation which is key to understanding the structure of cell membranes [2].

As mentioned earlier, multilayer formation has been observed in porcine and bovine samples of pulmonary surfactant *in vitro* by Follows *et al.* [14] using neutron reflectometry. The multilayer structure consists of lipid/protein bilayers alternating with aqueous layers which are laterally disordered. Kaschiev and Exerowa [18] have formulated a model for the surface energy of alveolar surfactant based on a structure

consisting of monolayers and bilayers. Their model assumes that the surfactant in the multilayer is uniformly distributed, the number of bilayers is known, and the bilayers are all of equal depth. They determine a relationship between the optimum depth of a bilayer and the known surface tension during inspiration and expiration, which qualitatively agrees with experimental observations. However, the surfactant properties that determine the formation of surfactant multilayers have yet to be fully characterised.

Mixed surfactant systems, *e.g.* mixed anionic/cationic or surfactant/electrolyte systems, exhibit more pronounced adsorption of surfactant at the interface [19]. In particular, the addition of calcium ions to a mixed surfactant solution may increase the concentration of surfactant adsorbed at the interface significantly compared with the solution in the absence of calcium ions (see for example [30]). In Chapters 4 and 5 we focus our attention on self-assembly of anionic surfactants at an air–water interface in the presence of multivalent counterions, as discussed in [30] and [31]. In both papers it was shown that there is a transition from a monolayer to a bilayer to a trilayer and finally to a multilayer structure at the interface as the concentration of the counterions is varied. Furthermore, in the context of detergency, hard water contains the divalent counterions calcium and magnesium, which are known to have profound effects on performance. Such applications have motivated us to study surfactant–electrolyte systems in this thesis.

1.2.2 Polymer–surfactant systems

In applications polymer is often added to a surfactant solution to control the rheology and stability of the system. Examples of such uses are in the lubricating effects of fabric and hair conditioners [28]. The addition of neutral or charged polymer to an aqueous ionic surfactant solution causes a marked change to the surface tension profile [37]. In the case where the polymer is neutral, the reactions between polymer and surfactants are mainly driven by weak hydrophobic forces, and the system is referred to as *weakly interacting*. In the case where the polymer is positively charged, the reactions between polymer and surfactant are mainly driven by strong electrostatic forces and the system is referred to as *strongly interacting*.

In this thesis we will focus our attention on models for the weakly interacting polymer–surfactant systems but note that they can be modified for the strongly-interacting polymer–surfactant systems.

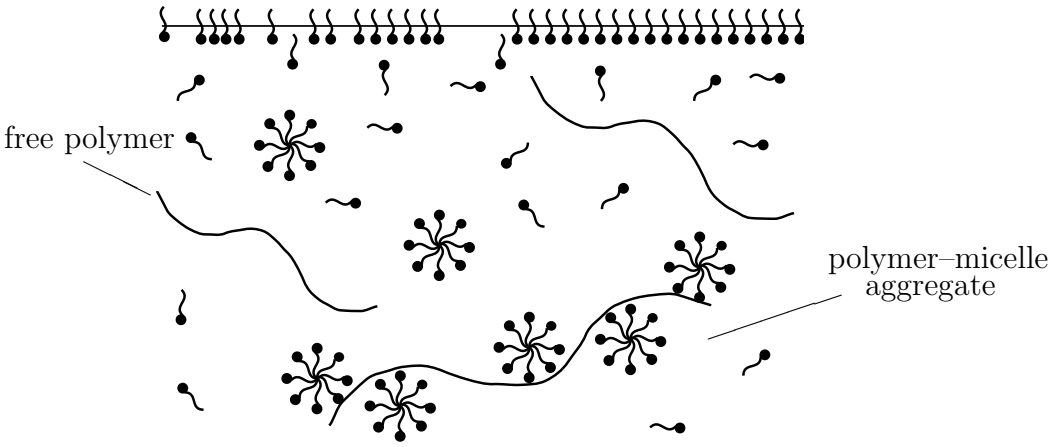

Figure 1.5: Schematic of a weakly interacting polymer–surfactant system.

1.2.2.1 Weakly interacting systems

In an aqueous weakly interacting polymer–surfactant system, surfactant still adsorbs at the surface but, if the surfactant concentration is sufficiently high, then it becomes energetically favourable for the ionic surfactant monomers to form complexes with the polymer in the bulk. The complex that characterises this system consists of a single polymer with surfactant micelles attached to it, as shown in Figure 1.5, and is commonly known as a *polymer–micelle aggregate*. The number of surfactant monomers that form a micelle in a polymer–micelle aggregate is typically lower than the number of monomers in a free micelle. The surfactant concentration at which polymer–micelle aggregates form in the bulk is known as the critical aggregation concentration (CAC); for the majority of weakly interacting systems this is below the CMC. If the surfactant concentration is above the CMC then there are both free micelles and polymer–micelle aggregates present in the bulk solution.

1.3 Terminology and basic concepts for modelling surfactants

In this section we present some of the fundamental models for surfactant and polymer–surfactant solutions and show how they couple to the equations for fluid dynamics. All the models we present in this section are given in three-dimensional Cartesian co-ordinates, $\mathbf{x} = (x, y, z)$ and in §1.3.2 and §1.3.3 the fluid velocity vector has components $\mathbf{u}(\mathbf{x}, t) = (u(x, y, z, t), v(x, y, z, t), w(x, y, z, t))$. We refer to 'bulk solution' and 'bulk species' as anything that is not an adsorbing interface or adsorbed onto an interface; it is common to abbreviate bulk solution to 'bulk' and we do so in this thesis.

1.3.1 A review of static surfactant and polymer–surfactant modelling

In this section, following the approach of Bell [4], we present a static macroscopic model for the species of a weakly interacting polymer–surfactant system. We note again that for the majority of such systems the CAC is lower than the CMC and so we consider a system above the CMC in order that micelles and polymer–micelle aggregates may form in the bulk from free surfactant monomers and free polymers. We denote the concentrations of surfactant monomer, micelles, polymer, and polymer–micelle aggregates by S, S_m, P, and P_m respectively, all having SI units $\mathrm{mol\,m^{-3}}$. It is worth noting that the model we present can be reduced to the surfactant-only case by setting $P = P_m = 0$, or similarly the model can be generalised to the strongly interacting polymer–surfactant system (*cf.* Bell [4]).

First we consider the formation of micelles and we let N be the number of surfactant monomers in a micelle, commonly known as the micelle *aggregation number*. In practice micelles lie in a narrow range of aggregate sizes but it is more energetically favourable for micelles to be of some mean aggregate size. We will, for simplicity, assume that the micelles are monodisperse and so the aggregation number is the same for every micelle in the system. Furthermore, we note that in practice aggregation occurs through a series of reactions in which monomers associate and dissociate with an aggregate of n monomers where n can take any integer value. However, the time scales on which these reactions occur are very small and so, following Breward and

Howell [6], we assume that full association or dissociation occurs as a single-step reaction of the form

$$NS \underset{k_0^-}{\overset{k_0^+}{\rightleftharpoons}} S_m,$$

for the reaction constants k_0^+, having units $\mathrm{m}^{3(N-1)}\,\mathrm{mol}^{1-N}\,\mathrm{s}^{-1}$, and k_0^-, having units s^{-1}. The law of mass action implies that the rate, j_0, at which surfactant changes phase from monomer to micelle is

$$j_0 = k_0^+ S^N - k_0^- S_m. \tag{1.1}$$

Next we consider the formation of polymer–micelle aggregates in solution. We let m denote the number of micelles that form a polymer–micelle aggregate, and suppose that each polymer-bound micelle contains n surfactant monomers. Again we assume that the aggregates are monodisperse and so n and m are the same for every polymer–micelle aggregate. Throughout this thesis the parameters n and m only appear as the product nm which we shall denote by M. We model polymer–micelle aggregate formation as a single-step reaction of the form

$$P + MS \underset{k_1^-}{\overset{k_1^+}{\rightleftharpoons}} P_m,$$

for the reaction constants k_1^+, having units $\mathrm{m}^{3M}\mathrm{mol}^{-M}\mathrm{s}^{-1}$, and k_1^-, having units s^{-1}. Invoking the law of mass action again implies that the rate, j_1, at which surfactant changes phase from monomer to aggregate is

$$j_1 = k_1^+ P S^M - k_1^- P_m. \tag{1.2}$$

The net concentration of surfactant, S_b, and polymer, P_b, in the bulk are given by the expressions

$$S_b = S + NS_m + MP_m, \quad \text{and} \quad P_b = P + P_m, \tag{1.3}$$

respectively.

If the system is in thermodynamic equilibrium then the the fluxes j_0 and j_1 must be zero and so we obtain the expressions for the micelle and polymer–micelle aggregate concentrations

$$S_m = \frac{k_0^+}{k_0^-} S^N, \quad \text{and} \quad P_m = \frac{k_1^+}{k_1^-} P S^M. \tag{1.4}$$

On substituting into (1.3) we obtain a single equation for S as a function of bulk polymer and surfactant concentrations

$$S_b = S + \frac{k_0^+}{k_0^-} N S^N + M P_b \left(\frac{S^M}{k_1^-/k_1^+ + S^M} \right). \tag{1.5}$$

Following [6] we define mathematically the CMC to be the concentration of surfactant, S_{CMC}, at which the number of monomers in the monomer and micellar phases occur in equal proportions in the absence of polymer–micelle aggregates and is thus given by the expression

$$S_{\text{CMC}} = \left(\frac{k_0^-}{N k_0^+} \right)^{\frac{1}{N-1}}. \tag{1.6}$$

It is also convenient to define the concentration

$$S_{\text{CAC}} = \left(\frac{k_1^-}{k_1^+} \right)^{\frac{1}{M}}, \tag{1.7}$$

which, as we shall show, turns out to be the CAC for a polymer–surfactant solution.

Thus, we re-write (1.5) using expressions (1.6) and (1.7):

$$S_b = S + S_{\text{CMC}} \left(\frac{S}{S_{\text{CMC}}} \right)^N + M P_b \left(\frac{\left(\frac{S}{S_{\text{CAC}}} \right)^M}{1 + \left(\frac{S}{S_{\text{CAC}}} \right)^M} \right). \tag{1.8}$$

Plots of the concentrations S, S_m, P, and P_m given by (1.3), (1.4), and (1.8) as the bulk surfactant concentration varies are shown in Figure 1.6. We observe there are four distinct regions AB, BC, CD, and DE as labelled in Figure 1.6 where there is a phase transition[1] in the system, namely

[1]In the context of this thesis a *phase transition* of a polymer–surfactant (or surfactant-only) system refers to the transition from a state where the type of species in solution differs. For example, in a surfactant-only solution that is below the CMC only free monomers will be present in solution but for bulk concentrations that exceed the CMC there will be coexistence of both monomer and micellar species and hence a phase transition will occur.

AB $S_b < S_{\mathrm{CAC}}$

The monomer concentration remains below the CAC so only free monomers and polymers exist in solution.

BC $S_{\mathrm{CAC}} < S_b < MP_b + S_{\mathrm{CAC}}$

The monomer concentration reaches the CAC at point B, *i.e.* $S \approx S_{\mathrm{CAC}}$, and so polymer–micelle aggregates start to form. Thus, S_{CAC} is the CAC for a weakly interacting polymer–surfactant solution. As the bulk surfactant concentration increases the additional surfactant is bound up in polymer–micelle aggregates until all the polymer has been bound (point C). Hence, the surfactant monomer concentration remains constant at the CAC which is referred to as the *CAC plateau*.

CD $MP_b + S_{\mathrm{CAC}} < S_b < MP_b + S_{\mathrm{CMC}}$

Free polymers no longer exist since they are all bound in polymer–micelle aggregates, and so the increase in bulk surfactant concentration results in an increase in the free monomer concentration until the monomer concentration reaches the CMC at point D.

DE $S_b > MP_b + S_{\mathrm{CMC}}$

The monomer concentration is now at the CMC and so micelles start to form as the bulk surfactant concentration increases and as a result the monomer concentration plateaus again.

Bell [4] used asymptotic techniques to analyse the critical points in the concentration profiles for both the weakly interacting and strongly interacting polymer–surfactant systems and hence, in the large aggregation-number-limit ($N, M \to \infty$), obtained leading-order explicit expressions for the concentrations of the four bulk species in terms of the physical parameters of the system. In Chapter 2 we shall generalise this work by using similar asymptotic techniques to analyse the solutions to the model for a straining flow of a weakly interacting polymer–surfactant solution.

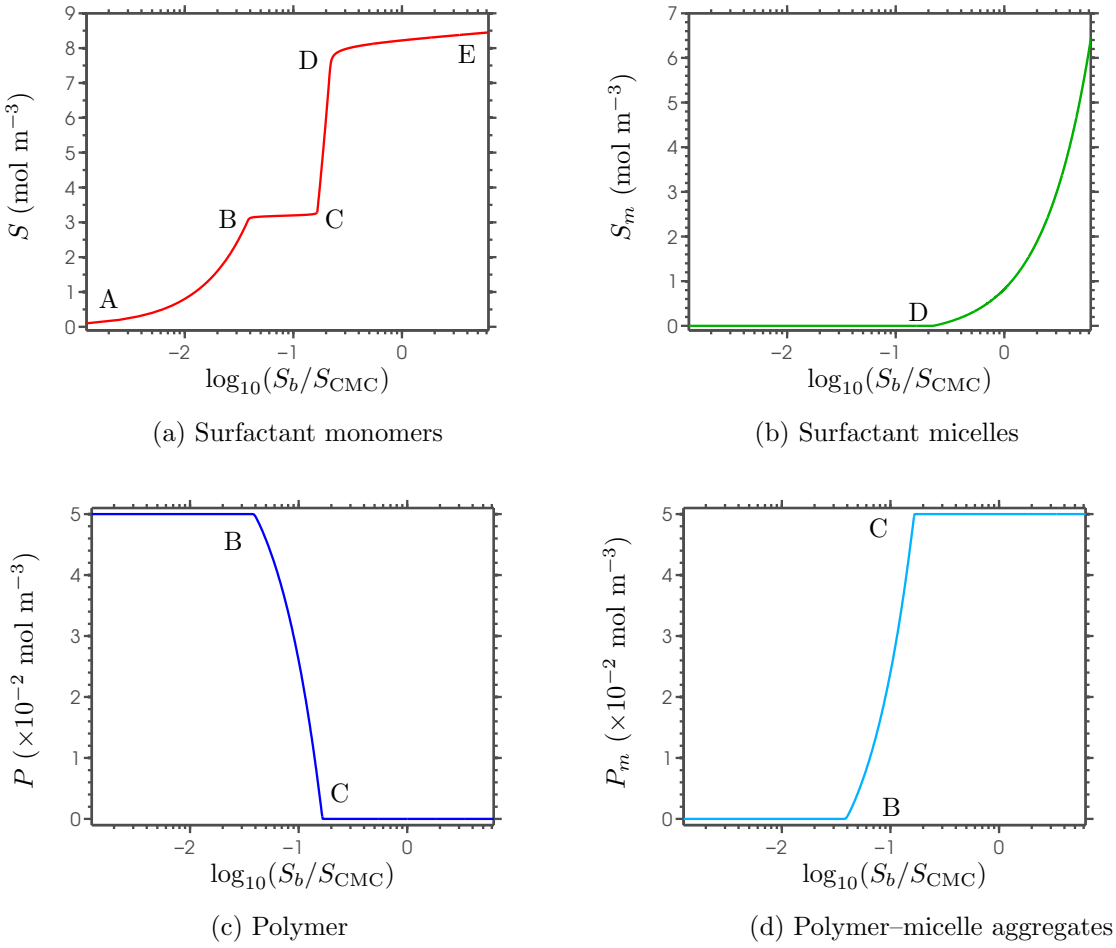

(a) Surfactant monomers

(b) Surfactant micelles

(c) Polymer

(d) Polymer–micelle aggregates

Figure 1.6: Plots showing the concentrations of (a) surfactant monomers, (b) surfactant micelles, (c) polymer, and (d) polymer–micelle aggregates as the dimensional bulk concentration, S_b, varies given by (1.3), (1.4) and (1.8). Parameters used are $S_{\mathrm{CMC}} = 8\,\mathrm{mol\,m^{-3}}$, $S_{\mathrm{CAC}} = 3.2\,\mathrm{mol\,m^{-3}}$, $P_b = 0.05\,\mathrm{mol\,m^{-3}}$, $N = 75$, and $M = 200$.

1.3.2 Adsorption and surface tension

In this section we quantify what is meant by the term 'surface excess' and describe the governing equations for surface excess concentration and the relationship with surface tension.

Surface excess

Following the description of Shaw [34] we first consider the idealised scenario where the interface between two phases is given by a plane, Σ, as shown schematically in Figure 1.7(a). In reality the adsorbed species lie in some region, σ, that encompasses the plane Σ as shown in Figure 1.7(b). We define the *surface excess*, n_i^σ, to be the number of moles of species i in the surface phase σ that is in excess of what would have been there if the bulk phases α and β had been extended to the plane Σ. Thus, the surface excess concentration (also referred to as adsorbed concentration) is given by

$$\Gamma_i = \frac{n_i^\sigma}{A}, \tag{1.9}$$

where A is the area of the interface Σ.

We note that although there is no distinction between the terms interface and surface we shall, as is customary, refer to the boundary between a gaseous phase and a non-gaseous phase as a surface and the boundary between two non-gaseous phases as an interface.

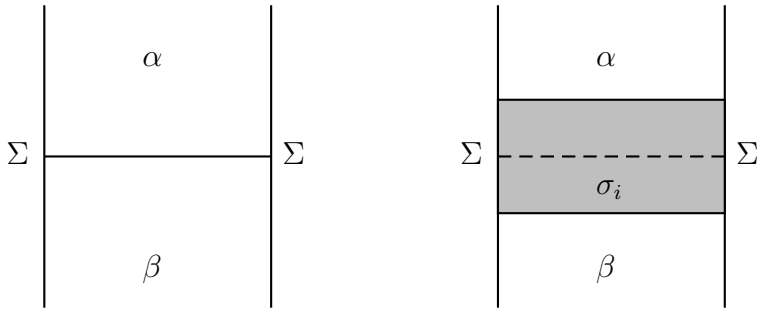

(a) ideal system (b) real system

Figure 1.7: Schematic of an adsorbing interface between two bulk phases α and β.

Adsorption

We assume that the adsorbed concentration for a single species, Γ, evolves by convection and diffusion at the surface and through exchange of molecules in the bulk. Thus, the equation for conservation of surfactant at the surface is

$$\frac{\partial \Gamma}{\partial t} + \nabla_s \cdot (\Gamma \mathbf{u}_s) + \Gamma(\mathbf{u} \cdot \mathbf{n})(\nabla_s \cdot \mathbf{n}) - D_\Gamma \nabla_s^2 \Gamma = j_s, \tag{1.10}$$

where $\mathbf{u}_s$ is the surface velocity, ∇_s is the surface gradient operator,[2] $\mathbf{n}$ is the unit outward normal to the surface, D_Γ is the surface diffusivity, and j_s is the source term associated with adsorption or desorption of surfactant onto or from the surface. For insoluble surfactants we can set $j_s = 0$ in (1.10). However, the surfactants of interest in this thesis are soluble and we only consider systems where surfactant monomers are the only surface-active species. We also assume that the interchange between the bulk and surface is diffusion controlled. Hence, the source term is given by some constitutive relation

$$j_s = j_s(\Gamma, S), \tag{1.11}$$

and is also equal to the flux of monomers from the bulk to the surface

$$j_s = -D_S \mathbf{n} \cdot \nabla_s S, \quad \text{on the surface}, \tag{1.12}$$

where S is the concentration of bulk surfactant monomers at the surface, and D_S is the diffusivity for surfactant monomers in the bulk. The concentration of surfactant monomers in the bulk must be prescribed in either (1.11) or (1.12), and we present the governing equation for S in §1.3.3.

For the surfactant systems of interest the most widely used constitutive relation for (1.11) assumes that the rate of adsorption is proportional to the sub-surface concentration of surfactant and the available space on the surface for adsorption and that the rate of desorption is proportional to the surfactant on the surface [8], *i.e.*

$$j_s = k^+(\Gamma_{\text{sat}} - \Gamma)S - k^-\Gamma, \tag{1.13}$$

[2]The surface gradient operator is defined as

$$\nabla_s := \nabla - \mathbf{n}\frac{\partial}{\partial n}.$$

where Γ_{sat} is the maximum concentration of adsorbed surfactant or the 'saturation concentration' and $k^{\pm}$ are the associated rate parameters for adsorption and desorption. We note that in practice Γ will never equal Γ_{sat} and so it is a theoretical limit.

Finally, we note that the adsorption process occurs very rapidly compared with the timescale for bulk processes and so this leads to the thermodynamic relationship known as the Langmuir isotherm [1]:

$$\Gamma = \frac{\Gamma_{\text{sat}} S}{k + S}, \tag{1.14}$$

where $k = k^{-}/k^{+}$ is referred to as the Langmuir rate constant.

Surface tension

The governing equations for the surfactant and fluid phases, which we present in §1.3.3, are coupled through two boundary conditions, one being the conservation equation for the adsorbed surfactant (1.10) and the second being a tangential-stress balance that we discuss in §1.3.3. This means that a relationship between the surfactant phases and surface tension must be prescribed. This is done via the Gibbs adsorption equation [34]:

$$\mathrm{d}\gamma = -RT\Gamma \ \mathrm{d}\left(\log \ S\right), \tag{1.15}$$

where γ is the surface tension, S is the concentration of free surfactant evaluated just below the surface, R is the universal gas constant, and T is the absolute temperature. Equation (1.15) assumes that for an ideal, dilute surfactant solution the relative activities are given by the free surfactant concentration.[3] For a more detailed discussion of the derivation of (1.15) we refer the reader to [34].

On substituting (1.14) for S into (1.15) and integrating we obtain the Frumkin equation

$$\gamma - \gamma_0 = RT\Gamma_{\text{sat}} \log\left(1 - \frac{\Gamma}{\Gamma_{\text{sat}}}\right), \tag{1.16}$$

[3]Note that for ionic surfactants that dissociate into two species at the surface there will be a modification to the right-hand side of (1.15) by a factor of two [34].

where γ_0 is the surface tension in the absence of adsorbed species. Alternatively, one could substitute (1.14) for Γ into (1.15) and on integrating would obtain the Szyszkowski equation of state

$$\gamma - \gamma_0 = -RT\Gamma_{\text{sat}} \log\left(1 + \frac{S}{k}\right). \tag{1.17}$$

Thus, if the velocity $\mathbf{u}$ is known and given suitable boundary conditions on the non-adsorbing surfaces we have sufficient information to close the problem for the adsorbed surfactant concentration.

1.3.3 Coupled surfactant–fluid models

In this thesis we assume that S evolves through convection and diffusion in the bulk given by

$$\frac{\partial S}{\partial t} + \mathbf{u} \cdot \nabla S = \nabla \cdot (D_S \nabla S) + J, \tag{1.18}$$

where J represents the mass transfer to and from other bulk phases. For example, if the surfactant solution is above the CMC then $J = -j_0$ given in (1.1) and we would require a similar equation to (1.18) for the micellar concentration S_m. We note that the monomer diffusivity, D_S, can in general depend upon the monomer concentration, S. However, in this thesis we assume that D_S and the diffusivities of any other bulk species are constant.

In Chapters 2 and 4 we model flowing surfactant solutions. If the velocity for the flow is not known at the outset and so must be determined as part of the problem, then the velocity vector, $\mathbf{u}$, and pressure, p, satisfy the incompressible Navier–Stokes equations

$$\nabla \cdot \mathbf{u} = 0, \quad \rho \frac{\mathrm{D}\mathbf{u}}{\mathrm{D}t} = -\nabla p + \mu \nabla^2 \mathbf{u} + \rho \mathbf{g}, \tag{1.19}$$

where ρ and μ are the constant fluid density and dynamic viscosity respectively, and $\mathbf{g}$ is acceleration due to gravity. Equations (1.19) are coupled to the surfactant equations given in §1.3.2 through the tangential stress balance at the free surface[4]

$$\mathbf{n} \cdot \boldsymbol{\sigma} \cdot \mathbf{t} = \nabla_s \gamma \cdot \mathbf{t}, \tag{1.20}$$

[4]Here the free surface is the air–water interface, hence the form of the left-hand side of (1.20).

where $\mathbf{t}$ is the unit tangent to the surface and

$$\boldsymbol{\sigma} = \begin{pmatrix} -p + 2\mu u_x & \mu(u_y + v_x) & \mu(u_z + w_x) \\ \mu(u_y + v_x) & -p + 2\mu v_y & \mu(v_z + w_y) \\ \mu(u_z + w_x) & \mu(v_z + w_y) & -p + 2\mu w_z \end{pmatrix}, \tag{1.21}$$

is the stress tensor. For closure, the fluid velocity must also satisfy the normal stress boundary condition

$$-\mathbf{n} \cdot \boldsymbol{\sigma} \cdot \mathbf{n} = \gamma \left(\nabla_s \cdot \mathbf{n} \right), \tag{1.22}$$

and kinematic boundary condition

$$\frac{\mathrm{D}}{\mathrm{D}t}\big(z - \eta(x, y, t)\big) = 0, \tag{1.23}$$

on the free surface, which is given by $z = \eta(x, y, t)$.

1.4 Typical parameter scales

In this section we detail typical sizes of the physical parameters which are relevant to the models presented in this thesis.

1.4.1 Typical lengthscales of surfactant systems

Chemical lengthscales are typically measured in Ångstroms where $1\,\text{Å} = 10^{-10}$ m. A single surfactant molecule is typically 20–30 Å. The number of surfactant bilayers in a multilayer typically ranges from 3 to 50 and the depth of a multilayer structure ranges from 10^2 Å to 10^4 Å (or 10^{-8} m to 10^{-6} m).

1.4.2 Typical concentrations of surfactant and polymer

Chemists typically express concentration in terms of molar concentration, M, and typical surfactant concentrations for the systems of interest are 10^{-4} M to 10^{-2} M. The SI unit for concentration is $\mathrm{mol\,m^{-3}}$ which we shall use throughout this thesis and we note that $1\,\mathrm{mol\,m^{-3}} = 1\,\mathrm{mM}$. Hence, the typical range for surfactant concentrations in SI units is $10^{-1}\,\mathrm{mol\,m^{-3}}$ to $10\,\mathrm{mol\,m^{-3}}$.

The concentration of adsorbed surfactant at an interface has units $\mathrm{mol\,m^{-2}}$ and is typically of order $10^{-6}\,\mathrm{mol\,m^{-2}}$.

The concentration of polymer in a polymer–surfactant system is very dilute and is typically an order of magnitude lower than that of the surfactant.

1.4.3 Estimating diffusivities

The diffusivities for surfactant monomers and micelles are typically of the order $10^{-10}\,\mathrm{m^2\,s^{-1}}$ and where possible we will quote experimentally obtained values. However, for the surfactant of interest in Chapter 3 the diffusivities are unknown and so we calculate them as follows. Assuming the micelles are spherically symmetric we use the Stokes–Einstein equation [1]:

$$D_{S_m} = \frac{k_B T}{6\pi\mu r}, \tag{1.24}$$

where r is the micelle radus, $k_B = 1.38 \times 10^{-23}\,\mathrm{J\,K^{-1}}$ is Boltzmann's constant, T is the absolute temperature, and μ is the viscosity of the solution. The ratio of the diffusivities can be estimated from the ratio of the molecular weights which suggests

$$\frac{D_S}{D_{S_m}} \sim N^{1/3}, \tag{1.25}$$

and hence if the aggregation number, N, is known the monomer diffusion coefficient can be determined.

The typical surface diffusivity for adsorbed surfactant is $D_\Gamma \leq 10^{-9}\,\mathrm{m^2\,s^{-1}}$ [17].

1.4.4 Other relevant physical parameters

Aggregation numbers

In this thesis we assume that micelles are monodisperse with a mean aggregation number, N, typically within the range 30–200. In general, the aggregation number for polymer–micelle aggregates, n, is lower than the aggregation number for free micelles, N. For example, for the weakly interacting system SDS/PVP[5] the number of monomers in a free micelle is approximately 80, compared with 20 in a polymer-bound micelle [33]. Cabane and Duplessix [7] determined the number of micelles in a polymer-bound micelle to be approximately 10.

Fluid properties

In this thesis we only consider very dilute surfactant and polymer–surfactant solutions and so for our purposes we take the fluid density, dynamic viscosity, and surface tension (in the absence of adsorbed species) to be those of water, *i.e.* $\rho = 10^3\,\mathrm{kg\,m^3}$, $\mu = 10^{-3}\,\mathrm{Pa\,s}$, and $\gamma_0 = 0.07\,\mathrm{N\,m^{-1}}$.

1.5 Neutron reflectometry

The most widely used technique to study surfactant and polymer–surfactant adsorption at an interface is neutron reflectometry (NR) [22]. This technique probes the surface of a thin film of surfactant or polymer–surfactant solution and determines the composition of surfactant and polymer at an interface. Other similar techniques, *e.g.* X-rays or ellipsometry use similar principles but neutron reflectometry (NR) has significant advantages over them. For example, the technique uses nuclear contrast (as opposed to electron contrast) and as a result is more sensitive to lighter elements such as hydrogen and carbon. In addition, neutrons are highly penetrating and, in general, non-perturbing, so are more advantageous to use over X-rays which may damage or modify some materials, in particular biological samples. One key attribute of NR is its sensitivity to isotopes so that isotopic substitution can be exploited by the method of *contrast variation*, which enables very accurate descriptions of composite surface structures to be determined.

[5] Sodium dodecyl sulfate/polyvunylpyrrolidone.

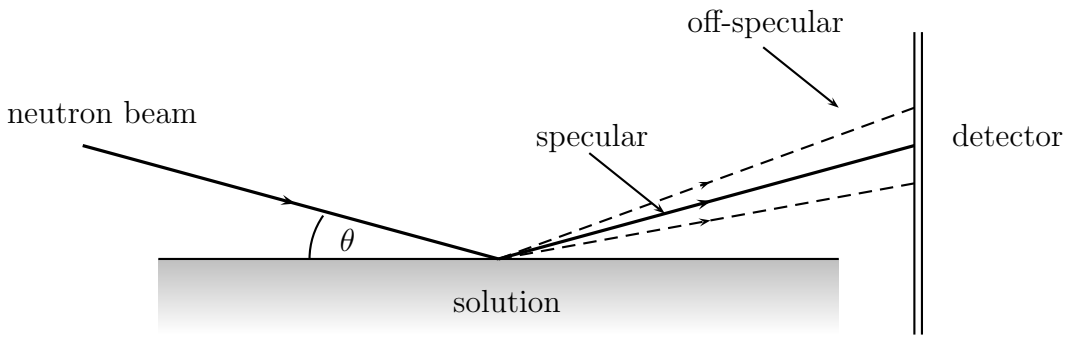

Figure 1.8: Schematic of a NR experiment set-up.

The technique itself uses a highly collimated beam of neutrons that is reflected off an extremely flat surface. The intensity of the reflected neutrons is measured as a function of the angle of incidence, θ, and the neutron wave length λ. A schematic diagram of NR experiment is shown in Figure 1.8. We refer the reader to the review paper of Lu and Penfold [22] for full details of NR techniques used to study surfactant (and polymer–surfactant) adsorption at the air–water interface. However, in the rest of this section we shall summarise the method to determine the concentration of adsorbed surfactant at an air–water interface, which is relevant to the experiments described in Chapter 3.

In neutron reflectivity experiments it is customary to define the reflectivity, R, in terms of the momentum transfer vector, which describes the change in momentum of a neutron after reflecting from the material. By convention the z-direction is taken normal to the solution interface and so the momentum transfer vector only has one component, Q, given by

$$Q = \frac{2\pi}{\lambda} \sin\theta. \tag{1.26}$$

The measured reflectivity data, $R(Q)$, is then fitted with an appropriate model in order to determine the amount and composition of surface species. One such model is given by the *kinetic approximation* [22]:

$$R(Q) = \frac{16\pi^2}{Q^2} \left| \int \rho(z) \mathrm{e}^{-iQz} \, \mathrm{d}z \right|^2, \tag{1.27}$$

where $\rho(z)$ is the scattering length density profile normal to the interface and is given by

$$\rho(z) = \sum_j b_j(z) n_j(z). \tag{1.28}$$

Here $b_j(z)$ is the scattering length and $n_j(z)$ is the number density of the jth atomic species. We note that in general $\rho(z)$ is modelled differently for different adsorption structures and used to fit (1.29) to the experimental data.

We consider the simplest model of a one-component, uniform surfactant monolayer to demonstrate how to determine the amount of adsorbed species at the interface. In this instance the simplified model for the reflectivity is given by [22]:

$$R(Q) = \frac{\pi^2}{Q^4}\Big((\rho_1-\rho_0)^2 + (\rho_2-\rho_1)^2 + 2(\rho_1-\rho_0)(\rho_2-\rho_1)\cos(2Qd)\Big), \tag{1.29}$$

where the subscripts denote the densities of (0) monolayer, (1) air, and (2) substrate and d is the thickness of the monolayer, which is to be determined from fitting to the data. Experimentally, one can add varying amounts of D_2O, which has a scattering length $b_D = 6.67 \times 10^{-5}$ Å, and H_2O, which has a scattering length $b_H = -3.74 \times 10^{-5}$ Å, such that the scattering length density of the substrate is the same as that of air, *i.e.* zero. Thus, for such a composition, 0.088 mole fraction of D_2O, there is no reflection from the air–water interface for water and we refer to it as null reflecting water (nrw). Hence, equation (1.29) simplifies greatly to

$$R(Q) = \frac{4\pi^2 b^2 n^2}{Q^4}\sin^2(Qd), \tag{1.30}$$

where the subscripts have been dropped for simplicity. The two parameters b and d can then be determined from fitting to the experimental data and used to give the concentration of adsorbed surfactant

$$\Gamma = \frac{1}{N_a A} = \frac{\rho d}{N_a b}\ , \tag{1.31}$$

where $N_a = 6.02 \times 10^{23}\,\text{mol}^{-1}$ is Avogadro's constant. More generally, the concentration of adsorbed surfactant for an arbitrary system would be given by

$$\Gamma = \frac{\rho d}{N_a \sum_j b_j}\ . \tag{1.32}$$

Characteristic reflectivity plots of the data and the fitted model for a surfactant monolayer, trilayer and multilayer are given in Figure 1.9. The peaks that occur in the fitted reflectivity plots are referred to as *Bragg peaks* and a more detailed description of their features is given in [22]. However, we note that the area under

the Bragg peak roughly scales with $1/N$ where N is the number of subsequent bilayers in the multilayer structure.

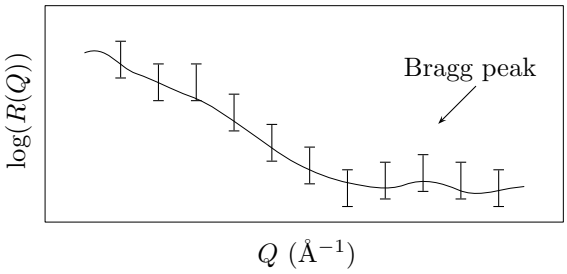

(a) monolayer

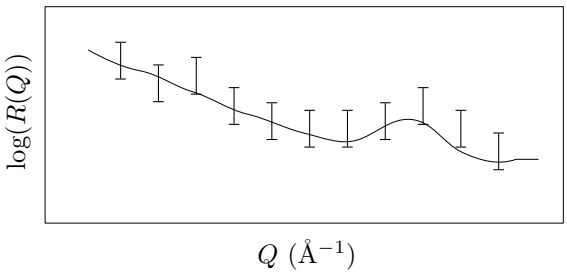

(b) trilayer

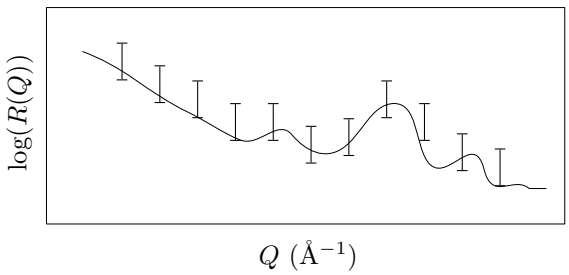

(c) multilayer

Figure 1.9: Typical reflectivity plots of the data (error bars) and fitted model (continuous line) for a surfactant (a) monolayer, (b) trilayer, and (c) multilayer.

1.6 Statement of originality

In Chapter 2 we follow the approach of Breward *et al.* [5] and Breward and Howell [6] in modelling the dynamics of the overflowing cylinder experiment. The flow field for the experiment at leading order is given in [5] in terms of the dilation rate which can be determined experimentally, as done in [6], or theoretically as done by Howell and Breward [16]. A more detailed review of papers [5, 6, 16] is given in §2.1.2. Our model differs from that of [6], which considers a surfactant-only solution, whereas we consider the effects of adding a weakly interacting polymer to the solution. The resulting model is then analysed using asymptotic techniques similar to those presented in Bell [4], but crucially our model is dynamic compared to the static models given in [4].

The mathematical models presented in Chapter 3 are based upon the experiments detailed in [25] and have not been considered before.

The theoretical models presented in Chapter 4 and 5 are all original work and the nonlinear third-order partial differential equation that underpins this work has not been derived systematically before. We note that Clarkson *et al.* [9] have looked at symmetry reductions to a class of PDEs, which for a special case ours falls into, but they did not compute any solutions analytically or numerically.

Chapter 2

Straining flow of a weakly interacting polymer–surfactant solution

In this chapter we consider the flow of a weakly interacting polymer–surfactant solution below a free surface, with the bulk surfactant concentration above the critical micelle concentration (CMC). We model mathematically the overflowing cylinder (OFC) experiment, shown in Figure 2.1. In this experiment water is pumped vertically through an inner cylinder and then flows over the rim into an outer cylinder, as shown schematically in Figure 2.2. The fluid that has overflowed into the outer cylinder is then recycled by the use of a pump, deeply submerged in the fluid, and a flow straightener is used to generate a flow profile that approximates plug flow well beneath the free surface (further details of the apparatus can be found in Manning-Benson *et al.* [23]). The flow at the free surface flows radially outwards from a stagnation point at the centre (see Breward *et al.* [5]). The cylinder is carefully levelled so that it overflows uniformly on all sides and once a stable flow has been established the free surface is indistinguishable from a horizontal plane (see Bain [3]). The OFC device is widely used for studying the dynamic surface properties of surfactant solutions. Non-invasive techniques such as surface light scattering, ellipsometry and neutron reflectometry can be used to determine the shape of the free surface, the surface tension and surface concentration of surfactant and subsurface velocities [3]. Details of OFC experiments performed on a surfactant-only solution can be found in Manning-Benson *et al.* [23, 24].

The mathematical model we propose describes the distribution of surfactant monomer, micelles, polymer, and polymer–micelle aggregates in the bulk and adsorbed surfactant

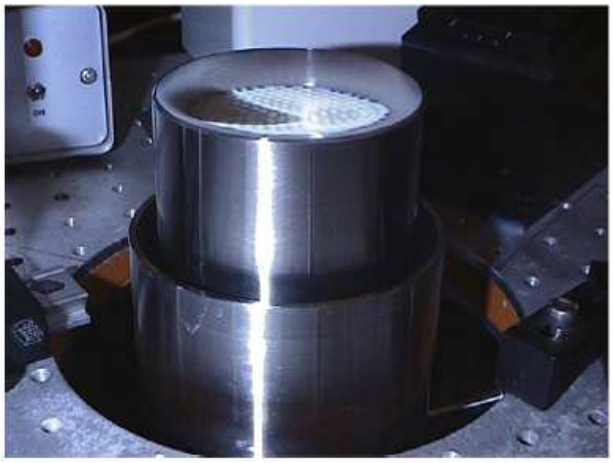

Figure 2.1: Image of the overflowing cylinder experiment taken from [3].

at the surface for given parameter regimes and follows closely methods used by Breward and Howell [6] for the OFC experiment performed on a surfactant-only solution above the CMC. Their model assumes that a single monolayer of surfactant forms at the free surface. If the free surface is expanding the concentration of adsorbed surfactant decreases and hence must be replenished from the bulk. Thus, there is a decrease in bulk surfactant concentration locally near the free surface and as a result micelles dissociate. In the model we propose, there will be polymer–micelle aggregates in the bulk that will also dissociate near the free surface because only surfactant monomers may adsorb at the free surface. The results of the model do indeed show a region near the free surface where no micelles or polymer–micelle aggregates are present. We are unable to compare our results for the polymer–surfactant system with any experimental data because at the time of writing no such data exists.

2.1 Review of the overflowing cylinder experiment

In this section we review the experimental observations and existing mathematical models of the overflowing cylinder experiment.

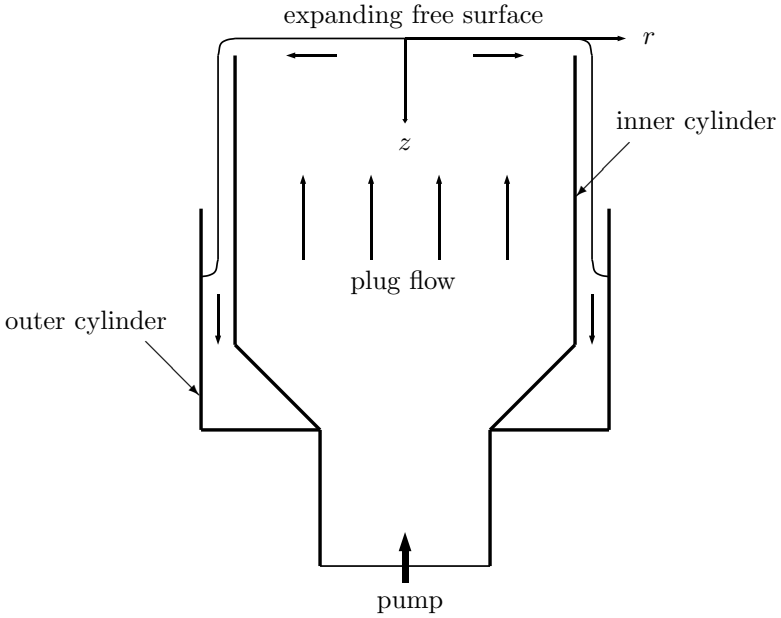

Figure 2.2: Schematic diagram of the overflowing cylinder experiment.

2.1.1 Experimental observations

The main experimental observations of the OFC experiment for a surfactant solution discussed in [3, 5, 16, 23, 24] are the following.

1. The overflowing cylinder has a typical radius of 4–8 cm and a typical pump velocity of $3\,\mathrm{mm\,s^{-1}}$.

2. The free surface is indistinguishable from a horizontal plane by the naked eye.

3. In the presence of surfactant the free surface can accelerate by more than an order of magnitude due to Marangoni effects. The radial surface velocity is zero at the centre of the cylinder and increases approximately linearly with distance from the stagnation point. The subsurface velocity decreases away from the free surface.

4. The adsorbed surfactant concentration is finite at the stagnation point and decreases slightly with distance from the centre. The value of the adsorbed concentration is significantly different from that which would be found under static conditions for the same bulk concentration.

5. Providing the pump velocity is above a critical value (to ensure the liquid overflows steadily) its effect on the surface velocity is negligible.

6. Similarly, the cylinder radius, so long as it is sufficiently large, has negligible effects on the flow.

2.1.2 Review of mathematical models of the OFC

A mathematical model for the fluid dynamics of the OFC for a sub-CMC surfactant-only solution has been developed in [5]. The model describes three coupled regions for the liquid velocity and surfactant concentration: (i) an inviscid bulk flow in which diffusion of surfactant is negligible, (ii) a hydrodynamic boundary layer in which viscous effects are significant, and (iii) a diffusive boundary layer where diffusion of surfactant is significant. The Froude number[1] for the experiment is at most 10^{-3} and so they make the assumption that gravity is strong enough to keep the free surface flat. They use asymptotic analysis to simplify the model and find that, because of a degeneracy in the boundary conditions at the free surface, the reduced model admits a one-parameter family of solutions. They suggest a method to determine the unknown parameter from experimental data and hence obtain a unique solution. Howell and Breward [16] extend the analysis of the model using asymptotic and numerical techniques to show that solutions typically develop one of two possible singularities. They show that, by eliminating both these singularities, there is a criterion to determine the free parameter (the surfactant concentration at the centre of the cylinder), namely that the surface concentration of surfactant is zero at the edge of the cylinder. We note that the free parameter determined experimentally or mathematically in either [5] or [16] is used to calculate the dilation rate of the expanding free surface.

This chapter extends the work of [6], who considered a mathematical model to describe the distribution of surfactant monomer and micelles in a steady straining flow beneath a fixed free surface. They use the results of [5, 16] to determine the coupling of the fluid dynamics to the surfactant solution but allow the bulk concentration to be above the CMC so that micelles will be present. The aggregation numbers for the surfactants of interest they consider are large, typically 80–100, and so they consider the large-aggregation-number limit in their asymptotic analysis. They also consider the limit where the monomer and micellar phases are everywhere in equilibrium, which simplifies the problem greatly. We shall consider both these limits in the analysis of the polymer–surfactant problem. More interestingly, [6] also showed that leading-order analytical solutions could be obtained in the non-equilibrium regime, and hence they determined the rate constant for micelle breakdown by comparison of their model with experimental data.

[1]The Froude number is given by $Fr = U_p/\sqrt{ag}$ where U_p is the pump velocity, a is the radius of the cylinder and g is acceleration due to gravity.

2.2 Derivation of the model

We consider an aqueous polymer–surfactant solution above the CMC so that micelles are present and, since we assume that the critical aggregation concentration (CAC) is lower than the CMC, polymer–micelle aggregates are also present in the solution. We denote the concentrations of surfactant monomers, micelles, polymers, and polymer–micelle aggregates by S, S_m, P, and P_m respectively, all of which have units mol m^{-3}. As discussed in §1.3.1 we assume that the formation of micelles and aggregates are single-step reactions and, invoking the law of mass action, we find that the rate, j_0, at which surfactant changes phase from monomer to micelle is given by

$$j_0 = k_0^+ S^N - k_0^- S_m, \tag{2.1}$$

where $k_0^\pm$ are the corresponding rate coefficients and N is the number of surfactant monomers in a free micelle. Similarly the rate, j_1, at which surfactant changes phase from monomer to aggregate is given by

$$j_1 = k_1^+ P S^M - k_1^- P_m, \tag{2.2}$$

where $k_1^\pm$ are the corresponding rate coefficients and $M = nm$ where n is the number of surfactant monomers in a polymer-bound micelle and m is the number micelles in a polymer–micelle aggregate. We refer to N and M as the aggregation numbers for a micelle and a polymer–micelle aggregate respectively in the rest of this chapter. Typical values for the aggregation numbers are $N \sim 80$ and $M \sim 200$ (see §1.4.4).

If all phases are advected with fluid velocity $\mathbf{u}$ whilst diffusing, then the four concentrations satisfy the reaction-advection-diffusion equations

$$\frac{\partial S}{\partial t} + \mathbf{u}\cdot\nabla S = D_S \nabla^2 S - N j_0 - M j_1, \tag{2.3a}$$

$$\frac{\partial S_m}{\partial t} + \mathbf{u}\cdot\nabla S_m = D_{S_m} \nabla^2 S_m + j_0, \tag{2.3b}$$

$$\frac{\partial P}{\partial t} + \mathbf{u}\cdot\nabla P = D_P \nabla^2 P - j_1, \tag{2.3c}$$

$$\frac{\partial P_m}{\partial t} + \mathbf{u}\cdot\nabla P_m = D_{P_m} \nabla^2 P_m + j_1, \tag{2.3d}$$

where D_S, D_{S_m}, D_P and D_{P_m} are the diffusion coefficients for each phase.

The fluid is assumed to be incompressible so that

$$\nabla \cdot \mathbf{u} = 0. \tag{2.4}$$

Following [6] we will focus on a model where the flow is radially symmetric below a flat air–liquid interface and the fluid is infinitely deep. Thus, we use polar co-ordinates (r, z), with the interface at $z = 0$ and the z-axis pointing vertically downwards into the fluid. Far away from the interface we assume that the surfactant and micelle concentrations are in equilibrium and also that the free polymer and aggregate concentrations are in equilibrium, *i.e.*

$$S_m \sim \frac{k_0^+}{k_0^-} S^N \qquad \text{and} \qquad P_m \sim \frac{k_1^+}{k_1^-} P S^M \qquad \text{as} \quad z \to \infty. \tag{2.5}$$

We also assume that, far away from the interface, the total bulk concentrations of surfactant and polymer, S_b and P_b respectively, are known, so that

$$S + N S_m + M P_m \to S_b \qquad \text{and} \qquad P + P_m \to P_b \qquad \text{as} \quad z \to \infty. \tag{2.6}$$

We assume that only surfactant monomers can adsorb at the interface and denote the concentration of adsorbed surfactant molecules by Γ. If we neglect surface diffusion, (for justification see [5]) then Γ evolves through advection along the interface, with surface velocity $\mathbf{u}_s(r, t) = \mathbf{u}(r, 0, t)$ and replenishment by monomer from the bulk:

$$D_S \frac{\partial S}{\partial z} = \frac{\partial \Gamma}{\partial t} + \nabla \cdot (\mathbf{u}_s \Gamma) \quad \text{at} \quad z = 0. \tag{2.7}$$

We also assume that the adsorbed phase is in thermodynamic equilibrium, with the monomer just below the surface so we can use the Langmuir isotherm [1] to determine Γ in terms of S, *i.e.*

$$\Gamma = \frac{\Gamma_{\text{sat}} S}{k + S} \quad \text{at} \quad z = 0, \tag{2.8}$$

where k is a constant measuring the ability of the surfactant monomers to adsorb at the interface and Γ_{sat} is the maximum concentration of the adsorbed surfactant monomers. For weakly interacting systems, the free polymers are not surface active and hence do not adsorb at the interface. Surfactant in micelles and polymer–micelle

aggregates does not directly adsorb without the micelles/aggregates first breaking up into monomers. Thus, the fluxes of S_m, P, and P_m must be zero at the interface:

$$D_{S_m}\frac{\partial S_m}{\partial z} = D_P\frac{\partial P}{\partial z} = D_{P_m}\frac{\partial P_m}{\partial z} = 0 \quad \text{at} \quad z = 0. \tag{2.9}$$

The initial profiles of all four concentrations are also assumed to be given:

$$S = S_I(r,z), \quad S_m = S_{mI}(r,z), \quad P = P_I(r,z), \quad P_m = P_{mI}(r,z) \quad \text{at} \quad t = 0. \tag{2.10}$$

If we assume that $\mathbf{u}$ is a known function of r, z, and t, then (2.3)–(2.10) form a closed system of equations for S, S_m, P, and P_m.

2.2.1 Nondimensionalisation

We nondimensionalise (2.3a)–(2.10) as follows:

$$\begin{aligned} &S = S_{\text{CMC}}S', \qquad S_m = \frac{S_{\text{CMC}}}{N}S'_m, \qquad P = P_bP', \qquad P_m = P_bP'_m, \qquad \Gamma = \Gamma_{\text{sat}}\Gamma', \\ &\mathbf{u} = \frac{D_S}{L}\mathbf{u}', \qquad r = Lr', \qquad z = Lz', \qquad t = \frac{L^2}{D_S}t', \end{aligned} \tag{2.11}$$

where L is a lengthscale to be determined and S_{CMC} is the CMC for the surfactant. We define the CMC and the CAC for the surfactant as in §1.3.1 by the expressions

$$S_{\text{CMC}} = \left(\frac{k_0^-}{Nk_0^+}\right)^{\frac{1}{N-1}} \quad \text{and} \quad S_{\text{CAC}} = \left(\frac{k_1^-}{k_1^+}\right)^{\frac{1}{M}}, \tag{2.12}$$

respectively. For ease of notation we drop the primes on the dimensionless variables and the resulting nondimensional equations are

$$\frac{\partial S}{\partial t} + \mathbf{u}\cdot\nabla S = \nabla^2 S - K_0\left(S^N - S_m\right) - K_1P^*\left(P\left(\frac{S}{\delta}\right)^M - P_m\right), \tag{2.13a}$$

$$\frac{\partial S_m}{\partial t} + \mathbf{u}\cdot\nabla S_m = D_1\nabla^2 S_m + K_0\left(S^N - S_m\right), \tag{2.13b}$$

$$\frac{\partial P}{\partial t} + \mathbf{u}\cdot\nabla P = D_2\nabla^2 P - K_1\left(P\left(\frac{S}{\delta}\right)^M - P_m\right), \tag{2.13c}$$

$$\frac{\partial P_m}{\partial t} + \mathbf{u}\cdot\nabla P_m = D_3\nabla^2 P_m + K_1\left(P\left(\frac{S}{\delta}\right)^M - P_m\right), \tag{2.13d}$$

with boundary conditions

$$S_m \sim S^N, \quad P_m \sim P\left(\frac{S}{\delta}\right)^M, \quad P + P_m \to 1, \quad S + S_m + P^* P_m \to S^* \quad \text{as} \quad z \to \infty, \tag{2.13e}$$

$$\frac{1}{\Gamma^*}\frac{\partial S}{\partial z} = \frac{\partial \Gamma}{\partial t} + \nabla \cdot (\mathbf{u}_s \Gamma), \quad \frac{\partial S_m}{\partial z} = \frac{\partial P}{\partial z} = \frac{\partial P_m}{\partial z} = 0, \quad \Gamma = \frac{S}{S+\beta} \quad \text{on} \quad z = 0, \tag{2.13f}$$

and initial conditions

$$S = S_I(r,z), \quad S_m = S_{mI}(r,z), \quad P = P_I(r,z), \quad P_m = P_{mI}(r,z) \quad \text{at} \quad t = 0, \tag{2.13g}$$

where the dimensionless parameters of the model are

$$\begin{aligned} &S^* = \frac{S_b}{S_{\text{CMC}}}, \quad P^* = \frac{MP_b}{S_{\text{CMC}}}, \quad \Gamma^* = \frac{\Gamma_{\text{sat}}}{LS_{\text{CMC}}}, \quad \delta = \frac{S_{\text{CAC}}}{S_{\text{CMC}}}, \quad \beta = \frac{k}{S_{\text{CMC}}}, \\ &K_0 = \frac{k_0^- L^2}{D_S}, \quad K_1 = \frac{k_1^- L^2}{D_S}, \quad D_1 = \frac{D_{S_m}}{D_S}, \quad D_2 = \frac{D_P}{D_S}, \quad D_3 = \frac{D_{P_m}}{D_S}. \end{aligned} \tag{2.13h}$$

2.2.2 Modelling the flow

We consider the OFC experiment, where the rate of expansion of the free surface is characterised by the dilation rate, α, which can be determined experimentally [5]. Thus, we assume that α is known and constant for steady flow. The flow near the interface is approximated by a steady stagnation point flow [5] with dimensional velocity field at leading order given by

$$\mathbf{u} = \frac{\alpha r}{2}\mathbf{e}_r - \alpha z \mathbf{e}_z, \tag{2.14}$$

where $\mathbf{e}_r$ and $\mathbf{e}_z$ are the unit vectors in the r and z directions respectively. Since α is known we choose the lengthscale L to satisfy

$$L = \sqrt{\frac{D_S}{\alpha}}. \tag{2.15}$$

The OFC experiment operates in steady state so we set all time derivatives to zero. We also assume that the concentrations S, S_m, P, and P_m only depend on z, so equations (2.13a)–(2.13d) reduce to

$$\frac{\mathrm{d}^2 S}{\mathrm{d}z^2} + z\frac{\mathrm{d}S}{\mathrm{d}z} = K_0\left(S^N - S_m\right) + K_1 P^*\left(P\left(\frac{S}{\delta}\right)^M - P_m\right), \tag{2.16a}$$

$$D_1\frac{\mathrm{d}^2 S_m}{\mathrm{d}z^2} + z\frac{\mathrm{d}S_m}{\mathrm{d}z} = -K_0\left(S^N - S_m\right), \tag{2.16b}$$

$$D_2\frac{\mathrm{d}^2 P}{\mathrm{d}z^2} + z\frac{\mathrm{d}P}{\mathrm{d}z} = K_1\left(P\left(\frac{S}{\delta}\right)^M - P_m\right), \tag{2.16c}$$

$$D_3\frac{\mathrm{d}^2 P_m}{\mathrm{d}z^2} + z\frac{\mathrm{d}P_m}{\mathrm{d}z} = -K_1\left(P\left(\frac{S}{\delta}\right)^M - P_m\right), \tag{2.16d}$$

with boundary conditions

$$S_m \sim S^N, \quad P_m \sim P\left(\frac{S}{\delta}\right)^M, \quad P + P_m \to 1, \quad S + S_m + P^* P_m \to S^* \quad \text{as} \quad z \to \infty, \tag{2.16e}$$

$$\frac{\mathrm{d}S}{\mathrm{d}z} = \frac{\Gamma^* S}{\beta + S} \quad \text{and} \quad \frac{\mathrm{d}P}{\mathrm{d}z} = \frac{\mathrm{d}S_m}{\mathrm{d}z} = \frac{\mathrm{d}P_m}{\mathrm{d}z} = 0 \quad \text{on} \quad z = 0. \tag{2.16f}$$

The dimensionless parameters N, M, β, δ, D_1, D_2, and D_3 depend only on the surfactant and polymer under consideration. Of these N and M are large, as discussed earlier, and β is usually small, typically about $O(10^{-2})$ [6]. The CAC is assumed to be less than the CMC but not by more than an order of magnitude, so typically $\delta = O(10^{-1})$ [6]. The diffusivities of the larger species S_m, P, and P_m are typically less than the diffusivity of the free monomers but not by more than an order of magnitude, *i.e.* $D_i = O(10^{-1})$ for $i = 1, 2, 3$ [27]. The parameters S^*, P^*, and Γ^* depend on the bulk concentrations of surfactant and polymer and the flow rate for the experiment but are all typically of order 1 [6]. The final parameters K_0 and K_1 are proportional to the micelle and polymer–micelle aggregate dissociation rates respectively, which in general are not known. However, these processes are widely believed to be instantaneous in the polymer–surfactant systems we are concerned with, which implies that K_0 and K_1 are large. Thus, in the following section we take the limit K_0, $K_1 \to \infty$ with K_0/K_1 fixed which corresponds to both the monomer/micellar phases and the monomer/polymer–micelle aggregate phases being in equilibrium everywhere.

2.2.3 The equilibrium limit

We simplify (2.16) by considering the equilibrium limit K_0, $K_1 \to \infty$ with K_0/K_1 fixed. In this limit we find that to leading order the monomer and micellar phases are in equilibrium

$$S_m = S^N, \tag{2.17}$$

and the free monomer and free polymer phases are in equilibrium with the polymer–micelle aggregate phase

$$P_m = P\left(\frac{S}{\delta}\right)^M. \tag{2.18}$$

As a result, the micellar concentration, S_m, and polymer–micelle aggregate concentration, P_m, decouple and we obtain the simplified system to leading order:

$$\frac{\mathrm{d}^2}{\mathrm{d}z^2}\left(S + D_1 S^N + D_3 P^* P\left(\frac{S}{\delta}\right)^M\right) + z\frac{\mathrm{d}}{\mathrm{d}z}\left(S + S^N + P^* P\left(\frac{S}{\delta}\right)^M\right) = 0, \tag{2.19}$$

$$\frac{\mathrm{d}^2}{\mathrm{d}z^2}\left(D_2 P + D_3 P\left(\frac{S}{\delta}\right)^M\right) + z\frac{\mathrm{d}}{\mathrm{d}z}\left(P + P\left(\frac{S}{\delta}\right)^M\right) = 0, \tag{2.20}$$

$$P + P\left(\frac{S}{\delta}\right)^M \to 1, \qquad S + S^N + P^* P\left(\frac{S}{\delta}\right)^M \to S^* \qquad \text{as} \quad z \to \infty, \tag{2.21}$$

$$\frac{\mathrm{d}S}{\mathrm{d}z} = \frac{\Gamma^* S}{\beta + S} \quad \text{and} \qquad \frac{\mathrm{d}P}{\mathrm{d}z} = 0 \qquad \text{on} \quad z = 0, \tag{2.22}$$

with micelle and polymer–micelle aggregate concentrations given by equations (2.17) and (2.18) respectively.

To make the problem more tractable, we will make further assumptions about the magnitudes of the diffusion coefficients of each phase. The rest of this chapter is divided into two cases:

(i) Case 1 – we assume that all four phases have equal diffusion coefficients;

(ii) Case 2 – we assume that the polymer and polymer–micelle aggregate phases only have equal diffusion coefficients.

2.3 Case 1: Diffusion coefficients for all phases equal

We first suppose the diffusion coefficients of all four phases are equal by setting $D_1 = D_2 = D_3 = 1$ in the model. This allows us to integrate equations (2.19) and (2.20) and we obtain the general solutions

$$S + S^N + P^* P \left(\frac{S}{\delta}\right)^M = a_0 + b_0 \mathrm{erfc}\left(\frac{z}{\sqrt{2}}\right), \tag{2.23a}$$

$$P + P\left(\frac{S}{\delta}\right)^M = a_1 + b_1 \mathrm{erfc}\left(\frac{z}{\sqrt{2}}\right), \tag{2.23b}$$

where a_0, b_0, a_1, and b_1 are constants of integration. Applying the boundary conditions as $z \to \infty$ sets $a_0 = S^*$, $a_1 = 1$ and the no flux boundary condition for P given in (2.22) sets $b_1 = 0$. Thus we can write

$$S + S^N + P^* \frac{S^M}{\delta^M + S^M} = S^* - \left(S^* - S_i - S_i^N - \frac{P^* S_i^M}{\delta^M + S_i^M}\right) \mathrm{erfc}\left(\frac{z}{\sqrt{2}}\right), \tag{2.24a}$$

$$P = \frac{\delta^M}{\delta^M + S^M}, \tag{2.24b}$$

where $S_i = S(0)$ is the subsurface monomer concentration and using the flux condition (2.22) for monomer we obtain the implicit equation for S_i

$$S_i + {S_i}^N + P^* \frac{{S_i}^M}{\delta^M + {S_i}^M} = S^* - \sqrt{\frac{\pi}{2}} \frac{\Gamma^*}{\beta + S_i} \left(S_i + N S_i^N + \frac{M P^* \delta^M S_i^M}{(\delta^M + S_i^M)^2}\right). \tag{2.25}$$

Hence, we have determined analytic expressions for all the species in the system with the micelle and polymer–micelle aggregate concentrations given by

$$S_m = S^N \qquad \text{and} \qquad P_m = \frac{S^M}{\delta^M + S^M}. \tag{2.26}$$

We note that

$$P + P_m = 1, \tag{2.27}$$

holds everywhere in the fluid, and represents conservation of polymer.

As discussed in [6] there is a complication to assuming the equilibrium limit. The flux boundary conditions (2.16f) for the micelle and polymer–micelle aggregates on the free surface are approximately satisfied providing the subsurface concentration is

below the CMC and CAC respectively. However, if S_i becomes sufficiently close to 1 or δ, then the flux boundary conditions are no longer satisfied to leading order. To illustrate this point, we consider the flux boundary condition for the polymer–micelle aggregate given by

$$\frac{\mathrm{d}P_m}{\mathrm{d}z}\Big|_{z=0} \approx \frac{M\delta^M S^{M-1}}{(\delta^M + S^M)^2}\frac{\mathrm{d}S}{\mathrm{d}z}\Big|_{z=0} = \frac{M\Gamma^*\delta^M S_i^M}{(\beta + S_i)(\delta^M + S_i^M)^2} \tag{2.28}$$

where the right-hand side is order one if

$$S_i \sim \delta\left(1 - \frac{1}{M}\log\left(\frac{M\Gamma^*}{\beta+\delta}\right)\right). \tag{2.29}$$

The leading order approximation solution to (2.25), assuming that S_i/δ is order one but $S_i < 1$, is given by

$$S_i \sim \delta\left[1 - \frac{1}{M}\log\left(\frac{M\Gamma^*}{\beta+\delta}\right) + \frac{1}{M}\log\left(\frac{\sqrt{2}}{P^*\sqrt{\pi}}\left(S^* - \delta\left(1 + \frac{\Gamma^*}{\beta+\delta}\sqrt{\frac{\pi}{2}}\right)\right)\right)\right]. \tag{2.30}$$

Thus, by (2.29) we must have that

$$S^* \sim S^*_{Pm} := \delta\left(1 + \sqrt{\frac{\pi}{2}}\frac{\Gamma^*}{\beta+\delta}\right) + \sqrt{\frac{\pi}{2}}P^*. \tag{2.31}$$

For parameters $\delta = 0.4$, $\Gamma^* = 2$, $P^* = 1.2$, and $\beta = 0.02$ the critical value of the bulk surfactant concentration, $S^*_{Pm} \approx 4.29$. For bulk surfactant concentrations higher than this the limit $K_1 \to \infty$ fails in a neighbourhood of the free surface $z = 0$.

Similarly, there is a critical bulk surfactant concentration at which the limit $K_0 \to \infty$ fails given by

$$S^* \sim S^*_{Sm} := 1 + P^* + \sqrt{\frac{\pi}{2}}\left(\frac{\Gamma^*}{\beta+1} + 1\right). \tag{2.32}$$

For parameters $\delta = 0.4$, $\Gamma^* = 2$, $P^* = 1.2$, and $\beta = 0.02$ the critical value of the bulk surfactant concentration, $S^*_{Sm} \approx 5.91$.

We note that in such cases as described above there will be weak boundary layers near $z = 0$ for the bulk concentration ranges:

$S^*_{Pm} \lesssim S^* < S^*_{Sm}$
: there will be a boundary layer at the surface of order $1/\sqrt{K_1}$, in which the polymer–micelle aggregate phase will be out of equilibrium with the monomer phase;

$S^*_{Sm} \lesssim S^*$
: there will be a second boundary layer at the surface of order $1/\sqrt{K_0}$, in which the micellar phase will be out of equilibrium with the monomer phase.

Figure 2.3 shows plots of the monomer concentration, S, which is given implicitly by equation (2.24a), and the polymer, micelle and polymer–micelle aggregate concentrations that are given by (2.24b) and (2.26). We first discuss the features of the most general case shown in the Figure 2.3(a) when S^* is less than the critical value, S^*_{Pm}, given in (2.31). At depth, the monomer concentration is at the CMC, *i.e.* $S \approx 1$, and all of the polymer is bound in aggregate form. As z decreases towards the interface at $z = 0$, the concentration of micelles decreases, representing depletion of monomer from the micelles as the fluid moves towards the interface where surfactant monomers can adsorb. Once the micelles have been fully depleted, the surfactant monomer concentration falls below the CMC, *i.e.* $S < 1$, and continues to decrease. This is because it is more energetically favourable for free monomer in the bulk to adsorb at the interface rather than form micelles. The monomer concentration has a plateau at the CAC, *i.e.* $S \approx \delta$. At this point, monomer begins to be depleted from the polymer–micelle aggregates and the concentration of aggregates in the bulk decreases, whilst the concentration of free polymer now increases. This continues until all of the surfactant has been depleted from the aggregates and the polymer concentration is at the bulk polymer concentration, i.e $P \approx 1$. At this point the monomer concentration now falls below the CAC and continues to decrease until it is at the surface concentration, *i.e.* $S = S_i$. In contrast, Figure 2.3(b) shows plots of the solutions for $S^*_{Pm} \lesssim S^* < S^*_{Sm}$ and so there is no longer a region near the surface where only free surfactant and polymer exists and we note that polymer–micelle aggregates are now present throughout the whole solution. Furthermore, the flux of polymer–micelle aggregates at the surface is clearly non-zero which agrees with our earlier analysis that there must be a region near the surface where the equilibrium limit for the polymer–micelle aggregates, $K_1 \to \infty$, no longer holds. Figure 2.3(c) shows plots of the solutions for $S^*_{Sm} \lesssim S^*$. In this case polymer-micelle aggregates and micelles exist all the way up to the surface $z = 0$ and the micellar flux is non-zero, indicating that the limit $K_0 \to \infty$ also fails in a small region near $z = 0$.

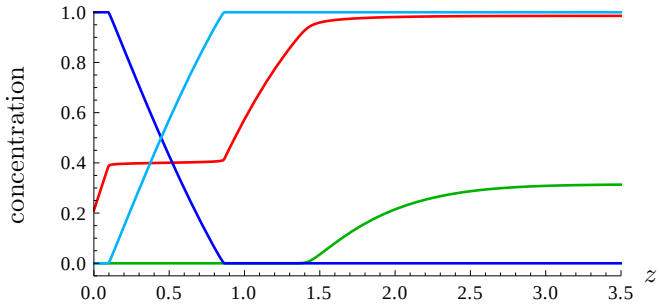

(a) $S^* = 2.5$

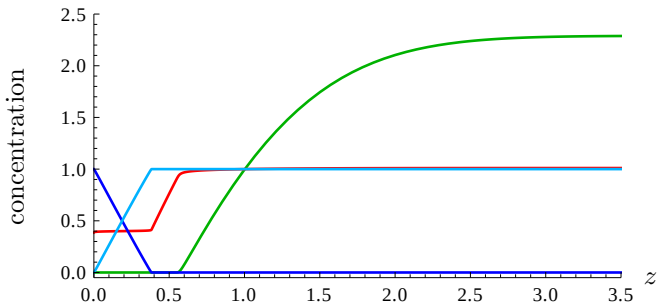

(b) $S^* = 4.5$

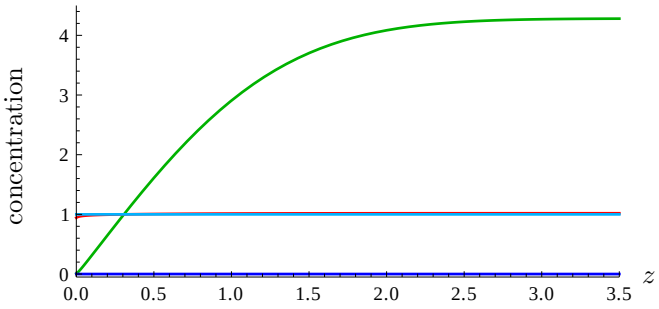

(c) $S^* = 6.5$

Figure 2.3: Graph of the concentrations S (red), S_m (green), P_m (light blue), and P (blue) obtained by solving (2.24) and (2.25). Parameters used are $P^* = 1.2$, $\Gamma^* = 2$, $\beta = 0.02$, $\delta = 0.4$, $N = 80$, and $M = 200$.

2.3.1 Large-aggregation-number limit

We now seek to explain the behaviour observed in Figure 2.3 by exploiting the fact that the aggregation numbers for micelles, N, and aggregates, M, are large. The asymptotic analysis is particularly straightforward in this simple example where the exact solutions (2.24a)–(2.26) are available, but will guide us in studying more realistic scenarios, such as Case 2. For simplicity, we shall assume that the equilibrium limits $K_0, K_1 \to \infty$ hold everywhere in the fluid, *i.e.* the bulk surfactant concentration is below the critical value given by (2.31).

By setting

$$\epsilon = 1/M \quad \text{and} \quad \nu = N/M < 1 \tag{2.33}$$

we consider the large-aggregation-number limit $\epsilon \to 0$ with ν fixed. We consider the richest asymptotic behaviour of the model by assuming that all other parameters are order 1 in (2.24a)–(2.26) and expand the dependent variables in the form

$$S \sim S_0 + \epsilon S_1 + \ldots \qquad P \sim P_0 + \epsilon P_1 + \ldots$$
$$S_m \sim S_{m_0} + \epsilon S_{m_1} + \ldots \qquad P_m \sim P_{m_0} + \epsilon P_{m_1} + \ldots$$

as $\epsilon \to 0$. As polymer is conserved, we only consider the aggregate concentration in the rest of this section, and note that the polymer concentration is given by $P = 1 - P_m$ to all orders of ϵ. Furthermore, since we assume that the CAC is always below the CMC for a weakly interacting polymer–surfactant system then $0 < \delta < 1$. Hence, there are four cases in our asymptotic approximations to equation (2.24a) to consider:

(i) $S < \delta$, the monomer concentration is below the CAC (and hence the CMC);

(ii) $S \approx \delta$, the monomer concentration is at the CAC ;

(iii) $\delta < S < 1$, the monomer concentration is above the CAC but below the CMC;

(iv) $S \approx 1$, the monomer concentration is at the CMC.

2.3.1.1 Leading-order solutions

Since micelles and polymer–micelle aggregates do not adsorb we assume that the monomer concentration at the interface is below the CAC, so that $S_i < \delta$. At leading order S_i is thus determined explicitly from (2.25) as

$$S_i = \frac{1}{4}\left(2S^* - 2\beta - \sqrt{2\pi}\Gamma^* + \sqrt{16S^*\beta + \left(2S^* - 2\beta - \sqrt{2\pi}\Gamma^*\right)^2}\right), \tag{2.34}$$

which is only valid when S^* is less than the critical concentration given in (2.31).

In a small region below the interface there is a region in which the monomer concentration is below the CAC and at leading order we assume this to be true. Thus, the leading-order solutions of (2.24a), (2.24b), and (2.26) are given by

$$S_0 = S^* - (S^* - S_i)\mathrm{erfc}\left(\frac{z}{\sqrt{2}}\right), \tag{2.35a}$$

$$S_{m_0} = 0, \tag{2.35b}$$

$$P_{m_0} = 0, \tag{2.35c}$$

provided that $S_0 < \delta$. As we would expect, only unbound surfactant monomers and polymers are present to leading order in a region near the interface.

The solutions (2.35) hold until the monomer concentration reaches the CAC when $S_0 = \delta$. This occurs at $z = z_1$ where z_1 is defined by the equation

$$\mathrm{erfc}\left(\frac{z_1}{\sqrt{2}}\right) = \frac{S^* - \delta}{S^* - S_i}. \tag{2.36}$$

As we would anticipate, for there to exist a solution of (2.36) for z_1 the bulk surfactant concentration must exceed the CAC, *i.e.* we must have $S^* > \delta$.

For $z > z_1$ we have a region where aggregates are present along with surfactant monomers and unbound polymers. For this region the approximations to the leading-order equations (2.24a), (2.24b), and (2.26) are given by

$$S_0 = \delta, \tag{2.37a}$$

$$S_{m_0} = 0, \tag{2.37b}$$

$$P_{m_0} = \frac{1}{P^*}\left(S^* - \delta - (S^* - S_i)\mathrm{erfc}\left(\frac{z}{\sqrt{2}}\right)\right), \tag{2.37c}$$

which hold until all of the unbound polymer has bound to surfactant to become aggregates. Thus, we have that $P_{m_0} = 1$ at $z = z_2$, where z_2 is defined by the equation

$$\operatorname{erfc}\left(\frac{z_2}{\sqrt{2}}\right) = \frac{S^* - P^* - \delta}{S^* - S_i}. \tag{2.38}$$

There exists a real solution of (2.38) for z_2 provided $S^* > P^* + \delta$, so the bulk surfactant concentration must be greater than the sum of the CAC and the concentration of aggregate-bound surfactant.

For $z > z_2$ there is a region of polymer–micelle aggregates and surfactant monomers and the concentration of unbound polymer is negligible. In this region the approximations to the leading-order equations (2.24a), (2.24b), and (2.26) are given by

$$S_0 = S^* - P^* - (S^* - S_i)\operatorname{erfc}\left(\frac{z}{\sqrt{2}}\right), \tag{2.39a}$$

$$S_{m_0} = 0, \tag{2.39b}$$

$$P_{m_0} = 1, \tag{2.39c}$$

which hold until the surfactant monomer concentration reaches the CMC. This occurs when $S \approx 1$ at $z = z_3$, where z_3 is defined by the equation

$$\operatorname{erfc}\left(\frac{z_3}{\sqrt{2}}\right) = \frac{S^* - P^* - 1}{S^* - S_i}. \tag{2.40}$$

For there to exist a solution of equation (2.40) for z_3 we require that $S^* > 1 + P^*$ so the bulk surfactant concentration must be greater than the sum of the CMC and the concentration of aggregate-bound surfactant.

For $z > z_3$, the surfactant monomer concentration is at the CMC and micelles form in the bulk. The approximations to the leading-order equations (2.24a), (2.24b), and (2.26) for this region are given by

$$S_0 = 1, \tag{2.41a}$$

$$S_{m_0} = S^* - 1 - P^* - (S^* - S_i)\operatorname{erfc}\left(\frac{z}{\sqrt{2}}\right), \tag{2.41b}$$

$$P_{m_0} = 1. \tag{2.41c}$$

Provided that we are in a regime where $S^* > 1 + P^*$ we have thus defined four distinct regions, which are separated by the boundaries at $z = z_1$, $z = z_2$, and

$z = z_3$. The boundaries can be expressed in terms of the dimensionless parameters δ, S^*, and P^*. Hence, we know explicitly how the positions of the boundaries depend on the parameters of the model, something that the exact solutions alone could not determine. Figure 2.4 compares the leading-order asymptotic solutions with the exact solutions (2.24)–(2.26). There is good agreement between the exact and asymptotic solutions and the agreement will improve as ϵ decreases.

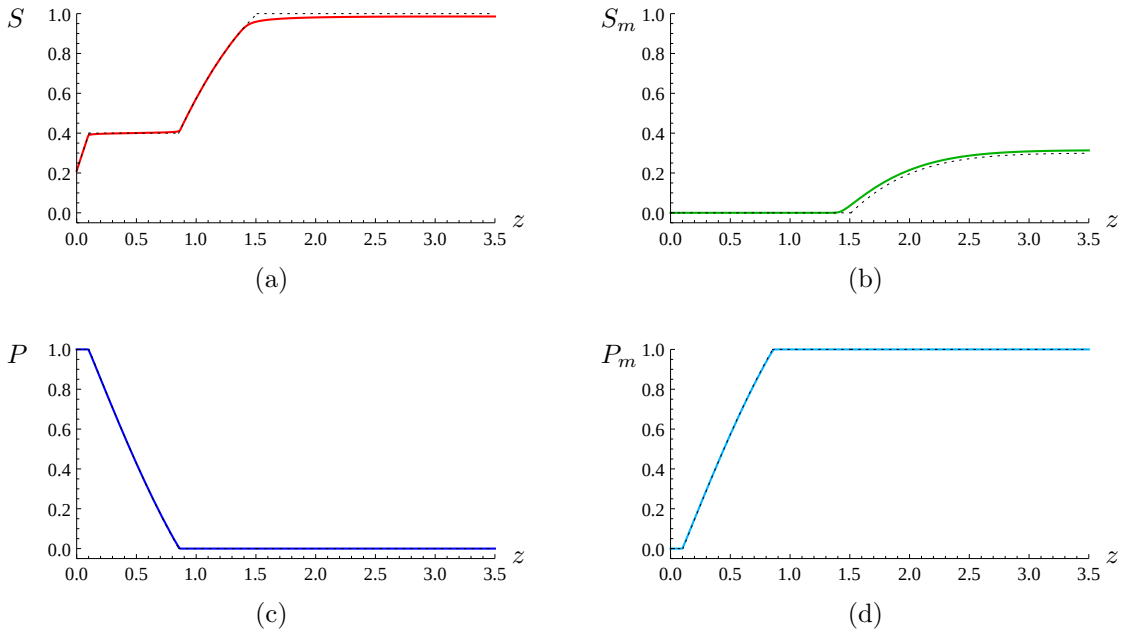

Figure 2.4: Graphs that compare the exact solutions (continuous curves) given in (2.24)–(2.26) with the leading-order asymptotic solutions (dotted curves) for the concentrations of (a) monomers, (b) micelles, (c) polymers, and (d) polymer–micelle aggregates. Parameters used are $S^* = 2.5$, $P^* = 1.2$, $\Gamma^* = 2$, $\beta = 0.02$, $\delta = 0.4$, $N = 80$, and $M = 200$.

We compare what happens to the agreement between the exact solutions (2.24)–(2.26) and the leading-order asymptotic solutions if we vary certain parameters of the model. Firstly, we consider the effect of varying S^* and P^*, which corresponds to varying the bulk surfactant and bulk polymer concentrations respectively. In Figure 2.5 we plot S, S_m, and P_m, as the parameters S^* and P^* are varied independently, while all other parameters are held constant.[2] The agreement between the exact solutions and leading-order asymptotic solutions improves as S^* increases as shown in Figures 2.5(a), 2.5(c), and 2.5(e). Conversely, if we now vary P^* and keep S^* fixed, as

[2]We omit plots for the polymer concentration, P, as it is directly related to the aggregate concentration, P_m, by (2.27) and thus P will behave in a similar way to P_m as the parameters S^* and P^* are varied.

shown in Figures 2.5(b), 2.5(d), and 2.5(f), the agreement between the exact solutions and leading-order asymptotic solutions decreases as P^* increases. We discuss further the observed dependence of the exact and leading-order asymptotic solutions agreement on the parameters S^* and P^* in §2.3.1.3.

Figure 2.5(e) shows that the depth at which polymer–micelle aggregates start to form decreases as S^* increases, whereas Figure 2.5(f) shows that an increase in P^* does not affect the depth at which aggregates form. Comparing Figure 2.5(a) with Figure 2.5(b) we observe that the length of the plateau of the monomer concentration at the CAC decreases as S^* increases but increases as P^* increases. On comparing Figure 2.5(c) with Figure 2.5(d) we observe that the depth at which micelles start to form decreases as S^* increases, and increases as P^* increases. This clearly indicates that there is a dependence of the key features of the graph on the bulk concentrations.

Secondly we vary the aggregation numbers N and M independently in our exact solutions and compare these with the leading-order asymptotic solutions, that are independent of N and M, as shown in Figure 2.6. By varying N and keeping M fixed we observe that there is a variation in the agreement between the exact and leading-order asymptotic solutions in the micellar region, *i.e.* for $z > z_3$, as shown in Figures 2.6(a) and 2.6(c). In Figure 2.6(e) there is no visible effect on the agreement between exact and leading-order asymptotic solutions for P_m as M increases.

Similarly, comparing the agreement between exact and leading-order asymptotic solutions as M varies with N fixed we observe a variation in agreement in the region where the monomer concentration plateaus. In particular, Figures 2.6(d) and 2.6(f) show that there is an improvement in the agreement as N increases near $z = z_2$ and $z = z_3$. Figure 2.6(d) shows that there is a negligible effect on the agreement for the micelle concentration as M increases. Therefore, for $0 < z < z_3$ we expect that the order ϵ correction terms for asymptotic expansions of S, P, and P_m will be non-zero whereas the order ϵ term in the asymptotic expansion of S_m will be zero. For $z > z_3$ we expect that the next order terms in the asymptotic expansions of S and S_m will be non-zero and will in-fact be of order $1/N$, *i.e.* order ϵ/ν, whereas the next order terms in the asymptotic expansions of P and P_m will be zero.

The disagreement between the exact and leading-order asymptotic solutions is small but persistent as we vary the parameters S^* and P^* in the model. To obtain a more accurate agreement for a wider range or parameter values we must seek the next order terms in the asymptotic expansion for S, S_m, P, and P_m, which we shall do next.

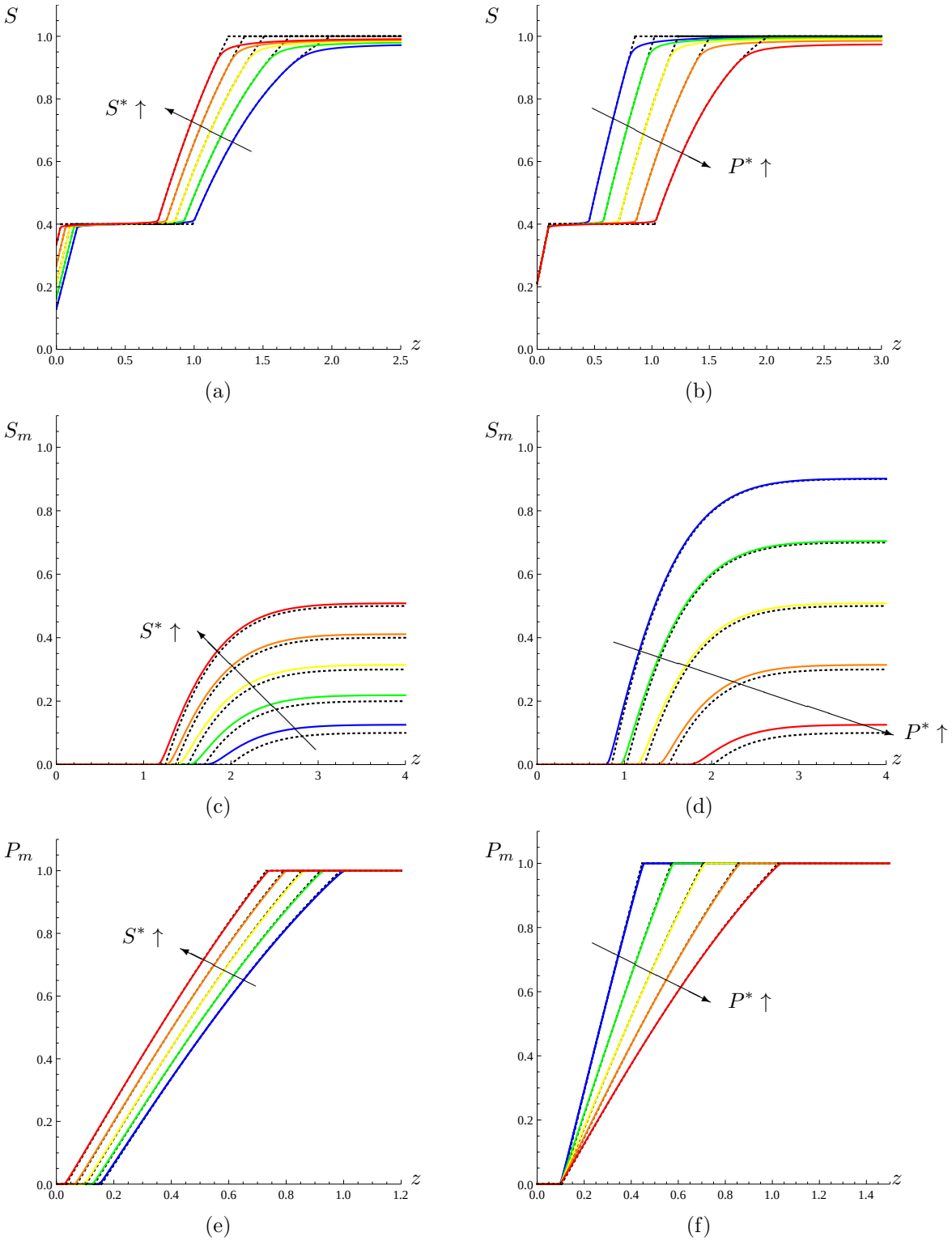

Figure 2.5: Graphs that compare the exact solutions (continuous curves) to the leading-order asymptotic solutions (dotted curves) for the concentrations of (a) monomers, (c) micelles, (e) polymer–micelle aggregates, with $S^* = [2.3,\ 2.4,\ 2.5,\ 2.6,\ 2.7]$, $P^* = 1.2$ and for the concentrations of (b) monomers, (d) micelles, (f) polymer–micelle aggregates, with $P^* = [0.6,\ 0.8,\ 1.0,\ 1.2,\ 1.4]$, $S^* = 2.5$. The other parameters used are $\Gamma^* = 2$, $\beta = 0.02$, $\delta = 0.4$, $N = 80$, and $M = 200$.

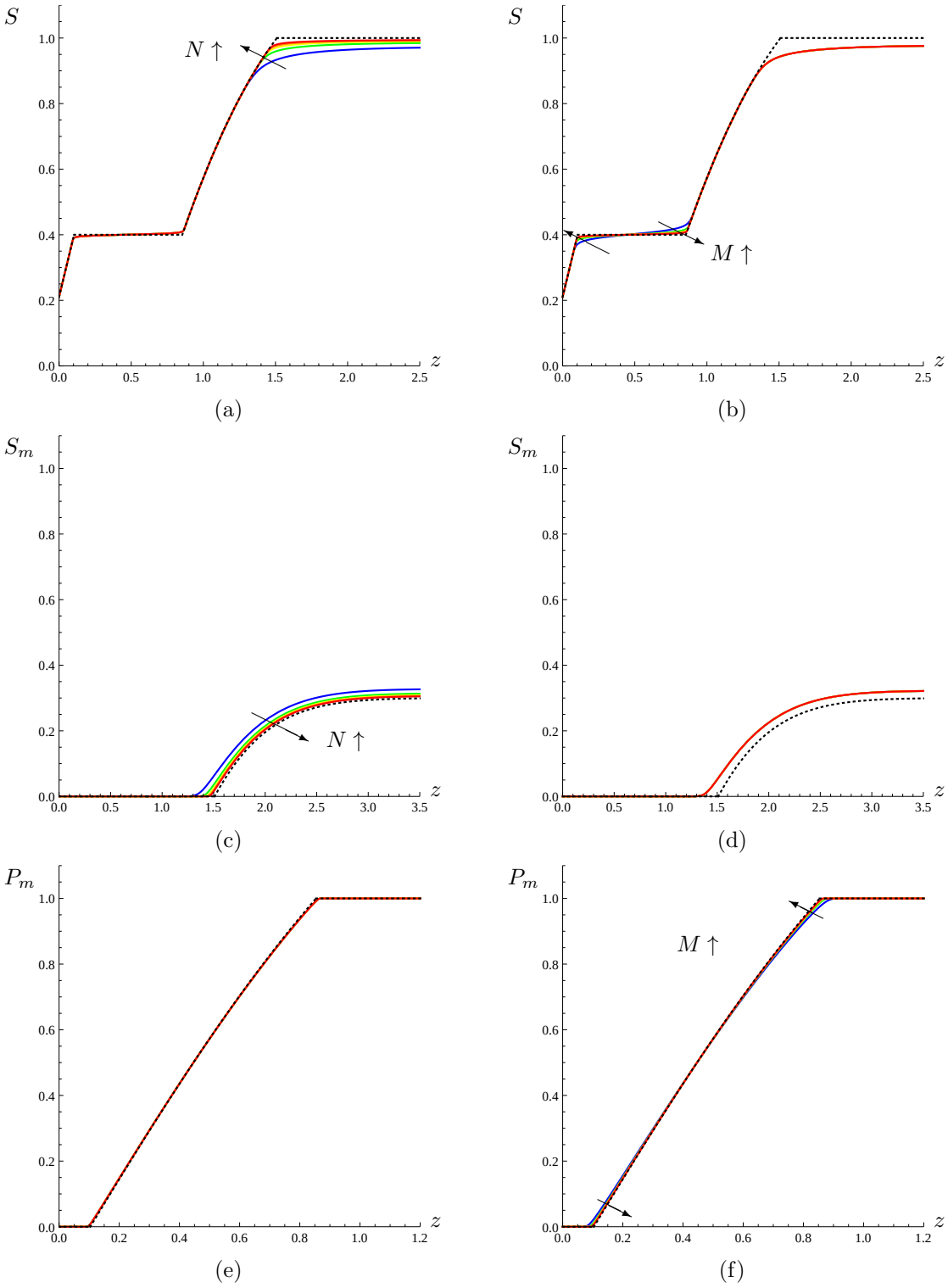

Figure 2.6: Graphs that compare the exact solutions (continuous curves) to the leading-order asymptotic solutions (dotted curves) for the concentrations of (a) monomers, (c) micelles, (e) polymer–micelle aggregates, with $N = [40,\ 80,\ 120,\ 160,\ 200]$ and $M = 200$ and for the concentrations of (b) monomers, (d) micelles, (f) polymer–micelle aggregates, with $M = [50,\ 100,\ 150,\ 200,\ 250]$ and $N = 50$. The other parameters used are $S^* = 2.5$, $P^* = 1.2$, $\Gamma^* = 2$, $\beta = 0.02$, and $\delta = 0.4$.

2.3.1.2 Asymptotic solutions to $O(\epsilon)$

In the region $0 < z < z_1$ we find that the leading-order solutions (2.34) and (2.35) are valid to all algebraic orders in ϵ.

In the region $z_1 < z < z_2$ we find that to order ϵ

$$S_1 = \delta \log\left(\frac{S^* - \delta(S^* - S_i)\mathrm{erfc}\left(z/\sqrt{2}\right)}{\delta + P^* - S^* + (S^* - S_i)\mathrm{erfc}\left(z/\sqrt{2}\right)}\right), \tag{2.42a}$$

$$S_{m_1} = 0, \tag{2.42b}$$

$$P_{m_1} = -\frac{\delta}{P^*}\log\left(\frac{S^* - \delta(S^* - S_i)\mathrm{erfc}\left(z/\sqrt{2}\right)}{\delta + P^* - S^* + (S^* - S_i)\mathrm{erfc}\left(z/\sqrt{2}\right)}\right). \tag{2.42c}$$

Thus, the asymptotic solutions for monomer, micelle and aggregate concentrations are given by the expressions

$$S \sim \delta\left[1 + \epsilon \log\left(\frac{S^* - \delta(S^* - S_i)\mathrm{erfc}\left(z/\sqrt{2}\right)}{\delta + P^* - S^* + (S^* - S_i)\mathrm{erfc}\left(z/\sqrt{2}\right)}\right)\right] + O(\epsilon^2), \tag{2.43a}$$

$$S_m \sim O(\epsilon^2), \tag{2.43b}$$

$$P_m \sim \frac{1}{P^*}\left[S^* - \delta - (S^* - S_i)\mathrm{erfc}\left(\frac{z}{\sqrt{2}}\right)\right] - \epsilon\left[\frac{\delta}{P^*}\log\left(\frac{S^* - \delta(S^* - S_i)\mathrm{erfc}\left(z/\sqrt{2}\right)}{\delta + P^* - S^* + (S^* - S_i)\mathrm{erfc}\left(z/\sqrt{2}\right)}\right)\right] + O(\epsilon^2), \tag{2.43c}$$

as $\epsilon \to 0$, in $z_1 < z < z_2$. Clearly, as $z \downarrow z_1$ or as $z \uparrow z_2$, these asymptotic approximations fail to hold. Therefore, we must seek an inner region both near $z = z_1$ and $z = z_2$, and match with the outer solutions, which we do in §2.3.1.3.

In the region $z_2 < z < z_3$ we find that the leading-order expressions (2.39) are correct to all algebraic orders in ϵ.

In the region $z_3 < z < \infty$ we find that at order ϵ

$$S_1 = \frac{1}{\nu}\log\left(S^* - 1 - P^* - (S^* - S_i)\mathrm{erfc}\left(\frac{z}{\sqrt{2}}\right)\right), \tag{2.44a}$$

$$S_{m_1} = -\frac{1}{\nu}\log\left(S^* - 1 - P^* - (S^* - S_i)\mathrm{erfc}\left(\frac{z}{\sqrt{2}}\right)\right), \tag{2.44b}$$

$$P_{m_1} = 0. \tag{2.44c}$$

Thus, the asymptotic solutions for monomer, micelle and aggregate concentrations are given by the expressions

$$S \sim 1 + \frac{\epsilon}{\nu}\log\left(S^* - 1 - P^* - (S^* - S_i)\mathrm{erfc}\left(\frac{z}{\sqrt{2}}\right)\right) + O(\epsilon^2), \tag{2.45a}$$

$$\begin{aligned} S_m \sim\ & S^* - 1 - P^* - (S^* - S_i)\mathrm{erfc}\left(\frac{z}{\sqrt{2}}\right) \\ & -\frac{\epsilon}{\nu}\log\left(S^* - 1 - P^* - (S^* - S_i)\mathrm{erfc}\left(\frac{z}{\sqrt{2}}\right)\right) + O(\epsilon^2), \end{aligned} \tag{2.45b}$$

$$P_m \sim 1 + O(\epsilon^2), \tag{2.45c}$$

as $\epsilon \to 0$, in $z_3 < z < \infty$. We note that the second term in the expansion for S and S_m is of $O(\epsilon/\nu)$ as we predicted in §2.3.1.1. Clearly as $z \downarrow z_3$ these asymptotic approximations fail to hold. We must also seek an inner region near $z = z_3$ and match the outer solutions given by (2.39) and (2.45) to the inner solutions.

2.3.1.3 Inner solutions

In the previous section we determined the outer solutions up to order ϵ in four distinct regions separated by the boundaries $z = z_1$, $z = z_2$, and $z = z_3$. We now seek inner solutions near these boundaries and match these with the outer solutions.

Near $z = z_1$

First, we consider solutions to (2.24a)–(2.26) near $z = z_1$ by introducing the inner variable

$$\zeta = \frac{1}{\epsilon}\left(z - z_1 - \epsilon\log(\epsilon)c_1\right), \tag{2.46}$$

where c_1 is an arbitrary constant. We try the ansatz

$$\tilde{S} = \delta\left(1 + \epsilon \log\left(\epsilon f_1(\zeta)\right)\right), \tag{2.47}$$

for the surfactant concentration in the inner region, where the function $f_1(\zeta)$ is to be determined. Substituting (2.46) and (2.47) into (2.24a), truncating, equating powers of ϵ and using (2.36), we have that

$$\delta\left(\log(f_1) + \log(\epsilon)\right) + P^* f_1 = (S^* - S_i)\sqrt{\frac{2}{\pi}}\mathrm{e}^{-{z_1}^2}(\zeta + c_1). \tag{2.48}$$

We note that the inner solutions to order ϵ^2 for the micellar and aggregate concentrations are given by

$$\tilde{S}_m = 0 \qquad \text{and} \qquad \tilde{P}_m = \epsilon f_1. \tag{2.49}$$

For convenience we choose the arbitrary constant c_1 such that

$$c_1 = \delta\sqrt{\frac{\pi}{2}}\frac{\mathrm{e}^{{z_1}^2/2}}{S^* - S_i}. \tag{2.50}$$

Thus, $f_1(\zeta)$ satisfies the transcendental equation

$$\log\left(f_1\right) + \frac{P^*}{\delta} f_1 = \frac{\zeta}{c_1}. \tag{2.51}$$

The solution of this implicit equation may be written as

$$f_1(\zeta) = \frac{\delta}{P^*}\mathbf{P}\left(\frac{P^*}{\delta}\mathrm{e}^{\zeta/c_1}\right), \tag{2.52}$$

where $\mathbf{P}(\cdot)$ is the *product-log* or *Lambert-W* function satisfying $\mathbf{P}(\zeta)\mathrm{e}^{\mathbf{P}(\zeta)} \equiv \zeta$. The far-field behaviour of the function $f_1(\zeta)$ is

$$f_1(\zeta) \sim \mathrm{e}^{\zeta/c_1} + O(\mathrm{e}^{2\zeta/c_1}) \qquad \text{as} \quad \zeta \to -\infty, \tag{2.53a}$$

$$f_1(\zeta) \sim \frac{\delta}{P^*}\left[\frac{\zeta}{c_1} - \log\left(\frac{\delta\zeta}{c_1 P^*}\right) + \frac{c_1}{\zeta}\log\left(\frac{\delta\zeta}{c_1 P^*}\right) + \ldots\right] \quad \text{as} \quad \zeta \to +\infty. \tag{2.53b}$$

We now match the inner solution to the outer solutions to the left and right of the inner region. We use Van Dyke's asymptotic matching principle (see VanDyke [42]) to show that the inner and outer solutions match and also determine the form of the

solution in the overlap region. We will then form composite uniformly valid solutions using the rule

$$S_{\text{composite}} \sim S_{\text{inner}} + S_{\text{outer}} - S_{\text{overlap}}.$$

Matching at the left

We first match the two-term inner solution for $\tilde{S}$ with the outer solution on the left, given by (2.35a), as $\zeta \to -\infty$. By substituting (2.53a) into (2.47) and rewriting in outer variables, we obtain

$$\tilde{S} = \delta\left(1 + \frac{1}{c_1}(z - z_1)\right) + \text{exponentially small terms.} \tag{2.54}$$

Similarly, it can be shown that the outer solution (2.35a) has the same expansion as $z \to z_1$, so that the common form of the solution in the overlapping region is given by (2.54). The exact solution to (2.24a), outer solution (2.35a), inner solution (2.47) and the composite solution for the monomer concentration are plotted in Figure 2.7.

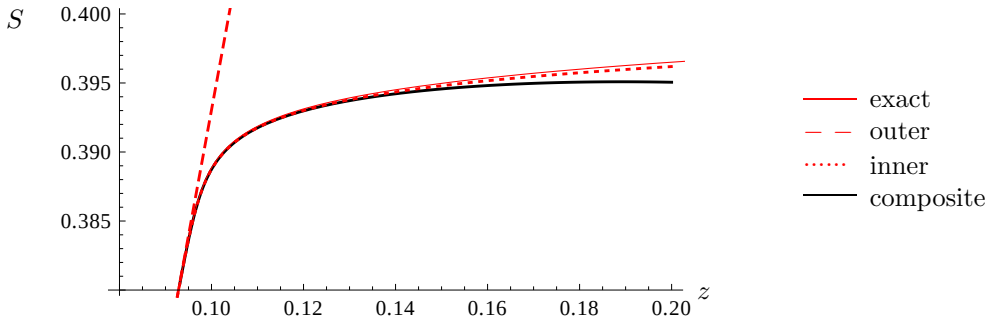

Figure 2.7: Graphs of the outer, inner and composite asymptotic solutions via matching at the left against the exact solution (2.24a) for monomer concentration near $z = z_1$. Parameters used are $S^* = 2.5$, $P^* = 1.2$, $\Gamma^* = 2$, $\beta = 0.02$, $\delta = 0.4$, $N = 80$, and $M = 200$.

Matching at the right

We now match the inner solution with the outer solution on the right, given by equation (2.43a), as $\zeta \to \infty$. We substitute (2.53b) into (2.47) and rewrite in outer variables to obtain

$$\tilde{S} \sim \delta\left[1 + \epsilon \log\left(\frac{\delta}{P^* c_1}(z - z_1)\right)\right]. \tag{2.55}$$

Similarly, we can show that the outer solution (2.43a) has the same expansion as $z \to z_1$, *i.e.* the common form of the solution in the overlapping region is given by (2.55). The exact solution to (2.24a), outer solution (2.37a), inner solution (2.47) and the composite solution for the monomer concentration are plotted in Figure 2.8.

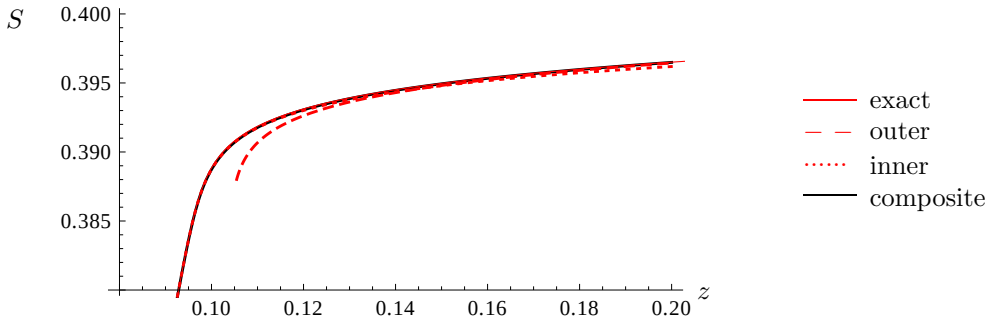

Figure 2.8: Graphs of the outer, inner and composite asymptotic solutions via matching at the right against the exact solution to (2.24a) for monomer concentration near $z = z_1$. Parameters used are $S^* = 2.5$, $P^* = 1.2$, $\Gamma^* = 2$, $\beta = 0.02$, $\delta = 0.4$, $N = 80$, and $M = 200$.

Near $z = z_2$

We now consider the inner region near $z = z_2$. Applying the same method as above, we find that the inner solutions are given by

$$\tilde{S} \sim \delta\left(1 + \epsilon \log\left(\frac{f_2(\zeta)}{\epsilon}\right)\right), \quad S_{m_I} \sim 0, \quad \text{and} \quad P_{m_I} \sim 1 - \frac{\epsilon}{f_2(\zeta)}, \tag{2.56}$$

with the inner variable ζ now given by

$$\zeta = \frac{1}{\epsilon}\left(z - z_2 - \epsilon \log(\epsilon) c_2\right) \quad \text{where} \quad c_2 = \delta\sqrt{\frac{\pi}{2}}\frac{\mathrm{e}^{{z_2}^2/2}}{S_i - S^*}. \tag{2.57}$$

The function $f_2(\zeta)$ satisfies the transcendental equation

$$\log(f_2) - \frac{P^*}{\delta}\frac{1}{f_2} = \frac{\zeta}{c_2}, \tag{2.58}$$

which again may be solved exactly in terms of the product-log function. Matching the inner solution with the outer solution at the left given by (2.43a), we find that the common form, S_C, of the solution in the overlapping region is given by

$$S_C \sim \delta\left[1 - \epsilon \log\left(\frac{\delta}{c_2 P^*}(z - z_2)\right)\right]. \tag{2.59}$$

Matching the inner solution with the outer solution at the right given by (2.39a), we find that the common form for the solution in the overlapping region is given by

$$S_C \sim \delta\left(1 - \frac{1}{c_2}(z - z_2)\right). \tag{2.60}$$

Near $z = z_3$

Finally we consider the inner region near $z = z_3$. Applying the same method as before we find that the inner solutions are given by

$$\tilde{S} \sim 1 + \frac{\epsilon}{\nu} \log\left(\frac{\epsilon}{\nu} f_3(\zeta)\right), \quad \tilde{S}_m \sim \frac{\epsilon}{\nu} f_3(\zeta), \quad \text{and} \quad \tilde{P}_m \sim 1, \tag{2.61}$$

with the inner variable ζ now given by

$$\zeta = \frac{\nu}{\epsilon}\left(z - z_3 - \frac{\epsilon}{\nu}\log\left(\frac{\epsilon}{\nu}\right) c_3\right) \quad \text{where} \quad c_3 = \sqrt{\frac{\pi}{2}} \frac{\mathrm{e}^{{z_3}^2/2}}{S^* - S_i}, \tag{2.62}$$

while the function $f_3(\zeta)$ satisfies the transcendental equation

$$\log(f_3) + f_3 = \frac{\zeta}{c_3}. \tag{2.63}$$

Matching the inner solution with the outer solution at the left given by (2.39a), we find that the common form of the solution in the overlapping region is given by

$$S_{\mathrm{C}} \sim 1 + \frac{1}{c_3}(z - z_3). \tag{2.64}$$

Matching the inner solution with the outer solution at the right given by (2.45a) we find that the common form of the solution in the overlapping region is given by,

$$S_{\mathrm{C}} \sim 1 + \frac{\epsilon}{\nu} \log\left(\frac{1}{c_3}(z - z_3)\right). \tag{2.65}$$

We omit the details for determining the common form of the micelle and aggregate solutions in the overlap regions near the boundaries z_1, z_2, and z_3, as the method used is the same as above. We have now obtained a full set of analytical solutions to order ϵ using matched asymptotic expansions for the monomer, micelle and aggregate concentrations. These solutions are plotted as dotted curves in Figure 2.9 against the exact solutions to (2.24)–(2.26), which are plotted using continuous curves. We see that the agreement is markedly improved compared with Figure 2.4. In particular, the inner layers near $z = z_1$, $z = z_2$, and $z = z_3$ smooth out the sharp transitions between the regions where $S < \delta$, $S \approx \delta$, $\delta < S < 1$, and $S \approx 1$.

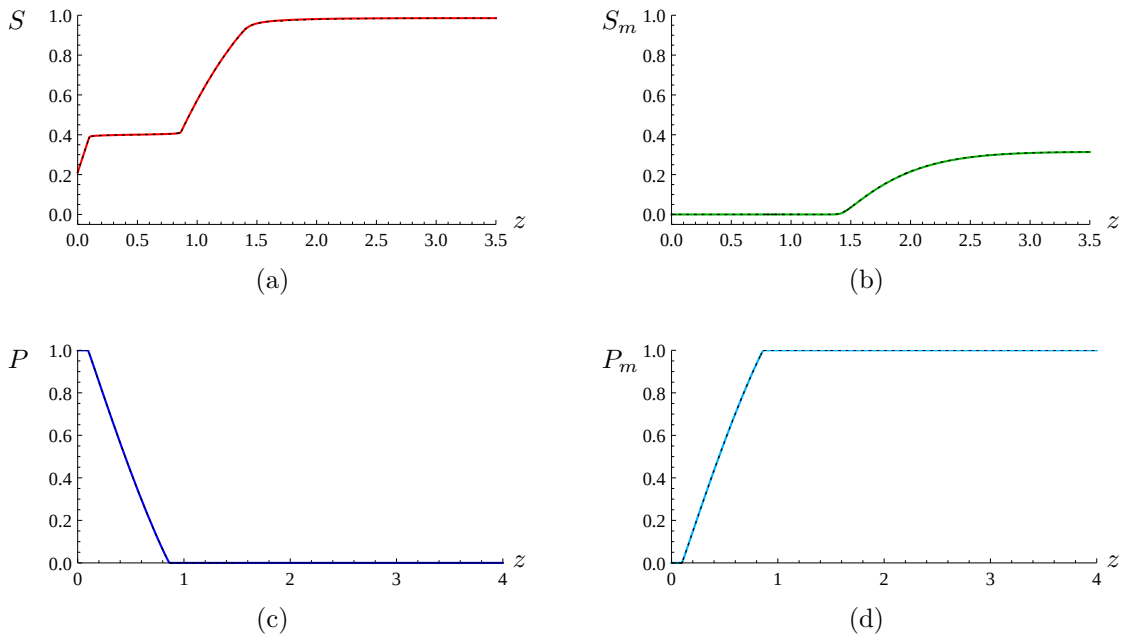

Figure 2.9: Graphs that compare the exact solutions (continuous curves) to the order ϵ asymptotic solutions (dotted curves) for the concentration of: (a) monomers, (b) micelles, (c) polymer–micelle aggregates, and (d) polymers. Parameters used are $S^* = 2.5$, $P^* = 1.2$, $\Gamma^* = 2$, $\beta = 0.02$, $\delta = 0.4$, $N = 80$, and $M = 200$.

2.4 Case 2: Diffusion coefficients for polymer and polymer–micelle aggregate phases equal

We now relax the assumption on diffusivities of the species to allow the diffusion coefficients for the polymer and polymer–micelle aggregates to differ from those for the surfactant monomer and micelles. The relative sizes of the polymer and polymer–micelle aggregates are similar compared to monomers and free micelles, thus it is reasonable to assume that the diffusivities of the polymer and polymer–micelle aggregate phases are the same and we set $D_2 = D_3 = D \neq 1$. Since micelles are comprised of many monomer molecules, it is also physically reasonable to assume that the diffusion coefficient for the surfactant monomer phase is less than the diffusion coefficient for the micellar phase, *i.e.* D_1 is less than 1. We will assume that polymers and polymer–micelle aggregates diffuse less easily through solution than micelles so that $D < D_1 < 1$.

We now integrate equation (2.20), and applying boundary conditions (2.21) and (2.22) we find that the polymer and aggregate concentrations are given by

$$P = \frac{\delta^M}{\delta^M + S^M} \qquad \text{and} \qquad P_m = 1 - P = \frac{S^M}{\delta^M + S^M}, \tag{2.66}$$

respectively. The micellar concentration is still given by (2.17). Thus (2.19) can be written as a second-order differential equation for the monomer, micellar, and polymer–micelle aggregate concentrations

$$\frac{\mathrm{d}^2}{\mathrm{d}z^2}\left(S + D_1 S_m + D P^* P_m\right) + z\frac{\mathrm{d}}{\mathrm{d}z}\left(S + S_m + P^* P_m\right) = 0, \tag{2.67}$$

with boundary conditions

$$\frac{\mathrm{d}S}{\mathrm{d}z} = \frac{\Gamma^* S_i}{\beta + S_i} \quad \text{on} \quad z = 0, \tag{2.68a}$$

$$S + S_m + P^* P_m \to S^* \quad \text{as} \quad z \to \infty, \tag{2.68b}$$

where S_i again denotes the surfactant concentration at the surface $z = 0$.

2.4.1 Numerical results

We note that, with S_m and P_m related to S by (2.17) and (2.66) respectively then (2.67) reduces to a nonlinear second-order differential equation for S, which we solve numerically. The concentration of the monomers, micelles, polymer–micelle aggregates and polymers exhibit behaviour similar to that observed in Case 1, as shown in Figure 2.10. Clearly there are again four distinct regions. However, the positions of the boundaries between the four regions have altered due to the dimensionless diffusivities not all being equal to 1.

Figure 2.11 shows plots of the monomer, micelle and polymer–micelle aggregate concentrations S, S_m, and P_m respectively as the diffusivities D and D_1 are varied independently. In Figures 2.11(a), 2.11(c), and 2.11(e) we increase D and keep D_1 fixed. The free polymers are able to diffuse throughout a greater depth range before they are completely used up in the formation of aggregates, which also results in a greater depth range where aggregates exist. Thus, the region where polymers and polymer–micelle aggregates co-exist increases with D and, as a result, the length of the monomer plateau at the CAC increases with D (see Figure 2.11(a) and Figure 2.11(e)). The boundary between the micellar and non-micellar phases moves further away from the surface $z = 0$ as D increases, as shown in Figure 2.11(e).

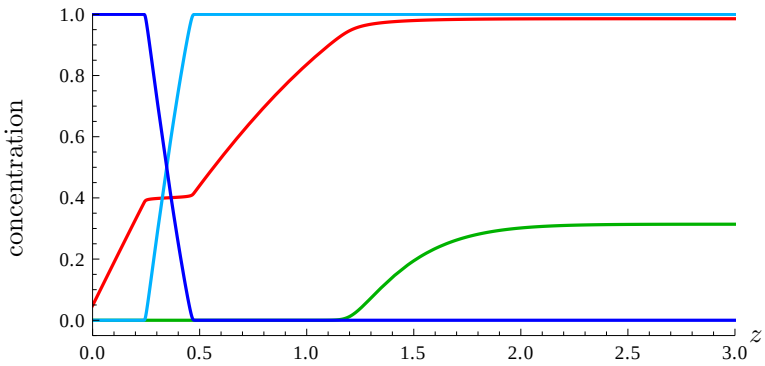

Figure 2.10: Graphs for the concentrations S (red), S_m (green), P_m (light blue), and P (blue) obtained by solving (2.17), (2.66)–(2.68b) numerically. Parameters used are $D = 0.2$, $D_1 = 0.4$, $S^* = 2.5$, $P^* = 1.2$, $\Gamma^* = 2$, $\beta = 0.02$, $\delta = 0.4$, $N = 80$, and $M = 200$.

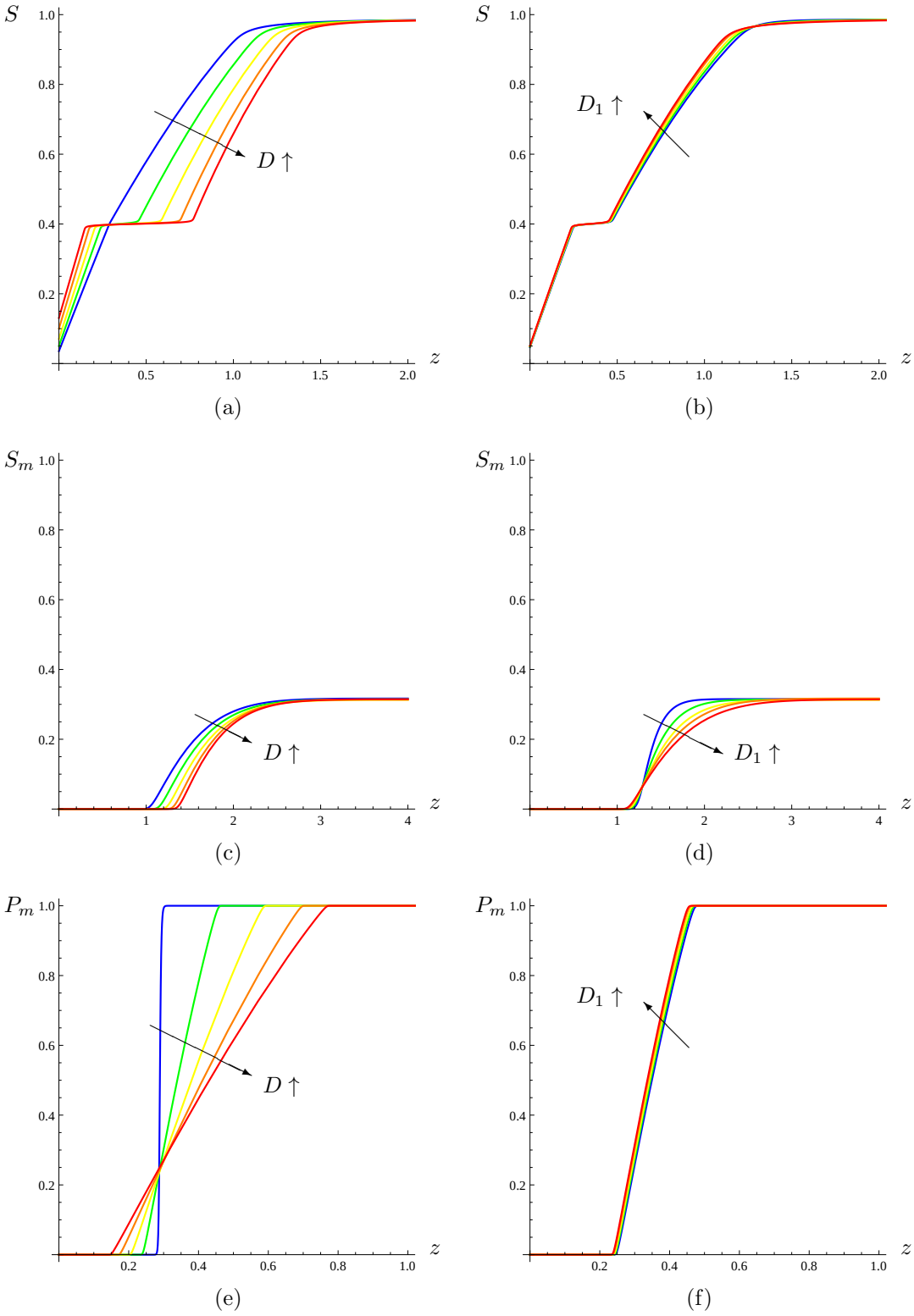

Figure 2.11: Graphs of the numerical solutions to (2.67)–(2.68b) with the diffusion coefficients D and D_1 varying. Plots for (a) monomer, (c) micelle, and (e) polymer–micelle aggregate concentrations with $D = [0,\ 0.2,\ 0.4,\ 0.6,\ 0.8]$ and $D_1 = 0.8$. Plots for (b) monomer, (d) micelle, and (f) polymer–micelle aggregate concentrations with $D_1 = [0.2,\ 0.4,\ 0.6,\ 0.8,\ 1]$ and $D = 0.2$. The other parameters used are $S^* = 2.5$, $P^* = 1.2$, $\Gamma^* = 2$, $\beta = 0.02$, $\delta = 0.4$, $N = 80$, and $M = 200$.

Conversely, keeping D fixed and increasing D_1 corresponds to greater diffusion of micelles through the fluid. As a result, the boundary between the micellar and non-micellar phases moves towards the surface $z = 0$ as D_1 increases, as shown in Figure 2.11(d). Moreover, the depth at which free polymers start to bind to monomers decreases as D_1 increases, see Figure 2.11(f). However, the length of the CAC plateau does not change as D_1 increases, see Figure 2.11(b), *i.e.* the CAC plateau is shifted due to the greater diffusion of micelles. We conclude that diffusion coefficient for the polymer and polymer–micelle aggregate phases, D, alters the length of the monomer plateau at the CAC, whereas the diffusion coefficient for the micellar phase, D_1, shifts the position of the CAC plateau.

2.4.2 Large aggregation-number limit

Using the insight we have gained from §2.3.1 we can determine asymptotic solutions for the four species in different regions of the fluid. Thus, we exploit the fact that the aggregation numbers N and M are large and asymptotically expand the dependent variables S, S_m, P, and P_m as in §2.3.1. We then consider the order-one and order-ϵ approximations to (2.67) and use asymptotic matching techniques to determine solutions for the overlap regions.

2.4.2.1 Leading-order solutions

As in Case 1, we assume that at the interface $z = 0$ the subsurface surfactant monomer concentration is below the CAC. Then, near the interface there will be a region where S is below the CAC and at leading order we find that S_0 satisfies the differential equation

$$S_0'' + zS_0' = 0, \tag{2.69}$$

and

$$S_{m_0} = 0, \qquad P_{m_0} = 0. \tag{2.70}$$

We expand S_i in the form

$$S_i \sim S_{i0} + \epsilon S_{i1} + \dots \tag{2.71}$$

as $\epsilon \to 0$. Then the boundary condition (2.68a) at leading order is

$$\frac{\mathrm{d}S_0}{\mathrm{d}z} = \frac{\Gamma^* S_{i0}}{\beta + S_{i0}} \quad \text{on} \quad z = 0. \tag{2.72}$$

Integrating (2.69) and applying (2.72) we find that

$$S_0 = S_{i0} + \sqrt{\frac{\pi}{2}}\frac{\Gamma^* S_{i0}}{\beta + S_{i0}}\mathrm{erf}\left(\frac{z}{\sqrt{2}}\right). \tag{2.73}$$

Equation (2.73) holds until the surfactant monomer concentration reaches the CAC, *i.e.* when $S_0 = \delta$ at $z = z_1$, where z_1 satisfies the equation

$$\sqrt{\frac{2}{\pi}}\frac{(\delta - S_{i0})(\beta + S_{i0})}{\Gamma^* S_{i0}} = \mathrm{erf}\left(\frac{z_1}{\sqrt{2}}\right). \tag{2.74}$$

For $z < z_1$ we have a region where only surfactant monomers and unbound polymers are present but for $z > z_1$ we have a region where polymer–micelle aggregates begin to form. In this region the leading-order surfactant concentration remains constant, *i.e.* $S_0 = \delta$, so the leading-order micelle concentration is given by $S_{m_0} = 0$. The polymer–micelle aggregate concentration at leading order satisfies the second-order differential equation

$$DP''_{m_0} + zP'_{m_0} = 0, \tag{2.75}$$

which has the general solution

$$P_{m_0} = a_2 + b_2\mathrm{erfc}\left(\frac{z}{\sqrt{2D}}\right), \tag{2.76}$$

for some constants a_2 and b_2. The general solution for P_{m_0} holds until all of the unbound polymer has become bound in aggregate form, *i.e.* when $P_{m_0} = 1$ at $z = z_2$, where z_2 is defined by

$$1 = a_2 + b_2\mathrm{erfc}\left(\frac{z_2}{\sqrt{2D}}\right). \tag{2.77}$$

The constants a_2 and b_2 are determined by matching the leading-order solutions for the polymer–micelle aggregate concentration in the regions $z < z_1$ and $z > z_2$.

For $z > z_2$ the monomer concentration starts to increase again and there is a region where only polymer–micelle aggregates and monomers are present. Hence,

$$S_{m_0} = 0, \qquad P_{m_0} = 1, \tag{2.78}$$

and S_0 satisfies the differential equation (2.69), which has the general solution

$$S_0 = a_3 + b_3\mathrm{erfc}\left(\frac{z}{\sqrt{2}}\right). \tag{2.79}$$

These approximations hold until the surfactant concentration reaches the CMC, *i.e.* when $S_0 = 1$ at $z = z_3$, where z_3 is defined by the equation

$$1 = a_3 + b_3 \mathrm{erfc}\left(\frac{z_3}{\sqrt{2}}\right). \tag{2.80}$$

We can determine the coefficients a_3 and b_3 by matching the solutions in $z < z_2$ and $z > z_3$.

For $z > z_3$ there is a region where the surfactant monomer concentration remains at the CMC and micelles form. In this region to leading order we find that

$$S_0 = 1, \qquad \text{and} \qquad P_{m_0} = 1, \tag{2.81}$$

while the micelle concentration at leading order satisfies the differential equation

$$D_1 S''_{m_0} + z S'_{m_0} = 0. \tag{2.82}$$

Applying the boundary condition at infinity the general solution for S_{m_0} is found to be

$$S_{m_0} = S^* - P^* - 1 + b_4 \mathrm{erfc}\left(\frac{z}{\sqrt{2D_1}}\right), \tag{2.83}$$

where b_4 can be determined from matching with the solution in $z < z_3$.

Matching the general solutions across the boundaries z_1, z_2, and z_3 we obtain the leading-order approximations, in terms of the unknowns z_1, z_2, z_3, and S_{i0}, in the four distinct regions as follows.

Region 1: $0 < z < z_1$

Free surfactant monomer concentration is below the CAC so only monomers and free polymers are present. The approximate solutions are

$$S \sim S_{i0} + \sqrt{\frac{\pi}{2}} \frac{\Gamma^* S_{i0}}{\beta + S_{i0}} \mathrm{erf}\left(\frac{z}{\sqrt{2}}\right) + O(\epsilon), \tag{2.84a}$$

$$S_m \sim O(\epsilon), \tag{2.84b}$$

$$P_m \sim O(\epsilon), \tag{2.84c}$$

where S_{i0} is defined in terms of z_1 by (2.74).

Region 2: $z_1 < z < z_2$

The surfactant monomer concentration has reached the CAC so polymer–micelle aggregates form. The approximate solutions are

$$S \sim \delta + O(\epsilon), \tag{2.85a}$$

$$S_m \sim O(\epsilon), \tag{2.85b}$$

$$P_m \sim \frac{\operatorname{erfc}(z_1/\sqrt{2D}) - \operatorname{erfc}(z/\sqrt{2D})}{\operatorname{erfc}(z_1/\sqrt{2D}) - \operatorname{erfc}(z_2/\sqrt{2D})} + O(\epsilon). \tag{2.85c}$$

Region 3: $z_2 < z < z_3$

All of the polymer is bound with surfactant so only surfactant monomers and polymer–micelle aggregates are present and the approximate solutions are

$$S \sim \frac{\operatorname{erfc}(z_2/\sqrt{2}) - \delta\operatorname{erfc}(z_3/\sqrt{2}) + (\delta - 1)\operatorname{erfc}(z/\sqrt{2})}{\operatorname{erfc}(z_2/\sqrt{2}) - \operatorname{erfc}(z_3/\sqrt{2})} + O(\epsilon), \tag{2.86a}$$

$$S_m \sim O(\epsilon), \tag{2.86b}$$

$$P_m \sim 1 + O(\epsilon). \tag{2.86c}$$

Region 4: $z > z_3$

The surfactant monomer concentration reaches the CMC and micelles form. The approximate solutions are

$$S \sim 1 + O(\epsilon), \tag{2.87a}$$

$$S_m \sim (S^* - P^* - 1)\left(1 - \frac{\operatorname{erfc}\left(z/\sqrt{2D_1}\right)}{\operatorname{erfc}(z_3/\sqrt{2D_1})}\right) + O(\epsilon), \tag{2.87b}$$

$$P_m \sim 1 + O(\epsilon). \tag{2.87c}$$

The approximations (2.84)–(2.87) are all dependent on S_{i0} and the boundaries z_1, z_2, and z_3 which we must locate. In region 1 only monomers and polymers are present but in region 2 there are also polymer–micelle aggregates. Thus, surfactant enters region 2 through $z = z_1$ in the form of monomer only and leaves region 2 through $z = z_1$ in the form of monomers and polymer–micelle aggregates. By setting the fluxes at $z = z_1$ equal to each other

$$\left.\frac{\mathrm{d}S}{\mathrm{d}z}\right|_{\text{region 1}} = \left.\left(\frac{\mathrm{d}S}{\mathrm{d}z} + DP^*\frac{\mathrm{d}P_m}{\mathrm{d}z}\right)\right|_{\text{region 2}} \quad \text{at} \quad z = z_1, \tag{2.88}$$

and we obtain the following equation for z_1 and z_2:

$$\exp\left(\frac{{z_1}^2}{2}\left(\frac{1-D}{D}\right)\right) = \sqrt{\frac{2D}{\pi}}\frac{P^*(\beta+S_{i0})}{\Gamma^* S_{i0}\left(\operatorname{erfc}(z_1/\sqrt{2D})-\operatorname{erfc}(z_2/\sqrt{2D})\right)}. \tag{2.89}$$

In region 3 there are only monomers and polymer–micelle aggregates so surfactant enters region 3 through $z = z_2$ in the form of monomers and polymer–micelle aggregates and similarly surfactant leaves region 3 through $z = z_2$ in the same form. By setting the fluxes at $z = z_2$ equal to each other

$$\left(\frac{\mathrm{d}S}{\mathrm{d}z}+DP^*\frac{\mathrm{d}P_m}{\mathrm{d}z}\right)\Bigg|_{\text{region 2}} = \left(\frac{\mathrm{d}S}{\mathrm{d}z}+DP^*\frac{\mathrm{d}P_m}{\mathrm{d}z}\right)\Bigg|_{\text{region 3}} \quad \text{at} \quad z=z_2, \tag{2.90}$$

and we obtain the following equation for z_1, z_2 and z_3:

$$\exp\left(\frac{{z_2}^2}{2}\left(\frac{1-D}{D}\right)\right) = \frac{P^*\sqrt{D}\left(\operatorname{erfc}(z_2/\sqrt{2})-\operatorname{erfc}(z_3/\sqrt{2})\right)}{(1-\delta)\left(\operatorname{erfc}(z_1/\sqrt{2D})-\operatorname{erfc}(z_2/\sqrt{2D})\right)}. \tag{2.91}$$

Finally we consider surfactant entering region 4 through $z = z_3$; it does so in the form of monomers and polymer–micelle aggregates. In region 4 there are micelles present, so surfactant leaves region 4 through $z = z_3$ in the form of monomers, polymer–micelle aggregates and micelles. By setting the fluxes at $z = z_3$ equal to each other

$$\left(\frac{\mathrm{d}S}{\mathrm{d}z}+DP^*\frac{\mathrm{d}P_m}{\mathrm{d}z}\right)\Bigg|_{\text{region 3}} = \left(\frac{\mathrm{d}S}{\mathrm{d}z}+DP^*\frac{\mathrm{d}P_m}{\mathrm{d}z}+D_1\frac{\mathrm{d}S_m}{\mathrm{d}z}\right)\Bigg|_{\text{region 4}} \quad \text{at} \quad z=z_3, \tag{2.92}$$

and we obtain the final equation for z_2 and z_3:

$$\exp\left(\frac{{z_3}^2}{2}\left(\frac{1-D_1}{D_1}\right)\right) = \frac{\sqrt{D_1}(S^*-P^*-1)\left(\operatorname{erfc}(z_2/\sqrt{2})-\operatorname{erfc}(z_3/\sqrt{2})\right)}{(1-\delta)\operatorname{erfc}(z_3/\sqrt{2D_1})}. \tag{2.93}$$

Hence, we have four implicit equations (2.74), (2.89), (2.91), and (2.93) that we solve numerically for z_1, z_2, z_3, and S_{i0} to determine the leading-order asymptotic solutions for S, S_m, P, and P_m. Note that for (2.93) to give a real solution for z_3, we require that $S^* > P^* + 1$, *i.e.* there must be enough surfactant in the bulk to fill up all the polymers and exceed the CMC. These asymptotic solutions only hold in such a regime. We also note that if we take $D = D_1 = 1$ in our analysis we recover the leading-order solutions for Case 1 found in §2.3.1.1. The leading-order asymptotic

solutions are denoted by the dotted curves in Figure 2.12 and we observe a visible discrepancy with the numerical solutions, denoted by the continuous curves, for S and S_m in region 3. Hence, we seek the order ϵ terms in the asymptotic expansions for S, S_m, P, and P_m to resolve this discrepancy in the following section.

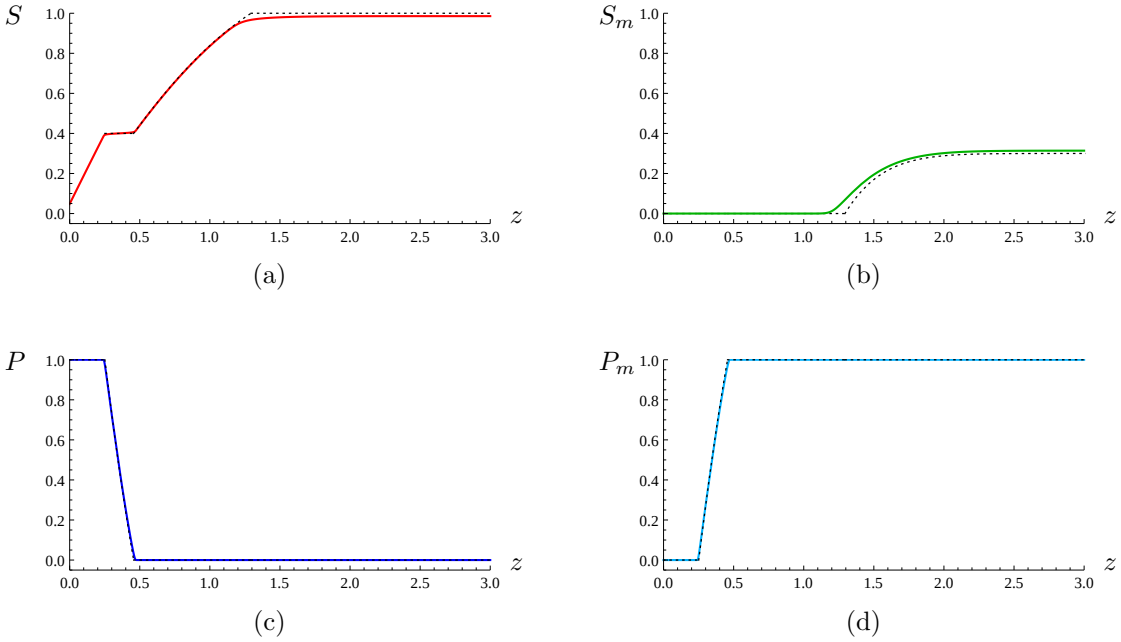

Figure 2.12: Graphs that compare the numerical solutions (continuous curves) to the leading-order asymptotic solutions (dotted curves) for the concentrations of: (a) monomers, (b) micelles, (c) polymers, and (d) polymer–micelle aggregates. Parameters used are $D = 0.2$, $D_1 = 0.4$, $S^* = 2.5$, $P^* = 1.2$, $\Gamma^* = 2$, $\beta = 0.02$, $\delta = 0.4$, $N = 80$, and $M = 200$.

2.4.2.2 Asymptotic solutions to $O(\epsilon)$

In this section we seek the order ϵ terms in the asymptotic expansions for S, S_m, and P_m in each of the four regions defined previously. We will find that some of the order ϵ terms in the asymptotic expansions of S, S_m, and P_m will blow up near their respective boundaries z_1, z_2, and z_3, and hence matching the flux of surfactant across the boundaries fails. Thus, we must seek three inner regions and match the solutions in these inner regions with the outer solutions.

For $0 < z < z_1$ we substitute the asymptotic expansions for S, S_m and P_m into equations (2.17) and (2.66) and find that at order ϵ

$$S_{m_1} = P_{m_1} = 0. \tag{2.94}$$

Next we substitute the asymptotic expansions into (2.67) and (2.68a) and find that, at order ϵ, S_1 satisfies the second-order differential equation

$$\frac{\mathrm{d}^2 S_1}{\mathrm{d}z^2} + z\frac{\mathrm{d}S_1}{\mathrm{d}z} = 0, \tag{2.95}$$

and boundary condition

$$\frac{\mathrm{d}S_1}{\mathrm{d}z} = \frac{\Gamma^*\beta S_{i1}}{(\beta + S_{i0})^2} \quad \text{on} \quad z = 0. \tag{2.96}$$

Thus,

$$S_1 = -b_5\left(\operatorname{erf}\left(\frac{z}{\sqrt{2}}\right) + \sqrt{\frac{2}{\pi}}\frac{(\beta + S_{i0})^2}{\Gamma^*\beta}\right), \tag{2.97}$$

where b_5 is a constant to be determined by matching with the inner region near $z = z_1$.

Similarly, by substituting the asymptotic expansions for S, S_m and P_m in the region $z_1 < z < z_2$ we find that at order ϵ

$$S_{m_1} = 0, \tag{2.98a}$$

$$P_{m_0} = \frac{\mathrm{e}^{S_1/\delta}}{1 + \mathrm{e}^{S_1/\delta}}, \tag{2.98b}$$

thus,

$$S_1 = \delta \log\left(\frac{\operatorname{erfc}(z/\sqrt{2D}) - \operatorname{erfc}(z_1/\sqrt{2D})}{\operatorname{erfc}(z_2/\sqrt{2D}) - \operatorname{erfc}(z/\sqrt{2D})}\right). \tag{2.99}$$

Also, P_{m_1} satisfies the differential equation

$$D\frac{\mathrm{d}^2 P_{m_1}}{\mathrm{d}z^2} + z\frac{\mathrm{d}P_{m_1}}{\mathrm{d}z} = -\frac{1}{P^*}\left(\frac{\mathrm{d}^2 S_1}{\mathrm{d}z^2} + z\frac{\mathrm{d}S_1}{\mathrm{d}z}\right), \tag{2.100}$$

where the boundary conditions are obtained through matching with the inner solutions as $z \downarrow z_1$ and $z \uparrow z_2$.

For $z_2 < z < z_3$ we find that at order ϵ

$$S_{m_1} = P_{m_1} = 0, \tag{2.101}$$

and S_1 also satisfies the differential equation (2.95). Thus, the general solution for S_1 is

$$S_1 = a_6 + b_6 \mathrm{erfc}\left(\frac{z}{\sqrt{2}}\right), \tag{2.102}$$

where the constants a_6 and b_6 are determined through matching with the inner solutions as $z \downarrow z_2$ and $z \uparrow z_3$.

For $z > z_3$ we substitute the asymptotic expansions for S, S_m, and P_m into equations (2.17) and (2.66) and we find that at order ϵ

$$P_{m_1} = 0 \tag{2.103a}$$

$$S_{m_0} = \mathrm{e}^{\nu S_1}. \tag{2.103b}$$

Therefore,

$$S_1 = \frac{1}{\nu} \log\left(\frac{(S^* - P^* - 1)}{\mathrm{erfc}(z_3/\sqrt{2D_1})}\left(\mathrm{erfc}\left(\frac{z_3}{\sqrt{2D_1}}\right) - \mathrm{erfc}\left(\frac{z}{\sqrt{2D_1}}\right)\right)\right). \tag{2.104}$$

By substitution into (2.67) and (2.68b), we find S_{m_1} satisfies the differential equation

$$D_1 \frac{\mathrm{d}^2 S_{m_1}}{\mathrm{d}z^2} + z\frac{\mathrm{d}S_{m_1}}{\mathrm{d}z} = -\left(\frac{\mathrm{d}^2 S_1}{\mathrm{d}z^2} + z\frac{\mathrm{d}S_1}{\mathrm{d}z}\right), \tag{2.105}$$

at order ϵ with the boundary condition at infinity now given by

$$S_{m_1} \sim \log\left(\frac{1}{S^* - P^* - 1}\right) \qquad \text{as} \quad z \to \infty, \tag{2.106}$$

while the other boundary condition is obtained through matching with the inner solution as $z \downarrow z_3$.

2.4.2.3 Inner solutions

We now seek inner solutions near the boundaries at $z = z_1$, $z = z_2$ and $z = z_3$ using a similar method to that used for Case 1. We will only concern ourselves with obtaining uniformly valid solutions for the monomer concentration, S, but in principle a similar method yields uniformly-valid solutions for the micelle and polymer–micelle aggregate concentrations too.

Near $z = z_1$

As in Case 1, we re-scale the independent variable, z, near the boundary z_1 by introducing the inner-variable ζ as defined in (2.46), where the constant c_1 is now unknown. We use the ansatz given by (2.47) and note that the function $f_1(\zeta)$ is also to be determined. We substitute (2.47) into (2.67) and find at leading order

$$\frac{\mathrm{d}^2}{\mathrm{d}\zeta^2}\left(\log\left(f_1\right) + \frac{DP^*}{\delta} f_1\right) = 0 \qquad \Rightarrow \qquad \delta \log\left(f_1\right) + DP^* f_1 = A_1\zeta + B_1. \quad (2.107)$$

Without loss of generality we can choose c_1 such that $B_1 = 0$. We then determine the constants A_1 and c_1 through matching with the outer solutions in $0 < z < z_1$ and $z_1 < z < z_2$.

Matching at left

Using Van Dyke's matching rule, we first match the two-term inner solution with the two-term outer solution in $0 < z < z_1$. Following the matching procedure used in §2.3.1.3 we find that

$$A_1 = \frac{\Gamma^* S_{i0}}{\beta + S_{i0}} \mathrm{e}^{-{z_1}^2/2}, \quad (2.108)$$

and

$$\log(\epsilon)\left(1 - \frac{A_1 c_1}{\delta}\right) = b_5\left(\mathrm{erf}\left(\frac{z_1}{\sqrt{2}}\right) - \sqrt{\frac{2}{\pi}}\frac{(\beta + S_{i0})^2}{\Gamma^* S_{i0}}\right). \quad (2.109)$$

Since c_1 is arbitrary we set

$$c_1 = \delta \frac{(\beta + S_{i0})}{\Gamma^* S_{i0}} \mathrm{e}^{\frac{{z_1}^2}{2}}, \quad (2.110)$$

which implies that $b_5 = 0$. Hence, the common form of the solution in the overlap region is given by

$$S_{\mathrm{C}} \sim \delta\left(1 + \frac{1}{c_1}(z - z_1)\right). \quad (2.111)$$

Matching at right

Next we match the two-term inner solution with the two-term outer solution in $z_1 < z < z_2$. We find that they do indeed match and the common form of the solution in the overlap region is given by

$$S_{\mathrm{C}} \sim \delta \left[1 + \epsilon \log \left(\frac{\delta}{DP^* c_1} (z - z_1) \right) \right]. \tag{2.112}$$

Near $z = z_2$

We now consider the inner region near $z = z_2$ and use the ansatz given by equation (2.56), with inner-variable ζ defined by (2.57), where the function $f_2(\zeta)$ and constant c_2 are to be determined. Applying the same method as before, we find that the function $f_2(\zeta)$ now satisfies the transcendental equation

$$\log(f_2) - \frac{DP^*}{\delta} \frac{1}{f_2} = \frac{\zeta}{c_2}, \tag{2.113}$$

and the constant c_2 is given by

$$c_2 = \frac{\delta}{(1-\delta)} \sqrt{\frac{\pi}{2}} \left(\operatorname{erfc}\left(\frac{z_3}{\sqrt{2}} \right) - \operatorname{erfc}\left(\frac{z_2}{\sqrt{2}} \right) \right) \mathrm{e}^{{z_2}^2/2}. \tag{2.114}$$

Matching the 2-term inner solution with the 2-term outer solutions in $z_1 < z < z_2$ and $z_2 < z < z_3$ we find that $a_6 = b_6 = 0$ and hence $S_1 = 0$ in $z_2 < z < z_3$. The common form of the solutions in the overlap regions are given by

$$S_{\mathrm{C}} \sim \delta \left[1 - \epsilon \log \left(\frac{\delta}{DP^* c_2} (z_2 - z) \right) \right], \tag{2.115}$$

via matching on the left and

$$S_{\mathrm{C}} \sim \delta \left(1 - \frac{1}{c_2} (z - z_2) \right), \tag{2.116}$$

via matching on the right.

Near $z = z_3$

We now consider the inner region near $z = z_3$ and use the ansatz given by equation (2.61), with the inner variable ζ defined by (2.62), and where the function $f_3(\zeta)$ and

constant c_3 are to be determined. Again we apply the same method as above and find that the function $f_3(\zeta)$ now satisfies the transcendental equation

$$\log(f_3) + D_1 f_3 = \frac{\zeta}{c_3}, \tag{2.117}$$

where the constant c_3 is given by

$$c_3 = \frac{1}{(1-\delta)}\sqrt{\frac{\pi}{2}}\left(\operatorname{erfc}\left(\frac{z_2}{\sqrt{2}}\right) - \operatorname{erfc}\left(\frac{z_3}{\sqrt{2}}\right)\right) \mathrm{e}^{{z_3}^2/2}. \tag{2.118}$$

Matching the two-term inner solution with the two-term outer solutions in $z_2 < z < z_3$ and $z > z_3$ we find that common form of the solutions in the overlap regions are given by

$$S_C \sim 1 + \frac{1}{c_3}(z - z_3), \tag{2.119}$$

via matching on the left and

$$S_C \sim 1 + \frac{\epsilon}{\nu}\log\left(\frac{1}{D_1 c_3}(z - z_3)\right), \tag{2.120}$$

via matching on the right.

Thus, we have a complete set of matched asymptotic solutions to order ϵ for the monomer concentration. These solutions are plotted in Figure 2.13. By considering the order ϵ terms in our asymptotic expansions the assumption that surfactant flux is conserved through the boundary breaks down, *i.e.* there is now a transition region through which the surfactant will change phase. These transition regions are represented by the expressions for the inner solutions, $\tilde{S}$. Equations (2.107), (2.113), and (2.117) show that the inner solutions depend on the diffusion coefficients D and D_1. Thus, the physical properties of the surfactant and polymer used will affect the size of the transition region through which surfactant and polymer change phase.

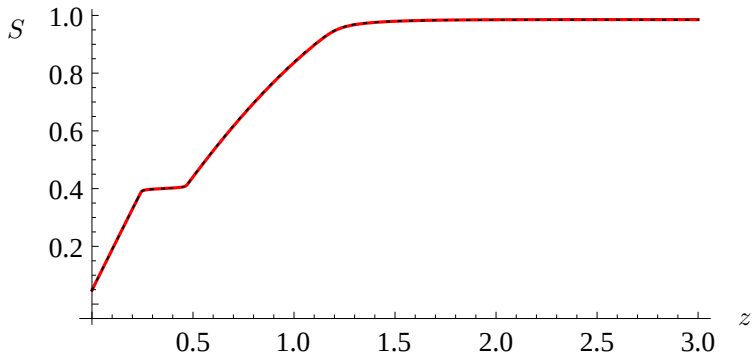

Figure 2.13: Graph that compares the numerical solution (continuous line) to the order ϵ asymptotic solution (dotted line) for monomer concentration. Parameters used are $D = 0.2$, $D_1 = 0.4$, $S^* = 2.5$, $P^* = 1.2$, $\Gamma^* = 2$, $\beta = 0.02$, $\delta = 0.4$, $N = 80$, and $M = 200$.

2.5 Summary

For the two cases described in this chapter Case 1 is a less reliable scenario as it requires one more assumption to the model than Case 2, namely that all the dimensionless diffusivities are equal to 1. Through discussions with our collaborators we conclude that for the polymer–surfactant systems we are considering the polymer and polymer–micelle aggregate molecules are typically of a similar size, and so it is reasonable to set their diffusion coefficients equal. Thus, the assumption on diffusivities used in Case 2 is a good approximation to the problem.

We performed asymptotic analysis on Case 1 in order to gain insight into the method required for Case 2, which is more physically relevant. The leading-order asymptotics for Case 2 give expressions for the boundaries between phases, something the numerics alone could not predict. Expressions were derived relating the phase boundaries to parameters in the model, $\delta, \beta, \Gamma^*, D$, and D_1, that represent physical properties of the polymer and surfactant used, and also the parameters S^* and P^* that represent bulk concentrations which can be controlled in an experiment. An expression was also derived for the amount of surfactant monomer at the boundary between the adsorbed layer and the subphase in terms of parameters listed above.

The second-order asymptotics create a more accurate approximation to the numerical solutions. Furthermore, the inner solutions define a region, as opposed to a boundary, where phase transition occurs and the expression for the inner-variables determines the error bound for the order-one predictions of the boundaries.

Finally, we note that there could be polymer–surfactant systems for which the parameters K_0 and K_1 are not typically large and so our analysis of the model using the equilibrium limit would not be valid for these systems. For such systems the full mathematical problem can still be reduced by using the large–aggregation limit but with K_0 and K_1 finite. On taking this limit the species in the model will satisfy linear, coupled, second-order differential equations, which will differ between the four regions that we found in our original analysis. In principle the resulting leading-order equations can be solved analytically and further details of this approach for the surfactant-only problem can be found in [6]. Furthermore, it would then be straight forward to determine the rate parameters K_0 and K_1 by matching the model solutions with experimental data. However, at present there exists no experimental data for the weakly interacting polymer-surfactant system and thus we did not continue this analysis.

Chapter 3

Kinetic adsorption–desorption of a monolayer at the air–liquid interface

3.1 Introduction

In this chapter we consider the kinetic adsorption–desorption of a surfactant monolayer at an air–liquid interface. We focus our attention on an experiment that our collaborator, Professor J. Penfold, and his co-workers at ISIS (Rutherford Appleton Laboratory, Didcot) perform to investigate surfactant desorption kinetics using neutron reflectometry (NR). The purpose of the experiment is to emulate a rinsing mechanism for the removal of a surfactant product, *e.g.* detergent, which is similar in principle to the mechanisms used in domestic and industrial applications of surfactant-containing products. To do this they use a specially designed flow cell, shown in Figure 3.1, to dilute the subphase of a surfactant solution so that the dissolution of an already established monolayer may be tracked with time using NR. Measurements are made on the INTER reflectometer for the anionic surfactant sodium para-dodecyl benzene-sulfonate (SDBS), commonly referred to as LAS (linear alkyl benzene sulfonate), in null reflecting water (nrw) at the air–water interface.

This chapter is laid out as follows. We first give details of the kinetic monolayer dilution experiment that our collaborator performs in §3.2. In §3.3 we consider a one-dimensional diffusion-limited model to describe the experiment. The dilution of the bulk solution is modelled using a discontinuous initial condition, parameterised by some unknown depth, H_c, which we use to fit the model to the experimental data. We extend the diffusion-limited model to incorporate the fluid dynamics of the flow

cell in §3.4 in order to obtain a semi-empirical relationship between H_c and the other physical parameters of the model. We summarise our results in §3.5 and conclude by suggesting a second experiment that could be performed to verify the model by determining the value H_c independently.

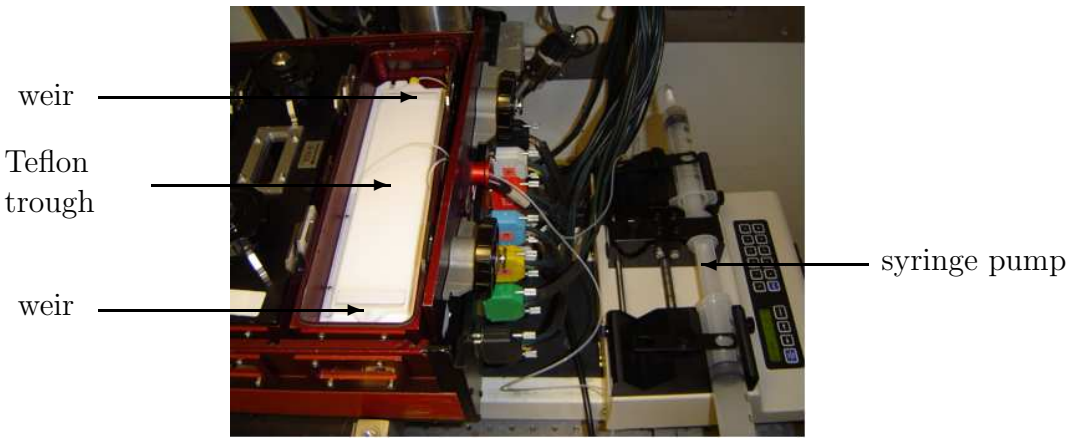

Figure 3.1: Experimental set-up of the flow cell and syringe pump.

3.2 The kinetic monolayer dilution experiment

In this section we detail the kinetic monolayer dilution experiment that our collaborator performs at ISIS.

3.2.1 The flow cell

The flow cell is a Langmuir trough made from Teflon with a weir at either end each of which is connected to a syringe pump (see Figure 3.1). The trough is filled with surfactant solution and a resulting monolayer is established at the free surface. The syringe pumps are used to exchange the solution sub-phase with another solution so that the inflow and outflow at each weir is at the same prescribed volumetric flow rate. We note that if the sub-surface is exchanged with a solution of the same surfactant concentration then there is no observed physical disruption to the free surface nor significant change to the measurements for the adsorbed surfactant concentration [27].

Three troughs were used for the experiments:

1. *Large footprint trough*: large surface area, small weir;
2. *Small footprint trough*: small surface area, small weir;
3. *Small footprint, large weir trough*: small surface area, large weir.

Each weir consists of 24 slits each 1 mm wide separated by prongs of width 1 mm; see Figure 3.2(b). A schematic of the trough is shown in Figure 3.2(a) and the dimensions of troughs 1–3 are summarised in Table 3.1.

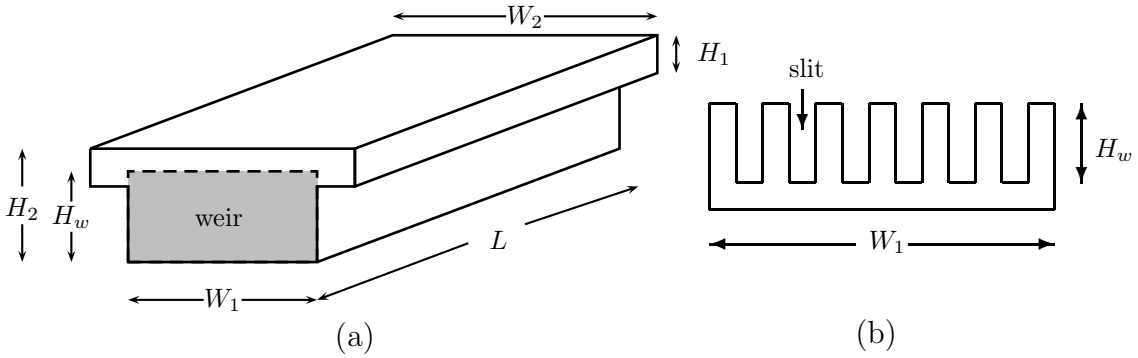

Figure 3.2: Schematic of (a) Lamgmuir trough and (b) flow-cell weir.

Trough no.	W_1 (mm)	W_2 (mm)	H_1 (mm)	H_2 (mm)	L (mm)	H_w (mm)
1	50	53	1	2	216	1.5
2	50	53	1	2	70	1.5
3	50	53	1	4	70	3

Table 3.1: Trough dimensions for the kinetic monolayer dilution experiment, where the dimensions are shown in Figure 3.2.

3.2.2 Experiment details

A surfactant monolayer is established at the air–liquid interface from a $2\,\mathrm{mol\,m^{-3}}$ LAS/nrw surfactant solution. The sub-phase is then diluted with nrw using a syringe pump and the dissolution of the monolayer is followed with time. Measurements of the adsorbed surfactant concentration are calculated from the NR data obtained on the INTER reflectometer at ISIS. The experiment is repeated for different trough

dimensions, weir height, volumetric flow rates, Q, and total volume exchanges. Details of six experiments are given in Table 3.2 (see Appendix A for experimental data).

We note that, due to the availability of the raw compounds, it was necessary to use two different structural isomers of LAS to produce the surfactant solution as indicated in column two of Table 3.2. The difference between these two isomers is the position of the sulfonated aromatic ring along the hydrocarbon tail. For the symmetric isomer, the aromatic ring is joined to the middle of the alkyl chain at the 'C6' position and so we refer to it as LAS-6. For the asymmetric isomer, the aromatic ring is joined at the 'C4' position so it is referred to as LAS-4. Tucker *et al.* [39] showed, using NR, that the position of the aromatic ring has a negligible effect on the adsorption properties of LAS.

Experiment no.	Surfactant	Trough no.	Volumetric flow rate (ml/min)	Solution vol. (mL)	Volume exchange	Time for dilution (mins)
1	2mM LAS-4	1	2.5	30	×2	24
2	2mM LAS-4	2	2.5	15	×2	12
3	2mM LAS-4	2	1.25	15	×4	48
4	2mM LAS-4	2	0.625	15	×2	48
5	2mM LAS-4	3	0.625	25	×2	80
6	2mM LAS-6	1	2.5	30	×2	24

Table 3.2: Summary of kinetic dilution experiments.

3.2.3 Results of the experiment

Figure 3.3 shows plots of the data for the dissolution of the monolayer with time after a dilution with nrw for each of the six experiments summarised in Table 3.2. The time between data points differs between experiments but is between 6 and 14 minutes; for full details of the experimental data see Appendix A. The measured adsorbed concentration has an error of $\pm 0.2 \times 10^{-6}\,\mathrm{mol\,m^{-3}}$, as shown by the error bars in Figure 3.3. The results of the six experiments shown in Figure 3.3 follow a broadly similar reduction in the surfactant surface concentration on the timescale of 70–120 minutes. The dilution starts at $t = 0$; however, since NR measurements were not made before the dilution there are no data points at $t = 0$. In §3.3 we use typical

values for the adsorbed concentration at equilibrium given in references [30, 39, 43] to compare with the results of our diffusion-limited model.

Experiments 1 and 6 shown in Figures 3.3(a) and 3.3(f) are for the same trough, dilution rate and volume exchange but for the isomers LAS-4 and LAS-6 respectively. For Experiment 1 we see a sharp drop off of the adsorbed concentration during the dilution phase (24 minutes) followed by a plateau at approximately $2.25\times10^{-6}\,\mathrm{mol\,m^{-2}}$ compared to Experiment 6 in which the adsorbed concentration remains approximately at $2.25\times10^{-6}\mathrm{mol\,m^{-2}}$ for the whole of the experiment. We note that if the adsorbed concentration had been recorded before the dilution at $t = 0$ then a drop in adsorbed concentration would also have been observed in Experiment 6 since the adsorbed concentration for a $2\,\mathrm{mol\,m^{-3}}$ LAS-6 solution given in [30] is $3.1 \pm 0.1 \times 10^{-6}\ \mathrm{mol\,m^{-2}}$. Thus, we conclude that the dissolution of the monolayer for Experiments 1 and 6 follow broadly the same pattern.

Experiments 2–4 are for the same surfactant (LAS-4), small footprint trough, and small weir but for different flow rates and volume exchanges. The dilution time for Experiment 2 is 12 minutes compared to 48 minutes for Experiments 3 and 4. The initial decrease in the adsorbed concentration occurs more rapidly in Experiment 2 than in Experiments 3 and 4 for which the initial dissolution happens over a comparable timescale. This suggests that the time for the initial sharp decrease in the adsorbed concentration is dependent on the time taken for the dilution to occur.

The initial sharp decrease in the adsorbed concentration in Experiment 5 is on a comparable timescale to that for Experiments 3 and 4. The adsorbed concentration for Experiment 5 reduces to approximately $2.25\times10^{-6}\,\mathrm{mol\,m^{-2}}$, which is not as significant a reduction as that for Experiments 3 and 4, where the adsorbed concentration reduces approximately to $1.5\text{–}1.7\times10^{-6}\,\mathrm{mol\,m^{-2}}$. However, the time for the dilution to occur (80 minutes) in Experiment 5 is much longer than that for Experiments 3 and 4 and is almost of the length of the recorded data. It is possible that if the NR data for Experiment 5 had been recorded over a longer timescale then there might have been a further reduction in the adsorbed concentration due to re-equilibration with the bulk, which happens over a longer, diffusive, timescale compared to the faster adsorption–desorption timescale [27].

In the following section we consider a simplified diffusion-limited mathematical model to describe the observed dynamics of the dissolution of the adsorbed surfactant and compare the results of the model with the experimental data.

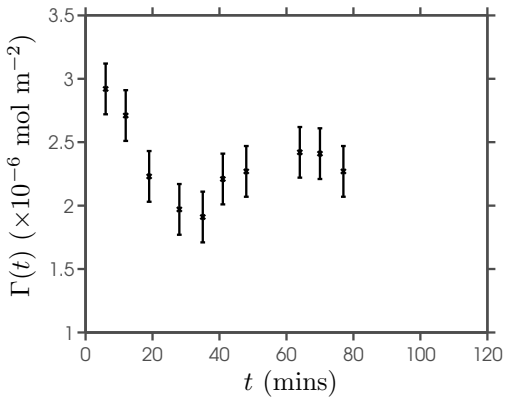

(a) Experiment 1

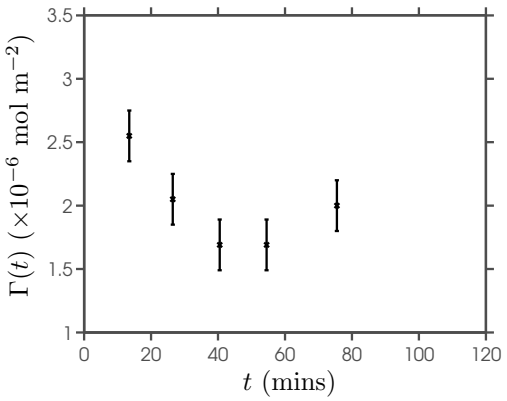

(b) Experiment 2

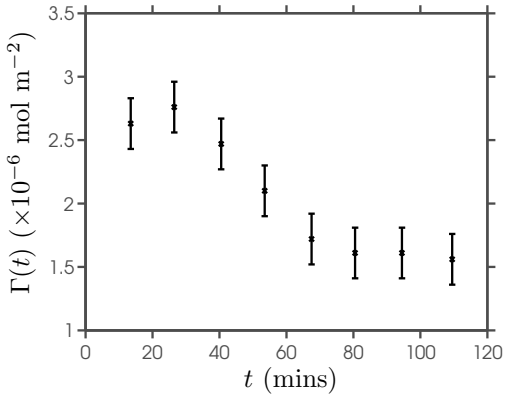

(c) Experiment 3

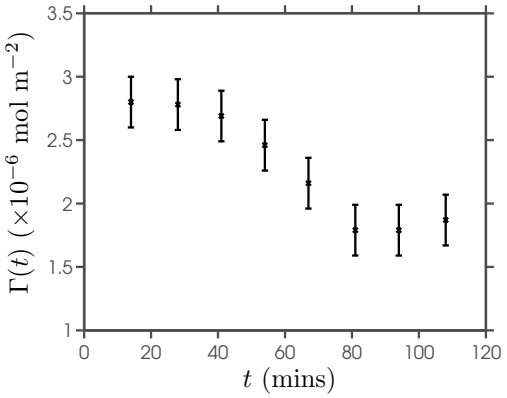

(d) Experiment 4

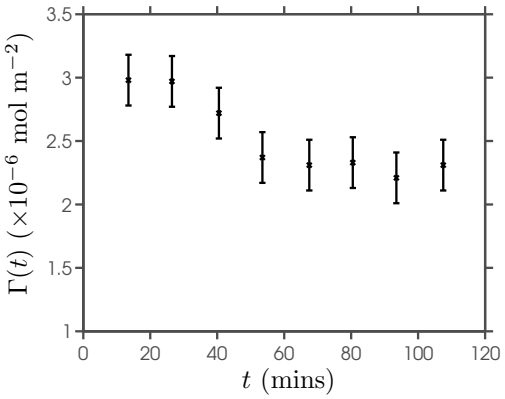

(e) Experiment 5

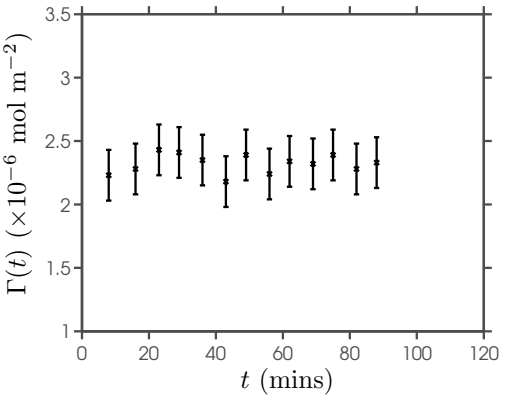

(f) Experiment 6

Figure 3.3: Results of the dilution Experiments 1–6 for the dissolution of the monolayer after one dilution has occurred. The plots show adsorbed concentration of LAS at the air–water interface against time.

3.3 Diffusion-limited model

In this section we present a model that describes the evolution of the surfactant concentration following the dilution phase for the kinetic monolayer experiment discussed in §3.2. Before the dilution phase the bulk surfactant concentration is above the critical micelle concentration (for all experiments) and so we model the evolution of the free surfactant monomers and micelles in the bulk and the adsorbed surfactant at the free surface. We assume that any flow in the trough is negligible after a brief transient following the dilution. Therefore, we consider a diffusion-limited model for the bulk surfactant phases. We simplify the model further by assuming that the timescales for the diffusion of the surfactant phases in the x- and z-directions are negligible compared to that for diffusion in the y-direction, [27], where we have taken the y-axis to point vertically upwards into the fluid. Thus, we consider a one-dimensional reaction-diffusion model for the surfactant phases in the bulk.

Excluding Experiment 5, the time for the dilution phase is 12–48 minutes and the dissolution of the monolayer occurs on a timescale of 80–100 minutes. Thus, the diffusive timescale on which the adsorbed monolayer evolves after the pump is switched off is longer than the timescale for the dilution. For mathematical simplicity we thus assume that the dilution phase occurs effectively instantaneously. Hence, initially there will be two distinct regions; one near the air–liquid interface where the surfactant phases are in equilibrium and one below where the bulk surfactant concentration is zero. Therefore, we model the dilution by imposing a discontinuous initial condition, parameterised by some unknown depth, H_c, which we use to fit the model to the experimental data. A schematic of the initial set-up we consider is shown in Figure 3.4 where S and S_m denote the bulk concentrations of monomer and micelles respectively, and Γ is the concentration of adsorbed surfactant at the interface. A more detailed derivation of the initial conditions is performed in the following section.

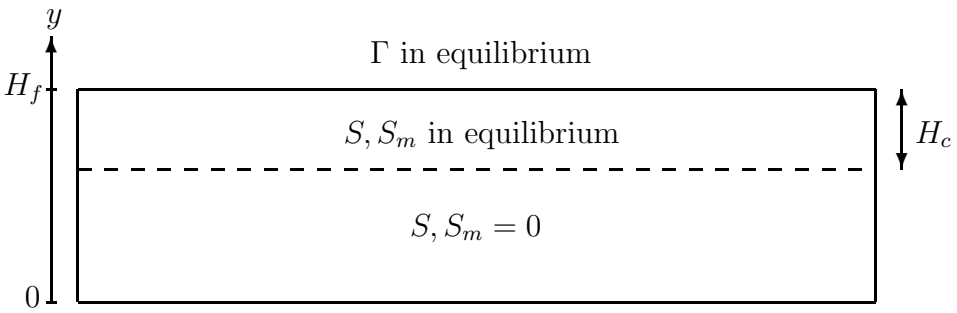

Figure 3.4: Schematic of the initial conditions for the diffusion-limited model.

3.3.1 Governing equations

The monomer and micellar concentrations are denoted by $S(y,t)$ and $S_m(y,t)$ respectively and have units $\mathrm{mol\,m^{-3}}$. Following Breward *et al.* [6] we assume the aggregation of monomers to form micelles can be modelled by a reversible, single-step reaction with rate constants $k_0^{\pm}$. Hence the monomer and micellar concentrations are governed by the coupled reaction-diffusion equations

$$S_t = D_s S_{yy} + N(k_0^+ S_m - k_0^- S^N), \qquad 0 < y < H_f, \tag{3.1a}$$

$$S_{mt} = D_{s_m} S_{myy} - (k_0^+ S_m - k_0^- S^N), \qquad 0 < y < H_f, \tag{3.1b}$$

where the subscripts t and y denote differentiation with respect to time and depth respectively, D_s and D_{s_m} are the diffusivities for the monomer and micellar phases respectively, and N is the micelle aggregation number.

The monomer diffusivity for LAS has not been determined experimentally, although the aggregation number is known; for LAS-4 and LAS-6 $N = 53$ and $N = 39 \pm 3$ respectively [39]. Hence, assuming the micelles are approximately spherical [39] we calculate the micelle diffusivity from the Stokes–Einstein equation (see §1.4.3). For the micelle radii given in [39] this gives $D_{s_m} = 1.5 \pm 0.1 \times 10^{-10}\ \mathrm{m^2\ s^{-1}}$ and $D_{s_m} = 1.4 \pm 0.1 \times 10^{-10}\,\mathrm{m^2\,s^{-1}}$ for LAS-4 and LAS-6 respectively. The ratio of the diffusivities can be estimated from the ratio of the molecular weights and the Stokes–Einstein equation, which suggests $D_{s_m}/D_s \sim N^{-1/3}$ and so the monomer diffusivity can be determined. The aggregation numbers for LAS-4 and LAS-6 give monomer diffusivities of $D_s = 5.5 \pm 0.4 \times 10^{-10}\ \mathrm{m^2\ s^{-1}}$ for LAS-4 and $D_s = 4.6 \pm 0.3 \times 10^{-10}\,\mathrm{m^2\,s^{-1}}$ for LAS-6.

We note that in general it is difficult to determine the value for the rate constants $k_0^{\pm}$ and for LAS the values are not known but we will estimate k_0^- in §3.3.1.3.

3.3.1.1 Boundary and initial conditions

We assume that surfactant monomers can only adsorb at the air–liquid interface and not at the boundaries of the trough. We denote the concentration of adsorbed surfactant by $\Gamma(t)$, which has units $\mathrm{mol\,m^{-2}}$. We note that the Froude number[1] is typically of order 10^{-3}. This implies that gravity ensures that the free surface is effectively flat and is given by $y = H_f$, where H_f is 2.2–6.9 mm for the six experiments detailed in §3.2. Thus, Γ evolves through replenishment by monomer in the bulk given by

$$\frac{\mathrm{d}\Gamma}{\mathrm{d}t} = -D_s S_y \quad \text{on} \quad y = H_f. \tag{3.2}$$

For LAS, the timescale for diffusion in the bulk is much longer than the timescale for re-equilibration of the surface excess [27] and so we assume that the surface concentration is in thermodynamic equilibrium with the sub-surface concentration. Thus, Γ satisfies the Langmuir isotherm

$$\Gamma = \frac{\Gamma_{\mathrm{sat}} S}{k + S}, \quad \text{on} \quad y = H_f, \tag{3.3}$$

where k is the ratio of the adsorption and desorption rate constants and Γ_{sat} is the saturation concentration of the surface excess, which we determine by fitting the NR data to (3.3). A typical value for k is $0.19\,\mathrm{mol\,m^{-3}}$ (see [32]).

We assume that micelles are not surface active and hence must dissociate into free monomers before they adsorb at the free surface. Therefore, the flux of micelles at the surface must be zero:

$$S_{my} = 0, \quad \text{on} \quad y = H_f. \tag{3.4}$$

On the base of the trough we assume that surfactant does not adsorb here, so there is no flux of surfactant monomer or micelles at the base of the trough, and hence

$$S_y = S_{my} = 0, \quad \text{on} \quad y = 0. \tag{3.5}$$

[1]The Froude number is defined to be $Fr := U/\sqrt{gH_f}$ where $U = Q/(W_1 H_f) = 5.6 \times 10^{-4}\,\mathrm{m\,s^{-1}}$ is the typical velocity scale, g is the acceleration due to gravity, and $H_f = 4.1 \times 10^{-3}$ m is the depth of the solution.

Before the dilution we assume that all the surfactant phases are in equilibrium and given by

$$S = S_{\mathrm{E}}, \quad S_m = \frac{k_0^+}{k_0^-} S_{\mathrm{E}}, \quad \Gamma = \frac{\Gamma_{\mathrm{sat}} S_{\mathrm{E}}}{k + S_{\mathrm{E}}}, \quad \text{at} \quad t = 0^-. \tag{3.6}$$

On summing (3.1a) and (3.1b) and applying boundary conditions (3.2)–(3.5) we find that the equilibrium monomer concentration, S_{E}, satisfies

$$S_T = S_{\mathrm{E}} + N \frac{k_0^+}{k_0^-} S_{\mathrm{E}}^N + \frac{\Gamma_{\mathrm{sat}} S_{\mathrm{E}}}{H_f (k + S_{\mathrm{E}})}, \tag{3.7}$$

where $S_T = 2\,\mathrm{mol\,m^{-3}}$ is the total concentration of surfactant in the trough. We note that, non-intuitively, the equilibrium monomer concentration depends weakly on the depth of the solution. However, the last term in (3.7) is effectively zero and so the depth of the solution has negligible effect on the equilibrium monomer concentration for the experiments we are modelling.

As discussed previously, we make the assumption that the dilution using nrw occurs effectively instantaneously compared to the much longer diffusive timescale. Hence, the initial conditions for the monomer, micellar and adsorbed concentrations are given by

$$S(y,0) = \begin{cases} 0, & 0 < y < H_f - H_c, \\ S_{\mathrm{E}}, & H_f - H_c < y < H_f, \end{cases} \tag{3.8a}$$

$$S_m(y,0) = \begin{cases} 0, & 0 < y < H_f - H_c, \\ \dfrac{k_0^+}{k_0^-} S_{\mathrm{E}}^N, & H_f - H_c < y < H_f, \end{cases} \tag{3.8b}$$

$$\Gamma(0) = \frac{\Gamma_{\mathrm{sat}} S_{\mathrm{E}}}{k + S_{\mathrm{E}}}, \tag{3.8c}$$

respectively, where H_c is unknown and is to be determined by fitting the model to the NR data presented in §3.2.

We note that no measurements were made for the concentration of adsorbed surfactant before the dilution, which we shall denote Γ_{exp}. However, measurements of adsorbed concentration at the air–water interface for a $2\,\mathrm{mol\,m^{-3}}$ LAS-6 solution in equilibrium were made using NR by [30] and [43] giving values of $3.1 \pm 0.1 \times 10^{-6}$ mol m^{-2} and $3.2 \pm 0.2 \times 10^{-6}$ mol m^{-2} respectively. Tucker *et al.* [39] measured the adsorbed concentration at the air–water interface for a $2\,\mathrm{mol\,m^{-3}}$ LAS-6/LAS-4 solution

mixtures in nrw (compositions were varied from from 90:10 to 20:80 mole ratio) at equilibrium using NR and concluded that the variation in the total adsorption with composition is relatively small. Thus, we assume that Γ_{exp} for LAS-4 is equivalent to Γ_{exp} for LAS-6. Assuming that the surface concentration is in thermodynamic equilibrium with the bulk phase then the Langmuir isotherm relates the initial adsorbed concentration, Γ_{exp}, to the unknown saturation concentration:

$$\Gamma_{\text{exp}} := \frac{\Gamma_{\text{sat}} S_{\text{E}}}{k + S_{\text{E}}}, \tag{3.9}$$

and we substitute the above expression into (3.7) to calculate the value S_{E} and hence determine the value of Γ_{sat}. For LAS-4 with $H_f = 4.1 \times 10^{-3}\,\text{m}$ this gives $S_E = 1.56\,\text{mol}\,\text{m}^{-3}$, $\Gamma_{\text{sat}} = 3.5 \times 10^{-6}\,\text{mol}\,\text{m}^{-2}$ and for LAS-6 with $H_f = 2.2 \times 10^{-3}\,\text{m}$ this gives $S_E = 1.74\,\text{mol}\,\text{m}^{-3}$, $\Gamma_{\text{sat}} = 3.4 \times 10^{-6}\,\text{mol}\,\text{m}^{-2}$.

3.3.1.2 Typical parameter values

The known parameter values for LAS-4 and LAS-6 are summarised in Table 3.3 where S_{CMC} is the critical micelle concentration.

Parameter	Description	LAS-4	LAS-6	Units
N	aggregation number	53	39	–
S_T	total surfactant conc.	2	2	$\text{mol}\,\text{m}^{-3}$
S_{CMC}	critical micelle conc.	1.6	1.8	$\text{mol}\,\text{m}^{-3}$
S_{E}	monomer equilibrium conc.	1.56	1.74	$\text{mol}\,\text{m}^{-3}$
Γ_{exp}	adsorbed conc. before dilution	3.1×10^{-6}	3.1×10^{-6}	$\text{mol}\,\text{m}^{-2}$
Γ_{sat}	adsorbed saturation conc.	3.5×10^{-6}	3.4×10^{-6}	$\text{mol}\,\text{m}^{-2}$
k	adsorption rate constant	1.9×10^{-1}	1.9×10^{-1}	$\text{mol}\,\text{m}^{-3}$
D_s	monomer diffusion coefficient	5.5×10^{-10}	4.6×10^{-10}	$\text{m}^2\,\text{s}^{-1}$
D_{s_m}	micelle diffusion coefficient	1.5×10^{-10}	1.4×10^{-10}	$\text{m}^2\,\text{s}^{-1}$
H_f	height of fluid	4.1×10^{-3}	2.7×10^{-3}	m

Table 3.3: Typical dimensional parameters for LAS-4 and LAS-6 given in [27, 30, 32, 39].

3.3.1.3 Nondimensionalisation

We nondimensionalise the variables as follows:

$$S = S_{\mathrm{CMC}} S', \qquad S_m = \frac{S_{\mathrm{CMC}}}{N} {S_m}', \qquad S_E = S_{\mathrm{CMC}} {S_E}', \tag{3.10}$$

$$t = H_f^2/D_s t', \qquad y = H_f y', \qquad \Gamma = \Gamma_{\mathrm{sat}} \Gamma', \tag{3.11}$$

where the critical micelle concentration, S_{CMC}, is defined in §1.3 and given by

$$S_{\mathrm{CMC}} = \left(\frac{k_0^-}{N k_0^+} \right)^{\frac{1}{N-1}}. \tag{3.12}$$

Substituting for the scaled variables and dropping primes we obtain the dimensionless model

$$S_t = S_{yy} + K(S_m - S^N), \qquad 0 < y < 1, \tag{3.13a}$$

$$S_{mt} = S_{myy} - K(S_m - S^N), \qquad 0 < y < 1, \tag{3.13b}$$

with boundary conditions

$$-S_y = \lambda_D \frac{\mathrm{d}\Gamma}{\mathrm{d}t}, \qquad \Gamma = \frac{S}{\beta + S}, \qquad S_{my} = 0, \qquad \text{on} \quad y = 1, \tag{3.14a}$$

$$S_y = S_{my} = 0, \qquad \text{on} \quad y = 0, \tag{3.14b}$$

and initial conditions

$$S(y,0) = \begin{cases} 0, & 0 < y < h, \\ S_{\mathrm{E}}, & H < y < 1, \end{cases} \tag{3.15a}$$

$$S_m(y,0) = \begin{cases} 0, & 0 < y < h, \\ S_{\mathrm{E}}^N, & h < y < 1, \end{cases} \tag{3.15b}$$

$$\Gamma(0) = \frac{S_{\mathrm{E}}}{\beta + S_{\mathrm{E}}}, \tag{3.15c}$$

where the equilibrium monomer concentration before the dilution, S_{E}, satisfies the dimensionless equation

$$S^* = S_{\mathrm{E}} + S_{\mathrm{E}}^N + \lambda_D \frac{S_{\mathrm{E}}}{\beta + S_{\mathrm{E}}}. \tag{3.16}$$

The dimensionless parameters of the model and typical values for LAS-4 and LAS-6 are summarised in Table 3.4.

The dimensionless rate parameter K is proportional to the micelle dissociation rate constant, k_0^-, whose value for LAS is not known. However, it is widely accepted that the timescale for dissociation k_0^- is much quicker than the timescale for diffusion in the y-direction [27] and hence $K \gg 1$. We note that if K is assumed to be an order-one parameter then k_0^- must be of order 10^{-5} s^{-1} *i.e.* the micelle dissociation timescale would be of the order of 1 day, which is clearly far greater than observed timescales, *e.g.* for the C_nE_m series the timescale is less than 10 ms [15]. Furthermore, a typical value for k_0^- for a 2.5 mol m^{-3} solution of C_{16}TAB obtained by Breward and Howell [6] is 20 s^{-1}, which gives $K = 6.1 \times 10^5$ for LAS-4 and $K = 3.2 \times 10^5$ for LAS-6.

Parameter	Expression	LAS-4	LAS-6
D	D_{s_m}/D_s	2.7×10^{-1}	3×10^{-1}
K	$H_f^2 k_0^-/D_S$	6.1×10^5	3.2×10^5
λ_D	$\Gamma_{\text{sat}}/H_f S_{\text{CMC}}$	5.1×10^{-4}	7×10^{-4}
β	k/S_{CMC}	1.2×10^{-1}	1.1×10^{-1}
S^*	S_T/S_{CMC}	1.11	1.25
S_E	S_E/S_{CMC}	9.8×10^{-1}	9.7×10^{-1}
N	–	53	39
h	$1 - H_c/H_f$	–	–

Table 3.4: Definitions of the dimensionless parameters and typical values for LAS-6 and LAS-4 with $k_0^- = 20$ s^{-1}, $H_f = 4.1 \times 10^{-3}$ m for LAS-4 and $H_f = 2.2 \times 10^{-3}$ m for LAS-6.

3.3.2 Analysis of the model

Equations (3.13)–(3.16) form a closed system for the concentrations S, S_m, and Γ whose solutions must be computed numerically. However, we can exploit the large parameter K to reduce the problem to a single partial differential equation for S. The problem can be simplified further since $\lambda_D \ll 1$, which physically corresponds to the concentration of the surface excess being negligible compared with the bulk surfactant concentration. Finally we exploit the large aggregation number, N, to determine the leading-order analytical solutions for all species in the model. We consider these limits in §3.3.2.1 and §3.3.2.3.

3.3.2.1 Model reduction via the equilibrium limit and the rapid-surface-reaction limit

We consider the equilibrium limit $K \to \infty$ in which

$$S_m = S^N, \tag{3.17}$$

except in a small boundary layer near the free surface. On summing (3.13a) and (3.13b) and taking the limit $K \to \infty$ the model reduces to a problem in S only:

$$\left(S + S^N\right)_t = \left(S + DS^N\right)_{yy}, \tag{3.18}$$

at leading order with boundary condition

$$S_y = 0, \quad \text{on} \quad y = 0. \tag{3.19}$$

We note that for sufficiently large bulk concentrations the flux boundary condition for S_m will not be satisfied in the equilibrium limit, $K \to \infty$ (*cf.* discussion in §2.3). Thus, in order to close the problem one must introduce a boundary layer of order $1/\sqrt{K}$ near the free surface where the monomer and micellar phases are not in equilibrium with each other and hence match the boundary layer solutions to the outer solutions. However, we shall circumvent this analysis by noting that $\lambda_D \ll 1$ and thus consider the rapid-surface-reaction limit to the problem, $\lambda_D \to 0$. In this limit the flux boundary condition in (3.14a) is in pseudo steady state on an order one timescale and so the adsorbed concentration reaches a pseudo steady state very quickly. Therefore, in the limit $K \to \infty$ and $\lambda_D \to 0$ the problem at leading order reduces to

$$\left(S + S^N\right)_t = \left(S + DS^N\right)_{yy}, \tag{3.20a}$$

$$S_y = 0, \qquad \text{on} \quad y = 0, 1, \tag{3.20b}$$

$$S(y,0) = \begin{cases} 0, & 0 < y < h, \\ S_{\mathrm{E}}, & h < y < 1, \end{cases} \tag{3.20c}$$

and the equilibrium monomer concentration, S_E, now satisfies

$$S^* = S_E + S_E^N. \tag{3.21}$$

The adsorbed concentration Γ decouples from the problem at leading order and is given by the Langmuir isotherm

$$\Gamma = \frac{S}{\beta + S}. \tag{3.22}$$

In the following section we present numerical solutions to (3.20)–(3.22).

3.3.2.2 Numerical results

We note that, in order to reconcile the reduction in the adsorbed surfactant concentration from the equilibrium value before the dilution with the first observed data point during the dilution phase, we add the additional data point $\Gamma = \Gamma_{\text{exp}}$ at $t = 0$ (where Γ and t are now dimensional variables) to the data given in Appendix A. We solve numerically (3.20) and (3.21) for S by fitting the unknown parameter H_c to the data via the method of least squares. We solve the parabolic PDE (3.20a) using Matlab's inbuilt solver `pdepe`. To determine H_c we solve the problem for H_c in some range and choose the value of H_c which minimises the residual in the least-squares method.

The values of H_c that minimise the residual are given in Table 3.5 for Experiments 1 to 6 with the corresponding parameter values used in the model. Plots of the fitted dimensionless solution against the experimental data for the adsorbed surfactant concentration are shown in Figure 3.5 and are in good agreement for all six experiments.

Given the values for H_c in Table 3.5 we consider whether there is an empirical relationship with the other parameters in the model. In Figure 3.6(a) we plot H_c/H_f against

Experiment no.	N	β	S^*	S_E	H_f (mm)	h	H_c (mm)
1	53	0.12	1.25	0.98	2.7	0.85	0.33
2	53	0.12	1.25	0.98	4.1	0.94	0.23
3	53	0.12	1.25	0.98	4.1	0.92	0.31
4	53	0.12	1.25	0.98	4.1	0.90	0.39
5	53	0.12	1.25	0.98	6.9	0.92	0.58
6	39	0.11	1.11	0.95	2.7	0.82	0.39

Table 3.5: Parameters used to fit the diffusion-limited model to the experimental data and the fitted values of h and H_c.

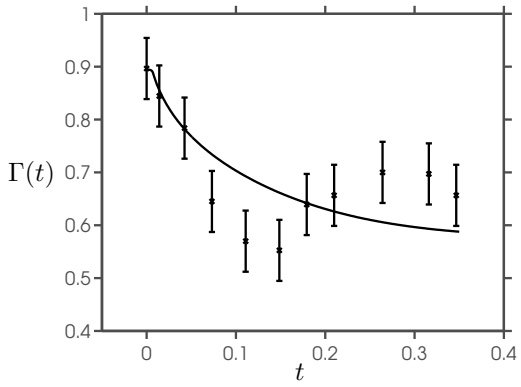

(a) Experiment 1: $h_c = 0.33$ mm

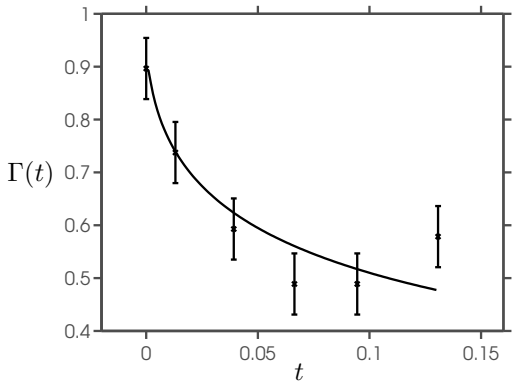

(b) Experiment 2: $h_c = 0.23$ mm

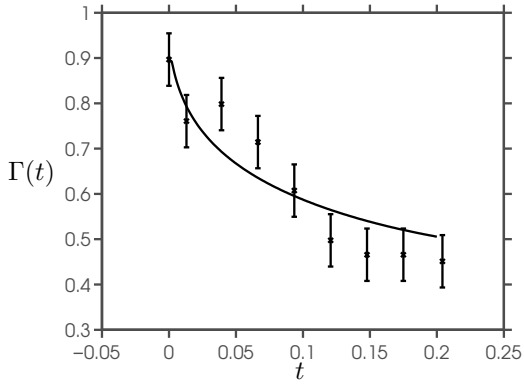

(c) Experiment 3: $h_c = 0.31$ mm

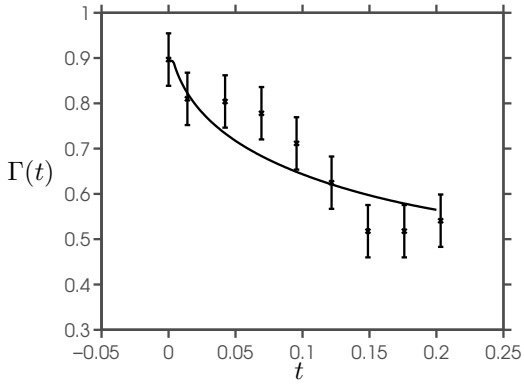

(d) Experiment 4: $h_c = 0.39$ mm

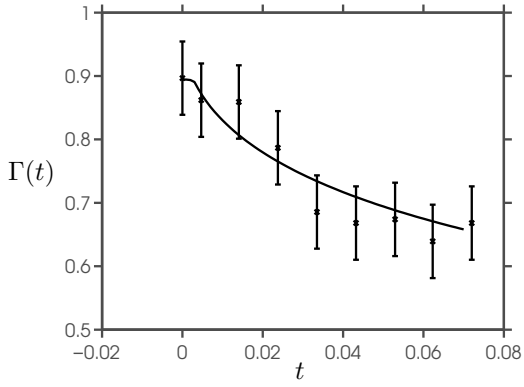

(e) Experiment 5: $h_c = 0.58$ mm

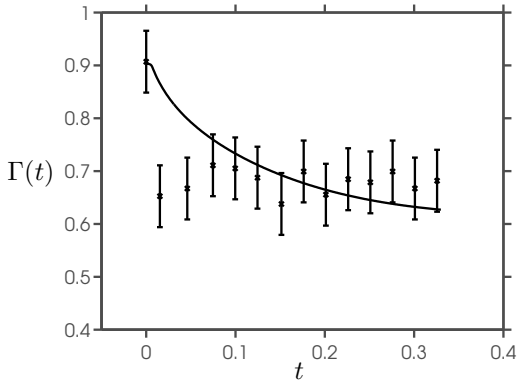

(f) Experiment 6: $h_c = 0.39$ mm

Figure 3.5: Plots of the dimensionless adsorbed surfactant concentration, Γ, against time for the fitted numerical solution to the diffusion-limited model given by (3.20), (3.21) and (3.22) against the experimental data for Experiments 1 to 6. The fitted plots were obtained via the method of least squares to determine the unknown parameter H_c. For Experiments 1–5 the parameter values $N = 53$, $\beta = 0.12$, and $S^* = 1.25$ for LAS-4 were used. For Experiment 6 the parameter values $N = 39$, $\beta = 0.11$, and $S^* = 1.11$ for LAS-6 were used.

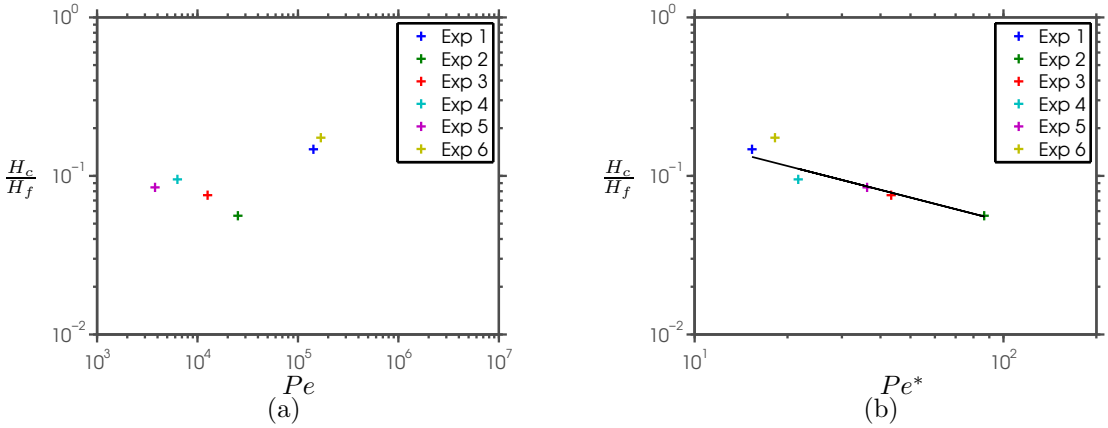

Figure 3.6: Plots of (a) H_c/H_f versus $Pe = UL/D_s$ and (b) H_c/H_f versus $Pe^* = \epsilon^2 UL/D_s$ for experiments 1 to 6 where $\epsilon = H_f/L$. The curve $H_c/H_f = \alpha/\sqrt{Pe^*}$, $\alpha = 0.52$, is plotted by the dashed line in (b). The parameter H_c was determined by fitting the diffusion-limited model in the limits $K \to \infty$ and $\lambda_D \to 0$ against the experimental data.

the Péclet number, $Pe = UL/D_s$, for the six experiments, where $U = Q/(W_1 H_f)$ is the typical velocity scale and W_1 is the width of the weir. We observe that the points plotted for Experiments 2–4 on a log-log plot lie on a linear curve, whereas Experiments 1, 5, and 6 are outliers to this curve. We note that Experiments 2–4 have the same trough dimensions which are different from the dimensions of the troughs used in Experiments 1,5 and 6. Thus, we must consider a relationship that takes into account the dimension of the troughs and so in Figure 3.6(b) we plot H_c/H_f against the reduced Péclet number, $Pe^* = \epsilon^2 Pe$, where $\epsilon = H_f/L$ is the aspect ratio for the trough. The fitted data points now all collapse onto the curve

$$\frac{H_c}{H_f} = \frac{\alpha}{\sqrt{Pe^*}}, \tag{3.23}$$

and the best-fit gives $\alpha = 0.52$.

In §3.4 we extend the diffusion-limited model by including the fluid dynamics of the flow cell. The fitted values for H_c suggest that, for large reduced Péclet number, there is a diffusive boundary layer of order $Pe^{*-1/2}$ near the free surface.

In the following sections we consider further asymptotic analysis of the diffusion-limited model to determine a closed-form solution for the problem and compare this to the experimental data.

3.3.2.3 The large-aggregation-number limit

In this section we derive analytical solutions for all the surfactant phases by taking the large-aggregation-number limit, $N \to \infty$. We consider the situation where the bulk surfactant concentration is above the CMC before the dilution, which corresponds to $S_{\mathrm{E}} \sim 1$. Then for the reduced problem (3.20) and S_E given by (3.21) there are two distinct regions:

(i) a sub-micellar region where $S < 1$ and $S_m \approx 0$;

(ii) a micellar region where $S \approx 1$ and $S_m > 0$.

If we consider the two regions defined above in the large–aggregation–number limit, $N \to \infty$, then to leading order:

(i) $S \sim S_0$ and $S_m \sim 0$, for $0 < y < \eta(t)$;

(ii) $S \sim 1$ and $S_m \sim S_{m0}$, for $\eta(t) < y < 1$;

where $\eta(t)$ is a free boundary between the micellar and sub-micellar regions and S_0, S_{m0} satisfy

$$S_{0t} = S_{0yy}, \qquad 0 < y < \eta(t), \tag{3.24a}$$

$$S_{m0t} = DS_{m0yy}, \qquad \eta(t) < y < 1, \tag{3.24b}$$

with the continuity conditions on the free boundary

$$S_0 = 1, \quad S_{m0} = 0, \quad S_{0y} = DS_{m0y}, \quad \text{on} \quad y = \eta(t), \tag{3.24c}$$

and fixed-boundary conditions

$$S_{0y} = 0, \quad \text{on} \quad y = 0, \tag{3.24d}$$

$$S_{m0y} = 0, \quad \text{on} \quad y = 1. \tag{3.24e}$$

The leading-order initial conditions are

$$\eta = h, \quad S_0 = 0, \quad S_{m0} = S^* - 1, \quad \text{at} \quad t = 0. \tag{3.24f}$$

Equations (3.24) define a classical two-phase Stefan problem with zero latent heat (for example, see [11]). Then for $t \ll \min\left(h^2, (1-h)^2\right)$ there exist similarity solutions to (3.24) of the form

$$\eta(t) = h + \eta_0\sqrt{t}, \quad S_0 = \frac{1+\operatorname{erf}\left(\frac{y-h}{2\sqrt{t}}\right)}{1+\operatorname{erf}\left(\frac{\eta_0}{2}\right)}, \quad S_{m0} = (S^*-1)\left(1 - \frac{\operatorname{erfc}\left(\frac{\sqrt{D}(y-h)}{2\sqrt{t}}\right)}{\operatorname{erfc}\left(\frac{\eta_0\sqrt{D}}{2}\right)}\right), \tag{3.25a}$$

where η_0 satisfies

$$\operatorname{erfc}\left(\frac{\eta_0\sqrt{D}}{2}\right) - D^{3/2}\left(S^*-1\right)\left(1+\operatorname{erf}\left(\frac{\eta_0}{2}\right)\right)\mathrm{e}^{(1-D)\eta_0^2/4} = 0. \tag{3.25b}$$

The surfactant solution will become sub-micellar everywhere after some critical time $t = t_c$ where $t_c := ((1-h)/\eta_0)^2$. For Experiment 2, equation (3.25b) gives $\eta_0 = 2.84$ and $t_c = 4.48 \times 10^{-4}$ when $N = 53$, $D = 0.27$, $S^* = 1.25$, and $h = 0.94$. We note that as the bulk concentration tends towards the CMC, i.e. $S^* \downarrow 1$ in (3.25b), then $\eta_0 \to \pm\infty$ and so $t_c \to 0$, which physically corresponds to the solution being sub-micellar everywhere for all t. A plot of η_0 against S^* given by (3.25b) is shown in Figure 3.7(a). The leading-order solutions (3.25a) for $0 < t < t_c$ are plotted in Figure 3.7 and as expected Figure 3.7(d) shows that $S_m \to 0$ as $t \to t_c$. Furthermore, for $0 < t < t_c$ the adsorbed surfactant concentration will remain constant to leading order, given by

$$\Gamma = \frac{1}{1+\beta}. \tag{3.26}$$

For $t > t_c$ the surfactant solution will be sub-micellar everywhere and the leading-order solutions for monomer and micellar concentrations are given by

$$S_m \sim 0, \quad S \sim \frac{1}{2}a_0 + \sum_{n=1}^{\infty} a_n \cos(n\pi y)\mathrm{e}^{-n^2\pi^2(t-t_c)}, \tag{3.27a}$$

where

$$a_0 = 2\int_0^1 S_0(y,t_c)\,\mathrm{d}y, \quad a_n = 2\int_0^1 S_0(y,t_c)\cos(n\pi y)\,\mathrm{d}y, \quad n \geq 1, \tag{3.27b}$$

and $S_0(y,t_c)$ is the numerical solution for S_0 to (3.24) at $t = t_c$. The red-dashed curve in Figure 3.8 denotes the analytical solution for Γ for times $t < t_c$ and $t > t_c$, which

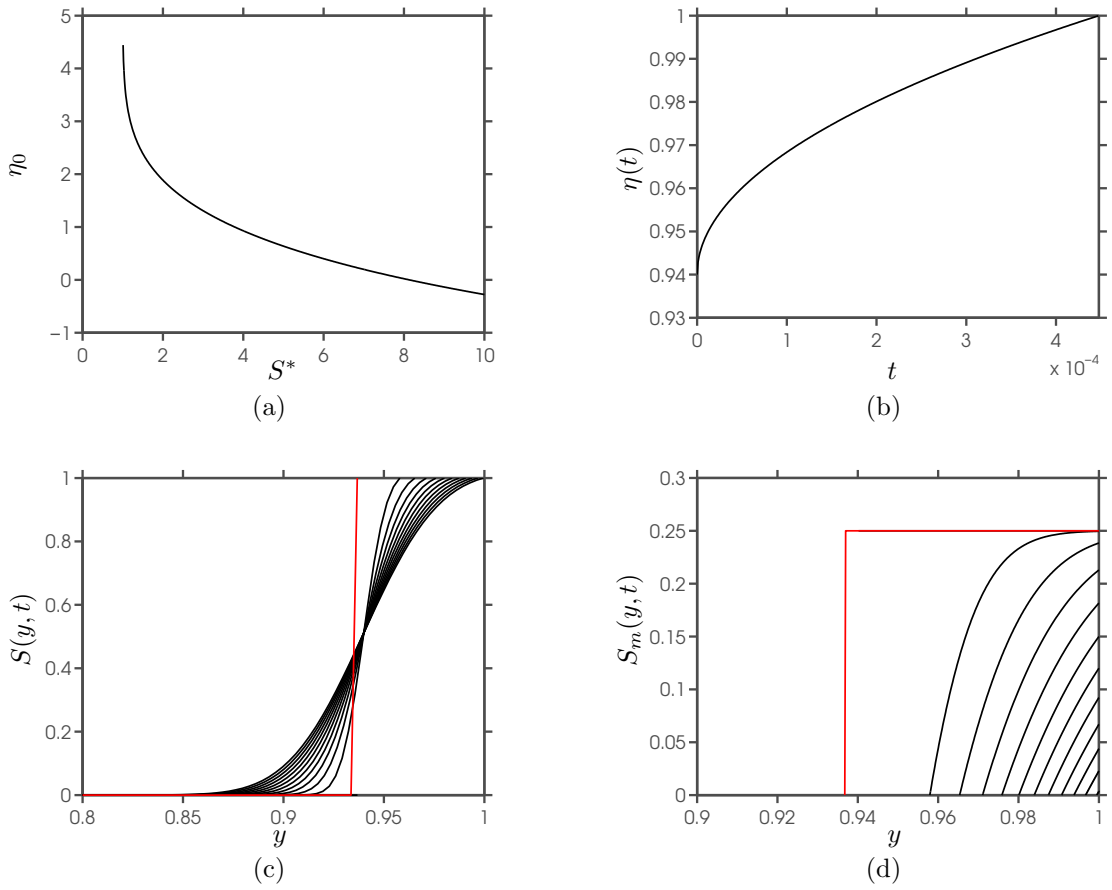

Figure 3.7: Plots of the leading-order analytical solutions (3.25a) to the diffusion-limited model in the limit $K, N \to \infty$ and $\lambda_D \to 0$. The red curves denote the initial condition in (c) and (d) and the black curves are plotted at time intervals $dt = 4 \times 10^{-5}$. Parameters used are $N = 53$, $D = 0.27$, $S_E = 0.98$, $S^* = 1.25$, and $h = 0.94$.

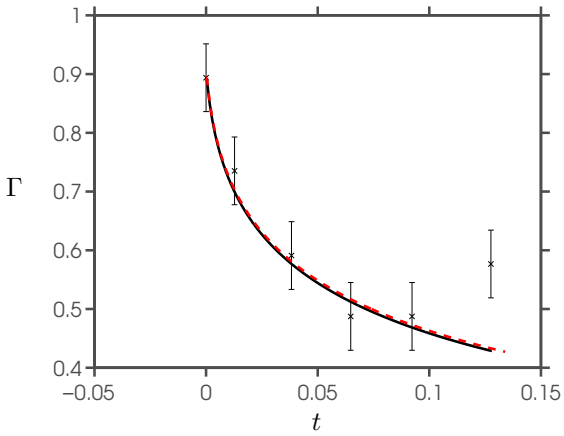

Figure 3.8: Plots of adsorbed concentration against time for Experiment 2; the error bars denote the experimental data, the numerical solution to (3.20)–(3.22) is denoted by the black continuous curve and the leading-order analytical solution as $N \to \infty$ is denoted by the red-dashed curve. Parameters used are $N = 200$, $D = 0.27$, $S_E = 0.98$, $\beta = 0.12$, $S^* = 1.25$, and $h = 0.94$.

agree well with both the the experimental data and the numerical solution to (3.20) with $N = 200$.

We note that it is possible to obtain a fully analytical solution to the diffusion model by considering the limit $S^* \to 1$, $h \to 1$ which implies that $t_c \sim 0$, and $S_{m_E} \sim 0$, *i.e.* the solution is sub-micellar everywhere. In this limit, the coefficients a_n in (3.27) depend only on the initial conditions $S(y, 0) = S_E$ where S_E is given by (3.21).

3.4 Mathematical model to estimate the thickness of the dilution layer

We now extend the model presented in §3.3 by coupling the fluid dynamics of the experiment described in §3.2 to the surfactant dynamics. We restrict our attention to a two-dimensional model; the set-up we consider is shown in Figure 3.9 where the free surface is assumed flat and given by $y = H_f$ (for justification see §3.3.1).

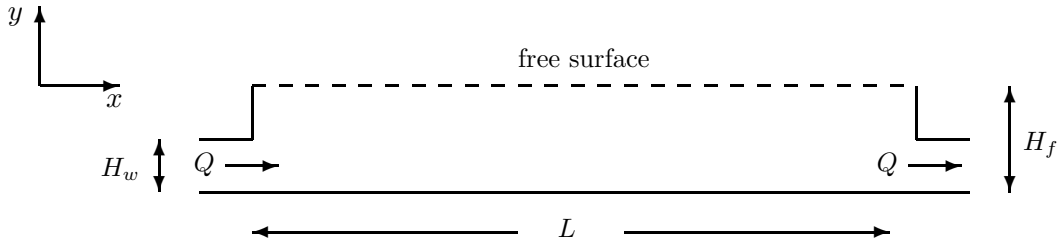

Figure 3.9: Schematic of the flow cell.

3.4.1 Governing equations

We consider a two-dimensional, incompressible flow with the velocity field given by $\mathbf{u} = (u(x, y, t), v(x, y, t))$ and excess pressure $p(x, y, t)$, which both satisfy the two-dimensional Navier–Stokes equations. Thus, the governing equations for the fluid phase are

$$\nabla \cdot \mathbf{u} = 0, \tag{3.28a}$$

$$\rho \frac{D\mathbf{u}}{Dt} = -\nabla p + \mu \nabla^2 \mathbf{u}, \tag{3.28b}$$

for $(x, y) \in [0, L] \times [0, H_f]$, where ρ and μ are the fluid density and dynamic viscosity respectively.

The monomer and micellar concentrations, denoted by $S(x, y, t)$ and $S_m(x, y, t)$ respectively, are governed by coupled reaction-advection-diffusion equations. Hence,

$$\frac{\partial S}{\partial t} + \mathbf{u} \cdot \nabla S = D_s \nabla^2 S + N(k_0^+ S_m - k_0^- S^N), \tag{3.29a}$$

$$\frac{\partial S_m}{\partial t} + \mathbf{u} \cdot \nabla S_m = D_{s_m} \nabla^2 S_m - (k_0^+ S_m - k_0^- S^N), \tag{3.29b}$$

for $(x, y) \in [0, L] \times [0, H_f]$.

Finally, the concentration of adsorbed surfactant, $\Gamma(x, t)$, evolves according to

$$-D_s S_y\big|_{y=H_f} = \Gamma_t + (u_s \Gamma)_x - D_\Gamma \Gamma_{xx}, \tag{3.30}$$

where u_s is the surface velocity and D_Γ is the surface diffusivity of the adsorbed monomer. For LAS, D_Γ is not known but $D_\Gamma \leq 10^{-9}$ m^2 s^{-1} for typical surfactants [17].

3.4.1.1 Boundary and initial conditions

The kinetic condition at the effectively flat surface reads

$$v = 0, \quad \text{on} \quad y = H_f, \tag{3.31}$$

and a balance of tangential stress gives

$$\mu u_y = \gamma_x, \quad \text{on} \quad y = H_f, \tag{3.32}$$

where $\gamma(x,t)$ is the surface tension.

Assuming that the surface concentration is in thermodynamic equilibrium with the sub-surface concentration then Γ satisfies the Langmuir isotherm

$$\Gamma = \frac{\Gamma_{\text{sat}} S}{k+S}, \quad \text{on} \quad y = H_f, \tag{3.33}$$

where Γ_{sat} and k are defined in §3.3.1. Since the surface is in thermodynamic equilibrium with the bulk, the surface tension is related to the surface concentration via the Frumkin equation [1, 8]:

$$\gamma - \gamma_0 = RT\Gamma_{\text{sat}} \log\left(1 - \frac{\Gamma}{\Gamma_{\text{sat}}}\right), \quad \text{on} \quad y = H_f, \tag{3.34}$$

where $\gamma_0 = 0.07$ N m^{-1} is the surface tension in the absence of adsorbed species, $T = 298$ K is the absolute temperature and $R = 8.31$ J mol^{-1} K^{-1} is the universal gas constant.

Assuming micelles are not surface active then S_m satisfies the no-flux condition on the free surface:

$$S_{my} = 0, \quad \text{on} \quad y = H_f. \tag{3.35}$$

On the base of the trough the standard no-slip and no-flow conditions apply to the fluid velocity and we assume that surfactant does not adsorb here, so there is no flux of surfactant monomer or micelles at the base of the trough, and hence

$$u = v = S_y = S_{my} = 0, \quad \text{on} \quad y = 0. \tag{3.36}$$

We assume that the flow that enters the trough from the weir is approximately Poiseuille and given by

$$u = \frac{6H_f U y}{H_w^2}\left(1 - \frac{y}{H_w}\right), \quad v = 0, \quad \text{on} \quad x = 0, \quad 0 < y < H_w. \tag{3.37}$$

The velocity scale, U, is determined from the known volumetric flux rate, Q, at the inlet

$$Q = \int_0^W \int_0^{H_w} \frac{6H_f U y}{H_w^2}\left(1 - \frac{y}{H_w}\right) \mathrm{d}y\mathrm{d}z = H_f W U, \quad \Longrightarrow \quad U = \frac{Q}{H_f W}, \tag{3.38}$$

where W is the width of the trough.

Since the dilution is with nrw, the surfactant concentration is zero for this flow and so the boundary conditions for the surfactant phases at the inlet weir are

$$S = S_m = 0, \quad \text{on} \quad x = 0, \quad 0 < y < H_w. \tag{3.39}$$

As for the trough base we apply the no-slip and no-flux conditions to the wall at $x = 0$:

$$u = v = S_x = S_{mx} = 0, \quad \text{on} \quad x = 0, \quad H_w < y < H_f. \tag{3.40}$$

In the absence of any information about the concentrations exiting the trough we apply the passive boundary conditions of zero diffusive flux and zero pressure, *i.e.*

$$S_x = S_{mx} = v = p = 0, \quad \text{on} \quad x = L, \quad 0 < y < H_w. \tag{3.41}$$

As for the inlet wall we apply the no-slip and no-flux conditions to the outlet wall:

$$u = v = S_x = S_{mx} = 0, \quad \text{on} \quad x = L, \quad H_w < y < H_f. \tag{3.42}$$

Initially the fluid is at rest, all the surfactant phases are in equilibrium and the concentration of adsorbed surfactant is known. Hence,

$$\mathbf{u} = \mathbf{0}, \quad S = S_\mathrm{E}, \quad S_m = \frac{k_0^+}{k_0^-} S_\mathrm{E}^N, \quad \Gamma = \Gamma_\mathrm{exp} \quad \text{at} \quad t = 0, \tag{3.43}$$

where the equilibrium concentration of monomer, S_E, is given by the equation

$$S_T = S_E + N\frac{k_0^+}{k_0^-}S_E^N + \frac{\Gamma_{\text{exp}}}{H_f}, \tag{3.44}$$

with $S_T = 2\,\text{mol}\,\text{m}^{-3}$.

3.4.1.2 Typical parameter values

Throughout the rest of this chapter, unless stated otherwise, we consider the parameters associated with Experiment 2 (LAS-4 and the small-footprint, small-weir trough) which are summarised in Table 3.6.

Parameter	Description	Typical value	Units
S_T	total surfactant conc.	2	$\text{mol}\,\text{m}^{-3}$
S_{CMC}	critical micelle conc.	1.6	$\text{mol}\,\text{m}^{-3}$
S_{E}	monomer concentration in equilibrium	1.56	$\text{mol}\,\text{m}^{-3}$
Γ_{exp}	adsorbed concentration in equilibrium	3.1×10^{-6}	$\text{mol}\,\text{m}^{-2}$
Γ_{sat}	adsorbed saturation concentration	3.5×10^{-6}	$\text{mol}\,\text{m}^{-2}$
D_s	monomer diffusion coefficient	5.5×10^{-10}	$\text{m}^2\,\text{s}^{-1}$
D_{s_m}	micelle diffusion coefficient	1.5×10^{-10}	$\text{m}^2\,\text{s}^{-1}$
D_Γ	surface diffusion coefficient	1×10^{-9}	$\text{m}^2\,\text{s}^{-1}$
k	adsorption rate constant	0.19	$\text{mol}\,\text{m}^{-3}$
k_0^-	micelle dissociation rate constant	20	s^{-1}
H_f	height of fluid	4.1×10^{-3}	m
H_w	height of weir	1.5×10^{-3}	m
L	length of trough	70×10^{-3}	m
w	width of trough	50×10^{-3}	m
Q	dilution rate	4.2×10^{-8}	$\text{m}^3\,\text{s}^{-1}$
U	mean horizontal velocity (Q/wH_w)	5.6×10^{-4}	$\text{m}\,\text{s}^{-1}$
ρ	density of water	10^3	$\text{kg}\,\text{m}^3$
μ	dynamic viscosity of water	10^{-3}	$\text{Pa}\,\text{s}$
γ_0	surface tension of water	7.0×10^{-2}	$\text{N}\,\text{m}^{-1}$
R	universal gas constant	8.31	$\text{J}\,\text{mol}^{-1}\,\text{K}^{-1}$
T	absolute temperature	298	K

Table 3.6: Typical dimensional parameters for the kinetic monolayer dilution Experiment 2 given in [6, 27, 30, 32, 39, 43].

3.4.1.3 Nondimensionalisation

In this section we nondimensionalise the problem to reduce the number of variable parameters and identify the relevant dimensionless groups. We nondimensionalise as follows:

$$\begin{aligned} &x = Lx', \qquad u = Uu', \qquad S = S_{\mathrm{CMC}}S', \qquad \Gamma = \Gamma_{\mathrm{sat}}\Gamma', \qquad t = \frac{L}{U}t', \\ &y = \epsilon Ly', \qquad v = \epsilon Uv', \qquad S_m = \frac{S_{\mathrm{CMC}}}{N}{S_m}', \qquad S_E = S_{\mathrm{CMC}}{S_E}', \qquad p = \frac{\mu U}{\epsilon^2 L}p', \end{aligned} \tag{3.45}$$

where $\epsilon = H_f/L$ is the aspect ratio of the trough, and the critical micelle concentration, S_{CMC}, is defined in (3.12). On substituting (3.45) into the model and dropping primes we obtain the dimensionless equations for the fluid

$$u_x + v_y = 0, \tag{3.46a}$$

$$Re^*\left(u_t + uu_x + vu_y\right) = -p_x + \epsilon^2 u_{xx} + u_{yy}, \tag{3.46b}$$

$$\epsilon^2 Re^*\left(v_t + uv_x + vv_y\right) = -p_y + \epsilon^4 v_{xx} + \epsilon^2 v_{yy}, \tag{3.46c}$$

where $Re^* = \epsilon^2\rho UL/\mu \approx 0.05$ is the reduced Reynolds number.

The equations for the surfactant phases are

$$Pe^*\left(S_t + \mathbf{u}\cdot\nabla S\right) = \epsilon^2 S_{xx} + S_{yy} + K\left(S_m - S^N\right), \tag{3.47a}$$

$$Pe^*\left(S_{mt} + \mathbf{u}\cdot\nabla S_m\right) = D\left(\epsilon^2 S_{mxx} + S_{myy}\right) - K\left(S_m - S^N\right), \tag{3.47b}$$

$$-S_y|_{y=1} = \lambda_D Pe^*\left(\Gamma_t + (u_s\Gamma)_x\right) - \epsilon^2\lambda_D D^*\Gamma_{xx}, \tag{3.47c}$$

where $Pe^* = \epsilon^2 UL/D_s \approx 89$ is the reduced Péclet number, $D^* = D_\Gamma/D_s = 1.8$ typically, and the parameters K, λ_D, and D are defined in §3.3.1.3.

The dimensionless boundary conditions are given by

$$x = 0: \qquad u = \frac{6}{h_w^3}y\left(h_w - y\right), \quad v = S = S_m = 0, \qquad \text{for} \quad 0 < y < h_w, \tag{3.48a}$$

$$u = v = S_x = S_{mx} = 0, \qquad \text{for} \quad h_w < y < 1, \tag{3.48b}$$

$$x = 1: \qquad v = p = S_x = S_{mx} = 0, \qquad \text{for} \quad 0 < y < h_w, \tag{3.48c}$$

$$u = v = S_x = S_{mx} = 0, \qquad \text{for} \quad h_w < y < 1, \tag{3.48d}$$

$$y = 0: \qquad v = u = S_y = S_{my} = 0, \tag{3.48e}$$

$$y = 1: \qquad v = S_{my} = 0, \quad \Gamma = \frac{S}{\beta + S}, \qquad M^* \left(u_y + \epsilon^2 v_x\right) = \frac{-\Gamma_x}{1 - \Gamma}, \tag{3.48f}$$

where we have used the Frumkin equation (3.34) to remove γ_x from the shear boundary condition (3.48f) and $M^* = \mu UL/RTH_f\Gamma_{\rm sat} = 4.1 \times 10^{-4}$ is the reduced, inverse Marangoni number.

The dimensionless initial conditions are

$$\mathbf{u} = \mathbf{0}, \quad S = S_E, \quad S_m = S_E^N, \quad \Gamma = \frac{S_E}{\beta + S_E}, \quad \text{at} \quad t = 0, \tag{3.49}$$

where S_E satisfies

$$S^* = S_E + S_E^N + \lambda_D \frac{S_E}{\beta + S_E}. \tag{3.50}$$

The definitions and typical values of the dimensionless parameters are summarised in Table 3.7.

Parameter	Expression	Description	Value
ϵ	H_f/L	aspect ratio	5.9×10^{-2}
Re^*	$\epsilon^2\rho UL/\mu$	reduced Reynolds number	2.9×10^{-2}
Pe^*	$\epsilon^2 UL/D_s$	reduced Péclet number	8.9×10^{1}
M^*	$\mu UL/RTH_f\Gamma_{\rm sat}$	reduced inverse Marangoni number	4.1×10^{-4}
λ_D	$\Gamma_{\rm sat}/H_f S_{\rm CMC}$	ratio of adsorbed to net surfactant conc.	5.3×10^{-4}
β	$k/S_{\rm CMC}$	dimensionless Langmuir rate constant	1.2×10^{-1}
S^*	$S_T/S_{\rm CMC}$	dimensionless total surfactant conc.	1.25
S_E	$S_E/S_{\rm CMC}$	dimensionless monomer equilibrium conc.	9.8×10^{-1}
h_w	H_w/H_f	dimensionless weir height	3.7×10^{-1}
K	$H_f^2 k_0^-/D_s$	dimensionless reaction rate constant	6.1×10^{6}
D	D_{s_m}/D_s	ratio of diffusion coefficients	2.7×10^{-1}
D^*	D_Γ/D_s	ratio of diffusion coefficients	1.8
N	–	aggregation number	53

Table 3.7: Definitions of the relevant dimensionless parameters and corresponding typical values for the kinetic monolayer dilution Experiment 2.

We suggest an *ad hoc* approach to simplifying the model (3.46)–(3.49) by exploiting the small and large dimensionless parameters of the model given in Table 3.7. As in §3.3.2.1 we first consider the equilibrium limit $K \to \infty$ in which the governing equations for the surfactant phases (3.47) to leading order are

$$S_m = S^N, \tag{3.51a}$$

$$Pe^* \left((S + S^N)_t + \mathbf{u} \cdot \nabla (S + S^N) \right) = \epsilon^2 (S + DS^N)_{xx} + (S + DS^N)_{yy}, \tag{3.51b}$$

$$-S_y|_{y=1} = \lambda_D Pe^* \left(\Gamma_t + (u_s \Gamma)_x \right) + \epsilon^2 \lambda_D D^* \Gamma_{xx}. \tag{3.51c}$$

The fluid equations (3.46), boundary conditions (3.48), and initial conditions (3.49) remain the same to leading order in this limit.

The outer problem, away from the boundaries $x = 0, 1$ and $y = 0, 1$, can be determined by neglecting terms of order $\epsilon, Re^*, M^*, \lambda_D$ and $1/Pe^*$ to obtain the thin-film model at leading order:

$$u_x + v_y = 0, \tag{3.52a}$$

$$-p_x + u_{yy} = 0, \tag{3.52b}$$

$$-p_y = 0, \tag{3.52c}$$

$$\left(S + S^N \right)_t + \mathbf{u} \cdot \nabla \left(S + S^N \right) = 0. \tag{3.52d}$$

In this limit we have neglected the highest-order derivatives of S in (3.51b) and so there will be diffusive boundary layers of order $1/\sqrt{Pe^*}$ near $x = 0, 1$, and $y = 0, 1$. However, it is not clear which terms in the free surface boundary conditions will balance to leading order under this boundary-layer scaling and so to gain further insight into the problem we consider numerical simulations of the model in the following section.

3.4.2 Numerical simulations

In this section we present numerical simulations of the model using COMSOL Multiphysics version 4.3 software. For simplicity, we assume that the solution is sub-micellear, *i.e.* the bulk concentration is below the CMC. This assumption is valid as the bulk concentration initially is just above the CMC, $S^* \approx 1.25$, and will quickly transition to sub-CMC during the dilution, as in §3.3.2.3. We solve the fluid problem using COMSOL's 'Laminar flow' node and note that it is necessary to rescale the variables of the governing equations (3.46)–(3.49) so that the Navier–Stokes equations are in the appropriate form for COMSOL. Hence, we apply the rescaling below

$$x, u \sim \epsilon, \quad p \sim \epsilon^2, \quad S \sim S^*. \tag{3.53}$$

so that the resulting diffusion coefficient in the surfactant governing equation is as small as possible, *i.e.* it is the reduced Péclet number. The scaling of the monomer concentration, S, in (3.53) corresponds to using S_b as the scaling for S instead of S_{CMC} in the nondimensionalisation of the equations. The problem is now given on the domain $(x, y) \in [0, 1/\epsilon] \times [0, 1]$ and full details of the rescaled equations are given in Appendix B. We note that the tangential stress boundary condition is now written explicitly in terms of the Marangoni number, Ma,

$$u_y + v_x = -\frac{Ma}{\epsilon}\frac{S_x}{\beta + S}, \tag{3.54}$$

where $Ma = RT\Gamma_{\mathrm{sat}}/\mu U$, and for Experiment 2 is 4.4×10^4.

Due to the extreme largeness of the parameters Pe^* and Ma, the problem we want to solve is numerically very stiff and so we are unable to compute a solution (for reasonable error tolerances) for the actual experimental values of Pe^* and Ma. Instead, we solve the problem for a range of values for Pe^* and Ma to determine the qualitative behaviour of the solution as these parameters vary. Details of the implementation in COMSOL are given in Appendix B. The solutions for the surfactant monomer concentration and flow profile are shown in Figures 3.10–3.13 and Figures 3.14 respectively.

Plots of the concentration profile at $t = 1$, corresponding to half-way through the dilution phase, are shown in Figure 3.10. As Pe^* increases, for a fixed value of Ma, the plots show that boundary layers on the trough base, $y = 0$, and free surface, $y = 1$, develop in which the surfactant concentration is greater than in the rest

of the domain. We note that in the limiting case $Ma = 10$ and $Pe^* = 1$, shown in Figure 3.10(a), no boundary layers are present. As Ma increases we first note that the concentration of surfactant in the boundary layer on the base of the trough decreases and the concentration of surfactant in the boundary layer on the free surface increases, *i.e.* for larger Marangoni numbers the boundary layer at the free surface dominates. Secondly, 'roll waves' develop near the free surface as Ma increases and are most noticeable when Pe^* is large. The presence of these roll waves is due to surface Marangoni effects, and they have a repeating structure similar to Marangoni-convection cells, which are typically present in steady problems with surface tension gradients. Significantly, however, the observed convection cells are advected along the trough by the bulk flow as opposed to typical Marangoni-convection cells that are stationary. The existence of these roll waves can be justified as follows; as the bulk solution is diluted from the left there will be a local region where the bulk surfactant decreases and so the surface concentration is no longer in equilibrium with the bulk. Thus, surfactant on the surface desorbs so that a new local equilibrium between the bulk and the surface is established. This results in there being a concentration gradient in the adsorbed surfactant on the whole trough scale and so the adsorbed surfactant tries to re-equilibrate with the bulk inducing a Marangoni flow at the surface. Plots of the concentration profile at the end of the dilution phase, $t = 2$, are shown in Figures 3.10 and 3.11, which show the persistence of the boundary layer near the free surface as Pe^* increases. However, the boundary layer near the trough base has vanished in most cases and is just visible when Pe^* is large, see Figures 3.12(a), 3.12(b), 3.13(a), and 3.13(b).

Figure 3.14 compares the surfactant concentration profile, $S(x, y, t)$, with the velocity profile given by $|\mathbf{u}(x, y, t)|$ at times $t = 0.5, 1, 1.5, 2$ for $Ma = 1000$ and $Pe^* = 75$. The plots of the velocity profile show the formation of Marangoni-convection cells that propagate along the trough and which agree with the observed roll waves in the surfactant concentration profiles. The flow in the boundary layer on the trough base is approximately zero and for $t \gtrsim 1$ the boundary layer near $y = 1$ is also approximately stagnant. In the rest of the domain the flow profile tends to that of an approximate Poiseuille flow as t increases, which agrees with the leading-order outer solution for large Pe^* and small M^* (large Ma) derived in the previous section. Plots of the surface velocity $u_s = u(x, 1, t)$ in Figure 3.15 show that the surface flow is not uni-directional, which is in agreement with the observed Marangoni-convection-like cells, and reaches velocities that are five times the magnitude of that in the bulk.

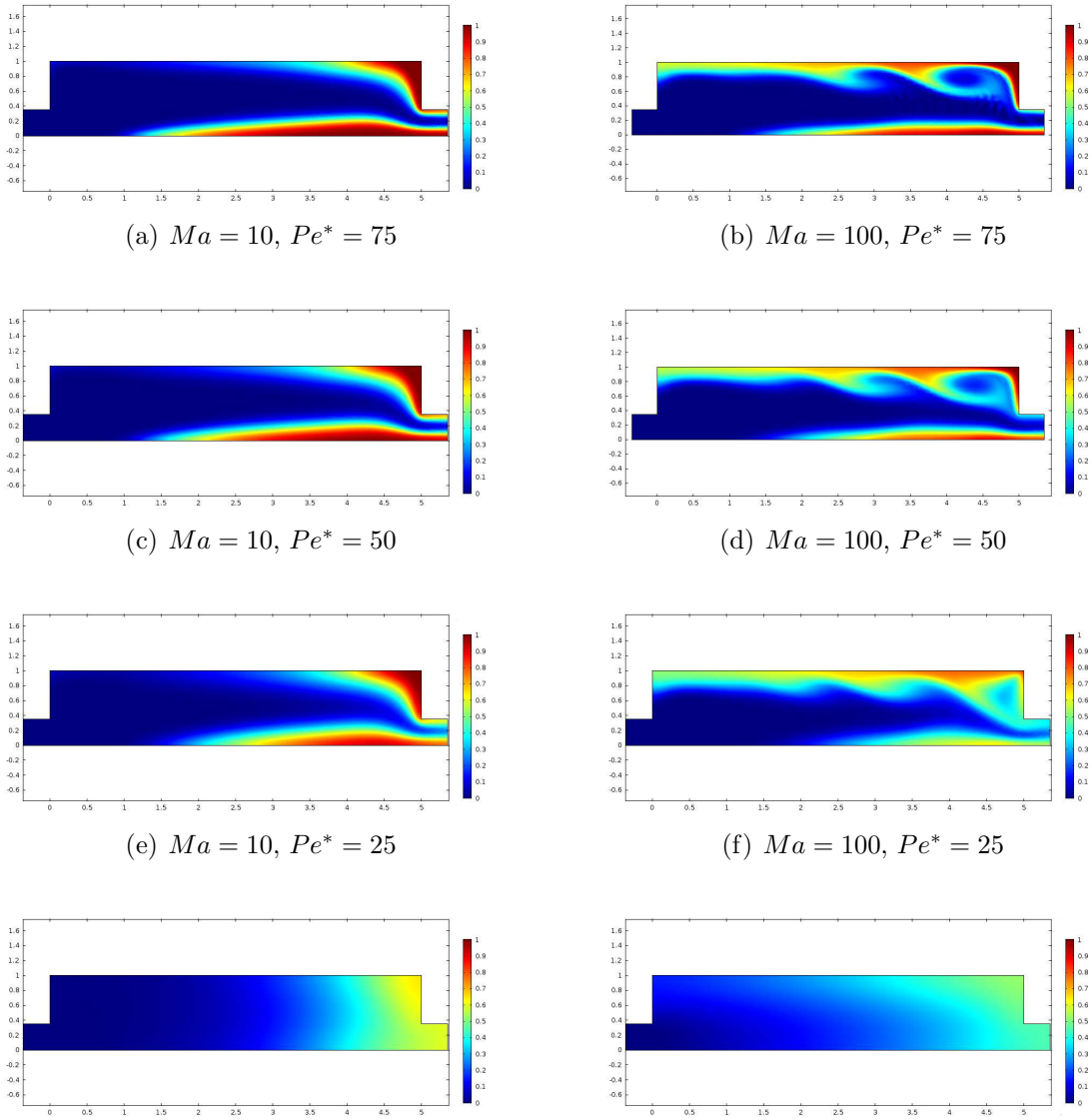

(a) $Ma = 10$, $Pe^* = 75$

(b) $Ma = 100$, $Pe^* = 75$

(c) $Ma = 10$, $Pe^* = 50$

(d) $Ma = 100$, $Pe^* = 50$

(e) $Ma = 10$, $Pe^* = 25$

(f) $Ma = 100$, $Pe^* = 25$

(g) $Ma = 10$, $Pe^* = 1$

(h) $Ma = 100$, $Pe^* = 1$

Figure 3.10: Plots of the monomer concentration profile, S, at the mid-point of the dilution phase, $t = 1$, as Ma and Pe^* vary. Other parameters used are $\epsilon = 0.2$, $Re^* = 0.05$, $\lambda_D = 4 \times 10^{-4}$, $D = 1.8$, $\beta = 0.11$, and $h_w = 0.35$.

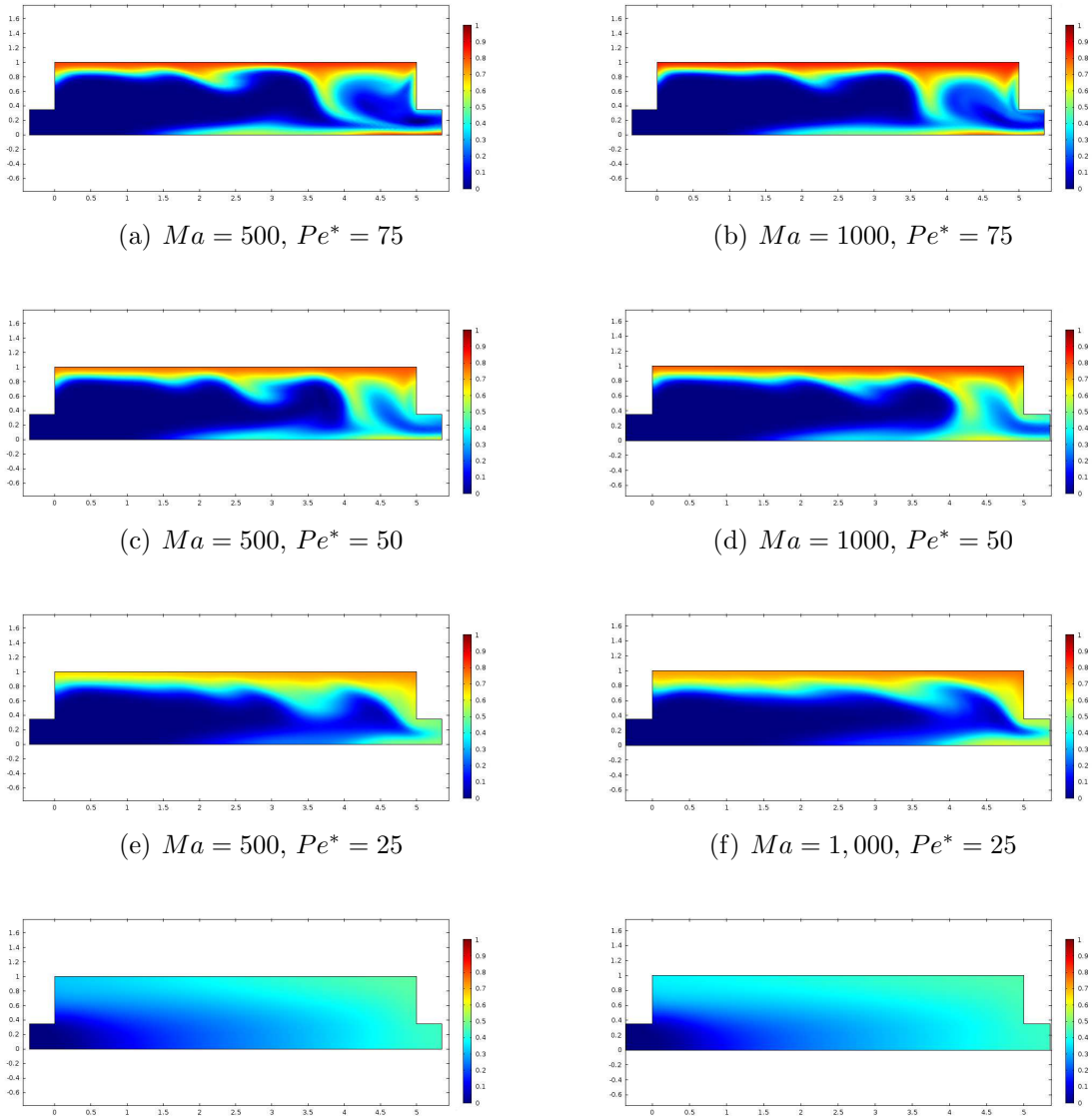

(a) $Ma = 500$, $Pe^* = 75$

(b) $Ma = 1000$, $Pe^* = 75$

(c) $Ma = 500$, $Pe^* = 50$

(d) $Ma = 1000$, $Pe^* = 50$

(e) $Ma = 500$, $Pe^* = 25$

(f) $Ma = 1,000$, $Pe^* = 25$

(g) $Ma = 500$, $Pe^* = 1$

(h) $Ma = 1000$, $Pe^* = 1$

Figure 3.11: Plots of the monomer concentration profile, S, at the mid-point of the dilution phase, $t = 1$, as Ma and Pe^* vary. Other parameters used are $\epsilon = 0.2$, $Re^* = 0.05$, $\lambda_D = 4 \times 10^{-4}$, $D = 1.8$, $\beta = 0.11$, and $h_w = 0.35$.

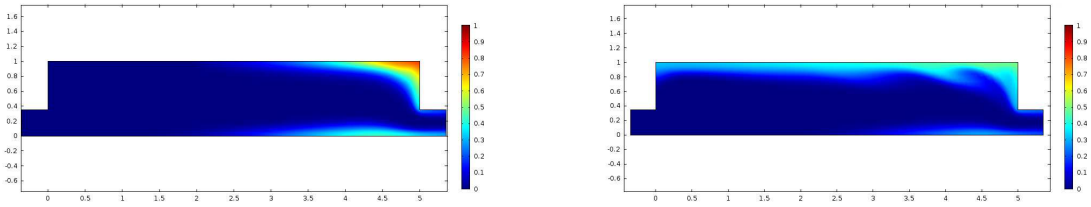

(a) $Ma = 10$, $Pe^* = 75$

(b) $Ma = 100$, $Pe^* = 75$

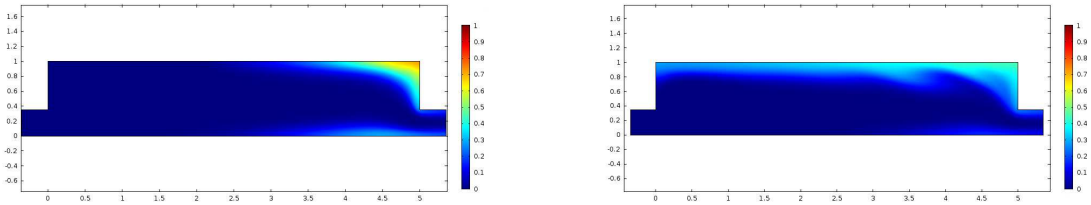

(c) $Ma = 10$, $Pe^* = 50$

(d) $Ma = 100$, $Pe^* = 50$

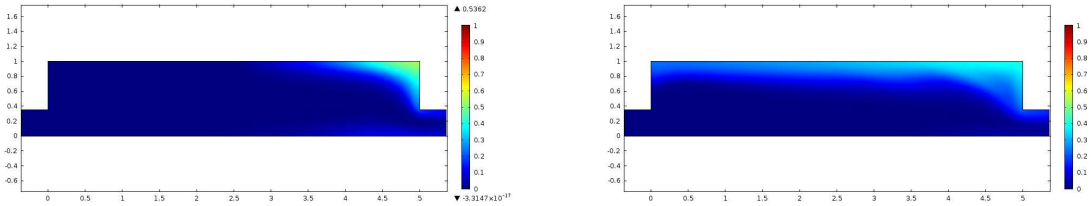

(e) $Ma = 10$, $Pe^* = 25$

(f) $Ma = 100$, $Pe^* = 25$

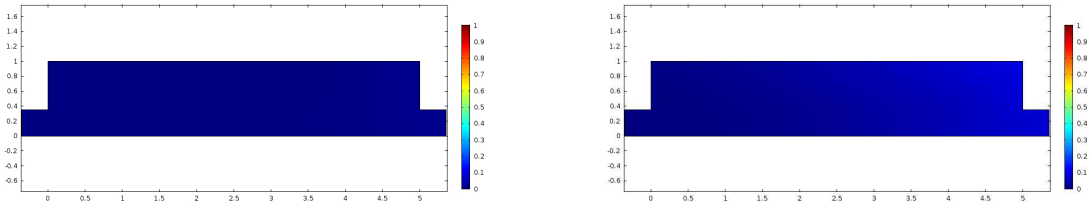

(g) $Ma = 10$, $Pe^* = 1$

(h) $Ma = 100$, $Pe^* = 1$

Figure 3.12: Plots of the monomer concentration profile, S, at the end of the dilution phase, $t = 2$, as Ma and Pe^* vary. Other parameters used are $\epsilon = 0.2$, $Re^* = 0.05$, $\lambda_D = 4 \times 10^{-4}$, $D = 1.8$, $\beta = 0.11$, and $h_w = 0.35$.

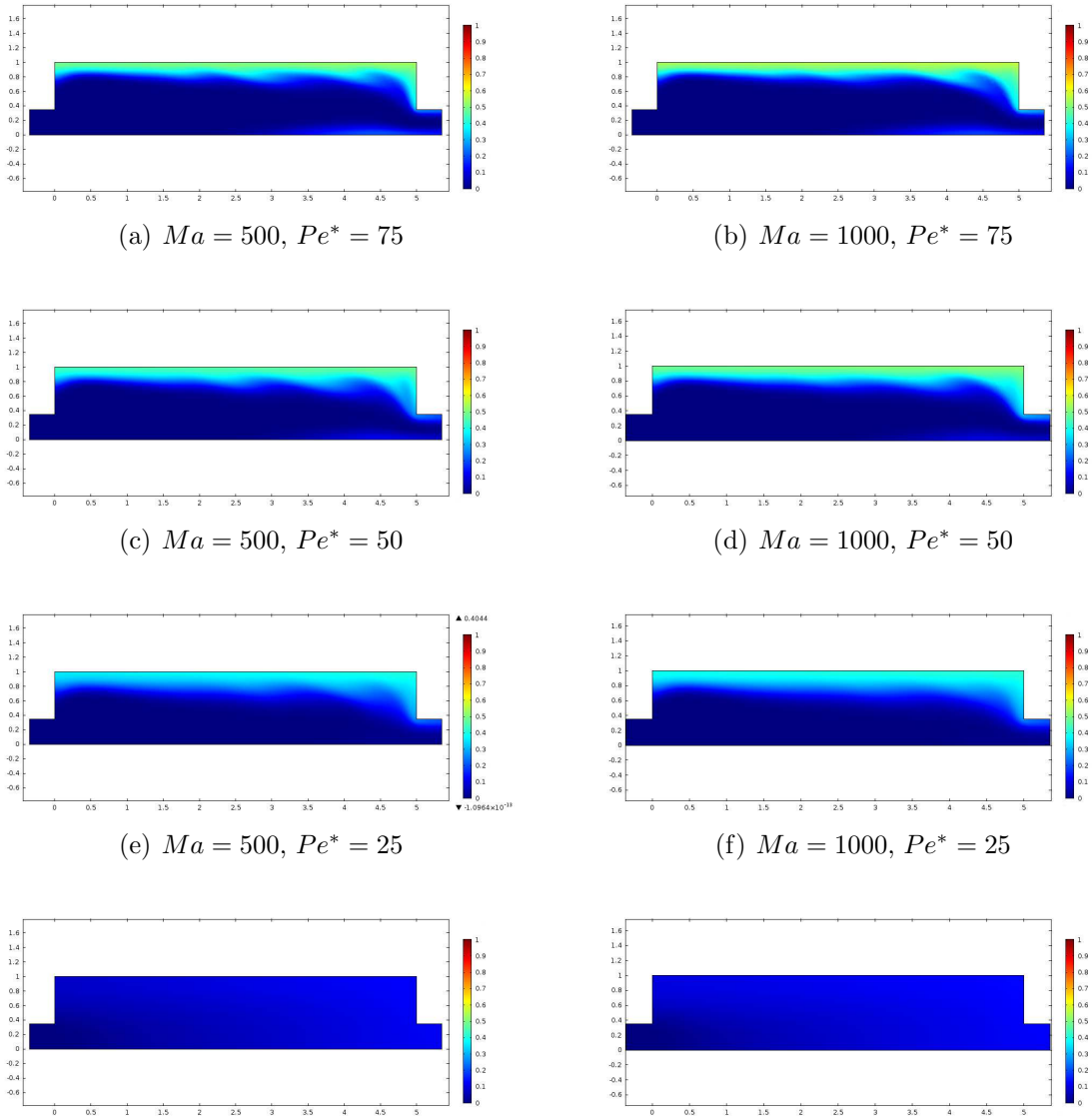

(a) $Ma = 500$, $Pe^* = 75$

(b) $Ma = 1000$, $Pe^* = 75$

(c) $Ma = 500$, $Pe^* = 50$

(d) $Ma = 1000$, $Pe^* = 50$

(e) $Ma = 500$, $Pe^* = 25$

(f) $Ma = 1000$, $Pe^* = 25$

(g) $Ma = 500$, $Pe^* = 1$

(h) $Ma = 1000$, $Pe^* = 1$

Figure 3.13: Plots of the monomer concentration profile, S, at the end of the dilution phase, $t = 2$, as Ma and Pe^* vary. Other parameters used are $\epsilon = 0.2$, $Re^* = 0.05$, $\lambda_D = 4 \times 10^{-4}$, $D = 1.8$, $\beta = 0.11$, and $h_w = 0.35$.

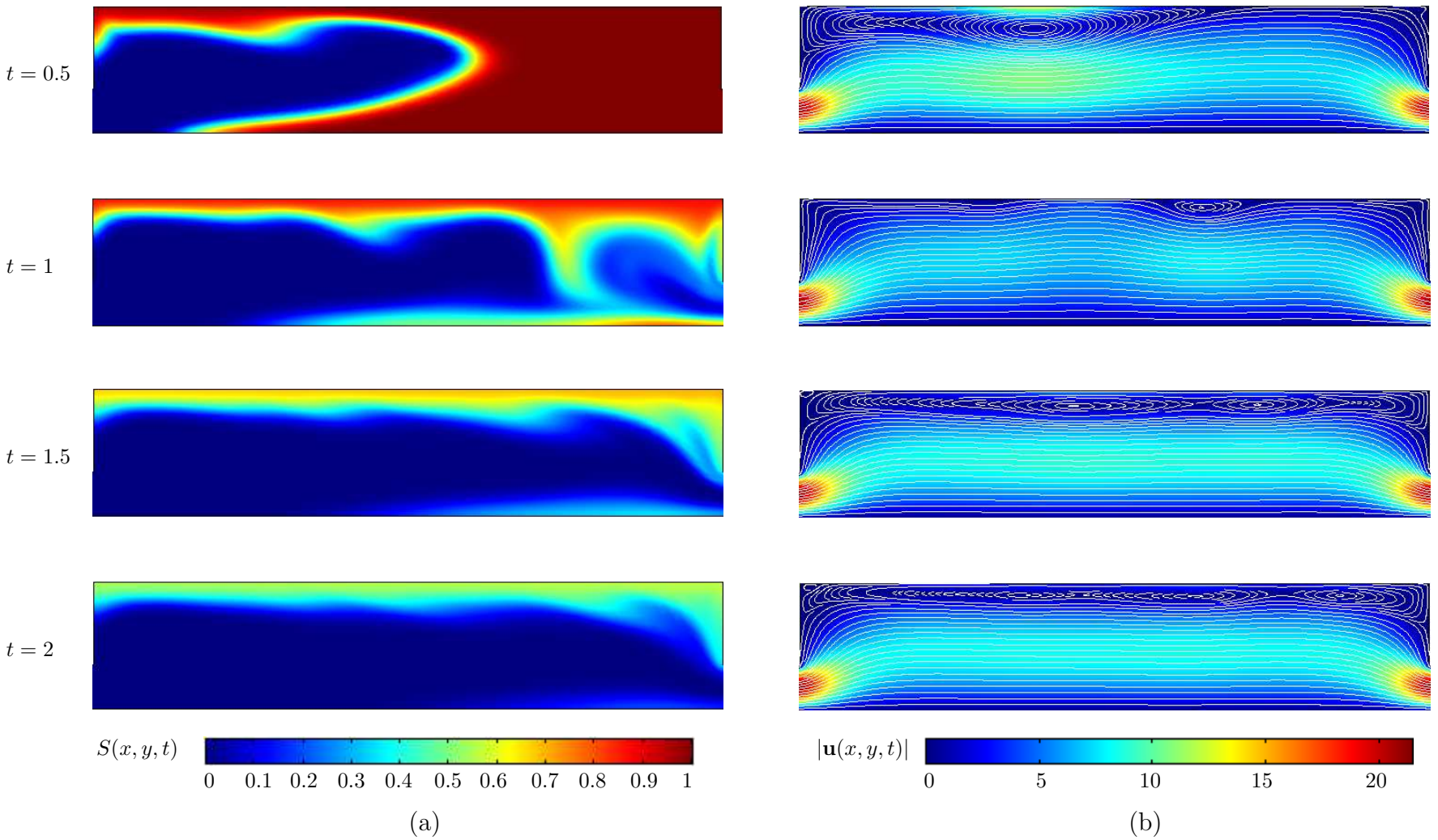

Figure 3.14: Plots of (a) concentration profile and (b) velocity profile and streamlines for $Ma = 1000$ and $Pe^* = 75$. The other parameters used are $\epsilon = 0.2$, $Re^* = 0.05$, $\lambda_D = 4 \times 10^{-4}$, $D = 1.8$, $\beta = 0.11$, and $h_w = 0.35$.

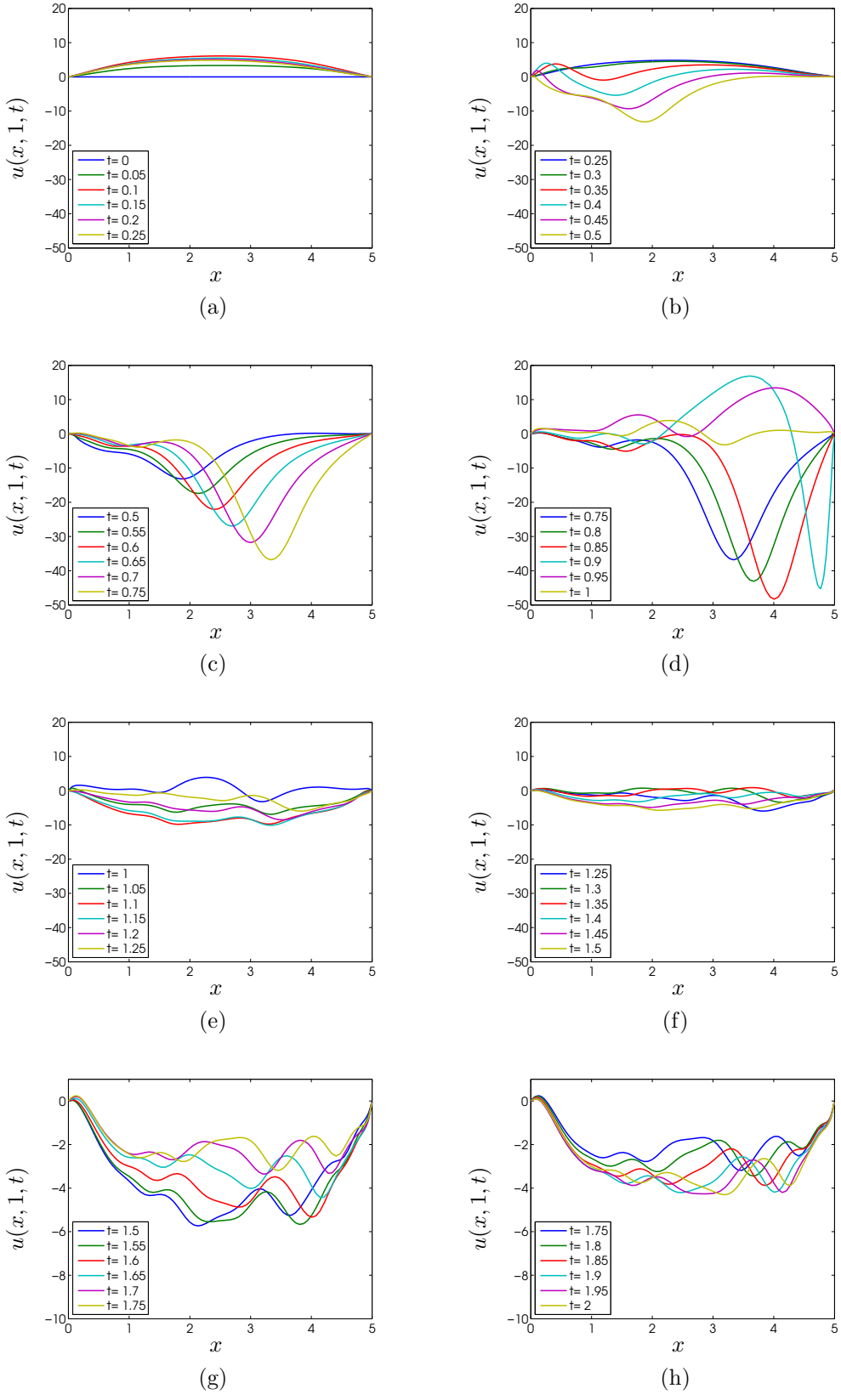

Figure 3.15: Plots of the surface velocity $u(x, 1, t)$ for different times during the dilution phase. Parameters used are $Ma = 1000$, $Pe^* = 75$, $\epsilon = 0.2$, $Re^* = 0.05$, $\lambda_D = 4 \times 10^{-4}$, $D = 1.8$, $\beta = 0.11$, and $h_w = 0.35$.

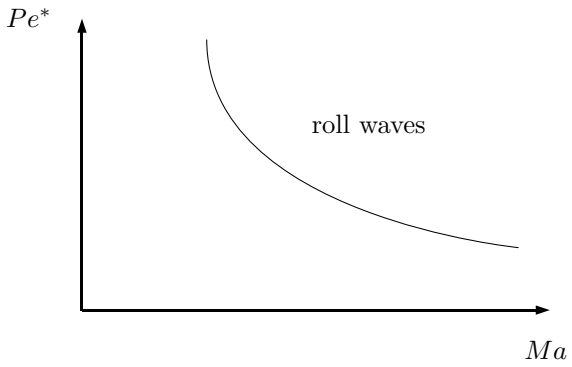

Figure 3.16: Schematic phase-diagram for the development of Marangoni-convection-like roll waves.

The development of the roll waves as the Marangoni number and reduced Péclet number increase suggest that the solution in the boundary layer near the free surface becomes unstable for critical values of Ma and Pe^*. A schematic phase-diagram summarising the existence of the Marangoni-convection-like roll waves is shown in Figure 3.16.

Figure 3.17 shows plots of the monomer concentration at the end of the dilution phase as a function of depth, y, evaluated at the mid-point of the trough, $x = 1/(2\epsilon)$, for large Marangoni number (Ma = 1000) and different values of Pe^*. As discussed earlier, there is a well-defined boundary layer at the free surface, $y = 1$, for $Pe^* \gtrsim 5$ and a second boundary layer develops on the base of the trough, $y = 0$, for larger Péclet numbers, namely $Pe^* \gtrsim 45$. The concentration of surfactant in the boundary layer at $y = 0$ is much less than the concentration in the diffusive boundary layer at $y = 1$. Furthermore, the surfactant concentration in both boundary layers increases with increasing Pe^*. The depth of the boundary layer at the free surface decreases nonlinearly with Pe^* and we estimate its depth, h_c, from the numerical solutions via the expression

$$S\left(1/2\epsilon, h_c, 2\right) = S_c, \tag{3.55}$$

where S_c is some critical surfactant monomer concentration to be prescribed. The results are shown in Figure 3.18 for $S_c = 0.05$. As Pe^* increases the results tend to the curve $h_c = \alpha/\sqrt{Pe^*}$ and the best-fit gives $\alpha = 2.7$. Thus, the dependence of the depth of the diffusive boundary layer near the free surface on the reduced Péclet number agrees with the results of the diffusion limited model described in §3.3. The discrepancy in the fitted parameter, α, for the two models can be accounted for by

noting that the other parameters of the fluid-surfactant model were not taken to be the exact experimental values.

We discuss the results of both the diffusion-limited model of §3.3 and the fluid-surfactant model presented in this section and draw comparisons between them in §3.5.

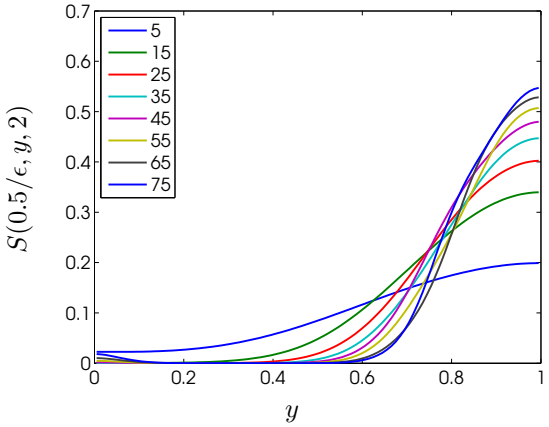

Figure 3.17: Plots of the monomer concentration at the end of the dilution phase as a function of depth evaluated at the mid-point of the trough for different values of Pe^*. Other parameters used are $Ma = 10^3$, $\epsilon = 0.2$, $Re^* = 0.05$, $\lambda_D = 4 \times 10^{-4}$, $D = 1.8$, $\beta = 0.11$, and $h_w = 0.35$.

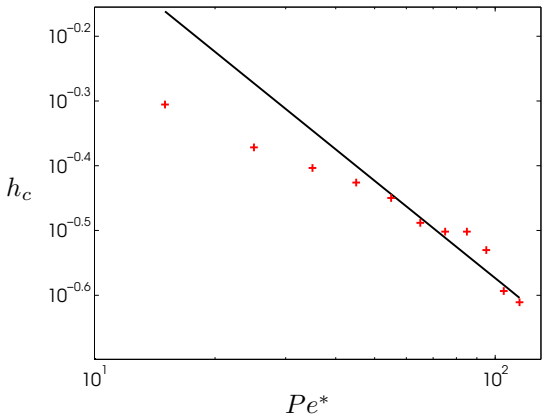

Figure 3.18: Plot of the depth of the diffusive boundary layer, h_c, estimated from the numerical simulations against the reduced Péclet number (red crosses). The black curve denotes the best fit to the data.

3.5 Summary and discussion

In this chapter we first considered a one-dimensional diffusion-limited model to describe the evolution of the surfactant monomer, micelle and adsorbed surface concentrations for the kinetic monolayer dilution experiment as described in §3.2. We assumed that the initial condition was given by a step function that is parametrised by H_c. We simplified the reaction-diffusion equations by considering the equilibrium limit for aggregation ($K \to \infty$) so that the micelle concentration, S_m, decouples from the problem and the monomer concentration, S, satisfies a nonlinear second-order PDE (3.20a). We solved (3.20a) subject to appropriate boundary conditions numerically by fitting the unknown parameter, H_c, in the initial condition and compared the results to the experimental data. We found good agreement between the model and the data for all six experiments, which suggested that H_c was given by the semi-empirical relationship

$$H_c = \alpha H_f / \sqrt{Pe^*}, \tag{3.56}$$

where α was determined from fitting to the experimental data and found to be 0.52. Thus, our diffusion-limited model can predict the adsorbed surfactant concentration for any given additional experiment.

We extended the one-dimensional diffusion-limited model to a two-dimensional problem coupled to the fluid dynamics of the flow cell. An *ad hoc* approach to simplifying the problem showed that there would be a diffusive boundary layer of order $Pe^{*-1/2}$ near the free surface which agrees with the scaling of the initial condition for the diffusion-limited problem presented in §3.3. Therefore, one could argue that during the relatively short timescale for the dilution the surfactant phases remain at equilibrium in a boundary layer near the free surface and so the initial condition for the diffusion-limited model is a good approximation to the problem. Furthermore, the coefficient α in the semi-empirical relationship (3.56) could be determined through a more rigorous asymptotic analysis of the fluid-surfactant problem where one would need to use matched asymptotics to solve for the outer and boundary layer solutions.

The numerical simulations for the two-dimensional model presented in §3.4.2 show that, for sufficiently large Marangoni number and reduced Péclet number, Marangoni-convection cells develop in a region near the free surface and are advected along the trough by the bulk flow, which is approximately Poiseuille. There is clearly a very interesting asymptotic analysis to perform to describe the outer bulk solution, which is approximated by a thin-film model, and the diffusive boundary layers near the

boundaries of the trough and the free surface. The numerical simulations suggest that Marangoni effects are significant in the free surface and so there should be a dominant balance between the shear stress and surface tension terms in the free surface boundary condition. However, such an analysis is non-trivial and is left for future work.

3.5.1 Suggested experimental extensions of this work

An experiment that is easy to perform to verify the value of H_c in the diffusion-limited model would be to measure the concentration of surfactant in the trough after the dilution has occurred, $S_{T\text{new}}$. By conservation of mass we have that

$$\frac{H_c}{H_f}\left(S_{\text{E}} + S_{\text{E}}^N\right) + \lambda_D \frac{S_{\text{E}}}{\beta + S_{\text{E}}} = S_{\text{new}}^* \tag{3.57}$$

where $S_{\text{new}}^* := S_{T\text{new}}/S_{\text{CMC}}$ is the dimensionless net surfactant concentration in the trough after the dilution has occurred. The diffusion-limited model can be further verified by plotting the newly determined values for H_c/H_f against the corresponding Péclet number and one would expect these to lie on the curve $H_c = \alpha H_f/\sqrt{Pe^*}$.

To gain further insight into the fluid dynamics of the experiment one could use flow-tracers to observe the Marangoni effect on the surface velocity and verify the results of the numerical simulations presented in §3.4.2.

Chapter 4

A mathematical model for self-assembly at interfaces

4.1 Introduction

In this chapter we model the process of self-assembly at interfaces exhibited by surfactant systems such as those discussed in [14, 18, 30, 31, 39]. A review of these systems and terminology has already been presented in §1.2.1.1, and we give the typical parameter scales for these systems in §4.1.1. We present a mathematical model for the self-assembly of surfactant in a multilayer structure near an adsorbing surface, neglecting any bulk solution effects. We consider two situations: (i) the adsorption of a surfactant multilayer at an interface, and (ii) the adsorption of a surfactant solution onto two surfaces that are in close proximity to one another. For both situations we first derive a mesoscopic model to describe the movement of surfactant between bilayers in the multilayer structure. We then extend the mesoscopic model by taking a continuum approximation in order to derive a one-dimensional, third-order, nonlinear partial differential equation to describe the spatio-temporal evolution of a multilayer structure. In Chapter 5 we will extend the mathematical model to incorporate free surfactant monomer and electrolyte, and couple it to bulk processes.

4.1.1 Typical parameter scales

This chapter's focus is on developing a theoretical model for surfactant self-assembly at an interface and we neglect bulk processes that would be present in a physical set-up such as the SDBS/Ca^{2+} and SLES/Al^{3+} systems described in [30] and [31] respectively. The characteristic lengthscales on which surfactant multilayers form are given in Table 4.1, and we can see that these are on a nanometre lengthscale.

	System	d (Å)	N
(i)	5 mM SLES/$AlCl_3$/NaCl	25.2 ±0.2	40
(ii)	2 mM $CaCl_2$ and 2 mM SDBS	16 ±0.2	30

Table 4.1: Typical lengthscales for (i) the SDBS/Ca^{2+} system described in [30] and (ii) the SLES/Al^{3+} system described in [31]. The depth of a single bilayer is denoted by d, and the typical number of bilayers in the multilayer is N. We note that 1 Å$= 10^{-10}$ m.

4.2 Mesoscopic model

4.2.1 Model formulation

We consider the situation in which a multilayer structure forms in a surfactant solution beneath a monolayer adsorbed at either a liquid–solid or liquid–gas interface. The multilayer structure consists of a series of stacked bilayers and each bilayer is a planar arrangement of surfactant monomer pairs that are referred to as 'surfactant pairs' or 'bilayer molecules' when in an adsorbed structure, as opposed to dimers when in the bulk solution. In this chapter we only model the behaviour of the surfactant in the multilayer structure and so neglect any free monomer or aggregates in the bulk that are typically present in such systems as those described in [30] and [31]. Thus, in our model, surfactant can only exist as either surfactant pairs in a bilayer within the multilayer or as adsorbed monomer in the monolayer at the surface. A schematic diagram of the multilayer structure is shown in Figure 4.1.

Neglecting any electrostatic effects that may be present between bilayers, we model the movement of bilayer molecules between adjacent layers as an adsorption process. We consider the one-dimensional domain $\mathcal{D} := \{x : x \in [0, L]\}$, where the x-axis

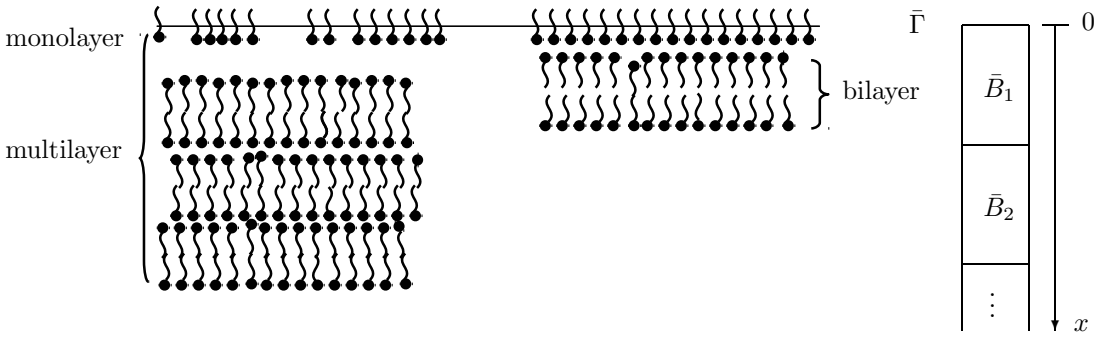

Figure 4.1: Schematic of a surfactant multilayer structure.

points downwards into the solution and the boundary $x = 0$ corresponds to the adsorbing surface. The domain $\mathcal{D}$ is divided into K compartments each of length h so that the ith compartment represents the ith bilayer in the multilayer structure for $i = 1, \ldots, K$, and h is the bilayer thickness. We denote the number of bilayer molecules in the ith compartment by $\bar{B}_i$, for $i = 1, \ldots, K$. We assume that surfactant must dissociate into monomers before adsorbing at the surface $x = 0$ and we denote the number of adsorbed surfactant monomers by $\bar{\Gamma}$. A schematic diagram of the domain $\mathcal{D}$ is shown in Figure 4.1.

In order to derive a mesoscopic model we will use mass action kinetics. We assume that bilayer molecules may only move to adjacent compartments and can only do so provided there is an available adsorption site. An adsorption site is simply a bilayer molecule in an adjacent compartment that has not been covered by another bilayer molecule in that layer. If we suppose that a molecule moves into the ith compartment then there are two possibilities for the adsorption site:

(i) the adsorption site is a molecule in the $(i-1)^{\text{th}}$ compartment; the number of available adsorption sites of this type is given by

$$\bar{V}_i = (\bar{B}_{i-1} - \bar{B}_i)^+, \qquad (4.1)$$

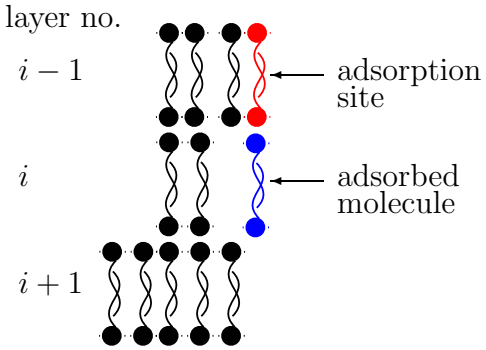

(ii) the adsorption site is a molecule in the $(i+1)^{\text{th}}$ compartment; the number of available adsorption sites of this type is given by

$$\bar{H}_i = (\bar{B}_{i+1} - \bar{B}_i)^+. \tag{4.2}$$

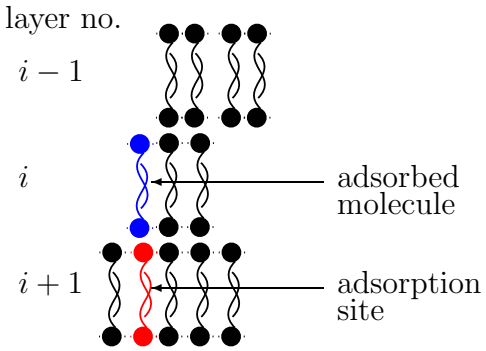

We shall use the notation $(\cdot)^+$ throughout this paper, which is defined by

$$(x)^+ = \begin{cases} x, & x \geq 0, \\ 0, & x < 0. \end{cases} \tag{4.3}$$

Assuming that the movement of bilayer molecules is spontaneous we may write down a series of single-step reactions for their movements:

Movement of $\bar{B}_{i+1}$ to the ith layer

$$\bar{B}_{i+1} + \bar{V}_i \xrightarrow{\bar{a}_i} \bar{B}_i \quad \text{for} \quad i = 1, \ldots, K, \tag{4.4a}$$

$$\bar{B}_{i+1} + H_i \xrightarrow{\bar{c}_i} \bar{B}_i \quad \text{for} \quad i = 2, \ldots, K, \tag{4.4b}$$

where $\bar{V}_1 = \bar{\Gamma} - \bar{B}_1$ is the vacancy in the first bilayer, and $\bar{a}_i$ and $\bar{c}_i$ denote the corresponding rate constants for the reactions.

Movement of $\bar{B}_{i-1}$ to the ith layer

$$\bar{B}_{i-1} + \bar{V}_i \xrightarrow{\bar{b}_i} \bar{B}_i \quad \text{for} \quad i = 2, \ldots, K, \tag{4.5a}$$

$$\bar{B}_{i-1} + \bar{H}_i \xrightarrow{\bar{d}_i} \bar{B}_i \quad \text{for} \quad i = 2, \ldots, K, \tag{4.5b}$$

and $\bar{b}_i$ and $\bar{d}_i$ denote the corresponding rate constants for the reactions.

At the adsorbing surface a bilayer molecule in the first bilayer may dissociate into two monomers which then adsorb onto the surface provided it is not saturated. If the monolayer is saturated with monomers then $\bar{\Gamma} = \bar{\Gamma}_{\text{sat}}$ and otherwise $\bar{\Gamma} < \bar{\Gamma}_{\text{sat}}$. If the monolayer is not saturated then the number of vacant adsorption sites is given by

$$\bar{V}_{\text{m}} = \bar{\Gamma}_{\text{sat}} - \bar{\Gamma}, \tag{4.6}$$

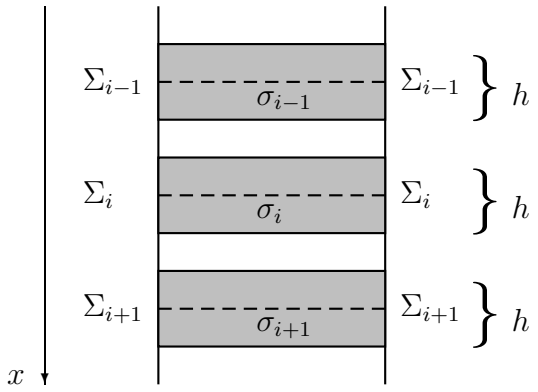

Figure 4.2: Schematic of bilayer interfaces in a multilayer structure.

where the subscript m represents the monolayer. Similarly, two adsorbed monomers from the monolayer may spontaneously desorb and form a bilayer molecule in the first bilayer provided there is an available adsorption site. The number of available adsorption sites in the first bilayer is given by expressions (4.1) and (4.2) with $i = 1$, and with $\bar{B}_0 := \bar{\Gamma}$. We assume that the adsorption–desorption processes associated with the monolayer occur as single-step reactions given by

$$\bar{B}_1 + 2\bar{V}_{\mathrm{m}} \overset{\bar{a}_{\mathrm{m}}}{\to} 2\bar{\Gamma}, \tag{4.7a}$$

$$2\bar{\Gamma} + \bar{V}_1 \overset{\bar{b}_{\mathrm{m}}}{\to} \bar{B}_1, \tag{4.7b}$$

$$2\bar{\Gamma} + \bar{H}_1 \overset{\bar{d}_{\mathrm{m}}}{\to} \bar{B}_1. \tag{4.7c}$$

Using the definition of *surface excess*, as discussed in §1.3.2, one can think of the multilayer structure as an idealised construction of stacked planar interfaces, Σ_i, on which the bilayer pairs lie and with bulk solution separating the interfaces as shown in Figure 4.2. In reality the interchange of bilayer pairs would occur by diffusion through the volume σ_i but assuming that the interfaces Σ_i are sufficiently close then we assume that this happens instantaneously. Furthermore, we assume that the distribution of surfactant is uniform in the y- and z-directions. Thus, we define the areal concentrations of adsorbed monomers in the monolayer and bilayer molecules in the ith bilayer by

$$\Gamma(t) = \frac{\bar{\Gamma}(t)}{A}, \quad \text{and} \quad B_i(t) = \frac{\bar{B}_i(t)}{A}, \tag{4.8}$$

respectively where A is the interfacial area and both $\Gamma(t)$ and $B_i(t)$ thus have SI units of $\mathrm{mol\,m^{-2}}$.

Hence, we invoke the law of mass action to obtain a system of $K+1$ ODEs for the concentrations $\Gamma, B_1, \ldots, B_K$,

$$\frac{\mathrm{d}\Gamma}{\mathrm{d}t} = 2\left(Q^a_{\mathrm{m}} - Q^b_{\mathrm{m}} - Q^d_{\mathrm{m}}\right), \tag{4.9a}$$

$$\frac{\mathrm{d}B_1}{\mathrm{d}t} = -\left(Q^a_{\mathrm{m}} - Q^b_{\mathrm{m}} - Q^d_{\mathrm{m}}\right) + Q^a_1 - Q^b_2 + Q^c_1 - Q^d_2, \tag{4.9b}$$

$$\frac{\mathrm{d}B_i}{\mathrm{d}t} = Q^a_i - Q^a_{i-1} + Q^b_i - Q^b_{i+1} + Q^c_i - Q^c_{i-1} + Q^d_i - Q^d_{i+1}, \quad \text{for} \quad i = 2, \ldots, K-2, \tag{4.9c}$$

$$\frac{\mathrm{d}B_{K-1}}{\mathrm{d}t} = Q^a_{K-1} - Q^a_{K-2} + Q^b_{K-1} - Q^b_K + Q^c_{K-1} - Q^c_{K-2} + Q^d_{K-1}, \tag{4.9d}$$

$$\frac{\mathrm{d}B_K}{\mathrm{d}t} = -Q^a_{K-1} + Q^b_K - Q^c_{K-1}, \tag{4.9e}$$

where the fluxes are given by

$$Q^a_{\mathrm{m}} = a_{\mathrm{m}} V^2_{\mathrm{m}} B_1, \tag{4.10a}$$

$$Q^b_{\mathrm{m}} = b_{\mathrm{m}} V_1 \Gamma^2, \tag{4.10b}$$

$$Q^d_{\mathrm{m}} = d_{\mathrm{m}} H_1 \Gamma^2, \tag{4.10c}$$

$$Q^a_i = a_i V_i B_{i+1}, \quad \text{for} \quad i = 1, \ldots, K-1, \tag{4.10d}$$

$$Q^b_i = b_i V_i B_{i-1}, \quad \text{for} \quad i = 2, \ldots, K, \tag{4.10e}$$

$$Q^c_i = c_i H_i B_{i+1}, \quad \text{for} \quad i = 1, \ldots, K-1, \tag{4.10f}$$

$$Q^d_i = d_i H_i B_{i-1}, \quad \text{for} \quad i = 2, \ldots, K-1, \tag{4.10g}$$

and

$$V_{\mathrm{m}} = \Gamma_{\mathrm{sat}} - \Gamma, \tag{4.11a}$$

$$V_1 = (\Gamma - B_1)^+, \tag{4.11b}$$

$$V_i = (B_{i-1} - B_i)^+, \quad \text{for} \quad i = 2, \ldots, K, \tag{4.11c}$$

$$H_i = (B_{i+1} - B_i)^+, \quad \text{for} \quad i = 1, \ldots, K-1, \tag{4.11d}$$

where $\Gamma_{\mathrm{sat}} = \bar{\Gamma}_{\mathrm{sat}}/h^2$ is the saturation concentration of the monolayer and has the same units as Γ; V_i and H_i correspond to the concentration of vacant areas within the bilayer and V_{m} corresponds to the vacant area in the monolayer.

To close the system we prescribe the initial conditions

$$\Gamma(0) = \Gamma_0 \quad \text{and} \quad B_i(0) = B_{i_0} \quad \text{for} \quad i = 1, \ldots, K. \tag{4.12}$$

The dimensions of the rate constants in (4.9) are given as follows:

$$\begin{aligned}
[a_{\mathrm{m}}], [b_{\mathrm{m}}], [d_{\mathrm{m}}] &= \mathrm{mol}^{-2}\,\mathrm{m}^4\,\mathrm{s}^{-1}, \\
[a_i] &= \mathrm{mol}^{-1}\,\mathrm{m}^2\,\mathrm{s}^{-1} \quad \text{for} \quad i = 1, \ldots, K-1, \\
[b_i] &= \mathrm{mol}^{-1}\,\mathrm{m}^2\,\mathrm{s}^{-1} \quad \text{for} \quad i = 2, \ldots, K, \\
[c_i] &= \mathrm{mol}^{-1}\,\mathrm{m}^2\,\mathrm{s}^{-1} \quad \text{for} \quad i = 1, \ldots, K-1, \\
[d_i] &= \mathrm{mol}^{-1}\,\mathrm{m}^2\,\mathrm{s}^{-1} \quad \text{for} \quad i = 2, \ldots, K-1.
\end{aligned}$$

We note that presently there is no experimental procedure to determine the rate constants a_i, b_i, c_i, and d_i and so we choose them freely. The rate constants a_{m}, b_{m}, and d_{m} should not be confused with the rate constants in the Langmuir-Hinshelwood equation [8] but it is reasonable to assume that they are of the same order of magnitude as those in the Langmuir-Hinshelwood equation [27]. In Chapter 5 we consider a model that allows the scalings for some of these rate constants to be determined.

As we expect, the model conserves mass, since on summing equations (4.9) we find that

$$\frac{\mathrm{d}\Gamma}{\mathrm{d}t} + 2\sum_{i=1}^{K} \frac{\mathrm{d}B_i}{\mathrm{d}t} = 0. \tag{4.13}$$

Thus, the model can be reduced to a system of K ODEs for $B_i(t)$, $i = 1, \ldots, K$, and Γ is found from the conservation-of-mass equation, given by

$$\Gamma(t) + 2\sum_{i=1}^{K} B_i(t) = \Gamma_0 + 2\sum_{i=1}^{K} B_{i_0} := hS_b, \tag{4.14}$$

where S_b is the net concentration of surfactant in the system.

4.2.2 Nondimensionalisation

We nondimensionalise the variables of the model as follows:

$$t = \frac{1}{a_1 \Gamma_{\rm sat} \epsilon^3} t', \qquad \Gamma = \Gamma_{\rm sat} \Gamma', \qquad B_i = \Gamma_{\rm sat} B_i', \quad \text{where} \quad \epsilon = \frac{h}{L} = \frac{1}{K}. \tag{4.15}$$

The timescale has been chosen to obtain the richest asymptotic limit in the continuum approximation to the mesoscopic model as $\epsilon \to 0$; this is done in §4.3. Substituting the rescaled variables (4.15) into (4.9) and dropping primes we obtain the system of dimensionless ODEs

$$\epsilon^3 \frac{\mathrm{d}\Gamma}{\mathrm{d}t} = 2\left(Q^a_{\rm m} - Q^b_{\rm m} - Q^d_{\rm m}\right), \tag{4.16a}$$

$$\epsilon^3 \frac{\mathrm{d}B_1}{\mathrm{d}t} = -\left(Q^a_{\rm m} - Q^b_{\rm m} - Q^d_{\rm m}\right) + Q^a_1 - Q^b_2 + Q^c_1 - Q^d_2, \tag{4.16b}$$

$$\epsilon^3 \frac{\mathrm{d}B_i}{\mathrm{d}t} = Q^a_i - Q^a_{i-1} + Q^b_i - Q^b_{i+1} + Q^c_i - Q^c_{i-1} + Q^d_i - Q^d_{i+1}, \quad \text{for} \quad i = 2, \ldots, K-2, \tag{4.16c}$$

$$\epsilon^3 \frac{\mathrm{d}B_{K-1}}{\mathrm{d}t} = Q^a_{K-1} - Q^a_{K-2} + Q^b_{K-1} - Q^b_K + Q^c_{K-1} - Q^c_{K-2} + Q^d_{K-1}, \tag{4.16d}$$

$$\epsilon^3 \frac{\mathrm{d}B_K}{\mathrm{d}t} = -Q^a_{K-1} + Q^b_K - Q^c_{K-1}, \tag{4.16e}$$

where the fluxes are now given in dimensionless form as

$$Q^a_{\rm m} = \alpha_{\rm m} V_{\rm m}^2 B_1 = \alpha_{\rm m} (1-\Gamma)^2 B_1, \tag{4.17a}$$

$$Q^b_{\rm m} = \beta_{\rm m} V_1 \Gamma^2 = \beta_{\rm m} \left(\Gamma - B_1\right)^+ \Gamma^2, \tag{4.17b}$$

$$Q^d_{\rm m} = \delta_{\rm m} H_1 \Gamma^2 = \delta_{\rm m} \left(B_2 - B_1\right)^+ \Gamma^2, \tag{4.17c}$$

$$Q^a_1 = \alpha_1 V_1 B_2 = \alpha_1 (\Gamma - B_1)^+ B_2, \tag{4.17d}$$

$$Q^a_i = \alpha_i V_i B_{i+1} = \alpha_i \left(B_{i-1} - B_i\right)^+ B_{i+1}, \quad \text{for} \quad i = 2, \ldots, K-1, \tag{4.17e}$$

$$Q^b_i = \beta_i V_i B_{i-1} = \beta_i \left(B_{i-1} - B_i\right)^+ B_{i-1}, \quad \text{for} \quad i = 2, \ldots, K, \tag{4.17f}$$

$$Q^c_i = \gamma_i H_i B_{i+1} = \gamma_i \left(B_{i+1} - B_i\right)^+ B_{i+1}, \quad \text{for} \quad i = 1, \ldots, K-1, \tag{4.17g}$$

$$Q^d_i = \delta_i H_i B_{i-1} = \delta_i \left(B_{i+1} - B_i\right)^+ B_{i-1}, \quad \text{for} \quad i = 2, \ldots, K-1, \tag{4.17h}$$

and the initial conditions become

$$\Gamma(0) = \Gamma_0 \quad \text{and} \quad B_i(0) = B_{i_0} \quad \text{for} \quad i = 1, \ldots, K. \tag{4.18}$$

Conservation of mass is now given in dimensionless form by

$$\Gamma(t) + 2\sum_{i=1}^{K} B_i(t) = \Gamma_0 + 2\sum_{i=1}^{K} B_{i_0} := \mathcal{S}. \tag{4.19}$$

The dimensionless parameters of the model are defined as follows

$$\begin{aligned}
\alpha_i &= \frac{a_i}{a_1} && \text{for} \quad i = 1, \ldots, K-1, \\
\beta_i &= \frac{b_i}{a_1} && \text{for} \quad i = 2, \ldots, K, \\
\gamma_i &= \frac{c_i}{a_1} && \text{for} \quad i = 1, \ldots, K-1, \\
\delta_i &= \frac{d_i}{a_1} && \text{for} \quad i = 2, \ldots, K-1, \\
B_{i_0} &= \frac{B_{i_0}}{\Gamma_{\text{sat}}} && \text{for} \quad i = 1, \ldots, K, \\
\Gamma_0 &= \frac{\Gamma_0}{\Gamma_{\text{sat}}}, \qquad \alpha_{\text{m}} = \frac{a_{\text{m}}}{a_1}\Gamma_{\text{sat}}, \qquad \beta_{\text{m}} = \frac{b_{\text{m}}}{a_1}\Gamma_{\text{sat}}, \qquad \delta_{\text{m}} = \frac{d_{\text{m}}}{a_1}\Gamma_{\text{sat}}, \qquad \mathcal{S} = \frac{S_b}{\Gamma_{\text{sat}}}.
\end{aligned} \tag{4.20}$$

4.2.3 Steady-state solutions

To determine the steady-state solutions of (4.16) we make the assumption that when in equilibrium $B_i \leq B_{i-1}$ for all i. This is physically reasonable since a decreasing concentration of surfactant with depth has been observed in such systems as those described in [30]. We note that there exists no method to measure all the rate parameters in the model and so to proceed further we make the plausible assumption that the constants a_i and b_i are equal, *i.e.* $\alpha_i = \beta_i = \alpha$ for $i = 1, \ldots, K$, which physically corresponds to there being no preference in which direction a bilayer molecule moves. Thus,

$$B_i = \Gamma\left(\frac{\Gamma^2}{\Gamma^2 + \alpha^*(1-\Gamma)^2}\right)^i \quad \text{for} \quad i = 1, \ldots, K, \quad \alpha^* = \frac{\alpha_{\text{m}}}{\beta_{\text{m}}}, \tag{4.21a}$$

and conservation of mass implies that

$$\mathcal{S} = \Gamma\left(1 + 2\sum_{i=1}^{K}\left(\frac{\Gamma^2}{\Gamma^2 + \alpha^*(1-\Gamma)^2}\right)^i\right). \tag{4.21b}$$

In the limit $K \to \infty$, when there is an infinite number of bilayers, (4.21b) reduces to a cubic equation for Γ:

$$\alpha^*(\Gamma - \mathcal{S})(1-\Gamma)^2 + 2\Gamma^3 = 0. \tag{4.22}$$

For all positive values of α^* and $\mathcal{S}$, there is a unique real solution of (4.22) for $\Gamma \in (0,1)$, which is plotted by the continuous curves in Figure 4.3(a) for $\alpha^* = 0.1, 1, 10$. In Figure 4.3(b) the corresponding steady-state solutions for B_i using (4.21a) are plotted for the fixed values $S = 200$ and $K = 500$. As observed in Figure 4.3(a) the behaviour of Γ as a function of $\mathcal{S}$ resembles a Langmuir-type isotherm between the bulk and surface concentrations. Furthermore, we note that from (4.22),

$$\Gamma \sim \mathcal{S} - 2\frac{\mathcal{S}^3}{\alpha^*} + \ldots \qquad \text{as} \quad \mathcal{S} \to 0, \tag{4.23a}$$

$$\Gamma \sim 1 - \sqrt{\frac{2}{\alpha^*\mathcal{S}}} + \ldots \qquad \text{as} \quad \mathcal{S} \to \infty, \tag{4.23b}$$

and the leading-order behaviour of Γ for large $\mathcal{S}$ is shown by the dashed lines in Figure 4.3(a). For the physical scenarios of interest, the net concentration of surfactant is large compared with concentration of surfactant in each cell so we shall consider the case $\mathcal{S} \gg 1$ in our future analysis.

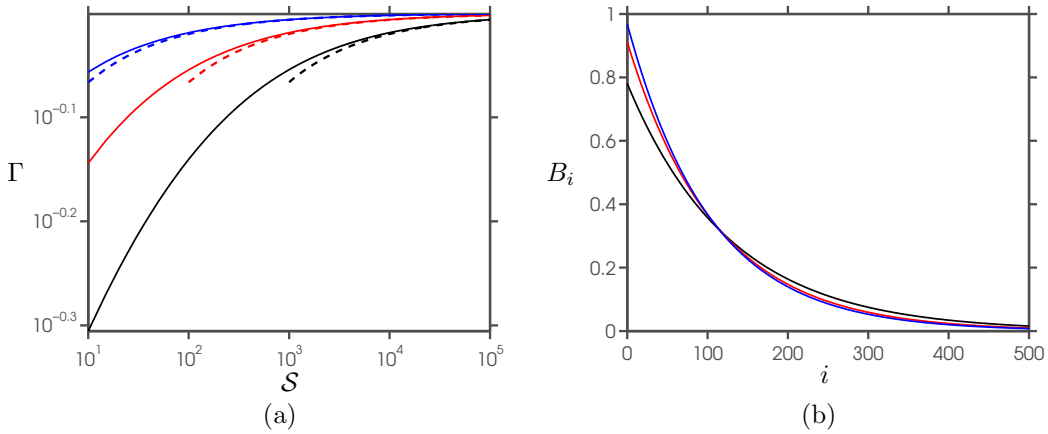

Figure 4.3: Steady-state solutions to the mesoscopic model. (a) Plots of the real root, Γ, of (4.22) (continuous lines) and leading-order asymptotic approximation (4.23b) (dashed lines) against total surfactant concentration, $\mathcal{S}$. (b) Plots of B_i given by (4.21a) for $\mathcal{S} = 200$. The values of $\alpha*$ used are 0.1 (black lines), 1 (red lines), and 10 (blue lines).

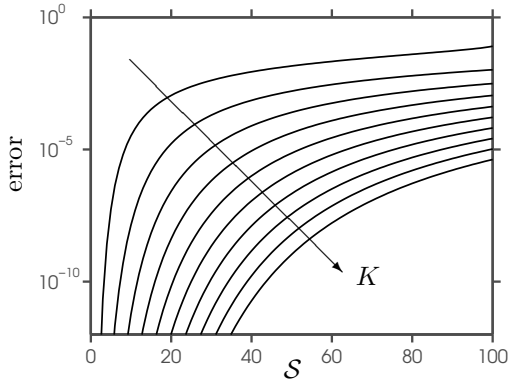

Figure 4.4: Plots of the difference between the solutions Γ to equations (4.21b) and (4.22) against $\mathcal{S}$ for $K \in [50, 100, \ldots, 450, 500]$ and $\alpha^* = 2$.

In the following section we compute the numerical solutions to (4.16) and compare them with the exact steady-state solutions (4.21). We note that solving the system of ODEs for very large K can be computationally expensive and so we take K sufficiently large (about 100) to generate physically relevant plots but small enough to avoid computational difficulties. For such a value of K the approximation (4.22) to the steady state may have noticeable errors. This is shown in Figure 4.4 where the difference in the two values of Γ given by (4.21b) and (4.22) is plotted against $\mathcal{S}$ for $\alpha^* = 1$.

4.2.4 Numerical solutions to mesoscopic model

In this section we compute the solutions to the system of ordinary differential equations (4.16) using Matlab's inbuilt solver `ode45` for the parameters $K = 100$, $\alpha_{\mathrm{m}} = 2$, $\beta_{\mathrm{m}} = \delta_{\mathrm{m}} = 0.2$, and $\alpha_i = \beta_i = \gamma_i = \delta_i = 1$ for $i = 1, \ldots, K$. We investigate three possible scenarios for the initial distribution of bilayers below:

1. Physically, one expects the distribution to be monotonically decreasing with depth [27] so it is reasonable to assume that the initial conditions are given by a monotonically decreasing distribution. Thus, we solve the system of ODEs (4.16) subject to the initial conditions

$$\Gamma_0 = 0.8, \quad \text{and} \quad B_{i_0} = \Gamma_0 \mathrm{e}^{-\left(\frac{i}{\sigma(K+1)}\right)^2}, \quad \text{for} \quad i = 1, \ldots, K, \quad \sigma = 0.3. \tag{4.24}$$

   Numerical solutions B_i are plotted by the black lines in Figure 4.5(a) at times $t \in [0.001, \ldots, 0.05]$ and show, as expected, the initial profile (red line) evolving

smoothly to the steady-state solution (4.21) as t increases. Figures 4.5(b)–4.5(d) show the excellent convergence of the numerical solutions (black lines) for Γ, B_{20} and B_{40} to their respective steady-state solutions (blue lines) given by (4.21).

2. We next consider the situation where surfactant bilayers have been stirred non-homogeneously such that the initial data is randomly distributed on $[0, 1]$. The initial data is denoted by the red crosses in Figure 4.6(a). Plots of the numerical solutions for the bilayer concentrations, B_i, are shown in Figures 4.6(b)–(f) for the various time intervals. As Figure 4.6 shows, there is a rapid transient from the noisy initial data to a seemingly smooth distribution by time $t \approx 10^{-3}$ which then converges to the steady-state distribution on an order one timescale. We also observe the formation of 'smooth humps' and 'sharp troughs' for small time in Figures 4.6(b) and 4.6(c). These features will be analysed in more detail in §4.4 for the macroscopic model.

3. Finally, we consider the situation where the bulk concentration is 'well-mixed' but the adsorbing surface has a lid on it (so that monomers cannot adsorb at $x = 0$) which is instantaneously removed at $t = 0$. Initially, therefore, the concentration of bilayers is uniformly distributed in the bulk solution and the concentration of adsorbed monomers is zero. Figure 4.7 shows that after an initial transient the distribution of bilayer molecules evolves in an almost identical way to that with the randomly distributed initial condition shown in Figure 4.6.

The temporal evolution of the bilayer concentration, B_i, shown in Figures 4.5–4.7 suggest that there is an almost smooth transition to a steady distribution which could be governed by a macroscopic model for the distribution of bilayers in the multilayer structure. Thus, in the following section we take a continuum approximation to the system of ODEs (4.16) in order to derive a partial differential equation that describes the macroscopic model.

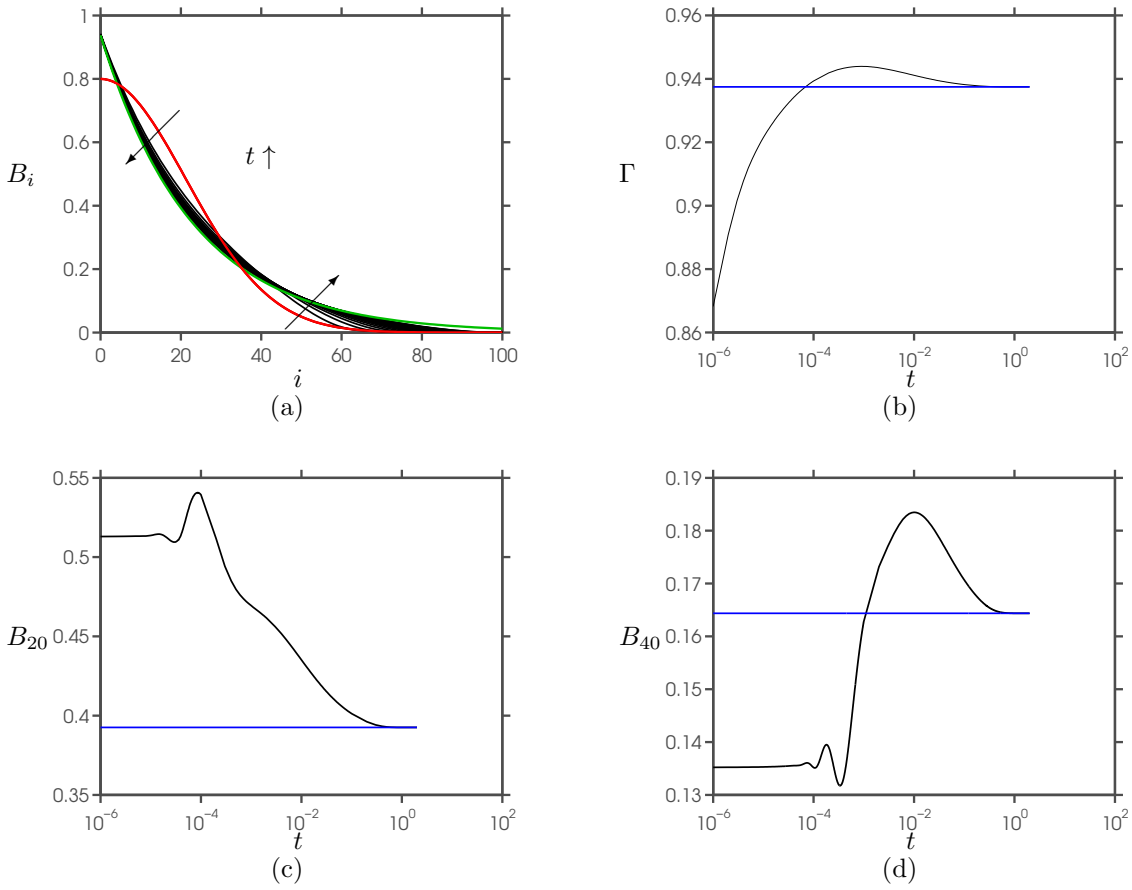

Figure 4.5: Plots of the numerical solutions to the system of ordinary differential equations (4.16) subject to the initial conditions (4.24). (a) Plots of the numerical solutions B_i (black lines) against i at times $t \in [0.005, \ldots, 0.1]$ and the initial conditions (4.24) (red line) for $\sigma = 0.3$. Comparison of the numerical solutions (black line) with the the steady-state solutions (4.21) (blue continuous line) for (a) Γ, (b) B_{20} and (c) B_{40}. The rate constants used were $\alpha_{\mathrm{m}} = 2$, $\beta_{\mathrm{m}} = \delta_{\mathrm{m}} = 0.2$, $\alpha_i = \beta_i = \gamma_i = \delta_i = 1$ for $i = 1, \ldots, K$ where $K = 100$.

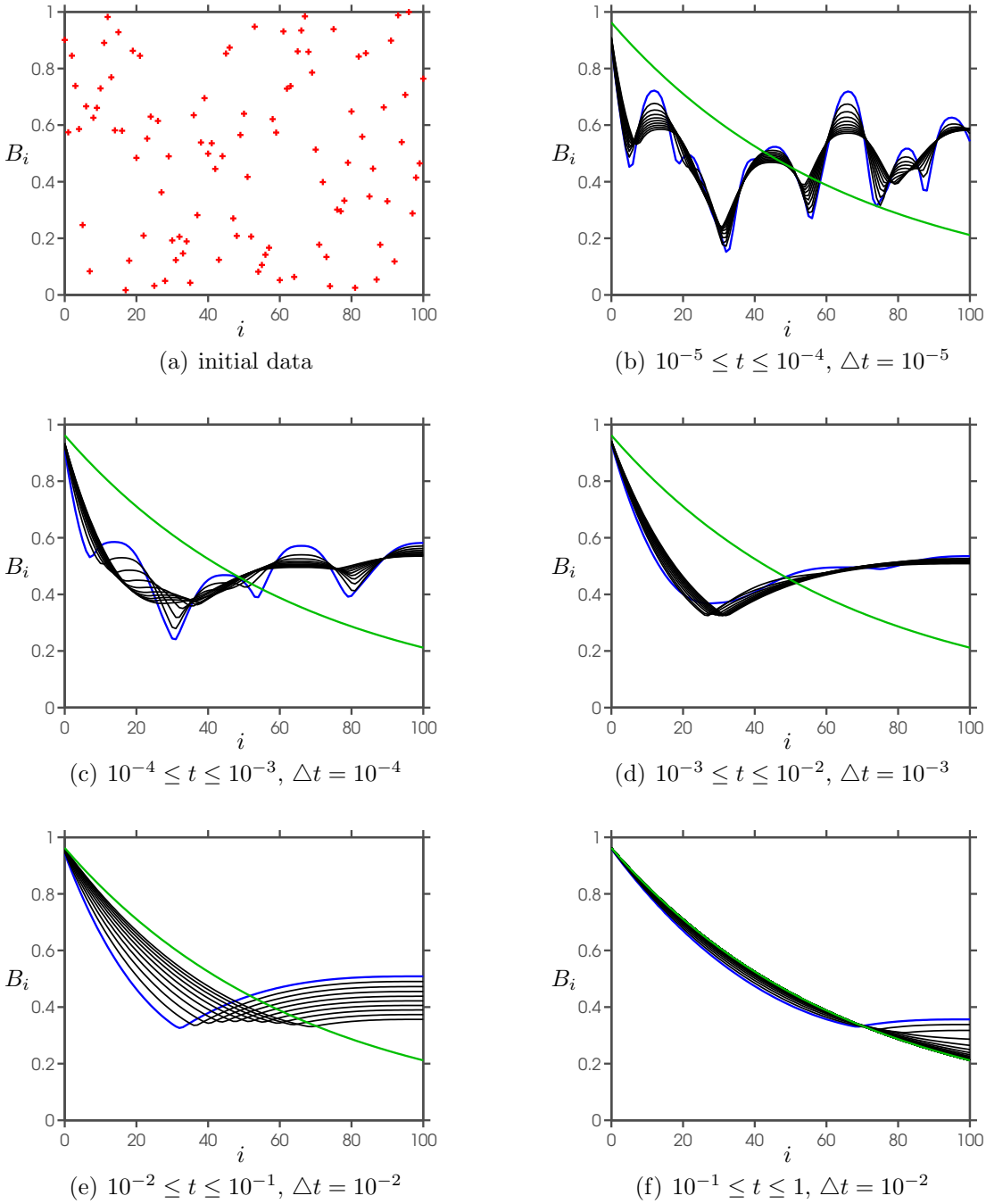

(a) initial data

(b) $10^{-5} \leq t \leq 10^{-4}$, $\triangle t = 10^{-5}$

(c) $10^{-4} \leq t \leq 10^{-3}$, $\triangle t = 10^{-4}$

(d) $10^{-3} \leq t \leq 10^{-2}$, $\triangle t = 10^{-3}$

(e) $10^{-2} \leq t \leq 10^{-1}$, $\triangle t = 10^{-2}$

(f) $10^{-1} \leq t \leq 1$, $\triangle t = 10^{-2}$

Figure 4.6: Plots of the numerical solutions to the system of ordinary differential equations (4.16) (black lines) for (a) random initial data (red crosses) and for the time intervals (b) $[10^{-5}, 10^{-4}]$, (c) $[10^{-4}, 10^{-3}]$, (d) $[10^{-3}, 10^{-2}]$, (e) $[10^{-2}, 10^{-1}]$ and (f) $[10^{-1}, 1]$ where the blue curves denote the solution at the start of the time interval and the green curve denotes the steady-state solution (4.21). The rate constants used were $\alpha_{\mathrm{m}} = 2$, $\beta_{\mathrm{m}} = \delta_{\mathrm{m}} = 0.2$, $\alpha_i = \beta_i = \gamma_i = \delta_i = 1$ for $i = 1, \ldots, K$ where $K = 100$.

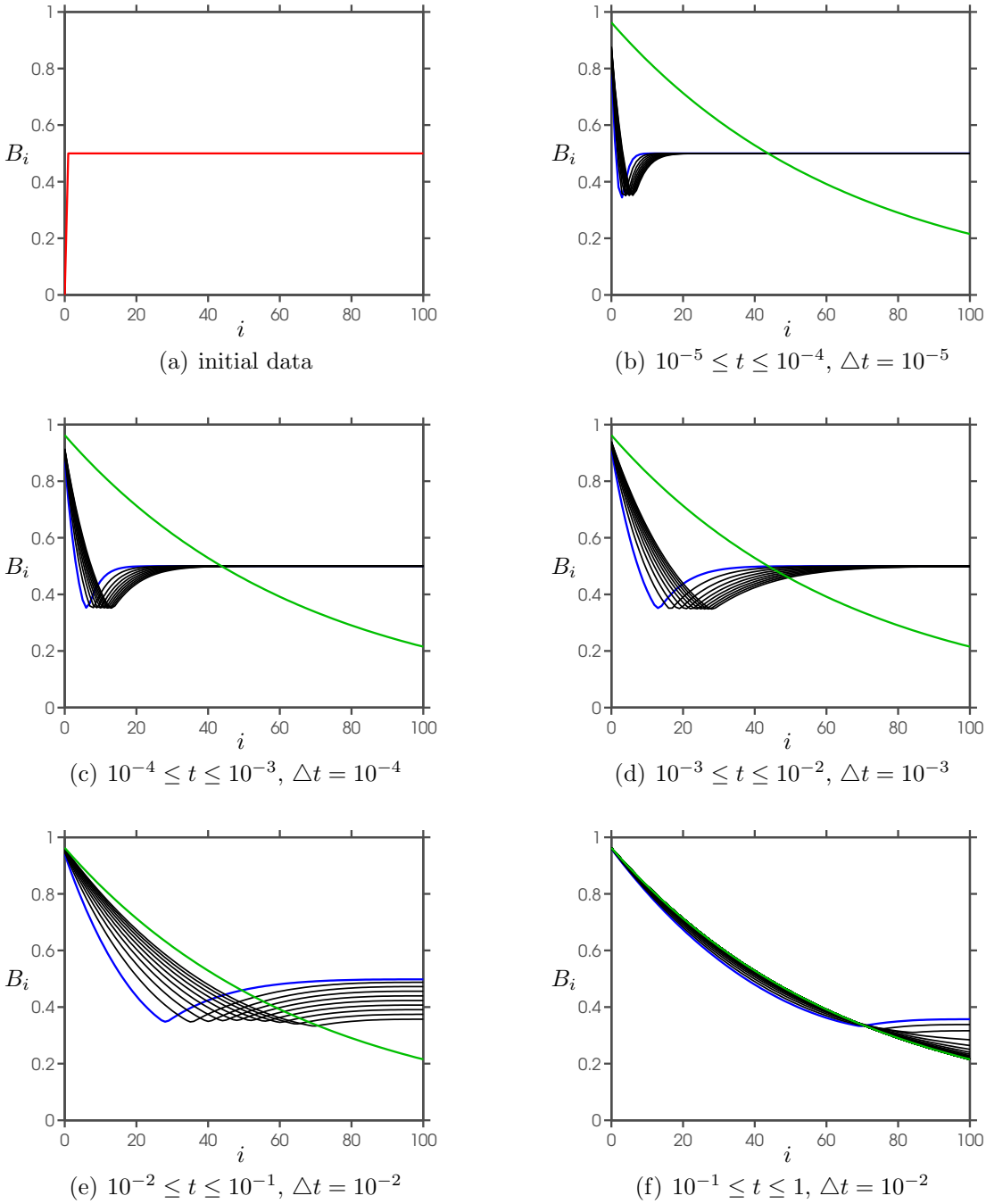

(a) initial data

(b) $10^{-5} \leq t \leq 10^{-4}$, $\triangle t = 10^{-5}$

(c) $10^{-4} \leq t \leq 10^{-3}$, $\triangle t = 10^{-4}$

(d) $10^{-3} \leq t \leq 10^{-2}$, $\triangle t = 10^{-3}$

(e) $10^{-2} \leq t \leq 10^{-1}$, $\triangle t = 10^{-2}$

(f) $10^{-1} \leq t \leq 1$, $\triangle t = 10^{-2}$

Figure 4.7: Plots of the numerical solutions to the system of ordinary differential equations (4.16) (black lines) for (a) uniform initial data (red line) and for the time intervals (b) $[10^{-5}, 10^{-4}]$, (c) $[10^{-4}, 10^{-3}]$, (d) $[10^{-3}, 10^{-2}]$, (e) $[10^{-2}, 10^{-1}]$, and (f) $[10^{-1}, 1]$ where the blue curves denote the solution at the start of the time interval and the green curve denotes the steady-state solution (4.21). The rate constants used were $\alpha_{\mathrm{m}} = 2$, $\beta_{\mathrm{m}} = \delta_{\mathrm{m}} = 0.2$, $\alpha_i = \beta_i = \gamma_i = \delta_i = 1$ for $i = 1, \ldots, K$ where $K = 100$.

4.3 Macroscopic model

4.3.1 Derivation of macroscopic model

Since the number of bilayers in a multilayer structure is typically large, it is reasonable to consider a continuum approximation to the system of ODEs in (4.16). We let ϵ, defined in (4.15), be our small parameter and $B(x,t)$ be the continuous approximation to the concentration of bilayer molecules in the ith compartment, *i.e.*

$$B(x,t) \approx B_i(t), \quad x = i\epsilon. \tag{4.25}$$

Similarly we define

$$Q_a(x,t) \approx Q_i^a(t), \quad Q_b(x,t) \approx Q_i^b(t), \quad Q_c(x,t) \approx Q_i^c(t), \quad Q_d(x,t) \approx Q_i^d(t). \tag{4.26}$$

Assuming that $B(x,t), Q_a(x,t), Q_b(x,t), Q_c(x,t), Q_d(x,t)$ are piecewise differentiable functions of x and t we expand (4.16c) as a Taylor series in x about $\epsilon = 0$. This leads to

$$\epsilon^3 \frac{\partial B}{\partial t} = \epsilon \frac{\partial}{\partial x}\left(Q_a - Q_b + Q_c - Q_d\right) - \frac{1}{2}\epsilon^2 \frac{\partial^2}{\partial x^2}\left(Q_a - Q_b + Q_c - Q_d\right) + \ldots, \tag{4.27}$$

where from (4.17e)–(4.17h) we have that

$$Q_a(x,t) = H[-B_x]\left(\alpha(x)\left(-\epsilon B B_x - \epsilon^2 {B_x}^2 + \frac{\epsilon^2}{2} B B_{xx}\right) - \epsilon^2 \alpha'(x) B B_x + \ldots\right), \tag{4.28a}$$

$$Q_b(x,t) = H[-B_x]\left(\beta(x)\left(-\epsilon B B_x + \epsilon^2 {B_x}^2 + \frac{\epsilon^2}{2} B B_{xx}\right) - \epsilon^2 \beta'(x) B B_x + \ldots\right), \tag{4.28b}$$

$$Q_c(x,t) = H[B_x]\left(\gamma(x)\left(\epsilon B B_x + \epsilon^2 {B_x}^2 + \frac{\epsilon^2}{2} B B_{xx}\right) + \epsilon^2 \gamma'(x) B B_x + \ldots\right), \tag{4.28c}$$

$$Q_d(x,t) = H[B_x]\left(\delta(x)\left(\epsilon B B_x - \epsilon^2 {B_x}^2 + \frac{\epsilon^2}{2} B B_{xx}\right) + \epsilon^2 \delta'(x) B B_x + \ldots\right). \tag{4.28d}$$

Here $H[\cdot]$ is the Heaviside step function and $'$ denotes differentiation with respect to x.

Equation (4.27) can be re-written in conservation form as

$$\epsilon^3 \frac{\partial B}{\partial t} \approx \frac{\partial}{\partial x}\left(J_a + J_b + J_c + J_d\right) \tag{4.29}$$

where terms of $O(\epsilon^4)$ have been neglected and the continuum fluxes are defined to be

$$J_a(x,t) = H[-B_x]\left(\alpha(x)\left(-\epsilon^2 B B_x + \epsilon^3\left(B B_{xx} - \frac{1}{2}{B_x}^2\right)\right) - \epsilon^3 \alpha'(x) B B_x\right) + \epsilon^3 \frac{\epsilon^3}{2} B B_x \frac{\partial}{\partial x}\left(\alpha(x) H[-B_x]\right), \tag{4.30a}$$

$$J_b(x,t) = H[-B_x]\left(\beta(x)\left(\epsilon^2 B B_x - \epsilon^3 \frac{1}{2}{B_x}^2\right) + \epsilon^3 \beta'(x) B B_x\right) + \frac{\epsilon^3}{2} B B_x \frac{\partial}{\partial x}\left(\beta(x) H[-B_x]\right), \tag{4.30b}$$

$$J_c(x,t) = H[B_x]\left(\gamma(x)\left(\epsilon^2 B B_x + \epsilon^3 \frac{1}{2}{B_x}^2\right) + \epsilon^3 \gamma'(x) B B_x\right) - \frac{\epsilon^3}{2} B B_x \frac{\partial}{\partial x}\left(\gamma(x) H[B_x]\right), \tag{4.30c}$$

$$J_d(x,t) = H[B_x]\left(\delta(x)\left(-\epsilon^2 B B_x + \epsilon^3\left(-B B_{xx} + \frac{1}{2}{B_x}^2\right)\right) - \epsilon^3 \delta'(x) B B_x\right) - \frac{\epsilon^3}{2} B B_x \frac{\partial}{\partial x}\left(\delta(x) H[B_x]\right). \tag{4.30d}$$

On the microscopic scale, a bilayer molecule presumably has no bias towards which direction it will move nor to which adsorption site it will occupy. Thus, it is physically reasonable to set the coefficients $\alpha(x)$, $\beta(x)$, $\gamma(x)$, and $\delta(x)$ equal (as in §4.2.3). Therefore, (4.29) reduces to the third-order nonlinear PDE

$$\frac{\partial B}{\partial t} = \frac{\partial}{\partial x}\left(\alpha(x)\mathrm{sgn}(B_x)\left({B_x}^2 - B B_{xx}\right)\right), \qquad 0 < x < \infty, \quad 0 < t, \tag{4.31}$$

at leading order.

In order to classify the third-order quasilinear PDE (4.31) we consider the system of first-order quasilinear equations by setting $\mathbf{u} = (u, v, w)^T = (B, B_x, B_{xx})^T$ to obtain

$$\mathbf{A}\mathbf{u}_x + \mathbf{B}\mathbf{u}_t = \mathbf{c}, \tag{4.32}$$

where

$$\mathbf{A} = \begin{pmatrix} \alpha\mathrm{sgn}(v)w & 0 & -\alpha\mathrm{sgn}(v)u \\ 1 & 0 & 0 \\ 0 & 1 & 0 \end{pmatrix}, \quad \mathbf{B} = \begin{pmatrix} 1 & 0 & 0 \\ 0 & 0 & 0 \\ 0 & 0 & 0 \end{pmatrix}, \quad \mathbf{c} = \begin{pmatrix} \alpha'\mathrm{sgn}(v)(v^2 - uw) \\ v \\ w \end{pmatrix}. \tag{4.33}$$

In general, for $n \times n$ symmetric matrices $\mathbf{A}$ and $\mathbf{B}$, n-vector $\mathbf{c}$, and provided that $\mathbf{A}$ is invertible, the characteristic projections[1] are defined to be the curves $(x(s), t(s))$ in the (x, t)-plane such that $\lambda = dt/dx$ where λ is given by $|\mathbf{B} - \lambda\mathbf{A}| = 0$. The n-dimensional system of PDEs (4.32) can then be classified by considering the eigenvalues, λ_i, and left eigenvectors, $\mathbf{l}_i$, of $(\mathbf{B} - \lambda\mathbf{A})$. For the case $n = 2$ (4.32) can be fully classified (see for example Ockendon *et al.* [26]), however, for $n \geq 3$ there is no exhaustive classification. We note some classifications can still be made for the case $n \geq 3$ [10]. Namely, if the system has n real eigenvalues, not necessarily distinct, and there are n linearly independent corresponding eigenvectors then the system is referred to as *hyperbolic*, if in addition the eigenvalues are all distinct then the system is referred to as *totally hyperbolic*. Conversely, if there are no real eigenvalues then the system is referred to as *elliptic*.

For $\mathbf{A}$ and $\mathbf{B}$ in (4.33) $\lambda = 0$ three times, and thus, the characteristic projections are given by the curves $t =$ constant. Moreover, there is a two-dimensional subspace of eigenvectors and so this suggests that (4.31) is of mixed hyperbolic–parabolic type.

4.3.2 Boundary conditions

We expect to impose three boundary conditions on the third-order PDE (4.31). These can be derived from the continuum approximation to the ODEs at either end of the discretised domain $\mathcal{D}$.

[1]For further discussions we refer the reader to Ockendon *et al.* [26].

4.3.2.1 Boundary conditions on the adsorbing surface

First we consider the boundary condition at $x = 0$ by expanding (4.16a)–(4.16c) for $i = 2$ in a Taylor series expansion about $\epsilon = 0$. Thus,

$$\epsilon^3 \dot{\Gamma} = 2J_{\mathrm{m}}, \qquad \text{at} \quad x = 0, \tag{4.34a}$$

$$\epsilon^3 B_t + \epsilon^4 B_{tx} + \ldots = J_1 - J_{\mathrm{m}}, \qquad \text{at} \quad x = 0, \tag{4.34b}$$

$$\epsilon^3 B_t + 2\epsilon^4 B_{tx} + \ldots = J_2 - J_1, \qquad \text{at} \quad x = 0, \tag{4.34c}$$

where $\dot{}$ denotes a time derivative and the expansion of the $J's$ are given by

$$\begin{aligned} J_{\mathrm{m}} = \;& Q^a_{\mathrm{m}} - Q^b_{\mathrm{m}} - Q^d_{\mathrm{m}} \\ \approx \;& \alpha_{\mathrm{m}} \left(1 - \Gamma(t)\right)^2 \left(B + \epsilon B_x + \frac{1}{2}\epsilon^2 B_{xx} \right) + \ldots \\ & - \beta_{\mathrm{m}} \Gamma(t)^2 H[\Gamma(t) - B] \left(\Gamma(t) - B - \epsilon B_x - \frac{1}{2}\epsilon^2 B_{xx} \right) + \ldots \\ & - \delta_{\mathrm{m}} \Gamma(t)^2 H[B_x] \left(\epsilon B_x + \frac{3}{2}\epsilon^2 B_{xx} \right) + \ldots \Bigg|_{x=0}, \end{aligned} \tag{4.35a}$$

$$\begin{aligned} J_1 = \;& Q^a_1 - Q^b_2 + Q^c_1 - Q^d_2 \\ \approx \;& \left(\alpha + \epsilon\alpha' + \ldots\right) H[\Gamma - B] \big((\Gamma - B)B + \epsilon \left(2\Gamma - 3B\right) B_x \\ & + \frac{\epsilon^2}{2} \left(4(\Gamma - B)B_{xx} - 4B_x^2 - BB_{xx} \right) + \ldots \big) \\ & + \left(\beta + \epsilon 2\beta' + \ldots\right) H[-B_x] \left(\epsilon B B_x + \epsilon^2 \left(B_x^2 + \frac{3}{2} B B_{xx} \right) + \ldots \right) \\ & + \left(\gamma + \epsilon\gamma' + \ldots\right) H[B_x] \left(\epsilon B B_x + \epsilon^2 \left(2B_x^2 + \frac{3}{2} B B_{xx} \right) + \ldots \right) \\ & - \left(\delta + \epsilon\delta' + \ldots\right) H[B_x] \left(\epsilon B B_x + \epsilon^2 \left(B_x^2 + \frac{5}{2} B B_{xx} \right) + \ldots \right) \Bigg|_{x=0}, \end{aligned} \tag{4.35b}$$

$$
\begin{aligned}
J_2 = \;& Q_2^q - Q_3^b + Q_2^c - Q_3^d \\
\approx & -(\alpha + \epsilon\alpha' + \ldots)\, H[-B_x]\left(\epsilon B B_x + \epsilon^2\left(3B_x^2 + \frac{3}{2}BB_{xx}\right) + \ldots\right) \\
& + (\beta + 3\epsilon\beta' + \ldots)\, H[-B_x]\left(\epsilon B B_x + \epsilon^2\left(2B_x^2 + \frac{5}{2}BB_{xx}\right) + \ldots\right) \\
& + (\gamma + 2\epsilon\gamma' + \ldots)\, H[B_x]\left(\epsilon B B_x + \epsilon^2\left(3B_x^2 + \frac{5}{2}BB_{xx}\right) + \ldots\right) \\
& - (\delta + 3\epsilon\delta' + \ldots)\, H[B_x]\left(\epsilon B B_x + \epsilon^2\left(2B_x^2 + \frac{7}{2}BB_{xx}\right) + \ldots\right)\Bigg|_{x=0}, \qquad (4.35c)
\end{aligned}
$$

as $\epsilon \to 0$ and $'$ denotes differentiation with respect to x. Summing (4.34a)–(4.34c) leads to

$$\frac{1}{2}\epsilon^3\dot{\Gamma} + 2\epsilon^3 B_t + 3\epsilon^4 B_{tx} + \ldots = J_2, \quad \text{at} \quad x = 0. \qquad (4.36)$$

On setting $\alpha(x) = \beta(x) = \gamma(x) = \delta(x)$ then (4.36) at leading order is

$$B_x^2 - BB_{xx} = 0, \quad \text{on} \quad x = 0, \qquad (4.37)$$

and (4.34c) at leading order is

$$0 = \alpha H[\Gamma - B](\Gamma - B)B, \quad \text{on} \quad x = 0. \qquad (4.38)$$

Assuming that $\alpha_{\mathrm{m}}, \beta_{\mathrm{m}}$, and δ_{m} are $O(1)$ constants then to leading order (4.34a) is

$$0 = \alpha_{\mathrm{m}}(1 - \Gamma)^2 B - \beta_{\mathrm{m}} H[\Gamma - B]\Gamma^2(\Gamma - B), \quad \text{on} \quad x = 0. \qquad (4.39)$$

Provided $B \neq 0$ then (4.38) implies that either $\Gamma = B$ or $\Gamma < B$. If the latter case held then (4.39) would imply that $B > 1$ which contradicts the modelling assumption that there is a dimensionless saturation concentration equal to 1 in the monolayer and bilayers. Thus, we are led to conclude that, to satisfy (4.38) and (4.39),

$$\Gamma = B = 1, \quad \text{on} \quad x = 0. \qquad (4.40)$$

This implies that the monolayer equilibrates much more rapidly than the multilayer.

4.3.2.2 Boundary condition for time-dependent surfactant concentration on the adsorbing surface

It is possible to obtain a limit in which the monolayer evolves on the same timescale as the multilayer structure if $\alpha_{\rm m}$, $\beta_{\rm m}$, and $\delta_{\rm m}$ are order ϵ^3. In this case on setting $\alpha_{\rm m} = \epsilon^3\bar{\alpha}_{\rm m}$, $\beta_{\rm m} = \epsilon^3\bar{\beta}_{\rm m}$, and $\delta_{\rm m} = \epsilon^3\bar{\delta}_{\rm m}$ the leading-order terms in (4.34a)–(4.36) lead to the boundary conditions

$$B_x^2 - BB_{xx} = 0, \quad \text{on} \quad x = 0, \tag{4.41a}$$

$$B(0,t) = \Gamma(t), \quad \text{and} \quad \frac{\mathrm{d}\Gamma}{\mathrm{d}t} = 2\bar{\alpha}_{\rm m}(1-\Gamma)^2\Gamma. \tag{4.41b}$$

Equation (4.41b) can be integrated with respect to t to obtain an implicit expression for $\Gamma(t)$ namely

$$\log\left(\frac{\Gamma}{1-\Gamma}\right) + \frac{1}{1-\Gamma} = 2\bar{\alpha}_{\rm m}t + \log\left(\frac{\Gamma_0}{1-\Gamma_0}\right) + \frac{1}{1-\Gamma_0}, \tag{4.42}$$

where $\Gamma(0) = \Gamma_0 < 1$. We note that the limiting behaviour of $\Gamma(t)$ in (4.42) as $t \to 0$ and $t \to \infty$ is given by

$$\Gamma \sim \Gamma_0(1 + 2\bar{\alpha}_{\rm m}(1-\Gamma_0)^2 t + \ldots) \qquad \text{as} \quad t \to 0, \tag{4.43a}$$

$$\Gamma \sim 1 - \frac{1}{2\bar{\alpha}_{\rm m}t} + \ldots \qquad \text{as} \quad t \to \infty. \tag{4.43b}$$

Thus, the adsorbed concentration will increase towards the dimensionless saturation concentration, 1, for large times. The evolution of Γ with time according to (4.42) is shown by the continuous curves in Figure 4.8, while the small and large time leading-order asymptotic solutions (4.43a) and (4.43b) are shown using the dashed curves.

4.3.2.3 Boundary condition at depth

Next we consider the boundary condition at the bottom of the multilayer by expanding the sum of (4.16d) and (4.16e) to get

$$3\epsilon^3 B_t - 3\epsilon^4 B_{tx} + \ldots = J_{K-1}, \quad \text{on} \quad x = 1, \tag{4.44}$$

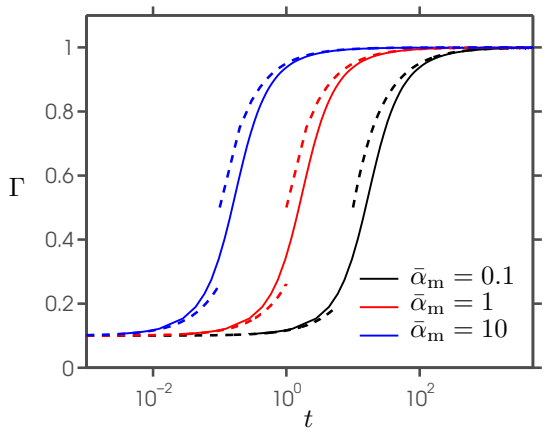

Figure 4.8: Evolution of surface concentration, Γ, with time given implicitly by (4.42) (continuous curves) against the small and large time leading-order asymptotic solutions (dashed curves) given by (4.43a) and (4.43b) respectively for different values of $\bar{\alpha}_{\mathrm{m}}$.

as $\epsilon \to 0$ where

$$\begin{aligned} J_{K-1} =& - Q^a_{K-2} + Q^b_{K-1} - Q^c_{K-2} + Q^d_{K-1} \\ \approx& - (\alpha - 2\epsilon\alpha' + \ldots)H[-B_x]\left(-\epsilon BB_x + \epsilon^2\left(B_x^2 + \frac{5}{2}BB_{xx}\right) + \ldots\right) \\ & - (\beta - \epsilon\beta' + \ldots)H[-B_x]\left(-\epsilon BB_x + \epsilon^2\left(2B_x^2 + \frac{3}{2}BB_{xx}\right) + \ldots\right) \\ & - (\gamma - 2\epsilon\gamma' + \ldots)H[B_x]\left(\epsilon BB_x - \epsilon^2\left(B_x^2 + \frac{3}{2}BB_{xx}\right) + \ldots\right) \\ & - (\delta - \epsilon\delta' + \ldots)H[-B_x]\left(\epsilon BB_x - \epsilon^2\left(2B_x^2 + \frac{1}{2}BB_{xx}\right) + \ldots\right)\Bigg|_{x=1}. \end{aligned} \tag{4.45}$$

Again we set $\alpha(x) = \beta(x) = \gamma(x) = \delta(x)$ to obtain at leading order

$$B_x^2 - BB_{xx} = 0, \quad \text{on} \quad x = 1. \tag{4.46}$$

4.3.2.4 Conservation of Mass

Integrating (4.31) with respect to x and applying boundary conditions (4.37) and (4.46) we find that

$$\frac{\mathrm{d}}{\mathrm{d}t}\left(\int_0^1 B(x,t)\,\mathrm{d}x\right) = 0, \tag{4.47}$$

and hence the net surfactant concentration is conserved. Equation (4.47) is consistent with (4.19) which gives, as $\epsilon \to 0$,

$$M = \int_0^1 B(x,t)\,\mathrm{d}x, \tag{4.48}$$

where $M = \epsilon\mathcal{S}/2$ is the net concentration of bilayers and assumed to be order one.

4.3.3 Steady-state solution

Suppose that $B_0(x)$ satisfies the steady-state version of (4.31). The boundary conditions (4.37) and (4.46) imply that $B_0(x)$ satisfies

$$(B_0')^2 - B_0 B_0'' = 0, \quad \text{where} \quad {}' := \frac{\mathrm{d}}{\mathrm{d}x}, \tag{4.49}$$

which can be integrated subject to the boundary condition (4.40) (or (4.41b)) and the conservation of mass constraint to give the general solution

$$B_0(x) = \mathrm{e}^{-kx}, \quad \text{where } k \text{ satisfies} \quad 1 - \mathrm{e}^{-k} = kM. \tag{4.50}$$

For the physical scenarios of interest we expect the concentration of bilayers in the multilayer to decrease with depth, *i.e.* we expect that $k > 0$.

In order to compare the steady-state solutions of the mesoscopic and macroscopic models we note that the surface concentration, Γ, in the mesoscopic model did not equal 1 in steady state but, as shown in (4.23b), does approach 1 asymptotically as $\mathcal{S} \to \infty$. Figure 4.9 compares the steady-state solutions (4.21a) and (4.22) for the mesoscopic model for different values of the parameter α^* (black curves) and (4.50) for the macroscopic model (blue curve). For α^* order one the difference between the steady states $B_0(x)$ and B_i is within the expected error $\epsilon = 1/K$. However, for $\alpha^* \ll 1$ and $\alpha^* \gg 1$ the difference between the steady-state solutions increases and decreases respectively, which is to be expected from the asymptotic expansion of Γ as $S \to \infty$ given in (4.23b).

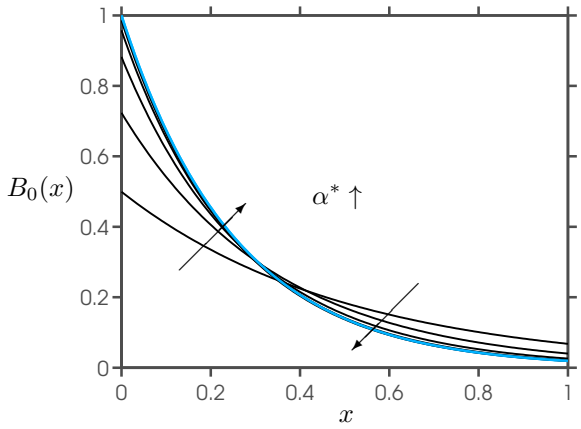

Figure 4.9: Comparison of the steady-state solution (4.50) of the macroscopic model (blue curve) with the steady-state solution (4.21a) and (4.22) of the mesoscopic model for $\alpha^* = 10^{-1}, 10^0, 10^1$, and 10^2 (black curves), with $K = 200$ and $\mathcal{S} = 100$.

4.3.4 Linear stability analysis

We consider a small perturbation to the steady-state solution (4.50), to determine if the perturbation decays with time and deduce whether the steady-state solution is linearly stable. Provided $B_x < 0$ for $x \in [0, 1]$ we perturb as follows

$$B(x,t) = \mathrm{e}^{-kx} + \delta b(x,t), \quad \delta \ll 1, \tag{4.51}$$

and on substituting into (4.31) and linearising with respect to δ we find that

$$b_t = -\mathrm{e}^{-kx}\left(k^3 b + k^2 b_x - k b_{xx} - b_{xxx}\right). \tag{4.52}$$

Seeking a separable solution, $b(x,t) = X(\xi)T(t)$ where $\xi = kx$, to (4.52) we find that

$$T(t) = T_0 \mathrm{e}^{\lambda k^3 t}, \tag{4.53}$$

for some constants λ and T_0, and $X(\xi)$ and λ satisfy the eigenvalue problem

$$X(1 + \lambda \mathrm{e}^{\xi}) + X' - X'' - X''' = 0, \qquad 0 < \xi < k, \tag{4.54a}$$

$$X = X'' + 2X' = 0, \qquad \text{on} \quad \xi = 0, \tag{4.54b}$$

$$X'' + 2X' + X = 0, \qquad \text{on} \quad \xi = k. \tag{4.54c}$$

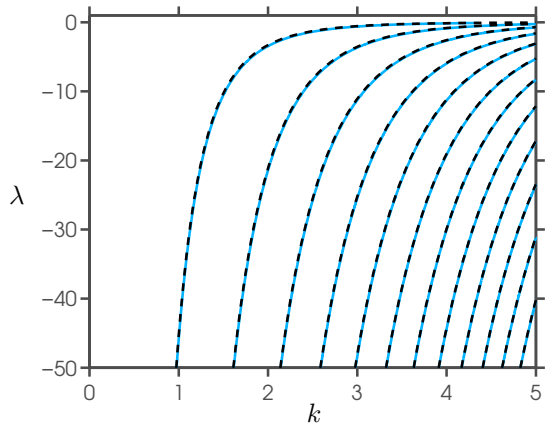

Figure 4.10: Linear growth rate λ versus effective domain size k for the eigenvalue problem (4.54). The solid blue curves are found by the numerical solution of (4.56); the black dashed curves show the approximation given by (4.62).

The amplitude of the eigenfunction $X(\xi)$ is arbitrary so we may set $X'(0) = 1$. We introduce the new dependent variables

$$u = \mathrm{e}^{\xi} X, \qquad v = \mathrm{e}^{\xi}(X' + X), \qquad w = \mathrm{e}^{-\xi}(X'' + 2X' + X), \tag{4.55}$$

and hence (4.54) may be written as the first-order system

$$u' = v, \quad v' = \mathrm{e}^{2\xi} w, \quad w' = \lambda \mathrm{e}^{-\xi} u, \tag{4.56}$$

subject to the boundary conditions

$$u = 0, \quad v = 1, \quad w = 0, \qquad \text{on} \qquad \xi = 0, \tag{4.57a}$$

$$w = 0, \qquad \text{on} \qquad \xi = k. \tag{4.57b}$$

If $\lambda > 0$ then (4.56) and (4.57a) imply that u, v, and w are all positive for $\xi > 0$ and hence condition (4.57b) can not be satisfied. Thus, either $\lambda < 0$ and the steady-state solution is linearly stable or $\lambda \in \mathbb{C}$.

The eigenvalues may be determined numerically by solving the initial value problem given by (4.56) and (4.57a) for a given (real, negative) value of λ and infer the corresponding value of k that satisfies (4.57b). The results are plotted by the blue curves in Figure 4.10. We note that for each effective domain length, k, there is a countably infinite set of negative eigenvalues λ. As k decreases we observe that $|\lambda|$ rapidly increases and for small values of $|\lambda|$, k must be large.

These observations suggest that the solution to (4.54) may be approximated using the WKBJ method, by setting $X(\xi) \sim A(\xi)\mathrm{e}^{\phi(\xi)}$, which is valid when either $|\lambda|$ or k is large. The general solution is approximately given by

$$X(\xi) \sim \mathrm{e}^{-2\xi/3}\left\{a_1\mathrm{e}^{3|\lambda|^{1/3}\mathrm{e}^{\xi/3}} + a_2\mathrm{e}^{-3|\lambda|^{1/3}\mathrm{e}^{\xi/3}/2}\cos\left(\frac{3\sqrt{3}|\lambda|^{1/3}\mathrm{e}^{\xi/3}}{2}\right)\right.$$
$$\left. + a_3\mathrm{e}^{-3|\lambda|^{1/3}\mathrm{e}^{\xi/3}/2}\sin\left(\frac{3\sqrt{3}|\lambda|^{1/3}\mathrm{e}^{\xi/3}}{2}\right)\right\}, \quad (4.58)$$

where a_1, a_2, and a_3 are arbitrary integration constants. The boundary conditions (4.54b)–(4.54c) then lead to the solvability condition

$$\frac{\sqrt{3}}{2}\sin\left(\frac{3\sqrt{3}|\lambda|^{1/3}}{2}\left(\mathrm{e}^{k/3}-1\right)\right) + \frac{1}{2}\cos\left(\frac{3\sqrt{3}|\lambda|^{1/3}}{2}\left(\mathrm{e}^{k/3}-1\right)\right)$$
$$= \frac{1}{2}\exp\left(\frac{9|\lambda|^{1/3}}{2}\left(\mathrm{e}^{k/3}-1\right)\right), \quad (4.59)$$

whose solution λ may be written in the form

$$\lambda = -\left(\frac{2\left(\theta+\pi/6\right)}{3\sqrt{3}\left(\mathrm{e}^{k/3}-1\right)}\right)^3, \quad (4.60)$$

where θ satisfies the transcendental equation

$$\sin\theta = -\frac{1}{2}\mathrm{e}^{-\sqrt{3}(\theta+\pi/6)}. \quad (4.61)$$

The solutions of (4.61) are approximately given by $\theta \approx n\pi$, where $n = 1, 2, 3, \ldots$, and hence the eigenvalues are given approximately by

$$\lambda \sim -\left(\frac{(6n+1)\pi}{9\sqrt{3}\left(\mathrm{e}^{k/3}-1\right)}\right)^3, \quad n = 1, 2, 3, \ldots. \quad (4.62)$$

The approximate eigenvalues (4.62) are plotted as the black dashed curves in Figure 4.10 and have excellent agreement with the numerically determined eigenvalues (solid blue curves).

We note that the steady-state solution (4.50) is exponentially small for large k, and in this limit we would be linearising (4.31) about an exponentially small function. Thus, the problem is non-uniform in the limit $k \to \infty$, corresponding to $M \to 0$ and which

physically corresponds to the surfactant being concentrated in a small region near the adsorbing interface. In this limit the eigenvalues, λ, in (4.62) are all exponentially small and the corresponding eigenfunctions, X, have unbounded amplitude.

4.3.5 Numerical solutions

Given smooth initial data $B(x,0) = f(x)$ the PDE (4.31) and boundary conditions (4.37), (4.40) (or (4.41b)), and (4.46) form a closed system. In this section we solve the system numerically for the following two possible boundary conditions at $x = 0$:

(i) the surfactant concentration on the adsorbing surface remains constant, (4.40);

(ii) the surfactant concentration on the adsorbing surface is time dependent, (4.41b);

and compare the results to the steady-state solution (4.50) and the mesoscopic model of §4.2.1.

We note that in general one might expect the rate parameter α to depend on the vacant adsorption sites, *i.e.* $\alpha = \alpha(B, x)$, but in this section we focus on the simplest case where $\alpha = 1$.

4.3.5.1 Constant surfactant concentration on the adsorbing surface

We restate the problem we wish to solve numerically:

$$\frac{\partial B}{\partial t} = \frac{\partial}{\partial x}\left(\operatorname{sgn}(B_x)\left({B_x}^2 - BB_{xx}\right)\right) \quad 0 < x < 1, \quad 0 < t, \tag{4.63a}$$

$$B = 1 \quad \text{on} \quad x = 0, \quad \text{and} \quad B_x^2 - BB_{xx} = 0 \quad \text{on} \quad x = 0, 1, \tag{4.63b}$$

subject to smooth initial data

$$B(x,0) = \mathrm{e}^{-(x/\sigma)^2}. \tag{4.63c}$$

We solve (4.63) using the method of lines; discretise in x and solve the resulting system of ODEs using an ODE solver such as Matlab's `ode45`. The truncation error for the discretization scheme we use is of order $\triangle x$, where $\triangle x$ is the space step (see Appendix C for details). The computed solution using this scheme with $\sigma = 0.2$ in the initial condition is plotted in Figure 4.11(a) for different values of t. The initial profile (red line) evolves smoothly to the steady-state solution (4.50) as t increases,

characterizing a diffusive process. Figure 4.11(b) shows the convergence of the numerical solution to the steady-state solution (4.50) evaluated at $x = 0.1$ and the difference between the numerical solution for large time and the steady-state solution is well within the truncation error for the numerical scheme, $\triangle x = 0.01$.

We compare the temporal evolution of $B(x,t)$ according to (4.63) with the mesoscopic model given by (4.16) in Figure 4.12 where the blue and black curves denote solutions to the meso- and macroscopic models respectively. Figure 4.12(a) shows the numerical solution for Γ to the mesoscopic model against its steady-state solution given by (4.22) and compares it with Γ for the macroscopic model which is equal to one. The discrepancy between the two models is accounted for by the evolution of Γ to steady state in the mesoscopic model, as discussed earlier in §4.3.3, and the difference $\sim \sqrt{2/\alpha^* \mathcal{S}}$. Similarly, on plotting B at $x = 0.1$ the discrepancy persists, see Figure 4.12(b).

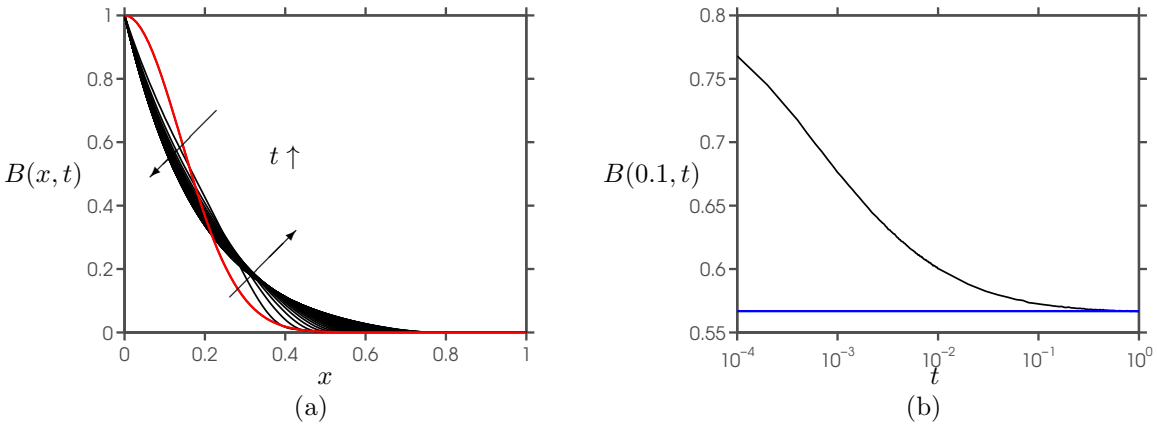

Figure 4.11: (a) Plots of the numerical solution to (4.63) (black curves) with space step $\triangle x = 0.01$ and at times $t \in [0, 0.001, \ldots, 0.05]$. The initial condition (4.63c) is plotted by the red curve for $\sigma = 0.2$. (b) Comparison of the numerical solution (black curve), against the steady-state solution, B_0, (blue curve) given by (4.50) at $x = 0.1$.

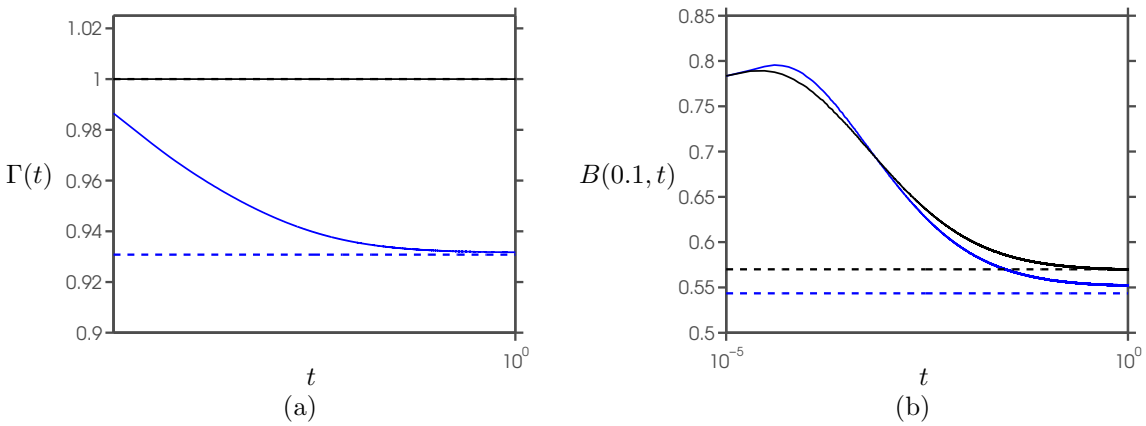

Figure 4.12: (a) Plots of the surface concentration, Γ, for the mesoscopic model (blue continuous line) and the macroscopic model (black continuous line) subject to the initial condition (4.63c) with $\sigma = 0.2$. The steady-state solution Γ for the mesoscopic model is plotted by the blue dashed line. (b) Plots of $B(0.1, t)$ for the mesoscopic model (blue continuous line) and the macroscopic model (black continuous line). The steady state solutions of B at $x = 0.1$ are plotted by the blue dashed line for the mesoscopic model and black dashed line for the macroscopic model. Parameters used were $\alpha_{\mathrm{m}} = 2$, $\beta_{\mathrm{m}} = \delta_{\mathrm{m}} = 1$, $\alpha_i = \beta_i = \gamma_i = \delta_i = 1$, and $K = 100$.

4.3.5.2 Time-dependent surfactant concentration on the adsorbing surface

In this section we consider the case where $\alpha_{\mathrm{m}}, \beta_{\mathrm{m}}$, and δ_{m} are $O(\epsilon^3)$. We restate the problem we wish to solve numerically:

$$\frac{\partial B}{\partial t} = \frac{\partial}{\partial x}\left(\mathrm{sgn}(B_x)\left({B_x}^2 - BB_{xx}\right)\right) \quad 0 < x < 1, \quad 0 < t, \tag{4.64a}$$

$$B = \Gamma(t) \quad \text{on} \quad x = 0, \quad \text{and} \quad B_x^2 - BB_{xx} = 0 \quad \text{on} \quad x = 0, 1, \tag{4.64b}$$

$$B(x, 0) = \Gamma_0 \mathrm{e}^{-(x/\sigma)^2}, \tag{4.64c}$$

where Γ satisfies the ODE

$$\frac{\mathrm{d}\Gamma}{\mathrm{d}t} = 2\bar{\alpha}_{\mathrm{m}}(1 - \Gamma)^2\Gamma. \tag{4.65}$$

We solve (4.64) using the method of lines as described in §4.3.5.1 but with the temporal boundary condition (4.65), full details are given in Appendix C. The solution is plotted in Figure 4.13(a) at times $t \in [0, 0.01, \ldots 0.5]$ and for parameters $\sigma = 0.3$, $\Gamma_0 = 0.8$, and $\bar{\alpha}_{\mathrm{m}} = 2$. As we expect the system evolves from this initial configuration in a qualitatively similar way to that for constant surfactant concentration on the adsorbing boundary in §4.3.5.1 but with the surfactant concentration at the adsorbing boundary now evolving with time. Figures 4.13(b) and 4.13(c) show the convergence for $\Gamma(t)$ and $B(0.1, t)$ of the numerical solution to the steady-state solution (4.50). The truncation error for the numerical scheme used to compute the solution is of order $\triangle x$ and for large t the difference between the steady state and the numerical solutions is within this error.

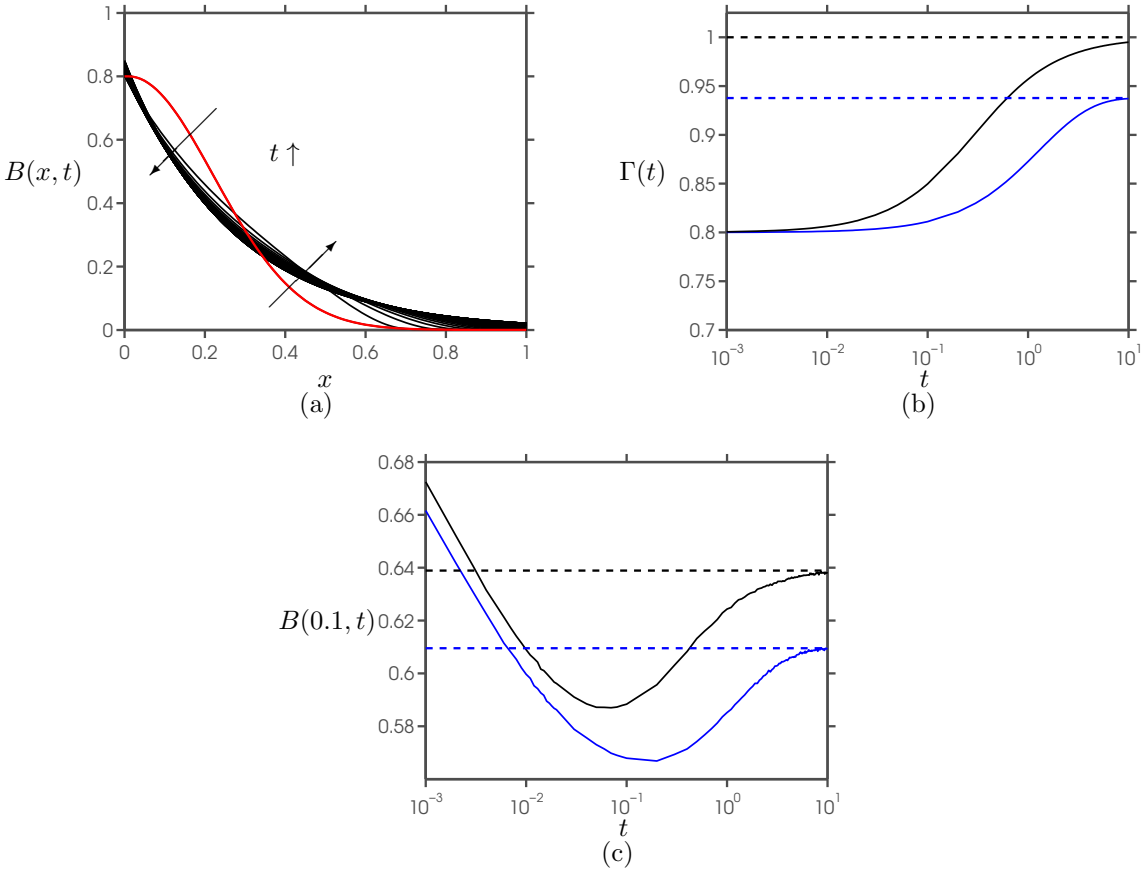

Figure 4.13: (a) Plots of the numerical solution to (4.64) (black lines) for space step $\triangle x = 0.01$ and times $t \in [0, 0.01, \ldots 0.5]$. The initial condition is denoted by the red line. (b) Plots of the evolution of surface concentration $\Gamma(t)$ according to (4.65) (black continuous line); the steady-state value for Γ (black dashed line); the mesoscopic model (4.16) (blue-continuous line) and the steady-state value (4.21b). (c) Comparison of the numerical solution (black continuous line), against the steady-state solution, B_0, (black dashed line) given by (4.50) at $x = 0.1$, and the corresponding plots for the mesoscopic model (blue curves). The parameters used were $\sigma = 0.3$, $\Gamma_0 = 0.8$, $\alpha_{\rm m} = 2$, $\beta_{\rm m} = \delta_{\rm m} = 0.2$, and $K = 100$.

4.3.6 A similarity solution

We now seek a similarity solution to the PDE (4.31) in order to reduce the problem to an ODE, which in theory is easier to solve. We note that Clarkson *et al.* [9] have categorised the symmetry reductions to a general class of third-order nonlinear partial differential equations including (4.31) using classical Lie methods. They found three reductions to equation (4.31), namely

$$B(x,t) = f(\eta), \qquad \eta = x - ct, \tag{4.66a}$$

$$B(x,t) = t^{3m} f(\eta), \qquad \eta = \frac{x}{t^{m+1/3}}, \tag{4.66b}$$

$$B(x,t) = \mathrm{e}^{3mt} f(\eta), \qquad \eta = x\mathrm{e}^{-mt}. \tag{4.66c}$$

In the context of the multilayer problem the physically relevant reduction is (4.66b) with $m = -1/12$ for mass to be conserved. In order for this similarity solution to be a solution of our model we reformulate the problem as follows.

We wish to determine the dynamics of the spreading out of the 'drop' of surfactant in the bilayer and so we assume that $B(x,t)$ evolves symmetrically about $x = 0$ and on the the infinite domain $x \in (-\infty, \infty)$. We suppose that initially surfactant is concentrated in some region near the adsorbing surface ($x = 0$) which is given by some symmetric distribution about $x = 0$. Thus, $B(x,t)$ satisfies the problem

$$B_t = -\left(B_x^2 - BB_{xx}\right)_x, \qquad 0 < x < \infty, \tag{4.67a}$$

$$B_x(0,t) = B_{xx}(0,t) = 0, \tag{4.67b}$$

$$B_x^2 - BB_{xx} \to 0, \qquad \text{as} \quad x \to \infty, \tag{4.67c}$$

subject to the constraint

$$\int_0^\infty B(x,t)\ \mathrm{d}x = 1, \tag{4.68}$$

which closes the problem. The adsorbed concentration, $\Gamma(t) := B(0,t)$, is now unknown and must be determined as part of the solution.

The problem (4.67) thus has a similarity solution with compact support of the form

$$B(x,t) = \begin{cases} t^{-1/4}\Gamma_0 f(\eta), & 0 < \eta < \eta_c, \\ 0, & \text{otherwise}, \end{cases} \tag{4.69}$$

where $\eta = xt^{-1/4}\Gamma_0^{1/3}$ and the parameters Γ_0 and η_c are to be determined as part of the solution. We note that this implies that the adsorbed concentration is given by $\Gamma(t) = \Gamma_0 t^{-1/4}$. Substituting (4.69) into (4.67), integrating (4.67a) with respect to η once and applying boundary conditions (4.67b) we obtain the initial-value problem:

$$f(\eta)f''(\eta) - (f'(\eta))^2 + \frac{1}{4}\eta f = 0, \quad f(0) = 1, \quad f'(0) = 0, \tag{4.70}$$

where η_c is determined from

$$f(\eta_c) = 0, \tag{4.71}$$

and Γ_0 is determined from the conservation of mass equation

$$\int_0^{\eta_c} f(\eta)\ \mathrm{d}\eta = \Gamma_0^{-4/3}. \tag{4.72}$$

The solutions to the initial-value problem (4.70) can be computed numerically (for example using Mathematica's `NDSolve`) to obtain numerical values for the parameters $\eta_c = 3.784$ and $\Gamma_0 = 0.523$. The resulting solution is shown by the red dashed curve in Figure 4.14(a). The numerical solution to (4.67) solved via the method of lines subject to the initial condition

$$B(x, t_0) = \Gamma_0 t_0^{-1/4} \mathrm{e}^{-x^2/\sigma^2}, \quad \sigma = \frac{2t_0^{-1/4}}{\sqrt{\pi}\Gamma_0}, \tag{4.73}$$

is shown by the blue curves in Figure 4.14(a) for different values of t and they converge to the similarity solution as t increases. For reference, in Figure 4.14(b) we plot the numerical solution to (4.67) against x at time-intervals $t \in [0.005, 0.01, \ldots, 0.1]$.

Finally, we note that by making a suitable change of variables (4.70) can be reduced to a second-order autonomous ODE, which has no known analytical solution.

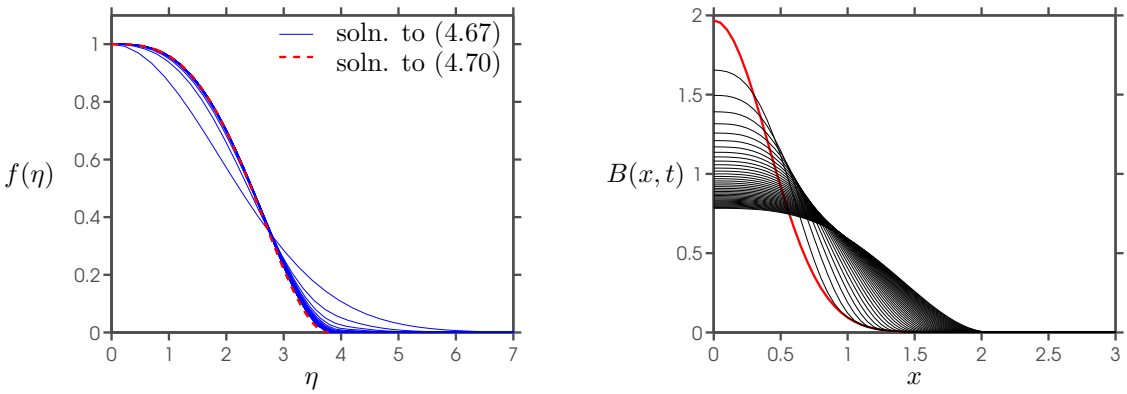

(a) (b)

Figure 4.14: (a) Comparison of the numerical solution to (4.67) (blue curves), with the similarity solution $f(\eta)$ given by the numerical solution to (4.70) (red dashed curve). (b) Numerical solution (black curves) to (4.67) subject to the initial condition (4.73) (red curve) on the truncated domain $x \in [0, 10]$ for $t \in [0.005, 0.01, \ldots, 0.1]$ and space step $\triangle x = 0.1$.

4.4 Model for self-assembly between two adsorbing surfaces

In this section we consider the situation in which a multilayer structure has formed between two adsorbing surfaces. Following the analysis above we derive mesoscopic and macroscopic models equivalent to those found in §4.2.1 and §4.3 respectively. In §4.3 we observed that, given a monotonic initial condition, the $\mathrm{sgn}(B_x)$ term in (4.31) has no effect on the evolution, whereas for the case where there are two adsorbing boundaries B_x must take different signs in the domain and so the $\mathrm{sgn}(B_x)$ term becomes more significant.

4.4.1 Mesoscopic model

We adapt the model derived in §4.2.1 for the finite domain $\mathcal{D} := \{x : x \in [0, L]\}$ with two monolayers at $x = 0$ and $x = L$. We define the dimensionless monolayer concentrations at the left- and right-hand boundaries to be $\Gamma_{\mathrm{L}}(t)$ and $\Gamma_{\mathrm{R}}(t)$ respectively. The two adsorbing surfaces may be distinct, for example one could be the air–liquid interface while the other could be the solid surface of the container of the solution. Thus, for generality we assume that there are distinct saturation concentrations Γ_{Lsat} and Γ_{Rsat} at the left and right boundaries respectively but without loss of generality

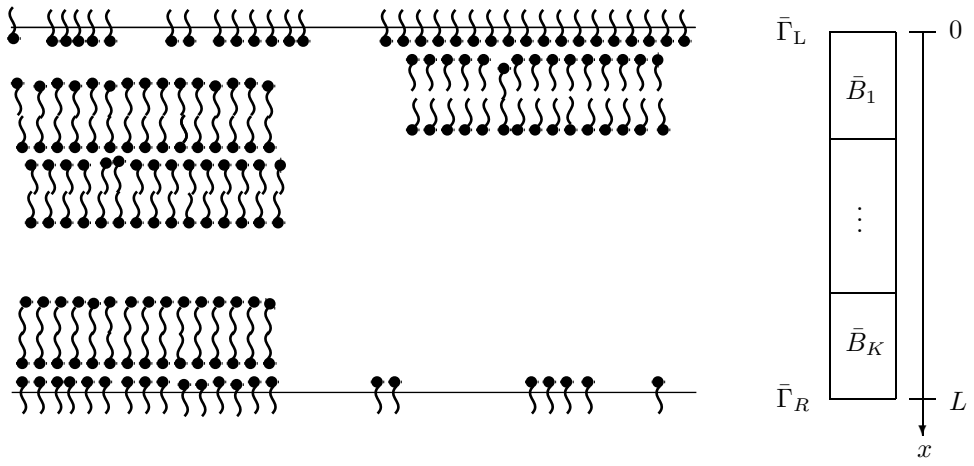

Figure 4.15: Schematic of multilayer compartments for the two-adsorbing-surfaces problem.

we assume that $\Gamma_{\mathrm{Rsat}} \leq \Gamma_{\mathrm{Lsat}}$. We discretise the domain $\mathcal{D}$ into K compartments as shown in Figure 4.15.

Analogous to section 4.2.1 we obtain the system of $K+2$ dimensionless ODEs

$$\epsilon^3 \frac{\mathrm{d}\Gamma_{\mathrm{L}}}{\mathrm{d}t} = 2\left(Q^a_{\mathrm{m_L}} - Q^b_{\mathrm{m_L}} - Q^d_{\mathrm{m_L}}\right), \tag{4.74a}$$

$$\epsilon^3 \frac{\mathrm{d}B_1}{\mathrm{d}t} = -\left(Q^a_{\mathrm{m_L}} - Q^b_{\mathrm{m_L}} - Q^d_{\mathrm{m_L}}\right) + Q^a_1 - Q^b_2 + Q^c_1 - Q^d_2, \tag{4.74b}$$

$$\epsilon^3 \frac{\mathrm{d}B_i}{\mathrm{d}t} = Q^a_i - Q^a_{i-1} + Q^b_i - Q^b_{i+1} + Q^c_i - Q^c_{i-1} + Q^d_i - Q^d_{i+1}, \tag{4.74c}$$

$$\text{for} \quad i = 2, \ldots, K-2,$$

$$\epsilon^3 \frac{\mathrm{d}B_K}{\mathrm{d}t} = -(Q^c_{\mathrm{m_R}} - Q^b_{\mathrm{m_R}} - Q^d_{\mathrm{m_R}}) - Q^a_{K-1} + Q^b_K - Q^c_{K-1} + Q^d_K, \tag{4.74d}$$

$$\epsilon^3 \frac{\mathrm{d}\Gamma_{\mathrm{R}}}{\mathrm{d}t} = 2(Q^c_{\mathrm{m_R}} - Q^b_{\mathrm{m_R}} - Q^d_{\mathrm{m_R}}), \tag{4.74e}$$

where the fluxes Q^a_i, Q^b_i, Q^c_i, and Q^d_i are given in (4.17e)–(4.17h) and the remaining

fluxes are defined as follows

$$\begin{aligned}
Q^a_{\mathrm{m_L}} = \quad & \alpha_{\mathrm{m_L}} V^2_{\mathrm{m_L}} B_1 \;=\; \alpha_{\mathrm{m_L}} (1-\Gamma_{\mathrm{L}})^2 B_1, && \text{(4.75a)}\\
Q^b_{\mathrm{m_L}} = \quad & \beta_{\mathrm{m_L}} V_1 \Gamma_L^2 \;=\; \beta_{\mathrm{m_L}} \left(\Gamma_{\mathrm{L}} - B_1\right)^+ {\Gamma_{\mathrm{L}}}^2, && \text{(4.75b)}\\
Q^d_{\mathrm{m_L}} = \quad & \delta_{\mathrm{m_L}} H_1 \Gamma_L^2 \;=\; \delta_{\mathrm{m_L}} \left(B_2 - B_1\right)^+ {\Gamma_{\mathrm{L}}}^2, && \text{(4.75c)}\\
Q^b_{\mathrm{m_R}} = \quad & \beta_{\mathrm{m_R}} V_K \Gamma^2_{\mathrm{R}} \;=\; \beta_{\mathrm{m_R}} \left(B_{K-1} - B_K\right)^+ {\Gamma_{\mathrm{R}}}^2, && \text{(4.75d)}\\
Q^c_{\mathrm{m_R}} = \quad & \gamma_{\mathrm{m_R}} V^2_{\mathrm{m_R}} B_K = \gamma_{\mathrm{m_R}} \left(\Gamma^*_{\mathrm{sat}} - \Gamma_{\mathrm{R}}\right)^2 B_K, && \text{(4.75e)}\\
Q^d_{\mathrm{m_R}} = \quad & \delta_{\mathrm{m_R}} H_K \Gamma^2_{\mathrm{R}} \;=\; \delta_{\mathrm{m_R}} \left(\Gamma_{\mathrm{R}} - B_K\right)^+ {\Gamma_{\mathrm{R}}}^2, && \text{(4.75f)}\\
Q^a_1 = \quad & \alpha_1 V_1 B_2 \;=\; \alpha_1 (\Gamma_{\mathrm{L}} - B_1)^+ B_2, && \text{(4.75g)}\\
Q^d_K = \quad & \delta_K H_K B_{K-1} = \delta_K \left(\Gamma_{\mathrm{R}} - B_K\right)^+ B_{K-1}, && \text{(4.75h)}
\end{aligned}$$

where $\Gamma^*_{\mathrm{sat}} = \Gamma_{\mathrm{R_{sat}}}/\Gamma_{\mathrm{L_{sat}}} \leq 1$.

The initial conditions are given by

$$\Gamma_{\mathrm{L}}(0) = \Gamma_{\mathrm{L}_0}, \quad \Gamma_{\mathrm{R}}(0) = \Gamma_{\mathrm{R}_0} \quad \text{and} \quad B_i(0) = B_{i_0}, \quad \text{for} \quad i = 1, \ldots, K. \tag{4.76}$$

The conservation-of-mass equation can be derived by summing (4.74a)–(4.74e) and integrating to give

$$\mathcal{S} = \Gamma_{\mathrm{L}} + \Gamma_{\mathrm{R}} + 2\sum_{i=1}^{K} B_i, \tag{4.77}$$

where as before $\mathcal{S}$ is the total concentration of surfactant in the system.

4.4.1.1 Steady-state solutions

To determine the steady-state solution to (4.74) we first define

$$J_i = Q^a_i - Q^b_{i+1} + Q^c_i - Q^d_{i+1}, \quad \text{for} \quad i = 1, \ldots K-1. \tag{4.78}$$

Then on setting all the time derivatives to zero in (4.74) we have that

$$0 = Q^a_{\mathrm{m_L}} - Q^b_{\mathrm{m_L}}, \tag{4.79a}$$
$$0 = Q^c_{\mathrm{m_R}} - Q^d_{\mathrm{m_R}}, \tag{4.79b}$$
$$0 = J_i, \qquad \text{for} \quad i = 1, \dots K-1. \tag{4.79c}$$

From (4.79a) and (4.79b) we find that

$$B_1 = \Gamma_{\mathrm{L}} \frac{\Gamma_{\mathrm{L}}^2}{\alpha^*(1-\Gamma_{\mathrm{L}})^2 + \Gamma_{\mathrm{L}}^2} \quad \text{and} \quad B_K = \Gamma_{\mathrm{R}} \frac{\Gamma_{\mathrm{R}}^2}{\gamma^*(\Gamma^*_{\mathrm{sat}} - \Gamma_{\mathrm{R}})^2 + \Gamma_{\mathrm{R}}^2}, \tag{4.80}$$

respectively, where $\alpha^* = \alpha_{\mathrm{m_L}}/\beta_{\mathrm{m_L}}$ and $\gamma^* = \gamma_{\mathrm{m_R}}/\delta_{\mathrm{m_R}}$.

As in §4.2.3 we make an assumption on the relative sizes of the B_i's in order to obtain expressions for the steady-state solution. Now let us suppose that there exists an n such that

$$(B_{i-1} - B_i) \begin{cases} > 0, & i = 2, \dots, n, \\ < 0, & i = n+1, \dots, K, \end{cases} \tag{4.81}$$

as shown in Figure 4.16(a). Similarly we could suppose there exists an n such that

$$(B_{i-1} - B_i) \begin{cases} > 0, & i = 2, \dots, n, \\ = 0, & i = n+1, \\ < 0, & i = n+2, \dots, K, \end{cases} \tag{4.82}$$

as shown in Figure 4.16(b).

We first consider the case (4.81), then on setting $i = n-1$ and $i = n$ in (4.79c) and rearranging we have that

$$B_n = \frac{B_{n-1}(B_{n-1} + B_{n+1})}{B_{n-1} + B_{n-2}} = \frac{B_{n+1}(B_{n-1} + B_{n+1})}{B_{n+1} + B_{n+2}}. \tag{4.83}$$

Similarly, we can determine recurrence relations for the B_i's from (4.79c) and hence

$$B_i = \begin{cases} \dfrac{B_{i-1}^2}{B_{i-2}}, & i = 2, \dots, n-1, \\ \dfrac{B_{i-1}(B_{i-1} + B_{i+1})}{B_{i-1} + B_{i-2}}, & i = n, \\ \dfrac{B_{i+1}^2}{B_{i+2}}, & i = n+1, \dots, K-1, \end{cases} \tag{4.84}$$

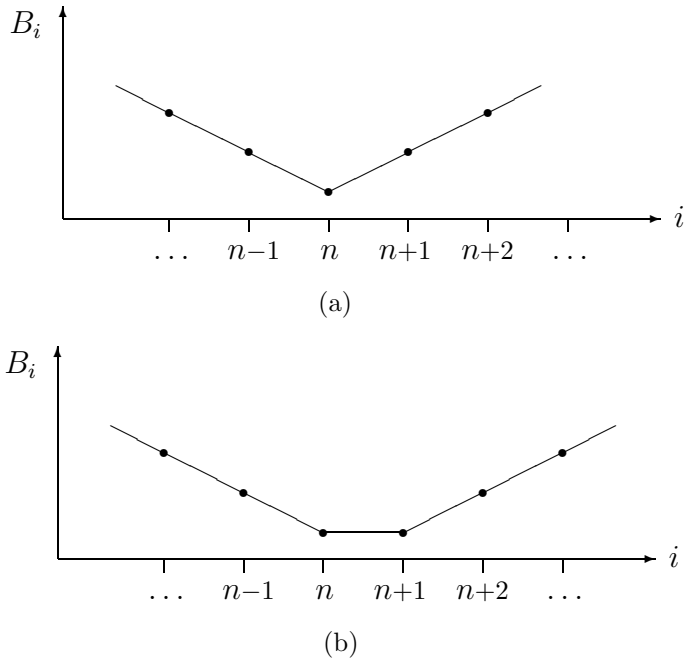

Figure 4.16: Schematic of steady-state set up for (a) n defined by (4.81) and (b) defined by (4.82).

where $B_0 := \Gamma_{\mathrm{L}}$ and $B_{K+1} := \Gamma_{\mathrm{R}}$. Using (4.80) we may re-write (4.84) as

$$B_i = \begin{cases} \Gamma_{\mathrm{L}}\Lambda_{\mathrm{L}}^i, & i = 1, \ldots, n-1, \\ B_n, & i = n, \\ \Gamma_{\mathrm{R}}\Lambda_{\mathrm{R}}^{K+1-i}, & i = n+1, \ldots, K, \end{cases} \tag{4.85}$$

where Λ_{L} and Λ_{R} are defined by

$$\Lambda_{\mathrm{L}} = \frac{\Gamma_{\mathrm{L}}^2}{\alpha^*(1-\Gamma_{\mathrm{L}})^2 + \Gamma_{\mathrm{L}}^2} \quad \text{and} \quad \Lambda_{\mathrm{R}} = \frac{\Gamma_{\mathrm{R}}^2}{\gamma^*(\Gamma_{\mathrm{sat}}^* - \Gamma_{\mathrm{R}})^2 + \Gamma_{\mathrm{R}}^2}. \tag{4.86}$$

From (4.83) and (4.85) it follows that $\Lambda_{\mathrm{L}} = \Lambda_{\mathrm{R}} = \Lambda$ and so we now write the expression for the B_i's as

$$B_i = \begin{cases} \Gamma_{\mathrm{L}}\Lambda^i, & i = 1, \ldots, n-1, \\ \dfrac{1}{1+\Lambda}\left(\Gamma_{\mathrm{L}}\Lambda^i + \Gamma_{\mathrm{R}}\Lambda^{K-i+1}\right), & i = n, \\ \Gamma_{\mathrm{R}}\Lambda^{K+1-i}, & i = n+1, \ldots, K. \end{cases} \tag{4.87}$$

Thus, the concentration of surfactant at the right surface, Γ_{R}, may be written in terms of the concentration at the left surface, Γ_{L}, by

$$\Gamma_{\mathrm{R}} = \Gamma^*_{\mathrm{sat}} \left(\frac{-\gamma^* \Gamma_{\mathrm{L}}^2 \pm \sqrt{\alpha^* \gamma^*} \Gamma_{\mathrm{L}} (1 - \Gamma_{\mathrm{L}})}{\alpha^* (1 - \Gamma_{\mathrm{L}})^2 - \gamma^* {\Gamma_{\mathrm{L}}}^2} \right), \tag{4.88}$$

and so the conservation-of-mass equation (4.77) reduces to

$$\mathcal{S} = \Gamma_{\mathrm{L}} + \Gamma_{\mathrm{R}} + \frac{\Lambda^n}{1+\Lambda} \left(\Gamma_{\mathrm{L}} + \Gamma_{\mathrm{R}} \Lambda^{K-2n+1} \right) + 2\Gamma_{\mathrm{L}} \sum_{i=1}^{n-1} \Lambda^i + 2\Gamma_{\mathrm{R}} \sum_{i=1}^{K-n} \Lambda^i. \tag{4.89}$$

The problem has now been reduced to one equation, (4.89), for two unknowns, Γ_{L} and n, and so we require one additional equation to close the system. This is possible by noting that n may be determined by the continuity of B_i on either side of $i = n$. Hence, n is the nearest integer where these two solutions coincide, *i.e.*

$$n = \left\lfloor \frac{1}{2} \left(K + 1 + \frac{\log(\Gamma_{\mathrm{R}}/\Gamma_{\mathrm{L}})}{\log(\Lambda)} \right) + \frac{1}{2} \right\rfloor. \tag{4.90}$$

For the situation where the two boundaries have the same physical properties we set $\Gamma^*_{\mathrm{sat}} = 1$ and $\alpha^* = \gamma^*$ in (4.88) and so Γ_{R} may be written as a function of Γ_{L}:

$$\text{either} \quad \Gamma_{\mathrm{R}} = \Gamma_{\mathrm{L}}, \tag{4.91a}$$

$$\text{or} \quad \Gamma_{\mathrm{R}} = \frac{\Gamma_{\mathrm{L}}}{2\Gamma_{\mathrm{L}} - 1}, \tag{4.91b}$$

where the second of these two solutions can be neglected since we require that $0 < \Gamma_{\mathrm{L}}, \Gamma_{\mathrm{R}} < 1$. Moreover, by the definition of B_n, K must be odd and by (4.90) it follows that

$$n = (K+1)/2. \tag{4.92}$$

Thus, the conservation-of-mass equation (4.77) reduces to an implicit equation for Γ_{L} is given by

$$\frac{\mathcal{S}}{2} = \Gamma_{\mathrm{L}} \left(\frac{1+\Lambda}{1-\Lambda} - \frac{4\Lambda^{(K+3)/2}}{1-\Lambda^2} \right). \tag{4.93}$$

In Figure 4.17 the blue curves show the solution, Γ_{L}, of (4.93) as the total surfactant concentration, $\mathcal{S}$, varies for different values of α^*. As we expect the concentration of adsorbed surfactant saturates to 1 suggesting that (4.93) is an adsorption isotherm for the semi-discrete model.

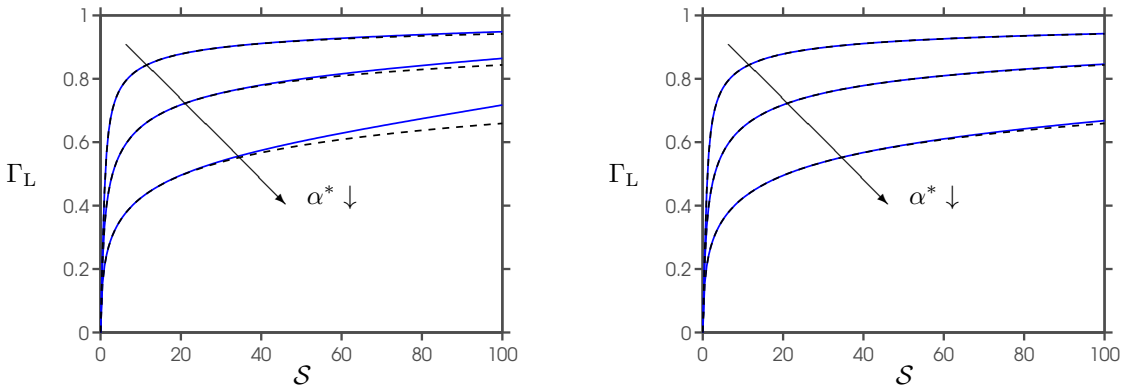

(a) $K = 99$ (b) $K = 199$

Figure 4.17: Comparison of the exact solution, Γ_L, of (4.93) (blue lines), for (a) $K = 99$ and (b) $K = 199$, with the solution in the limit $K \to \infty$ given in (4.94) (black dashed lines) for $\alpha = 0.1, 1, 10$.

If the distance between the two adsorbing boundaries is increased, equivalently taking the limit $K \to \infty$ (*i.e.* let $L \to \infty$ with h fixed) in (4.93), the limiting case would be that there is one adsorbing boundary in a semi-infinite domain. The result of taking such a limit in (4.93) is the cubic equation

$$\alpha^* \left(\Gamma_L - \frac{\mathcal{S}}{2} \right) (1 - \Gamma_L)^2 + 2\Gamma_L^3 = 0, \tag{4.94}$$

which is equivalent to (4.22) derived for the single adsorbing boundary in a semi-infinite domain in steady state with $\Gamma \to \Gamma_L$ and $\mathcal{S} \to \mathcal{S}/2$. The solution to (4.94) is plotted by the black dashed curves in Figure 4.17 for different values of α^* and it shows that the agreement between the solutions to (4.93) and (4.94) improves as K increases.

Repeating the earlier analysis for the case (4.82) gives the steady-state solution

$$B_i = \begin{cases} \Gamma_L \Lambda^i, & i = 1, \ldots, n-1, \\ \Gamma_L \Lambda^n = \Gamma_R \Lambda^{K-n}, & i = n, n+1, \\ \Gamma_R \Lambda^{K+1-i}, & i = n+2, \ldots, K, \end{cases} \tag{4.95}$$

where Λ is defined as above in (4.86) and Γ_R is a function of Γ_L as given by (4.88).

The conservation-of-mass equation (4.77) now reads

$$\mathcal{S} = \Gamma_{\mathrm{L}} + \Gamma_{\mathrm{R}} + 4\Gamma_{\mathrm{L}}\Lambda^n + 2\Gamma_{\mathrm{L}}\sum_{i=1}^{n-1}\Lambda^i + 2\Gamma_{\mathrm{R}}\sum_{i=1}^{K-n-1}\Lambda^i, \tag{4.96}$$

where n is defined by

$$n = \left\lfloor \frac{1}{2}\left(K + \frac{\log(\Gamma_{\mathrm{R}}/\Gamma_{\mathrm{L}})}{\log(\Lambda)}\right) + \frac{1}{2}\right\rfloor. \tag{4.97}$$

Note that, for identical adsorbing surfaces K must be even and so $n = K/2$.

4.4.1.2 Numerical solutions

In this section we compute the solutions to the system of ordinary-differential equations (4.74) using Matlab's inbuilt solver `ode45` for the parameters $K = 100$, $\alpha_{\mathrm{m_L}} = 2$, $\gamma_{\mathrm{m_L}} = 2$, and $\alpha_i = \beta_i = \gamma_i = \delta_i = \beta_{\mathrm{m_{L,R}}} = \delta_{\mathrm{m_{L,R}}} = 1$. We investigate three possible scenarios for the initial distribution of bilayers below. We note that the first two scenarios we consider are the same as those described in §4.2.4, so we omit the justification for them but shall compare the results of the two models.

1. We consider an initial distribution of surfactant adsorbed to only one surface as described earlier in §4.2.4, point 1, which for the two-adsorbing-boundary model gives the initial conditions:

$$\Gamma_{\mathrm{L}_0} = 1, \quad \Gamma_{\mathrm{R}_0} = \Gamma_{\mathrm{L}_0}\mathrm{e}^{-(\frac{K}{\sigma(K+1)})^2}, \quad B_{i_0} = \Gamma_{\mathrm{L}_0}\mathrm{e}^{-(\frac{i}{\sigma(K+1)})^2}, \quad \text{for} \quad i = 1, \ldots, K. \tag{4.98}$$

   The results are shown in Figure 4.18. We observe that for small time the monotonic evolution of the bilayers is qualitatively the same for the one-adsorbing-boundary problem, see Figure 4.18(a). However, when a significant accumulation of surfactant reaches the second adsorbing boundary it starts to form a monolayer on the adsorbing boundary on the other surface, as shown in Figure 4.18(b), and the distribution of bilayers becomes non-monotonic. The distribution then evolves smoothly to the steady-state solution denoted by the green curve in Figure 4.18(c). Throughout the evolution surfactant continues to be drawn from the adsorbing surface at $x = 0$ until the adsorbing surfaces reach an equilibrium with each other as shown by the plots of Γ_{L} and Γ_{R} in Figure 4.18(d).

If instead we assumed that the multilayer adsorbed to the surface at $x = 0$ is in equilibrium, *i.e.* is given by the steady-state solution given in §4.2.3, and suppose that the boundary at $x = 1$ is instantaneously switched on at $t = 0$ we observe very similar dynamics to those above. The resulting evolution is plotted in Figure 4.19.

2. We next consider the initial state where the bilayers are distributed randomly as shown in Figure 4.20(a). Figures 4.20(b)–4.20(e) shows the evolution of the distribution of bilayers at different time intervals and we note that the solutions exhibit 'smooth humps' and 'sharp troughs' similar to those for the one-adsorbing-boundary model shown in Figure 4.6. Figure 4.20(f) shows the evolution of the adsorbed concentration with time.

3. Finally, we consider the case where the two adsorbing boundaries have different saturation concentrations and set $\Gamma^*_{\text{sat}} = 0.8$. We prescribe quadratic initial conditions to model a set-up where two multilayers are adsorbed to either boundary and connected to each other with the quadratic:

$$\Gamma_{\text{L}_0} = B_0 + s_0^2, \quad \Gamma_{\text{R}_0} = B_0 + (1 - s_0)^2, \tag{4.99a}$$

$$B_{i_0} = B_0 + \left(\frac{i}{K+1} - s_0\right)^2, \quad \text{for} \quad i = 1, \ldots, K. \tag{4.99b}$$

The numerical solutions are plotted in Figure 4.21. We observe that a single 'sharp trough' or corner appears to form instantaneously from the smooth initial conditions which persists as t increases and is present in the initial condition plotted by the green curve in Figure 4.21(d). We shall consider the formation of such a corner in more detail by considering the small-time approximation to the macroscopic model in §4.4.2.3.

The temporal evolution of the B_i's shown in Figures 4.18–4.21 is similar to that for the one-absorbing-boundary model in that there is an almost smooth transition to a steady distribution indicating that a continuum approximation will be valid to derive a macroscopic model for the distribution of bilayers. We do this in the following section. The main difference between the the mesoscopic models for the one- and two-adsorbing-surfaces problems is that the steady-state solution for the latter case is not monotonic with depth. Thus, the evolution of the multilayer for the two-adsorbing-surfaces problem is non-monotonic in general and the $\text{sgn}(B_x)$ term in the

macroscopic model will be of greater significance than in the one-adsorbing-surface case.

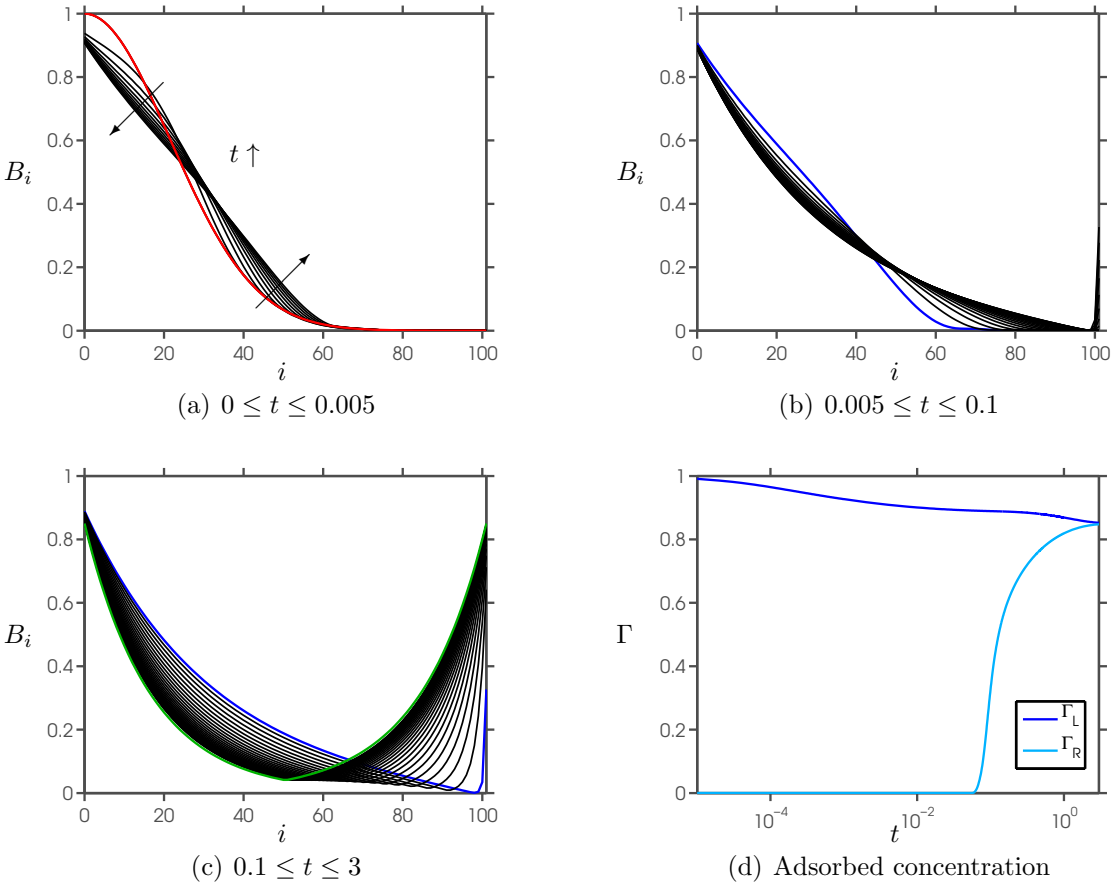

(a) $0 \leq t \leq 0.005$ (b) $0.005 \leq t \leq 0.1$

(c) $0.1 \leq t \leq 3$ (d) Adsorbed concentration

Figure 4.18: Plots of the numerical solutions to the system of ordinary differential equations (4.74) (black curves) subject to the initial conditions (4.98) (red curve) for times (a) $t \in [0.001, .002, \ldots, 0.005]$; (b) $t \in [0.005, 0.01, \ldots, 0.1]$; (c) $t \in [0.1, 0.2, \ldots, 3]$. In Figures (b) and (c) the blue curves denote the solution at the start of the time interval and the green curve in Figure (c) denotes the steady-state solution. Figure (d) shows the evolution of the adsorbed concentrations Γ_{L} and Γ_{R} with time. The parameters used are $\Gamma^*_{\mathrm{sat}} = 1$, $\alpha_i = \beta_i = \Gamma_i = \delta_i = \beta_{\mathrm{m_{L,R}}} = \delta_{\mathrm{m_{L,R}}} = 1$, $\alpha_{\mathrm{m_L}} = \gamma_{\mathrm{m_R}} = 2$.

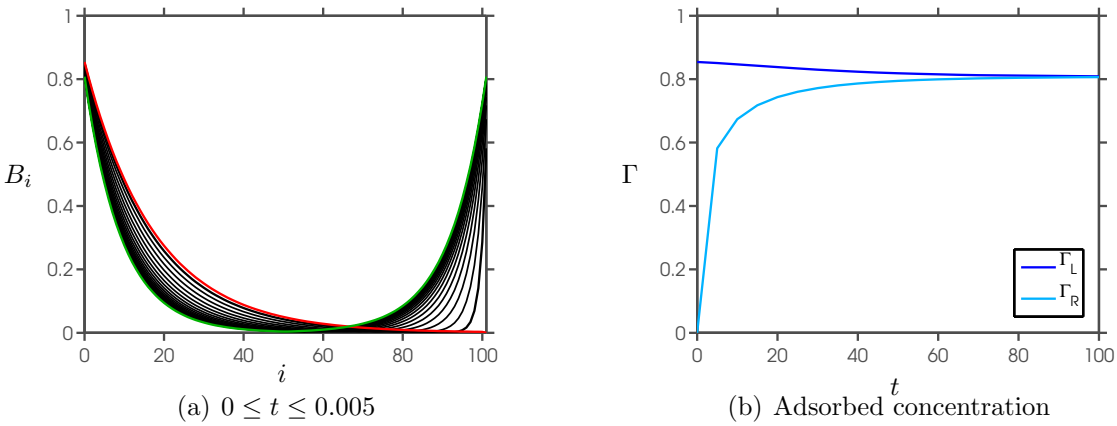

(a) $0 \leq t \leq 0.005$ (b) Adsorbed concentration

Figure 4.19: Plots of the numerical solutions to the system of ordinary differential equations (4.74) (black curves) subject to the initial conditions given by the steady-state solution (4.21) (red curve) for $\mathcal{S} = 2$ and the steady-state solution (green curve) for times (a) $t \in [0, 5, \ldots, 100]$. (b) Plots of the evolution of the adsorbed concentrations Γ_{L} and Γ_{R} with time. The parameters used are $\Gamma^*_{\mathrm{sat}} = 1$, $\alpha_i = \beta_i = \Gamma_i = \delta_i = \beta_{\mathrm{m_{L,R}}} = \delta_{\mathrm{m_{L,R}}} = 1$, $\alpha_{\mathrm{m_L}} = \gamma_{\mathrm{m_R}} = 2$.

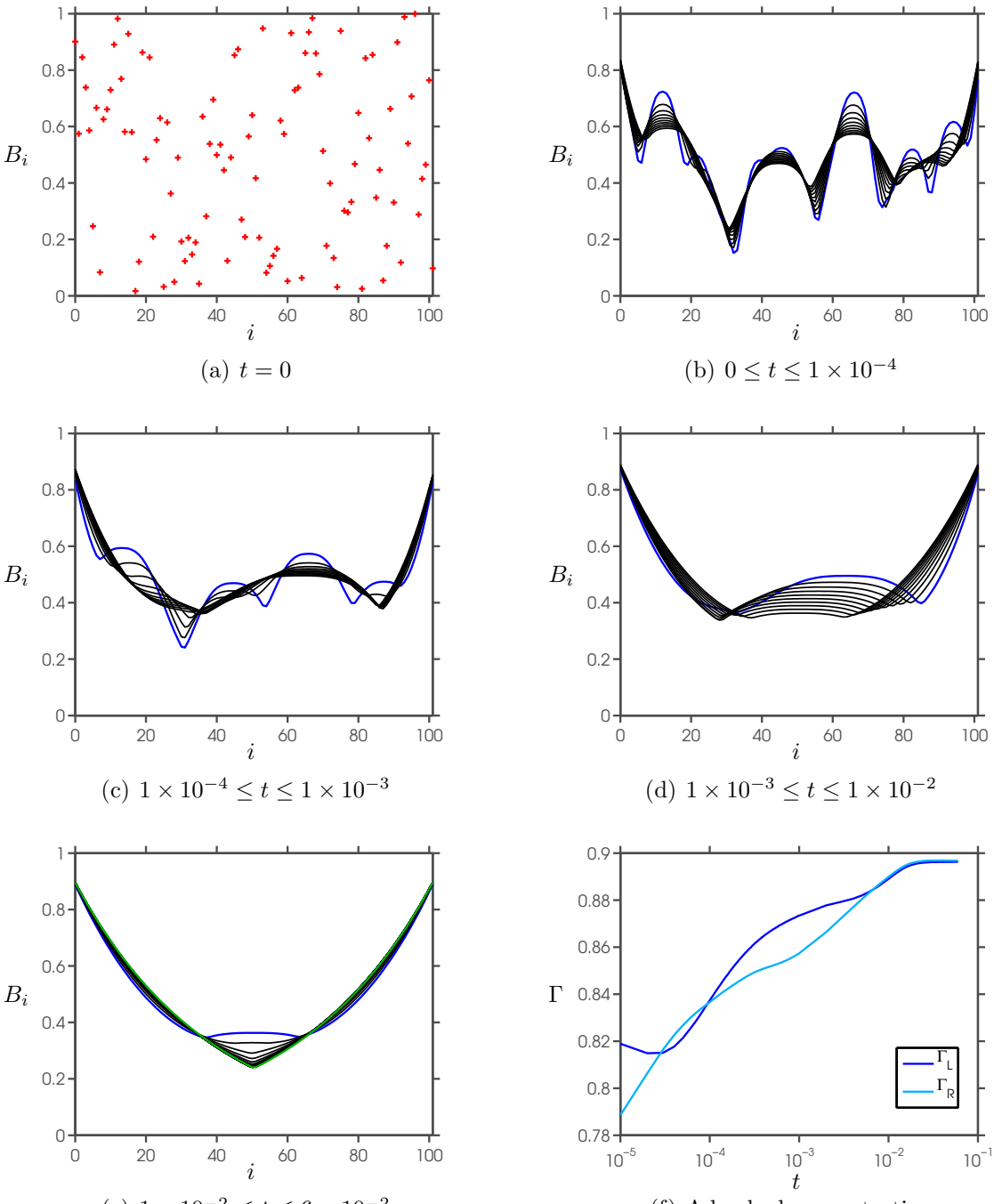

(a) $t = 0$

(b) $0 \leq t \leq 1 \times 10^{-4}$

(c) $1 \times 10^{-4} \leq t \leq 1 \times 10^{-3}$

(d) $1 \times 10^{-3} \leq t \leq 1 \times 10^{-2}$

(e) $1 \times 10^{-2} \leq t \leq 6 \times 10^{-2}$

(f) Adsorbed concentration

Figure 4.20: Plots of the numerical solutions to the system of ordinary differential equations (4.74) (black curves) subject to (a) random initial conditions and for time increments: (b) $dt = 10^{-5}$; (c) $dt = 10^{-4}$; (d) $dt = 10^{-3}$; (e) $dt = 2 \times 10^{-3}$ and in these plots the blue curves denote the solution at the start of the time interval. In Figure (e) the green curve denotes the steady-state solution. Figure (f) shows the evolution of the adsorbed concentrations Γ_{L} and Γ_{R} with time. The parameters used are $\Gamma^*_{\mathrm{sat}} = 1$, $\alpha_i = \beta_i = \Gamma_i = \delta_i = \beta_{\mathrm{m_{L,R}}} = \delta_{\mathrm{m_{L,R}}} = 1$, $\alpha_{\mathrm{m}_L} = \gamma_{\mathrm{m_R}} = 2$.

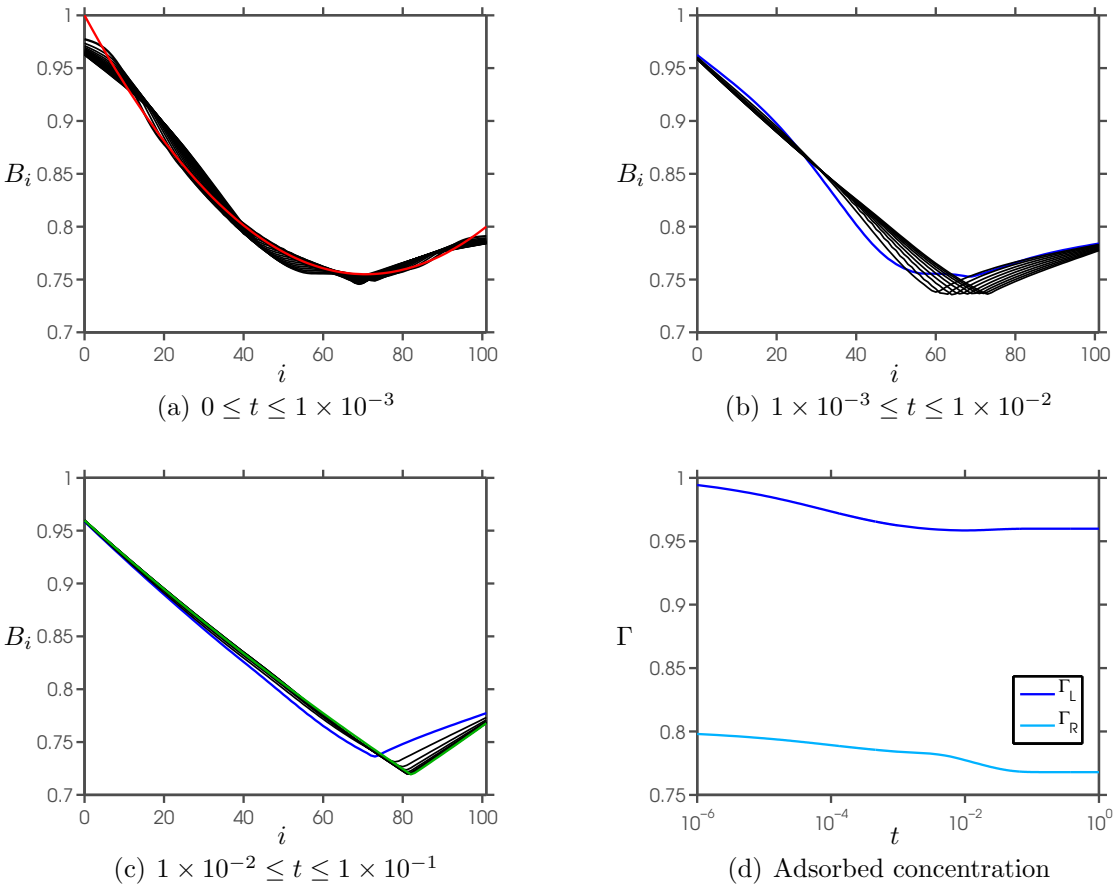

(a) $0 \leq t \leq 1 \times 10^{-3}$

(b) $1 \times 10^{-3} \leq t \leq 1 \times 10^{-2}$

(c) $1 \times 10^{-2} \leq t \leq 1 \times 10^{-1}$

(d) Adsorbed concentration

Figure 4.21: Plots of the numerical solutions to the system of ordinary differential equations (4.74) (black curves) subject to initial conditions (4.99) which are denoted by the red curve in Figure (a). The numerical solutions are plotted for time increments: (a) $dt = 10^{-5}$; (b) $dt = 10^{-4}$; (c) $dt = 10^{-3}$ and in Figures (b) and (c) the blue curves denote the solution at the start of the time interval. The green curve in Figure (c) denotes the steady-state solution. Figure (f) shows the evolution of the adsorbed concentrations Γ_{L} and Γ_{R} with time. The parameters used are $\Gamma^*_{\mathrm{sat}} = 0.8$, $B_0 = 0.755$, $s_0 = 0.7$, $\alpha_i = \beta_i = \Gamma_i = \delta_i = \beta_{m_{L,R}} = \delta_{m_{L,R}} = 1$, $\alpha_{m_L} = \gamma_{m_L} = 2$.

4.4.2 Macroscopic model

Through the same analysis of §4.3 one can derive the PDE (4.31) from equations (4.74) but with new boundary conditions:

$$\frac{\partial B}{\partial t} = \frac{\partial}{\partial x}\left(\alpha(x)\mathrm{sgn}(B_x)\left({B_x}^2 - BB_{xx}\right)\right), \quad 0 < x < 1, \quad 0 < t, \tag{4.100a}$$

subject to zero flux boundary conditions

$${B_x}^2 - BB_{xx} = 0, \quad \text{on} \quad x = 0, 1, \tag{4.100b}$$

and adsorbing boundary conditions

$$B(0,t) = \Gamma_{\mathrm{L}}, \quad \text{and} \quad B(1,t) = \Gamma_{\mathrm{R}}. \tag{4.100c}$$

The possible adsorbed concentrations Γ_{L} and Γ_{R} are given by

$$\text{either} \qquad \Gamma_{\mathrm{L}} = 1, \qquad \text{if} \quad \alpha_{\mathrm{m_L}}, \beta_{\mathrm{m_L}}, \delta_{\mathrm{m_L}} = O(1), \tag{4.101a}$$

$$\text{or} \qquad \frac{\mathrm{d}\Gamma_{\mathrm{L}}}{\mathrm{d}t} = 2\bar{\alpha}_{\mathrm{m_L}}(1-\Gamma_{\mathrm{L}})^2\Gamma_{\mathrm{L}}, \qquad \text{if} \quad \alpha_{\mathrm{m_L}}, \beta_{\mathrm{m_L}}, \delta_{\mathrm{m_L}} = O(\epsilon^3), \tag{4.101b}$$

where $\bar{\alpha}_{\mathrm{m_L}} = \epsilon^3\alpha_{\mathrm{m_L}}$ and

$$\text{either} \qquad \Gamma_{\mathrm{R}} = \Gamma^*_{\mathrm{sat}}, \qquad \text{if} \quad \gamma_{\mathrm{m_R}}, \beta_{\mathrm{m_R}}, \delta_{\mathrm{m_R}} = O(1), \tag{4.102a}$$

$$\text{or} \qquad \frac{\mathrm{d}\Gamma_{\mathrm{R}}}{\mathrm{d}t} = 2\bar{\gamma}_{\mathrm{m_R}}\left(\Gamma^*_{\mathrm{sat}} - \Gamma_{\mathrm{R}}\right)^2\Gamma_{\mathrm{R}}, \qquad \text{if} \quad \gamma_{\mathrm{m_R}}, \beta_{\mathrm{m_R}}, \delta_{\mathrm{m_R}} = O(\epsilon^3), \tag{4.102b}$$

where $\bar{\gamma}_{\mathrm{m_R}} = \epsilon^3\gamma_{\mathrm{m_R}}$.

Note that there are now four boundary conditions (4.100b)–(4.100c) for (4.100) rather than three.[2] Thus, the problem (4.100) is over-prescribed unless there exists a free boundary, at say $x = s(t)$, where B changes sign. We then require three more conditions to close the system and determine $s(t)$. One of the conditions is that $B(x,t)$ is continuous across $x = s(t)$, *i.e.*

$$[B]^+_- = 0, \tag{4.103}$$

[2] In general, we need two boundary conditions at an interface where $\mathbf{n}\cdot\nabla B > 0$, and one where $\mathbf{n}\cdot\nabla B < 0$.

where the square brackets, $[\cdot]_-^+$, denote the jump in the expression across the curve $x = s(t)$. The second condition on $x = s(t)$ is derived by approximating

$$B_n(t) \approx B(s(t), t), \quad s(t) = n(t)\epsilon, \tag{4.104}$$

where $n \in \mathbb{Z}^+$, and expanding the ODE for B_n from the semi-discrete model that is given by

$$\begin{aligned}
\epsilon^3 \frac{\mathrm{d}B_n}{\mathrm{d}t} &= J_n - J_{n-1} \\
&= \alpha_n B_{n+1} \left((B_{n-1} - B_n)^+ + (B_{n+1} - B_n)^+ \right) \\
&\quad - \alpha_{n+1} B_n \left((B_n - B_{n+1})^+ + (B_{n+2} - B_{n+1})^+ \right) \\
&\quad - \Big(\alpha_{n-1} B_n \left((B_{n-2} - B_{n-1})^+ + (B_n - B_{n-1})^+ \right) \\
&\quad - \alpha_n B_{n-1} \left((B_{n-1} - B_n)^+ + (B_{n+1} - B_n)^+ \right) \Big).
\end{aligned} \tag{4.105}$$

Assuming that the derivative of B changes sign across $x = s(t)$, there are four possibilities to consider near $i = n(t)$ as shown in Figure 4.22.

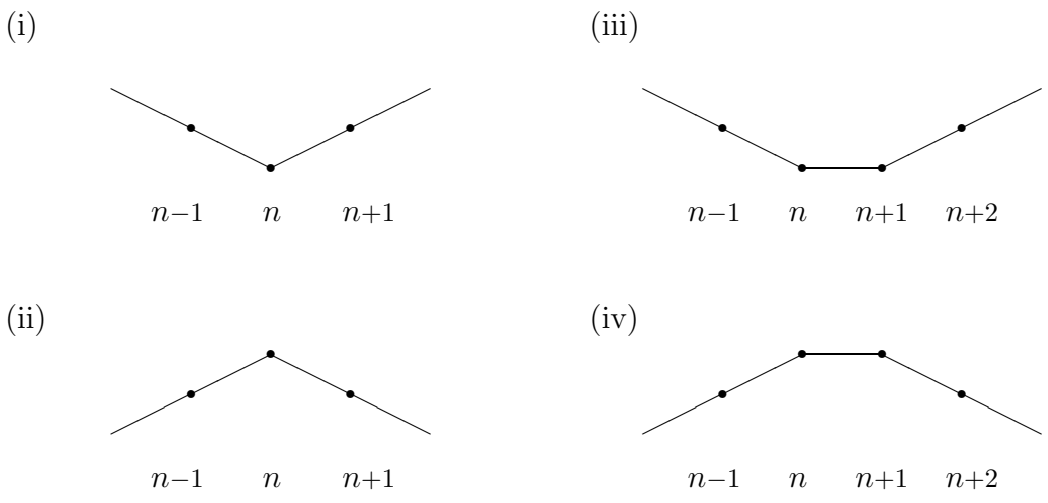

Figure 4.22: Schematic of $B(i\epsilon, t)$ near $i = n$.

For cases (i) and (ii) as depicted in Figure 4.22 we expand $B_{n\pm i}$ in the limit $\epsilon \to 0$ as follows

$$s = n\epsilon, \quad \epsilon = \frac{1}{K+2}, \tag{4.106a}$$

$$B_{n-i} = B(s) - i\epsilon B'_- + \frac{i^2\epsilon^2}{2}B''_- + \ldots, \qquad \text{for} \quad i = 1, 2, \tag{4.106b}$$

$$B_{n+i} = B(s) + i\epsilon B'_+ + \frac{i^2\epsilon^2}{2}B''_+ + \ldots, \qquad \text{for} \quad i = 2, 3, \tag{4.106c}$$

where $B_-(s)$ and $B_+(s)$ denote the limits of $B(x)$ as $x \uparrow s$ and $x \downarrow s$ respectively. Substituting into (4.105) we find that to leading order $[B_x]^+_- = 0$, which contradicts the assumption that B_x is discontinuous across $x = s(t)$. Thus, cases (i) and (ii) are not possible. For cases (iii) and (iv) $B_n = B_{n+1}$ and we consider the following expansions as $\epsilon \to 0$:

$$s = n\epsilon, \quad \epsilon = \frac{1}{K+2}, \tag{4.107a}$$

$$B_{n-i} = B(s) - i\epsilon B'_- + \frac{i^2\epsilon^2}{2}B''_- + \ldots, \qquad \text{for} \quad i = 1, 2, \tag{4.107b}$$

$$B_{n+i} = B(s) + (i-1)\epsilon B'_+ + \frac{(i-1)\epsilon^2}{2}B''_+ + \ldots, \qquad \text{for} \quad i = 2, 3. \tag{4.107c}$$

Substituting into (4.105) we find that to leading order

$$[|B_x|]^+_- = 0. \tag{4.108}$$

Finally, if we consider the sum of (4.74c) for $i = n-1, n, n+1, n+2$ we have that

$$\frac{\mathrm{d}}{\mathrm{d}t}\left(B_{n-1} + B_n + B_{n+1} + B_{n+2}\right) = J_{n+2} - J_{n-2}, \tag{4.109}$$

and substituting the expansions (4.107) we find that to leading order

$$\left[\alpha(x)\mathrm{sgn}(B_x)(B_x^2 - BB_{xx})\right]^+_- = 0, \tag{4.110}$$

which now closes the problem.

In summary, the implicit free-boundary problem that describes the re-arrangement of bilayers in a multilayer structure is:

$$\frac{\partial B}{\partial t} = -\frac{\partial}{\partial x}\left(\alpha(x)\left({B_x}^2 - BB_{xx}\right)\right), \quad 0 < x < s(t), \quad 0 < t, \tag{4.111a}$$

$$\frac{\partial B}{\partial t} = \frac{\partial}{\partial x}\left(\alpha(x)\left({B_x}^2 - BB_{xx}\right)\right), \quad s(t) < x < 1, \quad 0 < t, \tag{4.111b}$$

$$B = \Gamma_{\mathrm{L}}, \qquad {B_x}^2 - BB_{xx} = 0, \qquad \text{on} \quad x = 0, \tag{4.111c}$$

$$B = \Gamma_{\mathrm{R}}, \qquad {B_x}^2 - BB_{xx} = 0, \qquad \text{on} \quad x = 1, \tag{4.111d}$$

$$[B]_-^+ = [|B_x|]_-^+ = \left[\alpha(x)\mathrm{sgn}(B_x)(B_x^2 - BB_{xx})\right]_-^+ = 0, \quad \text{at} \quad x = s(t), \tag{4.111e}$$

$$B(x,0) = f(x), \tag{4.111f}$$

where Γ_{L} and Γ_{R} are given by the two possible expressions in (4.101) and (4.102) respectively and $f(x)$ is some given initial data.

4.4.2.1 Steady-state solution

The steady-state solution to (4.111) is defined as

$$B_0(x) = \begin{cases} B_1(x), & 0 \le x < s, \\ B_2(x), & s \le x \le 1, \end{cases} \tag{4.112}$$

where B_1 and B_2 satisfy

$$\left(\alpha(x)({B_1}'^2 - B_1 B_1'')\right)' = 0, \qquad 0 < x < s, \tag{4.113a}$$

$$\left(\alpha(x)({B_2}'^2 - B_2 B_2'')\right)' = 0, \qquad s < x < 1, \tag{4.113b}$$

$${B_1}'^2 - B_1 B_1'' = 0, \qquad B_1 = 1, \qquad \text{on} \quad x = 0, \tag{4.113c}$$

$${B_2}'^2 - B_2 B_2'' = 0, \qquad B_2 = \Gamma_{\mathrm{sat}}^*, \qquad \text{on} \quad x = 1, \tag{4.113d}$$

$$B_1 = B_2, \quad B_1' = -B_2', \qquad \text{on} \quad x = s, \tag{4.113e}$$

$$-({B_1}'^2 - B_1 B_1'') = {B_2}'^2 - B_2 B_2'', \qquad \text{on} \quad x = s. \tag{4.113f}$$

Thus, for the case where the two boundaries are identical, *i.e.* $\Gamma^*_{\rm sat} = 1$, the solution to (4.113) is given by

$$B_0(x) = \begin{cases} \mathrm{e}^{-kx}, & 0 \le x < 1/2, \\ \mathrm{e}^{-k(1-x)}, & 1/2 \le x \le 1, \end{cases} \tag{4.114a}$$

where $s = 1/2$ and k is given by the implicit equation

$$M = \frac{2}{k}\left(1 - \mathrm{e}^{-k/2}\right), \tag{4.114b}$$

where $M = \mathcal{S}/\epsilon = \int_0^1 f(x)\,\mathrm{d}x$.

For the case where the two boundaries are physically different, *i.e.* $\Gamma^*_{\rm sat} < 1$, the solution to (4.113a)–(4.113f) is now given by

$$B_0(x) = \begin{cases} {\Gamma^*_{\rm sat}}^{x/(2s-1)}, & 0 \le x < s, \\ {\Gamma^*_{\rm sat}}^{(2s-x)/(2s-1)}, & s \le x \le 1, \end{cases} \tag{4.115}$$

where s is given by the implicit equation

$$M = \frac{(2s-1)}{\log(\Gamma^*_{\rm sat})}\left(2{\Gamma^*_{\rm sat}}^{s/(2s-1)} - \Gamma^*_{\rm sat} - 1\right). \tag{4.116}$$

Moreover, since $\Gamma^*_{\rm sat} < 1$ (4.116) implies that $s > 1/2$ and in the limit $M \to 0$, with $\Gamma^*_{\rm sat}$ fixed, and $s \to 1/2$. Conversely, in the limit $s \to 1$ we find that the maximum total surfactant concentration is given by

$$M \sim \frac{1}{\log(\Gamma^*_{\rm sat})}\left(\Gamma^*_{\rm sat} - 1\right). \tag{4.117}$$

The above features of (4.116) are summarised in Figure 4.23. In Figure 4.23(a) we show total surfactant concentration, M, against s for different values of the saturation concentration, $\Gamma^*_{\rm sat}$. In Figure 4.23(b) we show the steady-state solution, $B_0(x)$, given in (4.115) for different values of M and $\Gamma^*_{\rm sat} = 0.8$. The discontinuity in B_0' at $x = s$ can be observed in Figure 4.23(b) and appears to vanish as $M \to 0$. The corresponding curve for the value of $\Gamma^*_{\rm sat}$ we will use in plotting Figure 4.23(b) is given by the red curve in Figure 4.23(a).

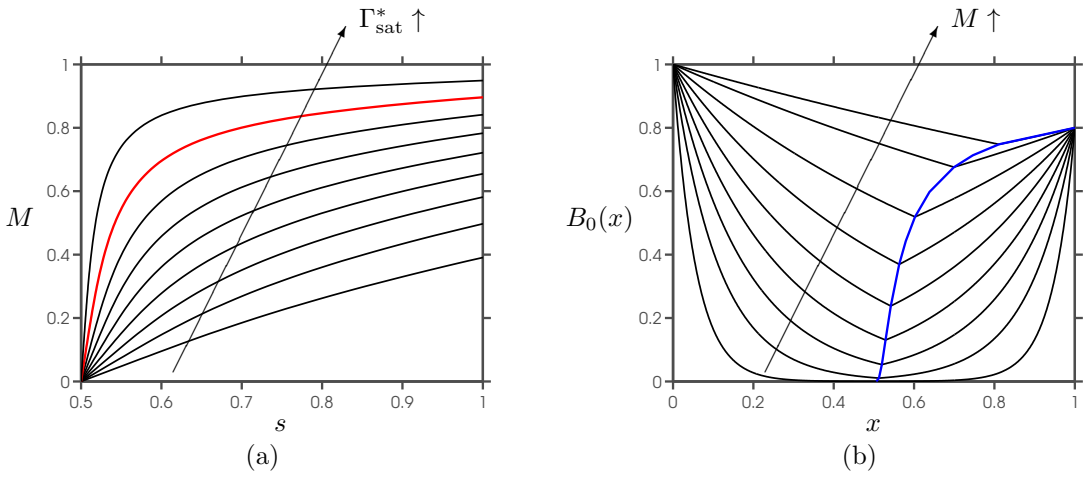

Figure 4.23: (a) Plots of total surfactant concentration, M, against s given by (4.116) for $\Gamma^*_{\text{sat}} \in [0.1, 0.2, \ldots, 0.9]$. The red curve denotes $\Gamma^*_{\text{sat}} = 0.8$. (b) The steady-state solution, $B_0(x)$, given by (4.115) are plotted by the black curves for $M \in [0.1, 0.2, \ldots, 0.8, 0.85]$, and $\Gamma^*_{\text{sat}} = 0.8$. The blue curve denotes $B_0(s)$.

4.4.2.2 Numerical solutions

For the simplest scenario possible we assume that the concentration of surfactant at the adsorbing boundaries is time independent and we set $\Gamma^*_{\text{sat}} = 1$. Then given symmetric initial conditions about $x = 1/2$ we have that $s = 1/2$ for all t. Thus, one can compute the solution for $x \in [0, 1/2]$ using the same numerical scheme as that detailed in §4.3.5.1, an example of such a solution is plotted in Figure 4.24.

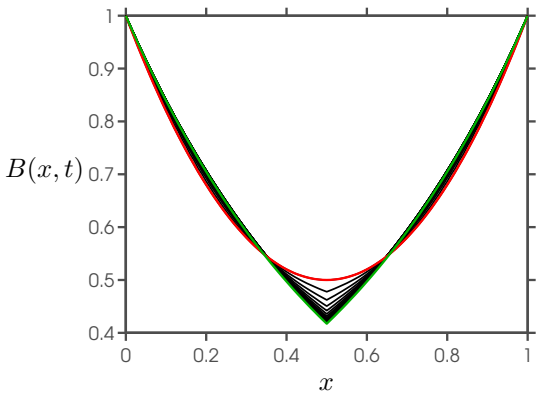

Figure 4.24: Plots of the numerical solution to (4.111) at times $t \in [0, 0.01, \ldots, 0.02]$ (black lines) with $\Gamma_{\text{L}} = \Gamma_{\text{R}} = 1$ and symmetric initial conditions (red line). The steady-state solution (4.114) is plotted by the green curve.

We now consider the more general problem where the adsorbed concentrations may vary with time and the initial conditions are arbitrary. We discuss and implement two approaches to solving (4.111) numerically.

The first approach is to reformulate the problem (4.111) to a fixed domain via the transformation:

$$0 < x < s(t): \qquad X = \frac{x}{s(t)}, \qquad B(x,t) = U(X,t), \tag{4.118a}$$

$$s(t) < x < 1: \qquad X = \frac{1-x}{1-s(t)}, \qquad B(x,t) = V(X,t). \tag{4.118b}$$

Substituting the above into (4.111) results in the problem given on $X \in [0,1]$:

$$\frac{\partial U}{\partial t} = \frac{1}{s(t)^3}\frac{\partial}{\partial X}\left(\operatorname{sgn}(U_X)\left({U_X}^2 - UU_{XX}\right)\right) + \frac{X}{s(t)}\frac{\mathrm{d}s}{\mathrm{d}t}U_X, \tag{4.119a}$$

$$\frac{\partial V}{\partial t} = -\frac{1}{(1-s(t))^3}\frac{\partial}{\partial X}\left(\operatorname{sgn}(-V_X)\left({V_X}^2 - VV_{XX}\right)\right) - \frac{X}{(1-s(t))}\frac{\mathrm{d}s}{\mathrm{d}t}V_X, \tag{4.119b}$$

$$U = \Gamma_{\mathrm{L}}, \quad V = \Gamma_{\mathrm{R}}, \qquad U_X^2 - UU_{XX} = V_X^2 - VV_{XX} = 0 \qquad \text{on} \quad X = 0, \tag{4.119c}$$

$$U = V, \qquad (s(t)-1)U_X = -s(t)V_X, \qquad \text{on} \quad X = 1, \tag{4.119d}$$

$$s(t)^2\left(V_X^2 - VV_{XX}\right) = -(s(t)-1)^2\left(U_X^2 - UU_{XX}\right) \qquad \text{on} \quad X = 1, \tag{4.119e}$$

with initial conditions

$$U(X,0) = f(s(0)X), \qquad V(X,0) = f(1 + (s(0)-1)X). \tag{4.119f}$$

The discretisation scheme for (4.119) which we shall implement later in this section is discussed in §C.2.2 of Appendix C and has a truncation error of order $\triangle X$, where $\triangle X$ is the step-size.

The second approach is to regularise the PDE (4.100a) by including the order ϵ term in the Taylor expansion from the derivation of the PDE and boundary conditions (4.100b) and (4.100c). The resulting equation is a is fourth-order hyperbolic PDE and so the boundary conditions at the free boundary are not required. The regularised problem is given by:

$$\frac{\partial B}{\partial t} = \frac{\partial}{\partial x}\left(\operatorname{sgn}(B_x)\left({B_x}^2 - BB_{xx}\right) + \epsilon\left(B_xB_{xx} - BB_{xxx}\right)\right), \quad 0 < x < 1, \quad 0 < t, \tag{4.120a}$$

$$B = \Gamma_{\mathrm{L}}, \quad \mathrm{sgn}(B_x)(B_x^2 - BB_{xx}) + \epsilon(B_xB_{xx} - BB_{xxx}) = 0, \qquad \text{on} \quad x = 0, \quad (4.120b)$$

$$B = \Gamma_{\mathrm{R}}, \quad \mathrm{sgn}(B_x)(B_x^2 - BB_{xx}) + \epsilon(B_xB_{xx} - BB_{xxx}) = 0, \qquad \text{on} \quad x = 1. \quad (4.120c)$$

The free boundary can now be tracked by solving numerically the regularised problem in the limit $\epsilon \to 0$.

Figures 4.25 and 4.26 show computed solutions for the two numerical schemes described above subject to the initial condition for the bilayer concentration

$$B(x, 0) = B_0 + \kappa(x - s_0)^2, \tag{4.121}$$

for parameters B_0, κ, and s_0 and for the first scheme we impose the initial condition on s:

$$s(0) = s_0. \tag{4.122}$$

Plots of the numerical solutions to the problem given in (4.119) for $B(x, t)$ are shown in Figure 4.25(a) and we observe that the solution evolves from the initial profile to the steady state with the persistence of a corner at the moving boundary $x = s(t)$. The corresponding plot for the evolution of the moving boundary is shown in Figure 4.25(b) and for large t there is excellent agreement with the steady-state solution. We also observe that for small t the moving boundary is almost stationary and we investigate the small-time dynamics of the problem in the following section.

For the regularised problem (4.120) we discretise using the method of lines, full details are presented in Appendix C, and note that the scheme has a truncation error of order $\triangle x$, where $\triangle x$ is the step-size. Plots of the bilayer concentration, $B(x, t)$, are shown in Figures 4.26(a) and 4.26(b) for $\epsilon = 0.1$ and 0.05. To compute these solutions we used a step-size $\triangle x = 0.005$. The evolution of the moving boundary with time is shown in Figure 4.27 for the case $\epsilon = 0.1$ and evolves to the steady state in an identical way to that for the problem given in (4.119) and shown in Figure 4.25(b). As we reduce ϵ from 0.1 to 0.05 we observe that the solution for large time (plotted by the blue curves) approaches the steady-state solution to the original problem (4.111) (plotted by the green curves). To improve the agreement between the numerical and the steady-state solutions one must reduce ϵ and also $\triangle x$ in order for the scheme to converge. However, for the discretisation scheme we have used the resulting system of ODEs is very stiff and so on reducing ϵ and $\triangle x$ appropriately the computation becomes very inefficient. Thus, we conclude that the first of the two approaches,

mapping the moving-boundary problem onto a fixed domain, is computationally more efficient for the same truncation errors.

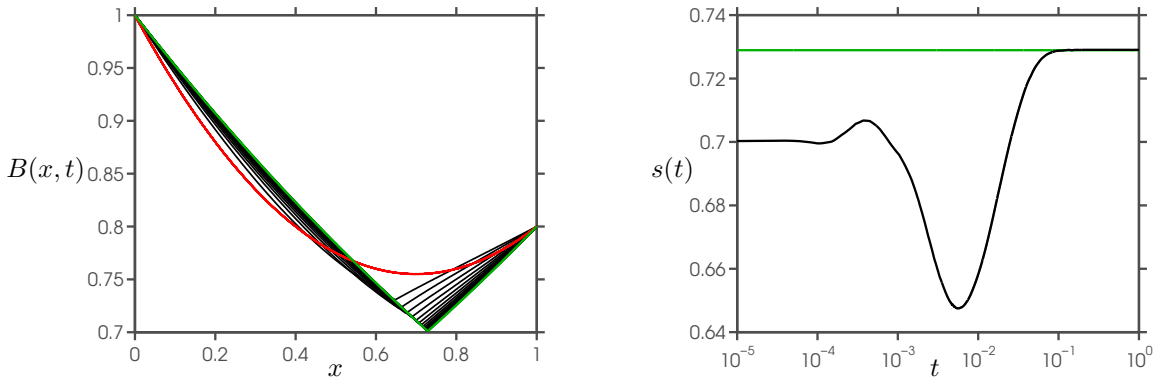

(a) (b)

Figure 4.25: Plots of the numerical solution to the macroscopic model for the two-adsorbing-surfaces problem given by (4.119) subject to the initial conditions (4.121) and (4.122) (red curve) and for space-step $\triangle X = 0.01$. Figure (a) shows plots of $B(x,t)$ at times $t \in [0.005, 0.01, \ldots, 0.1]$ (black curves) and the steady-state solution given by (4.115)–(4.116) is denoted by the green curve. The black curve in Figure (b) shows the evolution of the moving boundary $s(t)$ and compares it with the steady-state solution for s, denoted by the green curve. Parameters used are $B_0 = 0.755, \kappa = 0.5, and s_0 = 0.7$.

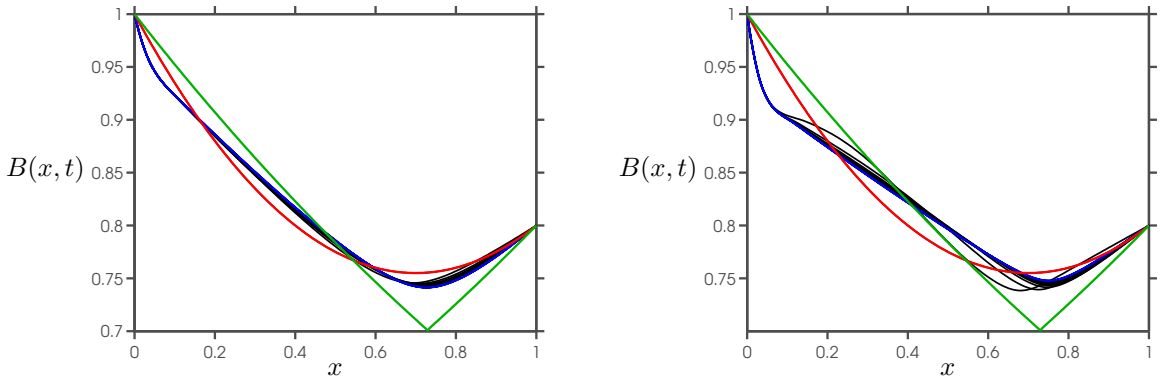

(a) $\epsilon = 0.1$ (b) $\epsilon = 0.05$

Figure 4.26: Plots of the numerical solution to the macroscopic model for the two-adsorbing-surfaces problem given by (4.120) subject to the initial condition (4.121) (red curve) and for space-step $\triangle x = 0.005$. Figures (a) and (b) shows plots of $B(x,t)$ for $\epsilon = 0.1$ and $\epsilon = 0.05$ respectively at times $t \in [0.005, 0.01, \ldots, 0.1]$ (black curves). The solution at $t = 0.1$ is denoted by the blue curve and the steady-state solution given by (4.115)–(4.116) is denoted by the green curve. Parameters used are $B_0 = 0.755, \kappa = 0.5$, and $s_0 = 0.7$.

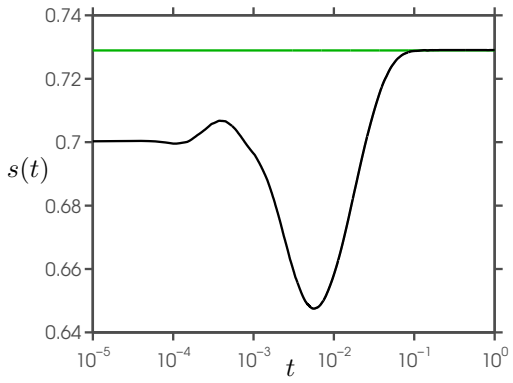

Figure 4.27: Plots of the moving boundary $s(t)$ (black curve) and steady-state solution (green curve) for the two-adsorbing-surfaces problem given by (4.120) subject to the initial condition (4.121) and for space-step $\triangle x = 0.005$. Parameters used are $\epsilon = 0.1$, $B_0 = 0.755$, $\kappa = 0.5$, and $s_0 = 0.7$.

4.4.2.3 Small-time analysis for the formation of 'sharp troughs'

We now consider the formation of the 'sharp troughs' as exhibited by the mesoscopic-model in Figure 4.20 or the corner at the moving boundary for the macroscopic model shown in Figures 4.24 and 4.25. To investigate the latter case we consider the asymptotic expansion of $B(x,t)$:

$$B \sim B_0 + f_1(\eta)t^{2/3} + f_2(\eta)t^{4/3} + \ldots, \quad \text{as} \quad t \to 0, \tag{4.123}$$

where $\eta = (x - s_0)t^{-1/3}$ is order one, and $s(0) = s_0$. Substituting into (4.100a) we obtain an equation for $f_1(\eta)$ at leading order

$$B_0 \left(\text{sgn}(f_1')f_1''\right)' - \frac{1}{3}\eta f_1' + \frac{2}{3}f_1 = 0, \tag{4.124}$$

where $'$ denotes differentiation with respect to η.

We suppose that the initial condition for B is given by a polynomial of degree n such that

$$B(x,t) \sim B_0 + \kappa(x - s_0)^n + \ldots, \quad \text{as} \quad t \to 0, \tag{4.125}$$

then (4.125) and the boundary conditions (4.111e) to leading order give

$$f_1(\eta) \sim \kappa\eta^n, \qquad \text{as} \quad \eta \to \pm\infty, \tag{4.126}$$

$$[f_1]_-^+ = [|f_1'|]_-^+ = [\text{sgn}(f_1')f_1'']_-^+ = 0, \qquad \text{on} \quad \eta = 0. \tag{4.127}$$

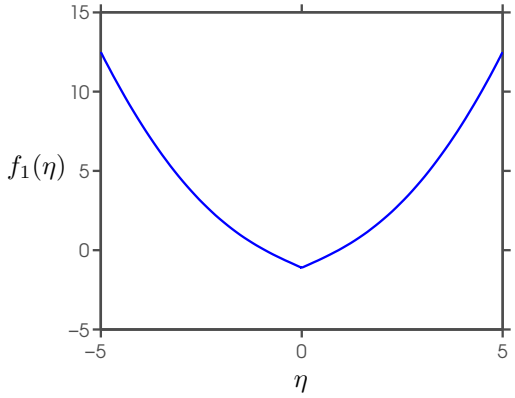

Figure 4.28: Plot of the leading-order similarity solution in the small t analysis given by (4.129) for $\kappa = 0.5$.

We note that (4.124) is invariant under the transformation $\eta \to -\eta$ and so $f_1(\eta)$ is an odd function. Hence, we may solve the reduced problem on the half-space $\eta > 0$:

$$f_1''' - \frac{1}{3}\eta f_1' + \frac{2}{3} f_1 = 0, \tag{4.128a}$$

$$f_1(\eta) \sim \kappa \eta^n, \qquad \text{as} \quad \eta \to \infty, \tag{4.128b}$$

$$f_1'' = 0, \qquad \text{on} \quad \eta = 0, \tag{4.128c}$$

where we have scaled $\eta \sim B_0^{-1/3}$ and $\kappa \sim B_0^{2/3}$.

The solution to problem (4.128) for $n = 2$ is given by

$$f_1(\eta) = \frac{9\kappa \; {}_1F_2(-\frac{2}{3}; \frac{1}{3}, \frac{2}{3}; \frac{\eta^3}{27})}{\Gamma\left[-1/3\right]} + \frac{2\kappa \; {}_1F_2(-\frac{1}{3}; \frac{2}{3}, \frac{4}{3}; \frac{\eta^3}{27})}{\Gamma\left[4/3\right]}, \tag{4.129}$$

where ${}_pF_q(a_1, \ldots, a_p; b_1, \ldots, b_q; z)$ is the generalised hypergeometric function[3] and in abuse of notation $\Gamma[z]$ denotes the gamma function[4] (*i.e.* not adsorbed concentration). The solution (4.129) is plotted in Figure 4.28 for $\kappa = 1/2$ which shows the presence of a corner at $\eta = 0$.

[3]The generalised hypergeometric function is defined by the power series expansion

$${}_pF_q(a_1, \ldots, a_p; b_1, \ldots, b_q; z) = \sum_{n=0}^{\infty} \frac{(a_1)_n \ldots (a_p)_n}{(b_1)_n \ldots (b_q)_n} \frac{z}{n!},$$

where $(a)_n$ is the Pochhammer symbol given by $(a)_n = a(a+1)(a+2)\ldots(a+n-1)$, for $n \geq 1$ and $(a)_0 = 1$.

[4]The gamma function is defined as $\Gamma[z] = \int_0^\infty \mathrm{e}^{-t} t^{z-1} \, \mathrm{d}t$.

4.5 Summary

In this chapter we first considered a semi-discrete kinetic model based on mass-action kinetics to describe the evolution of surfactant pairs in a multilayer structure that consists of repeating bilayers. The model was extended in two ways, firstly by taking the large-bilayer limit to derive a continuum model and secondly to the situation where a surfactant multilayer exists between two adsorbing boundaries. The resulting partial differential equation in this limit is third order and nonlinear and to the best of our knowledge this equation has not been derived for a physical model elsewhere. The introduction of an additional adsorbing boundary to the model presented in §4.3 results in a free-boundary problem and appropriate extra conditions were derived to close the problem in §4.4.2.

Broadly speaking the features of the macroscopic models for both the one and two-adsorbing-surfaces scenarios are similar to those of the mesoscopic models they were derived from. For the macroscopic models of both scenarios we showed that a Langmuir-Hinshelwood-type equation could be derived to describe the evolution of the adsorbed surfactant concentration at the surface. The steady-state distribution of surfactant, for only one adsorbing surface, decays exponentially with depth, which qualitatively agrees with what is observed experimentally [27]. This suggests that the number of bilayers in the multilayer structure $\sim 1/(\epsilon b)$ where b is the exponential decay constant, which depends on the net surfactant concentration.

If the initial conditions are monotonic, which typically is the case in a surfactant multilayer set-up, the numerical solutions suggest that the signum term in the governing equation is negative for all time and so the $\mathrm{sgn}(B_x)$ term has minimal significance to the PDE (4.31). Conversely, if the initial conditions are not monotonically decreasing the $\mathrm{sgn}(B_x)$ is significant and we observe 'smooth humps' and 'sharp troughs' in the solution that eventually decay for large time. These nonlinear features in the evolution of the bilayer distribution, for certain initial conditions, suggest that the multilayer structure transitions through a non-homogeneous state. Furthermore, our collaborators observe experimentally that during the formation of a multilayer in LAS the structure is often fragmented into lamellae, which they refer to as a disordered mosaic spread in the structure. Hence, the fact that our model is able to reproduce such features that are characteristic of the transition that the multilayer structure evolves through is quite remarkable.

For the two-adsorbing-surfaces problem we showed that the steady-state solution forms a corner that persists for large time and which for the continuum case corresponds to a discontinuity in the spatial derivative of the bilayer concentration. For the time-dependent model we showed in §4.4.2.3 that the formation of such a corner occurs instantaneously in the limit $t \to 0$ and that there exists a leading-order similarity solution to describe the formation.

The theoretical models presented in this chapter will be extended in the next chapter to more realistic models that incorporate free monomer, aggregates in the bulk and electrolyte, *e.g.* calcium ions, that will facilitate self-assembly of the multilayer structure.

Chapter 5

Electrolytic self-assembly at interfaces

It has been shown experimentally that for certain surfactants, which on their own do not exhibit multilayer formation, the addition of an electrolyte can induce self-assembly at an interface, leading to multilayer formation above critical concentrations of surfactant and electrolyte [27, 30, 31, 39]. It is also known that in domestic and industrial applications of detergents with hard water containing divalent calcium and magnesium cations, there is a profound effect on the performance of the product [30]. Thus, the presence of electrolytes will significantly impact the design and performance of such products [31, 39]. Therefore, in this chapter we extend the macroscopic model for multilayer rearrangement derived in Chapter 4 to describe the formation of bilayer molecules from free surfactant monomers in the bulk. We then extend the macroscopic model that includes free surfactant monomers by including an electrolytic dependence on the bilayer formation reaction. We determine the steady-state solutions to the models presented in this chapter and show how they can determine the number of bilayers in the multilayer structure, which depend on the physical parameters of the model: bulk surfactant concentration, bulk electrolyte concentration, and reaction rates for the formation of bilayers.

This chapter is laid out as follows. We first discuss experimental observations for electrolytic self-assembly at interfaces given in the literature and those that our experimental collaborator, Jeff Penfold based at ISIS, has performed. In §5.2 we derive a free-surfactant model that describes the formation and rearrangement of bilayer molecules in a multilayer structure, which couples to the the free surfactant in the bulk. We then extend this model in §5.3 to incorporate the effect of electrolyte on the self-assembly process and focus on the LAS/calcium ion system that is common in detergent formulations and is of interest to our collaborator. Finally, we compare the

results of the two models in §5.4.1 and discuss future work relating to this research in §5.4.3.

5.1 Experimental observations

In this section we discuss the experimental observations of electrolytic multilayer formation given in the literature and the unpublished data for multilayer kinetic experiments performed by our experimental collaborator. In this literature review we focus our attention on the work of Penfold *et al.* [30] and Tucker *et al.* [39], who consider the LAS/$CaCl_2$ system, and Petkov *et al.* [31] who consider the similar anionic surfactant sodium dodecyl dioxyethylene sulfate, which is commonly referred to as SLES, with aluminium cations as the electrolyte. These papers focus on the static adsorption structure, whereas the experimental results we discuss in §5.1.3 are for the kinetic formation of a multilayer for the LAS/$CaCl_2$ system.

5.1.1 Penfold *et al.* 2007 [30]

Penfold *et al.* [30] studied the formation of multilayer structures for the LAS/$CaCl_2$ system (LAS-6 isomer). They also observed multilayer structures at the air–water interface for the mixed surfactant system LAS with the non-ionic co-surfactant monododecyl octaethylene glycol ($C_{12}EO_8$) in the presence of calcium chloride, $CaCl_2$. For compositions of 80:100 and richer in the non-ionic surfactant $C_{12}EO_8$ multilayer formation was found to be increasingly difficult. Furthermore, the use of $6\,\mathrm{mol\,m^{-3}}$ sodium chloride, NaCl, (which has the same ionic strength as $2\,\mathrm{mol\,m^{-3}}$ $CaCl_2$) at the same surfactant concentrations does not result in multilayer formation. The measurements they obtained for the multilayer structure at the air–water interface for $2\,\mathrm{mol\,m^{-3}}$ LAS/$C_{12}EO_8$ solution with varying $CaCl_2$ concentration are summarised in Table 5.1.

In this paper bulk measurements were also made to determine the structure of the solution aggregates. We omit the full details of these experiments but note that, for the composition range of the surfactant mixture LAS/$C_{12}EO_8$ that exhibits multilayer formation with the addition of $CaCl_2$, the bulk species are typically in the form of vesicles (liposomes) and/or lamellar fragments. The addition of $CaCl_2$ triggers a transition from a globular micellar phase to a vesicle/lamellar phase at relatively low

$CaCl_2$ concentration ($mol\,m^{-3}$)	Solution composition (mol % LAS)	d_m (Å)	d (Å)	n
0.25	1	45±0.1	34±0.2	4
0.5	1	45±0.1	32±0.2	20
	0.05	45±0.1	32±0.2	3
1	1	45±0.1	32±0.2	30
	0.95	45±0.1	32±0.2	20
	0.9	45±0.1	34±0.2	3
2	1	45±0.1	32±0.2	30
	0.95	45±0.1	32±0.2	30
	0.9	45±0.1	33±0.2	20

Table 5.1: Key model parameters for the analysis of LAS/$C_{12}EO_8$ surface adsorption in $CaCl_2$ reproduced from [30], where the depth of the monolayer is denoted d_m, the depth of a bilayer is denoted d, and the number of bilayers is denoted n.

surfactant concentrations. In comparison, for LAS-only solutions such a transition in the structure of the bulk aggregates would only occur at a much higher bulk surfactant concentration.

5.1.2 Tucker *et al.* 2011 [39]

This paper is concerned with the role of the different structural isomers of the anionic surfactant sodium para-dodecyl benzene sulfonate, LAS, on surface adsorption and solution self-assembly. The structure of the two isomers of relevance, LAS-4 and LAS-6, has already been discussed in §3.2.2. In the bulk, the LAS isomer mixtures form small charged globular micelles whose aggregation number increases with increasing asymmetric isomer, LAS-4, content. For bulk surfactant concentrations above the CMC the composition of the surface concentration is similar to that in the bulk. The addition of $CaCl_2$ promotes the formation of planar aggregates (vesicles/lamellar fragments) in the bulk but only when the symmetric isomer, LAS-6, is the major component of the mixture. This is because of the asymmetry of the alkyl chain in LAS-4, which has a significant effect on the curvature and packing within the micelle structure. In contrast, the multilayer structure that forms due to the presence of calcium ions has a greater tendency to form multilayers with the LAS-4 dominant mixtures. This is due to improved chain packing associated with the LAS-4 isomer that promotes surfactant-ion/Ca^{2+} binding. Table 5.2 summarises the key parameters obtained from fits to the NR data for a $2\,mol\,m^{-3}$ LAS-6/LAS-4 mixture

Solution composition (mol % LAS-6:LAS-4)	Contrast (LAS-6/LAS-4)	d ($\pm$0.5 Å)	n
80:20	dh	31.0	11
	hd	33.0	19
60:40	dh	31.4	11
	hd	33.0	19
50:50	dh	31.4	11
	hd	32.0	19
40:60	dh	31.4	17
	hd	33.0	19
20:80	dh	31.4	17
	hd	35.0	19

Table 5.2: Key model parameters for the analysis of surface adsorption of a $2\,\mathrm{mol\,m^{-3}}$ LAS-6/LAS-4 mixture in $1\,\mathrm{mol\,m^{-3}}$ $CaCl_2$ reproduced from [39], where the depth of a bilayer is denoted d, and the number of bilayers is denoted n.

in $1\,\mathrm{mol\,m^{-3}}$ $CaCl_2$. These measurements were made using contrast matching where the hydrogeneous component (e.g. h-surfactant) reflectivity is insignificant as it has been contrast-matched with the solution, nrw, and so only the deuterated component (e.g. d-surfactant) contributes to the reflectivity data.

5.1.3 Kinetic multilayer formation for LAS-6/$CaCl_2$

Our collaborators, Jeff Penfold and his co-workers, study the surface kinetics of multilayer formation for a LAS-6 solution in the presence of calcium chloride using NR. In these experiments a monolayer is established at the air–water interface from a surfactant-only solution and once an equilibrium between the surface and bulk phases has been reached they add calcium chloride in either of the two methods below:

Experiment 1 — by pipette from above, *i.e.* onto the solution surface;

Experiment 2 — via the subphase using a syringe pump.

The syringe pump used in (ii) is identical to that discussed in §3.2. Temporal measurements are then made of the resulting adsorbed structure using NR. A summary of the results is presented in Table 5.3 and reflectivity plots at different times during the multilayer evolution are shown in Figure 5.1 and Figure 5.2. The reflectivity plots for both cases show the formation of a Bragg peak over time, which indicates the formation of a multilayer structure. Notably, at 27 and 47 minutes for Experiment 1,

Experiment 1				Experiment 2			
Time (mins)	d_m (Å)	d (Å)	n –	Time (mins)	d_m (Å)	d (Å)	n –
0	30	31.4	4	0	16	–	–
11	40	31.4	4	10	17	–	–
14	55	30.6	5	13	24	31.4	4
17	53	31.0	5	16	33	31.4	8
27	53	31.0	5	20	36	31.4	8
34	52	31.0	6	23	46	31.4	8
47	52	31.4	7	30	48	31.4	9
				40	53	31.4	11

Table 5.3: Experimental data for multilayer formation for Experiment 1, where $CaCl_2$ is added to solution using a pipette and Experiment 2, where $CaCl_2$ is added via the subphase using a pump.

and 30 and 40 minutes for Experiment 2 the plots show that there are a number of secondary Bragg peaks. The secondary Bragg peaks for Experiment 1, where $CaCl_2$ is added to the surface using a pipette, are more well-defined compared to those observed in Experiment 2, where $CaCl_2$ is added to the subphase using a syringe pump. This suggests that for Experiment 1 the multilayer has a more ordered structure than that for Experiment 2. At $t = 0$ a small number of multilayers are observed for Experiment 1, whereas for Experiment 2 it takes 13 minutes for multilayers to be first observed. In addition, after approximately 40 minutes the number of bilayers observed for Experiment 1 is 7 compared to 11 for Experiment 2. This suggests that the initial method used to add calcium ions has an effect on the formation of the mutilayer structure. Furthermore, for the two methods for addition of calcium ions described in (i) and (ii), the NR data suggests that the process to form these structures could be diffusion limited. We note that for the second experiment the multilayer structure was at the resolution limit of the apparatus used, *i.e.* there may be more than 11 layers formed but these could not be observed without significant errors being introduced into the data.

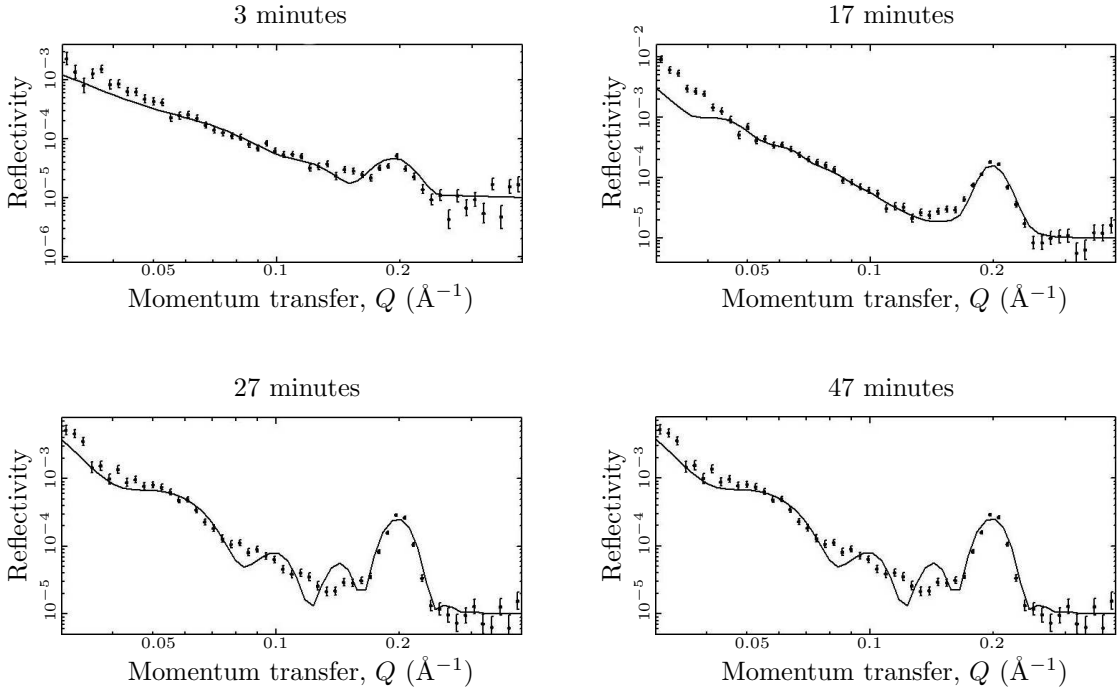

Figure 5.1: Reflectivity plots of the NR data for Experiment 1 where $CaCl_2$ is added onto the solution surface using a pipette [27].

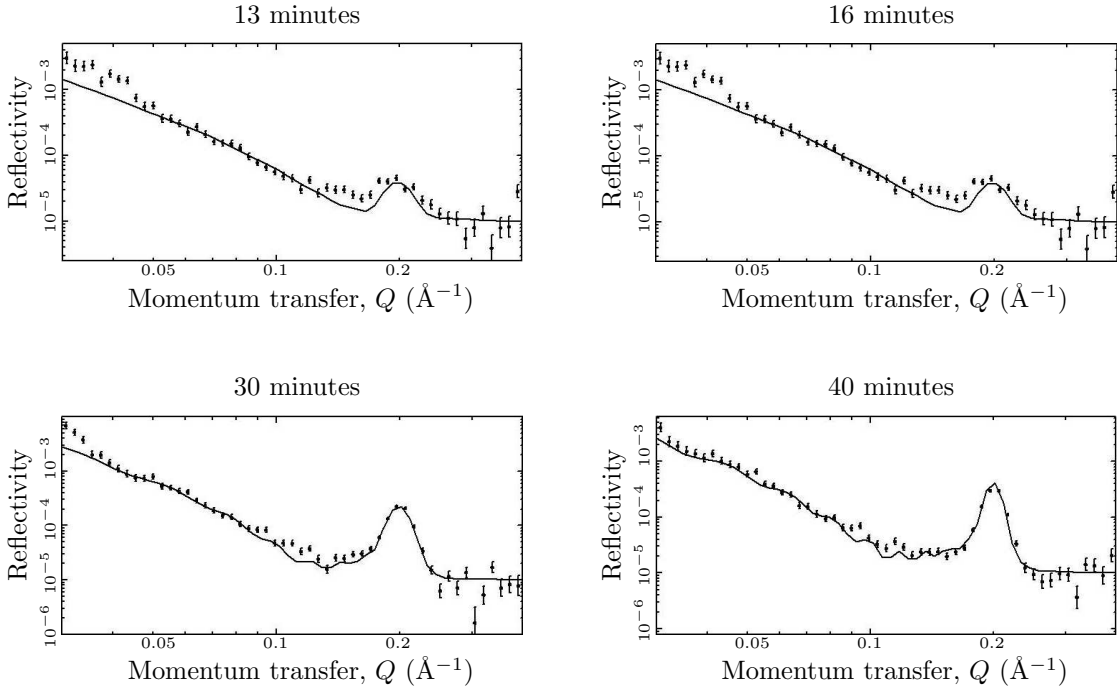

Figure 5.2: Reflectivity plots of the NR data for Experiment 2 where $CaCl_2$ is added to the subphase using a syringe pump [27].

5.1.4 Petkov *et al.* 2010 [31]

In this paper the effect of the multivalent calcium and aluminium cations, Ca^{2+} and Al^{3+} respectively, on aggregation and adsorption is investigated using small angle neutron scattering (SANS) and NR, respectively, for the anionic surfactant sodium dodecyl dioxyethylene sulfate, which is commonly referred to as SLES. For $20\,\mathrm{mol\,m^{-3}}$ the micelle aggregation number is approximately 90. The addition of Ca^{2+} increases the aggregation number from 160 in $3.8\,\mathrm{mol\,m^{-3}}$ $CaCl_2$ to 570 in $24\,\mathrm{mol\,m^{-3}}$ $CaCl_2$. For the addition of Al^{3+} the aggregation number increases from 170 in $2.4\,\mathrm{mol\,m^{-3}}$ $CaCl_2$ to 1200 in $7.8\,\mathrm{mol\,m^{-3}}$ $CaCl_2$. Thus, there is a transition in the bulk solution aggregates from predominantly globular micellar to lamellar structures as the concentration of the cation increases, which is more noticeable for the cation with the greater ionic charge. The electrolyte-dependent growth in bulk aggregates is due to the strong binding of Ca^{2+} and Al^{3+} ions to the micellar surface, which reduces the local curvature and hence promotes aggregate growth. The effect is more pronounced with the Al^{3+} ions as they are able to form trimers with the surfactant monomers compared to the dimers formed from Ca^{2+}/SLES molecules.

The adsorption of SLES/Al^{3+} at the air–water interface was investigated using NR at surfactant concentrations of $1\,\mathrm{mol\,m^{-3}}$ and $5\,\mathrm{mol\,m^{-3}}$; a summary of the results is reproduced in Table 5.4. At the lower surfactant concentration they observed a transition from a monolayer to a trilayer to a multilayer at the interface, indicating that the number of bilayers in the multilayer is dependent on the counterion concentration. For the higher concentration, which is significantly above the CMC ($= 0.8 \pm 0.1\,\mathrm{mol\,m^{-3}}$), the transition from monolayer to multilayer is more abrupt suggesting that there is a more complex interaction with the bulk aggregates. The number of bilayers for the higher surfactant concentration was greater, 40, compared to 30 for $1\,\mathrm{mol\,m^{-3}}$ of SLES, which also suggests the number of bilayers depends on the bulk surfactant concentration.

Petkov *et al.* also investigated the effect of the multivalent ions on the anionic/non-ionic surfactant mixture where the non-ionic co-surfactant monododecyl dodecaethylene glycol, $C_{12}E_{12}$ is used. The addition of $C_{12}E_{12}$ essentially suppresses the dimer and trimer formation of SLES/Ca^{2+} and SLES/Al^{3+} molecules respectively, which results in smaller aggregates in the bulk for equivalent surfactant/electrolyte concentrations. At the surface the addition of the non-ionic co-surfactant suppresses the transition from an adsorbed monolayer to multilayer structure.

$1\,\mathrm{mol\,m^{-3}}$ SLES			$5\,\mathrm{mol\,m^{-3}}$ SLES		
$AlCl_3$/NaCl conc. ratio ($\mathrm{mol\,m^{-3}}$)	d (Å)	n –	$AlCl_3$/NaCl conc. ratio ($\mathrm{mol\,m^{-3}}$)	d (Å)	n –
0.12/2.4	46.0 ±0.1	1	1.9/4.6	43.0 ±0.1	1
0.24/1.8	46.0 ±0.2	3	2.0/4.0	50.4 ±0.2	40
0.3/1.5	46.0 ±0.2	3	2.1/3.75	50.4 ±0.2	40
0.6/0.0	49.0 ±0.2	30	2.4/2.5	50.4 ±0.2	40

Table 5.4: Experimental data for multilayer formation for SLES/$AlCl_3$/NaCl.

5.1.5 Summary of experimental observations

The experimental observations given in [30, 31, 39] show that, for the anionic surfactants LAS and SLES, multilayer formation at the air–water interface will only occur in the presence of a suitable electrolyte. The addition of an electrolyte also leads to more planar aggregates in the bulk solution, which are not typically present in the absence of electrolyte. In the context of detergency, a greater accumulation of surfactant at an interface is a desirable property in formulations that are used to remove dirts, oils, fats *etc.* from surfaces. It was shown that the increase in the surfactant concentration at an interface is induced by the presence of electrolytes such as calcium ions, which are typically present in hard water that is often used in applications of detergents. Furthermore, most detergent formulations contain mixtures of the anionic surfactants, such as SLES and LAS, and non-ionic co-surfactants. The experimental results for the mixed anionic/non-ionic systems suggest that the non-ionic co-surfactants weakly suppress the formation of the multilayer structures and so, in general, higher concentrations of surfactant and electrolyte are required to achieve similar structures at the interface with co-surfactants present. This result is of importance to detergent manufactures who wish to optimize their products for performance, component usage, and environmental impact.

5.2 Free-surfactant model

In this section we extend the model for multilayer re-arrangement presented in Chapter 4 to include free surfactant monomers that enable bilayer formation. Hence, the structure of the multilayer will now depend on the bulk surfactant concentration. We assume the formation of bilayer molecules, B, from free surfactant monomers, S, is through the single-step reaction

$$2S + \text{adsorption site} \rightleftharpoons B, \tag{5.1}$$

where S has units $\mathrm{mol\,m^{-3}}$ and B has units $\mathrm{mol\,m^{-2}}$. The formation of the adsorbed monolayer at the surface from free surfactant monomers is given by the surface reaction

$$S + \text{adsorption site in surface} \rightleftharpoons \Gamma, \tag{5.2}$$

where Γ is the concentration of surfactant in the adsorbed monolayer and has units $\mathrm{mol\,m^{-2}}$.

By the law of mass action one can derive a mesoscopic model for the free-surfactant model, equivalent to that derived in §4.2 for the bilayer model. A full derivation is given in Appendix D. Assuming that the number of bilayers is large we take a continuum limit to derive a macroscopic model that describes the bilayer formation, rearrangement and diffusion of free surfactant monomers, details of which can be found in Appendix D. We present the dimensionless governing equations for the macroscopic model in §5.2.1.

5.2.1 Governing equations

The dimensionless concentrations of free monomer, S, adsorbed surfactant, Γ, and bilayer molecules, B, satisfy the governing equations

$$B_t = \left(\alpha(x)\mathrm{sgn}(B_x)({B_x}^2 - BB_{xx})\right)_x + \kappa\left(|B_x|S^2 - B\right), \tag{5.3a}$$

$$\frac{1}{\Gamma^*}S_t = S_{xx} - 2\kappa\left(|B_x|S^2 - B\right), \tag{5.3b}$$

for $t > 0$ and $0 < x < l$, and boundary conditions

$$B = \Gamma, \quad S_x = {B_x}^2 - BB_{xx} = 0, \qquad \text{on} \quad x = 0, \tag{5.3c}$$

$$\frac{\mathrm{d}\Gamma}{\mathrm{d}t} = \kappa_0^+(1-\Gamma)S - \kappa_0^-\Gamma + 2\alpha_m(1-\Gamma)^2\Gamma, \qquad \text{on} \quad x = 0, \tag{5.3d}$$

$$S_x = {B_x}^2 - BB_{xx} = 0, \qquad \text{on} \quad x = l. \tag{5.3e}$$

The dimensionless parameters of the model are defined below:

$$\kappa = \frac{k^- H^3}{a_0\Gamma_{\mathrm{sat}}}, \qquad \Gamma^* = \frac{\Gamma_{\mathrm{sat}}}{h}\sqrt{\frac{k^+}{k^- H}}, \qquad l = \frac{h}{H}, \qquad S^* = \frac{hS_b}{\Gamma_{\mathrm{sat}}},$$

$$\alpha_{\mathrm{m}} = \frac{k_{\mathrm{m}}\Gamma_{\mathrm{sat}}H^3}{a_0}, \qquad \kappa_0^+ = \frac{k_0^+ H^3}{a_0\Gamma_{\mathrm{sat}}}\sqrt{\frac{k^- H}{k^+}}, \qquad \kappa_0^- = \frac{k_0^- H^3}{a_0\Gamma_{\mathrm{sat}}}, \tag{5.4}$$

where the characteristic lengthscale, H, is given by

$$H = \left(\frac{\sqrt{k^+}a_0\Gamma_{\mathrm{sat}}^2}{\sqrt{k^-}hD_s}\right)^{1/3}. \tag{5.5}$$

The first term on the right-hand side of (5.3a) represents the rearrangement of bilayer molecules within the multilayer structure, the second and third terms denote formation of bilayer molecules and dissociation of bilayer molecules into free monomers respectively, where the flux term, B_x, denotes the available adsorption sites in the multilayer. The free monomer concentration, S, evolves according to the reaction-diffusion equation (5.3b), where the dimensionless parameter Γ^* represents the typical concentration ratio of free monomers to bilayer molecules in the multilayer structure. At the free surface the multilayer is assumed to be in equilibrium with the monolayer and hence $\Gamma = B$. However, the monolayer is not in equilibrium with the free surfactant at the surface and so the concentration of surfactant in the monolayer evolves

according to (5.3d). The flux of free monomers into the monolayer is assumed to be very slow and so S satisfies the no flux condition. Finally, for mass to be conserved we have the flux condition for B given in (5.3c) and (5.3e).

We note that it is possible to derive an alternative boundary condition on the free surface in which the adsorbed surfactant concentration, Γ, is in equilibrium with the bulk phases, the details of which can be found in Appendix D.

On summing (5.3a) and (5.3b), integrating with respect to x and applying the boundary conditions (5.3c) and (5.3e) we obtain the equation for conservation of surfactant

$$\int_0^l \left(2B + \frac{1}{\Gamma^*}S\right)\,\mathrm{d}x = lS^*, \tag{5.6}$$

where S^* is the dimensionless net concentration of surfactant.

The expression for the characteristic lengthscale, H, given in (5.5) suggests, counter-intuitively, that as the depth of a single bilayer, h, increases, and assuming all other parameters in expression (5.5) are constant, then the depth of the multilayer decreases. However, the depth of a bilayer depends on the geometry of the surfactant molecule used and so for different surfactants we expect the parameters h, a_0, and $k^{\pm}$ to vary significantly and so one should not draw conclusions on the dependence of the depth of the multilayer on the depth of a single bilayer from (5.5).

The other dimensional parameters are summarised in Table 5.5. In the following section we discuss how some of the unknown dimensional parameters may be estimated and hence estimate the values of the dimensionless parameters.

We note that in deriving (5.3) we have made the simplifying assumption that the diffusivity of the surfactant monomers is constant. However, in practice the ability of free surfactant monomers to diffuse through the multilayer structure is reduced as the structure becomes more dense, *i.e.* as the concentration of bilayer molecules increases. Thus, a more physically relevant assumption would be to allow the diffusivity of the surfactant monomers to depend on B; for example, in dimensional form

$$D_S(B) = D_{\mathrm{mon}}\left(1 - \frac{B}{\Gamma_{\mathrm{sat}}}\right), \tag{5.7}$$

where D_{mon} is the diffusivity of surfactant monomers in the bulk solution, and in general is known.

Parameter	Description	Units
k^+	rate parameter associated with bilayer formation	$\mathrm{mol}^{-2}\,\mathrm{m}^7\,\mathrm{s}^{-1}$
k^-	rate parameter associated with bilayer dissociation	s^{-1}
a_0	characteristic rate parameter for the rearrangement of the bilayers within the multilayer structure	$\mathrm{mol}^{-1}\,\mathrm{m}^5\,\mathrm{s}^{-1}$
k_m	rate parameter for the movement of surfactant between the first bilayer and the monolayer	$\mathrm{mol}^{-2}\,\mathrm{m}^4\,\mathrm{s}^{-1}$
k_0^+	rate parameter associated with monolayer formation	$\mathrm{mol}^{-1}\,\mathrm{m}^3\,\mathrm{s}^{-1}$
k_0^-	rate parameter associated with monolayer dissociation	s^{-1}
D_S	diffusivity of free surfactant monomers	$\mathrm{m}^2\,\mathrm{s}^{-1}$
h	depth of a single bilayer	m
S_b	bulk surfactant concentration	$\mathrm{mol}\,\mathrm{m}^{-3}$
Γ_sat	monolayer saturation concentration	$\mathrm{mol}\,\mathrm{m}^{-2}$

Table 5.5: Dimensional parameters of the free-surfactant model for self-assembly.

5.2.1.1 Parameter estimates

In this section we estimate the dimensionless parameters of the model given in (5.4) for the surfactant LAS and consider the symmetric isomer LAS-6.

For a bulk surfactant concentration, $S_b = 2\,\mathrm{mol}\,\mathrm{m}^{-3}$, the mean depth of a bilayer is $h = 3.2 \times 10^{-9}\,\mathrm{m}$ and the typical depth of the multilayer is $1 \times 10^{-8}\,\mathrm{m}$. If we assume that the depth of the multilayer is of order H then for a typical solution depth of a few millimetres we have that $l = O(10^5)$.

For monolayer adsorption in equilibrium, the ratio of the rate parameters $k_0^\pm$ and Γ_sat are determined from fitting the Langmuir isotherm to experimental data. However, they will, in general, take different values to those estimated from the standard Langmuir isotherm. Moreover, we have to estimate the value for the additional rate parameter k_m in the isotherm. To avoid this indeterminacy one could assume that the monolayer establishes itself on a much shorter timescale after which the multilayer then begins to form. Mathematically this is equivalent to assuming $\alpha_\mathrm{m} \ll \kappa_0^\pm$. Thus, under this assumption, and for $S_b = 2\,\mathrm{mol}\,\mathrm{m}^{-3}$, the adsorbed saturation concentration, Γ_sat, is approximately $3.4 \times 10^{-6}\,\mathrm{mol}\,\mathrm{m}^{-2}$ and the ratio of the rate parameters, k_0^-/k_0^+, is approximately $0.19\,\mathrm{mol}\,\mathrm{m}^{-3}$. We note that if we did not make this assumption we still would expect Γ_sat to be the same order of magnitude as the adsorbed monolayer, *i.e.* $\sim 10^{-6}\,\mathrm{mol}\,\mathrm{m}^{-2}$.

The timescale over which the multilayer structure evolves is given by

$$[t] = \frac{H^3}{a_0 \Gamma_{\text{sat}}}, \tag{5.8}$$

and is typically 2 hours [27]. Therefore, the parameter a_0 can be estimated, which gives $a_0 \approx 4.1 \times 10^{-23}\ \text{mol}^{-1}\,\text{m}^5\,\text{s}^{-1}$.

The diffusivity of surfactant monomers in solution is typically $D_{\text{mon}} = 5 \times 10^{-10}\,\text{m}^2\,\text{s}^{-1}$. However, the diffusivity of free monomers in the multilayer structure, D_S, is not known. Moreover, as discussed earlier, a better assumption is to allow the diffusivity of the free monomers to depend on the bilayer concentration, but we shall not complicate the model with this assumption. Instead, to accommodate the reduced diffusivity in the multilayer structure we make the plausible assumption that D_S is an effective reduced diffusivity, which we choose here to be two orders of magnitude smaller than D_{mon}, *i.e.* $D_S = 5 \times 10^{-12}\,\text{m}^2\,\text{s}^{-1}$.

The typical monomer concentration scale can be written as

$$[S] = \sqrt{\frac{k^- H}{k^+}} = \frac{H^2 \Gamma_{\text{sat}}}{[t] h D_S} = 5.6 \times 10^{-9}\,\text{mol}\,\text{m}^{-3}, \tag{5.9}$$

where we have used the value for the diffusivity quoted above. Thus the ratio of rate parameters k^-/k^+ can be estimated and is approximately $8.7 \times 10^{-4}\ \text{mol}^2\,\text{m}^{-7}$.

The remaining dimensionless parameter to estimate is κ, which depends explicitly on the rate constant k^- and is not known in general. The estimated values for the dimensionless parameters are summarised in Table 5.6. Since Γ^* is large then for κ order one this implies that the surfactant monomer concentration is in pseudo-steady-state to leading order, *i.e.* we can neglect the left-hand side of (5.3b). However, as the value for κ is unknown we note that there are clearly other interesting distinguished limits that we could analyse, namely $\kappa \ll 1/\Gamma^*$, $\kappa = O(1/\Gamma^*)$, $1/\Gamma^* \ll \kappa \ll 1$, $\kappa = O(1)$, $\kappa \gg 1$. Such analysis is left for future work.

In the following section we consider the steady-state solutions to (5.3), and show how the solutions can be compared with experimental data to determine the values for the unknown parameters.

Parameter	Expression	Estimated value
Γ^*	$\Gamma_{\rm sat}\sqrt{k^+}/h\sqrt{k^-H}$	3.6×10^8
S^*	$hS_b/\Gamma_{\rm sat}$	1.9×10^{-3}
κ	$k^-H^3/a_0\Gamma_{\rm sat}$	–
l	L/H	10^5
κ_0^-/κ_0^+	$k_0^-\sqrt{k^+}/k_0^+\sqrt{Hk^-}$	6.4×10^4
$\alpha_{\rm m}$	$k_{\rm m}\Gamma_{\rm sat}H^3/a_0$	–

Table 5.6: Approximate values for the dimensionless parameters of the free-surfactant model for self-assembly.

5.2.2 Steady-state solutions

In this section we make the plausible assumption, as in Chapter 4, that $B_x<0$. Then on setting all time derivatives to zero we obtain the steady-state problem

$$\left((B')^2-BB''\right)'=-\kappa(B'S^2+B), \tag{5.10a}$$

$$S''=-2\kappa(B'S^2+B), \tag{5.10b}$$

$$B(0)=\Gamma \quad\text{and}\quad 0=(B')^2-BB''=S', \quad\text{on}\quad x=0,l, \tag{5.10c}$$

where $'$ denotes differentiation with respect to x and Γ satisfies the adsorption isotherm

$$0=(1-\Gamma)S-\frac{\kappa_0^-}{\kappa_0^+}\Gamma+2\frac{\alpha_m}{\kappa_0^+}(1-\Gamma)^2\Gamma, \quad\text{at}\quad x=0. \tag{5.11}$$

The solution to (5.10) is given by

$$S=\frac{1}{\sqrt{b}}, \quad B=\Gamma \mathrm{e}^{-bx}, \tag{5.12}$$

where $b>0$, and is determined from the conservation-of-mass equation

$$\frac{2}{b}\Gamma\left(1-\mathrm{e}^{-bl}\right)+\frac{1}{\Gamma^*}\frac{l}{\sqrt{b}}=lS^*, \tag{5.13}$$

and the adsorption isotherm (5.11).

The number of bilayers in the multilayer structure at equilibrium, n, can be estimated from the steady-state solution by

$$n\sim\frac{H}{hb}. \tag{5.14}$$

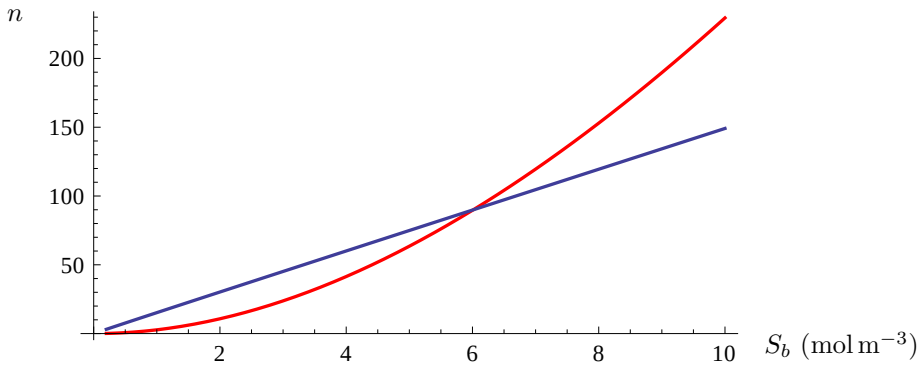

Figure 5.3: Plots of the number of bilayers in the multilayer structure, n, against the dimensional bulk surfactant concentration, S_b, determined from the steady-state conservation of mass equation (5.13) and the adsorption isotherm (5.11). The blue curve denotes the solution for the dimensionless parameters $\Gamma^* = 10^8$, $S^* = 3 \times 10^{-6}$, $l = 10^4$, $\kappa_0^-/\kappa_0^+ = \alpha_\mathrm{m}/\kappa_0^+ = 0.1$, and the red curve denotes the solution for the dimensionless parameters $\Gamma^* = 10^3$, $S^* = 3$, $l = 10^5$, and $\kappa_0^-/\kappa_0^+ = \alpha_\mathrm{m}/\kappa_0^+ = 1$. The dimensional parameters used are $h = 3.2 \times 10^{-9}\,\mathrm{m}$ and $\Gamma_\mathrm{sat} = 3.4 \times 10^{-6}\,\mathrm{mol\,m^{-2}}$.

We note that the number of bilayers depends on the two unknown dimensionless parameters κ_0^-/κ_0^+ and $\alpha_\mathrm{m}/\kappa_0^+$ but not on κ. The parameters κ_0^-/κ_0^+ and $\alpha_\mathrm{m}/\kappa_0^+$ in principle can be determined by fitting the adsorption isotherm (5.11) to experimental data. We do not have sufficient data to determine these parameters accurately for LAS-6, but a typical plot of n against S^* for $\kappa_0^-/\kappa_0^+ = \alpha_\mathrm{m}/\kappa_0^+ = 0.1$ is shown by the blue linear curve in Figure 5.3. The red curve denotes the solution for a different set of parameter values but assuming Γ^* and l are large, which shows that, depending on the choice of the model parameters, the relationship between the the bulk surfactant concentration and the number of bilayers is nonlinear, as observed for the SLES/$AlCl_3$ system in [31] (see §5.1.4).

Finally, we note that if instead we had assumed that the timescale for the monolayer formation is much quicker than the multilayer formation, *i.e.* $\alpha_\mathrm{m}/\kappa_0^+ \ll 1$ then the adsorption isotherm simplifies to the Langmuir isotherm

$$\Gamma \approx \frac{S}{k_0^-/k_0^+ + S}, \tag{5.15}$$

where κ_0^-/κ_0^+ is known and so there are no longer any unknown parameters in the equilibrium model.

5.3 Free-surfactant and free-electrolyte model

In this section we extend the free-surfactant model derived in §5.2 to incorporate the observed dependency of multilayer formation on electrolyte as discussed in §5.1. The reaction stoichiometry for the formation of the multilayer structure from surfactant monomers and electrolyte is unknown. Through discussions with our chemistry collaborators, Jeff Penfold and Robert Thomas, we make the plausible assumption that the formation of bilayer molecules, B, is through the single-step reaction of surfactant monomers, S, and electrolyte ions, E, given by

$$\nu S + E + \text{adsorption site} \underset{r^-}{\overset{r^+}{\rightleftharpoons}} B, \tag{5.16}$$

where ν is the ionic charge of the electrolyte, S and E have units $\mathrm{mol\,m^{-3}}$, and B has units $\mathrm{mol\,m^{-2}}$. We note that a different reaction stoichiometry from (5.16) could be used, which would alter the exponents of the S and C concentrations in the reaction term of the governing equations for the macroscopic model.

The system of interest that our experimental collaborators study and that has motivated this work is LAS/$CaCl_2$. Hence, for the remainder of this chapter we assume that the electrolyte is Ca^{2+} and we denote the concentration of Ca^{2+} by C and note that $\nu = 2$. Furthermore, for brevity, we use 'calcium' to refer to calcium ions, Ca^{2+}, in the remainder of this chapter. The derivation of the macroscopic model is analogous to that for the free-surfactant model, given in Appendix D, and so we omit the details and only present the dimensionless governing equations in the following section.

5.3.1 Governing equations

The dimensionless concentrations of free monomer, S, calcium, C, adsorbed surfactant, Γ, and bilayer molecules, B, satisfy the equations

$$B_t = \left(\alpha(x)\mathrm{sgn}(B_x)({B_x}^2 - BB_{xx})\right)_x + \kappa(|B_x|CS^2 - B), \tag{5.17a}$$

$$\frac{1}{\Gamma^*}S_t = S_{xx} - 2\kappa\left(|B_x|CS^2 - B\right), \tag{5.17b}$$

$$\frac{1}{\Gamma^*}C_t = DC_{xx} - \kappa\left(|B_x|CS^2 - B\right), \tag{5.17c}$$

$$C_x = S_x = B_x^2 - BB_{xx} = 0, \qquad \text{on} \quad x = 0, l, \tag{5.17d}$$

$$B = \Gamma, \qquad \text{on} \quad x = 0, \tag{5.17e}$$

for $t > 0$ and $0 < x < l$ where D is the dimensionless diffusivity for the calcium and Γ satisfies

$$\frac{\mathrm{d}\Gamma}{\mathrm{d}t} = \kappa_0^+(1-\Gamma)S - \kappa_0^-\Gamma + 2\alpha_m(1-\Gamma)^2\Gamma, \quad \text{on} \quad x = 0. \tag{5.17f}$$

On summing (5.17a)–(5.17b), integrating with respect to x, and applying the appropriate boundary conditions we obtain the equation for conservation of surfactant

$$\int_0^l \left(2B + \frac{1}{\Gamma^*}S\right)\,\mathrm{d}x = lS^*, \tag{5.18}$$

where S^* is dimensionless net concentration of surfactant. Similarly, one can obtain the equation for conservation of calcium

$$\int_0^l \left(B + \frac{1}{\Gamma^*}C\right)\,\mathrm{d}x = lC^*, \tag{5.19}$$

where C^* is dimensionless net concentration of calcium.

The dimensionless parameters of the model are defined below:

$$\kappa = \frac{k^-H^3}{a_0\Gamma_{\mathrm{sat}}}, \qquad \Gamma^* = \frac{\Gamma_{\mathrm{sat}}}{h}\left(\frac{k^+}{k^-H}\right)^{1/3}, \qquad D = \frac{D_C}{D_S}, \qquad l = \frac{h}{H},$$

$$\alpha_{\mathrm{m}} = \frac{k_{\mathrm{m}}\Gamma_{\mathrm{sat}}H^3}{a_0}, \qquad \kappa_0^+ = \frac{k_0^+H^3}{k^+a_0\Gamma_{\mathrm{sat}}}\left(\frac{k^-H}{k^+}\right)^{1/3}, \qquad \kappa_0^- = \frac{k_0^-H^3}{a_0\Gamma_{\mathrm{sat}}}, \tag{5.20}$$

where D_C is the diffusivity for the calcium ions. Estimates of the dimensional parameters were given earlier in §5.2.1.1. However, we note that the typical scaling for

the depth of the multilayer is different from the result for the surfactant-only model, (5.5) and is given by

$$H = \left(\frac{k^+ a_0^3 \Gamma_{\text{sat}}^6}{k^- h^3 D_s^3} \right)^{1/4}. \tag{5.21}$$

Furthermore, the typical scaling for the surfactant monomer concentration is also different from that for the surfactant-only model and is given by

$$[S] \sim \left(\frac{k^- H}{k^+} \right)^{1/3} = \left(\frac{a_0 k^- \Gamma_{\text{sat}}^2}{h k^+ D_S} \right)^{1/4}. \tag{5.22}$$

The typical concentrations of calcium used are the same as that for the surfactant monomer.

5.3.2 Steady-state solutions

The solution to the steady-state version of (5.17) is given by

$$S = S_0, \qquad C = \frac{1}{b S_0^2}, \qquad B = \Gamma \mathrm{e}^{-bx}, \tag{5.23a}$$

where S_0 and b are the solutions to

$$2\frac{\Gamma}{b}\left(1 - \mathrm{e}^{-bl}\right) + lS_0 = lS^*, \qquad \frac{\Gamma}{b}\left(1 - \mathrm{e}^{-bl}\right) + \frac{l}{bS_0^2} = lC^*, \tag{5.23b}$$

and Γ satisfies the adsorption isotherm (5.11). Hence, the number of bilayers, n, which is given by expression (5.14), depends on the adsorption isotherm parameters, α_{m}, $\kappa_0^{\pm}$, and also the bulk concentrations of surfactant and calcium, S^* and C^*. Therefore, the model (5.17) is able to describe fully the dependence of the adsorbed multilayer structure on both the bulk surfactant and calcium concentrations.

In the following section we compare the two models presented for multilayer formation and rearrangement. In §5.4.3 we suggest future work that could be performed to reconcile our model with experiments that our collaborator performs.

5.4 Summary

5.4.1 Comparison of the two models

Experimental observations have shown that, in the absence of calcium ions, monolayer adsorption will occur in LAS and so we made the assumption that calcium ions do not reside in the monolayer. Hence, both models, when in equilibrium, have the same adsorption isotherm for the concentration of surfactant in the monolayer. The dimensional form of the isotherm depends on the three dimensional parameters $\Gamma_{\rm sat}$, k_0^-/k_0^+ and $k_{\rm m}/k_0^+$, which can, in principle, be determined by fitting to experimental data for the adsorbed concentration at the surface.

In comparison, and as discussed in §5.1, multilayer formation for the anionic surfactants of interest is initiated by the addition of electrolyte. Thus, the surfactant-only model does not incorporate this key physical assumption. However, the model can be modified by appropriately introducing a rate constant that depends on the bulk calcium concentration, C_b, into the bilayer formation term, *i.e.* the surfactant equation would read

$$\frac{1}{\Gamma^*}S_t = S_{xx} - 2\kappa\left(K(C_b)|B_x|S^2 - B\right). \tag{5.24}$$

A semi-empirical relationship for the rate function $K(C_b)$ could be determined by fitting the number of bilayers, n, determined from the steady-state model to experimental data for varying bulk surfactant and calcium concentrations. Thus, there would be one less equation to fit to the data compared to the free-surfactant and free-calcium steady-state model of §5.3.2. However, as discussed in §5.1.3 the temporal evolution of the multilayer depends on the method of initial addition of calcium to the surfactant solution. Hence, the modification to the surfactant-only model given above would not capture the diffusion of the calcium ions and so an additional equation for the calcium concentration is still required.

5.4.2 A note on microscopic reversibility

In this chapter we extended the existing model for bilayer rearrangement in the multilayer structure to incorporate more of the physical chemistry of the systems described in §5.1. Thus, one should check that the new models preserve *microscopic reversibility*, a principle first postulated by Richard C. Tolman in 1924 [38]. It states that for a system in thermodynamic equilibrium

"*the total number of molecules leaving a given quantum state in unit time shall equal the number arriving in that state in unit time, but also the the number leaving by any one particular path shall be equal to the number arriving by the reverse of that particular path*".

Put simply, this means that at equilibrium each individual reaction of a system occurs in such a way that the forward and backward rates are equal. Usually, this is made clear if the reactions can be written down such that the 'reversing' of reaction arrows corresponds to the microscopic 'reversing of time'. At first glance, it is not clear that the microscopic multilayer model presented in Chapter 4 preserves microscopic reversibility. However, it is possible for microscopic reversibility to hold provided there is a constraint on the rate parameters. We illustrate this by considering the movement of a bilayer molecule in the ith layer to the $(i-1)^{\text{th}}$ layer shown schematically in Figure 5.4(a) and given by the 'forward reaction'

$$\bar{B}_i + \bar{V}_{i-1} \overset{\bar{a}_{i-1}}{\rightarrow} \bar{B}_{i-1}, \tag{5.25}$$

where we use the over-bar notation from §4.2.1 to represent the number of molecules of a species. The reverse of this reaction is the movement of a bilayer molecule in the $(i-1)^{\text{th}}$ layer to the ith layer shown schematically in Figure 5.4(b) and given by the 'backward reaction'

$$\bar{B}_{i-1} + \bar{H}_i \overset{\bar{d}_i}{\rightarrow} \bar{B}_i. \tag{5.26}$$

The increase/decrease in the different states for the forward/backward reactions are summarised in Table 5.7. Hence, for the reactions above the number of molecules (in this definition we assume a vacancy to be a molecule) leaving and entering a state in unit time are equal provided that $\bar{a}_{i-1} = \bar{d}_i$. Similarly, if we considered all other possible reactions we would require that $\bar{b}_{i-1} = \bar{c}_i$. For the system to be in equilibrium we also require that the product of the individual reaction rates to reach a given state is equal to the product of the reaction rates for the reverse steps. We

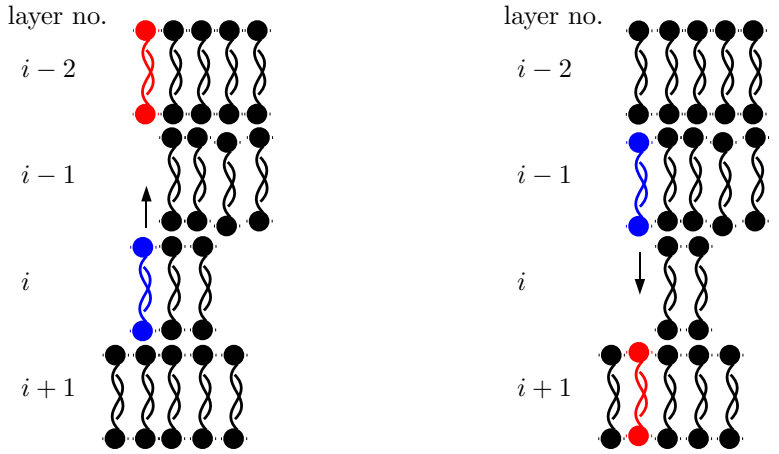

(a) forward reaction (b) backward reaction

Figure 5.4: Schematic of (a) the forward reaction (5.25) and (b) the backward reaction (5.26). The blue bilayer molecule denotes the molecule that is moving between layers and the red bilayer molecule denotes the site for adsorption.

	B_{i-1}	B_i	V_{i-1}	V_i	H_{i-1}	H_i
Forward reaction	$+1$	-1	-1	$+1$	-1	$+1$
Backward reaction	-1	$+1$	$+1$	-1	$+1$	-1

Table 5.7: The change in the number of molecules in different states per unit time for the forward and backward reactions (5.25) and (5.26).

note that if we assume all the rate constants are equal then this holds. Thus, for the macroscopic model the rearrangement function α should either be constant or time dependent such that in the large t limit $\alpha(x,t)$ tends towards a constant.

The reaction for formation of bilayer molecules from free surfactant monomer given by (5.1) is a simplification of the full multi-step reaction

$$2\bar{S}_i \rightleftharpoons \text{dimer}_i \overset{+\text{adsorption site}}{\rightleftharpoons} \bar{B}_i, \tag{5.27}$$

where dimer_i denotes a free pair of surfactant molecules in the ith compartment that are not adsorbed to a bilayer. The intermediate step for the formation of free dimers is assumed to occur instantaneously and so we have neglected this step in our model. However, the reversibility of this multi-step reaction indicates that microscopic reversibility holds for the free-surfactant model. A similar justification can be used for the calcium-surfactant model of §5.3.

5.4.3 Future work

A significant limitation of the two models presented in this chapter is the assumption that the diffusivities for surfactant monomers and calcium ions are constant. It is more physically relevant to assume that the diffusion of the bulk species through the multilayer depends on its structure and so an extension to both models would be to allow the diffusivities to depend on the bilayer concentration. Such an extension of the models may not guarantee the form of the steady-state solutions presented in §5.2.2 and §5.3.2, and so may introduce additional unknown parameters to fit with equilibrium data.

At present, there is insufficient equilibrium data to fit our steady-state models for the number of bilayers and determine the unknown parameters. However, more recently our collaborators have made some preliminary measurements for the dissolution of a multilayer structure for the LAS/Ca^{2+} system. The experimental set-up they consider is identical to that presented in Chapter 3 for the monolayer case. They use NR measurements to track the net concentration of adsorbed surfactant at the interface with time. Thus, future work would be to consider a similar mathematical model to that presented in Chapter 3, which incorporates the multilayer dynamics. A similar diffusion-limited model could be used, with H_c known from the monolayer dilution experiments, to determine the unknown parameters of the new model from fitting to the experimental data.

Chapter 6

Conclusions

In this chapter we summarise the main results of our work and suggest related theoretical and experimental work that could be carried out in future. Finally, we discuss the implications of our work for the theoretical framework of surfactant self-assembly at interfaces.

6.1 Summary

In Chapter 1 we gave an overview of surfactant and polymer–surfactant systems and the self-assembled structures at interfaces exhibited by these systems. We discussed the domestic, industrial, and biological applications of surfactants and polymers and how self-assembled structures can be exploited in such applications, which motivated the work done in this thesis. We presented a review of terminology, existing mathematical models, and adsorption isotherms for surfactant and polymer–surfactant systems. We briefly discussed how neutron reflectometry is used to probe the surface of the air-water interface of surfactant-containing solutions and hence, how self-assembled structures residing there can be interpreted.

We extended the work of Breward and Howell [6] in Chapter 2 by considering the straining flow of a weakly interacting polymer–surfactant solution. We discussed how the mathematical model could be applied to the overflowing cylinder experiment, and hence, described the resulting dynamics of the polymer-surfactant solution. In the analysis of the model we considered both the equilibrium limit and the large-aggregation-number limit and hence showed that there are four distinct regions in the solution domain, in which phase transitions occur. We were able to determine analytical expressions that depend upon the physical parameters of the model for the boundaries of these regions.

In Chapter 3 we presented results of the kinetic monolayer dissolution experiments performed by our experimental collaborators, Jeff Penfold and co-workers, using NR. The experiment was performed for the surfactant LAS, using different geometries and different dilution regimes. The experimental results show that the dissolution of the adsorbed monolayer at the surface follows a broadly similar pattern for the six different experimental set-ups. For simplicity, we first neglected the flow of the experiment and considered a diffusion-limited model for the surfactant phases that was parameterised by an unknown depth, H_c. By using H_c to fit the diffusion-limited model to the data we obtained very good agreement between the two. We also observed that there is a relationship between H_c and the reduced Péclet number, Pe^*, for the experiment. By coupling the surfactant phases to the fluid dynamics of the problem we demonstrated that there would be a diffusive boundary layer near the free surface whose dimensionless thickness scales with $(Pe^*)^{-1/2}$, which corroborates the results of matching the diffusion-limited model to the data. The numerical simulations of the full problem agree with this hypothesis and give further insight into the dynamics near the surface characterised by advected Marangoni-convection cells. Thus, we were able to deduce a semi-empirical relationship between H_c and the reduced Péclet number.

In Chapter 4 we considered the dynamics of the rearrangement of surfactant in a multilayer structure that forms beneath an adsorbed monolayer at an interface. We considered the microscopic movement of bilayer molecules between layers in the multilayer and under these assumptions were able to derive a mesoscopic model. The numerical solutions to the mesoscopic model show interesting features of the dynamics of the bilayer re-arrangement. Most notable is the existence of 'smooth humps' and 'sharp troughs' in the solution, which can be thought to describe the heterogeneous mosaic spread of the lamellar stacks observed experimentally [27]. By considering the large bilayer-limit we derived a macroscopic model described by a novel third-order nonlinear PDE for the distribution of bilayer molecules. The evolution of the monolayer for both the meso- and macroscopic models is governed by an ODE similar to the Langmuir-Hinshelwood equation [8]. We also showed that the models can be extended to a situation where the surfactant adosrbs onto two surfaces that are in close proximity to one another. The resulting macroscopic model is an implicit free-boundary problem, in which the derivative of the bilayer concentration is discontinuous across the free boundary for all time. We were able to show, in the small time analysis, that a corner forms instantaneously in the solution from smooth initial

data. Thus, for this physical set-up and the surfactant systems of interest there will always be a global minimum in the bilayer distribution in the multilayer structure.

We extended the multilayer model of Chapter 4 to include free surfactant monomers and free electrolyte in Chapter 5. We first reviewed the current literature for electrolytic self-assembly of surfactants, which then instructed us on the modelling assumptions for §5.2 and §5.3. The two models for free surfactant and free surfactant/electrolyte presented in §5.2 and §5.3 describe the dynamics of bilayer formation and rearrangement, the diffusion of the free surfactant monomers and electrolyte, and the adsorption of surfactant in the monolayer. The isotherm we derived for the adsorbed surfactant in the monolayer takes into account the movement of surfactant between the monolayer and the first bilayer in the structure but can be reduced to the Langmuir isotherm under certain parameter constraints. For the case where the system is assumed to be in steady state we derived a relationship between the number of bilayers in the multilayer structure and the bulk concentrations of surfactant and electrolyte. Finally we discussed how one could, in principle, compare the results of the two models to experimental data.

6.2 Future work

The majority of the models in this thesis have been made more tractable by asymptotic methods that exploit the large (or small) parameters of the model. Thus, there is much work that could be done to determine numerical solutions to the full models.

In Chapter 2 we considered the equilibrium limit in which we assumed that the micellar and polymer-micelle aggregate rate parameters K_0 and K_1 respectively were infinitely large. As discussed in §2.3, there will in general be small regions near the surface where this assumption fails and so a more detailed asymptotic analysis is required to determine the dynamics of the solution in this region. Furthermore, these two dimensionless parameters depend on the rate parameters k_0^- and k_1^-, which are in general unknown. Thus, provided that there is experimental data available, an extension to this work would be to determine the values of these rate parameters by matching the solutions to the model for finite values of K_0 and K_1 (*cf.* [6]).

In Chapter 3 we suggest two experiments that could be performed to verify the results of our models and gain more insight into the surface dynamics of the flow cell. We omit a detailed discussion of this here and refer the reader to §3.5.1. Although

the numerical solutions to the fluid-surfactant model agree qualitatively with the experimental data, we were unable to determine a full asymptotic description of the model. It is hoped that future analysis of this interesting matched-asymptotic problem would provide further corroboration for the semi-empirical relationship (3.56) between the depth of the diffusive boundary layer and the physical parameters of the model.

The majority of the analysis performed in Chapter 4 was of mathematical interest and so there are few extensions that would be of interest to our chemistry collaborators. However, there are many aspects of the analysis that require continuation in order to obtain a complete description of the macroscopic model. The questions we wish to answer and that form the basis of future work for this chapter are as follows.

(i) How do different forms of the rearrangement parameter, $\alpha(B, x, t)$, influence the resulting multilayer evolution?

(ii) In the linear stability analysis of §4.3.4, can the stability of the solution for the case when the eigenvalue λ is complex be determined?

(iii) If one relaxes the assumption that $B(x, t)$ is monotonic either side of the free boundary in the two-adsorbing boundary macroscopic model of §4.4.2, then what happens to the resulting evolution of $B(x, t)$?

The results of Chapter 5 are very much preliminary work in the modelling of electrolytic self-assembly at interfaces. Thus, there is much more theoretical and experimental work to be done with these models and a detailed discussion of future work was given in §5.4.3.

6.3 Discussion

In this thesis we have developed dynamic models for the description of self-assembly of surfactant solutions at interfaces. We systematically derived a range of models that describe the adsorption processes for surfactant-only, polymer–surfactant, and surfactant–electrolyte systems in either static or flowing regimes. These models provide fundamental understanding of the dynamic processes involved in self-assembly at interfaces. Where possible we were able to draw good comparisons with experimental data and use the models to predict features not known from the experiments themselves. Where experimental data was not available we discussed how one might in future perform and/or design experiments to test the results of the models presented in this thesis.

Appendix A

Experimental data for the kinetic monolayer dilution experiment

The data obtained for the kinetic monolayer dilution experiments described in Chapter 3 using NR are presented in Tables A.1–A.6.

Time (mins)	3	9	15.5	23.5	31.5	38	44.5	56	67	73.5
Adsorbed concentration ($\times 10^{-6}$ mol m^{-2})	2.92	2.71	2.23	1.97	1.91	2.21	2.27	2.42	2.41	2.27

Table A.1: Experiment 1: large footprint trough, small weir, 2.5 ml/min flow rate, 30 mL solution volume and a $\times 2$ volume exchange. Surfactant: 2 mM LAS-4.

Time (mins)	6.5	19.5	33	47	65
Adsorbed concentration ($\times 10^{-6}$ mol m^{-2})	2.55	2.05	1.69	1.69	2

Table A.2: Experiment 2: small footprint trough, small weir, 2.5 ml/min flow rate, 15 mL solution volume and a $\times 2$ volume exchange. Surfactant: 2 mM LAS-4.

Time (mins)	6.5	19.5	33	46.5	60	73.5	87	101.5
Adsorbed concentration ($\times 10^{-6}$ mol m^{-2})	2.63	2.76	2.47	2.1	1.72	1.61	1.61	1.56

Table A.3: Experiment 3: small footprint trough, small weir, 1.25 ml/min flow rate, 15 mL solution volume and a $\times 4$ volume exchange. Surfactant: 2 mM LAS-4.

Time (mins)	7	21	34.5	47.5	60.5	74	87.5	101
Adsorbed concentration ($\times 10^{-6}$ mol m^{-2})	2.8	2.78	2.69	2.46	2.16	1.79	1.79	1.87

Table A.4: Experiment 4: small footprint trough, small weir, 0.625 ml/min flow rate, 15 mL solution volume and a $\times 2$ volume exchange. Surfactant: 2 mM LAS-4.

Time (mins)	6.5	19.5	33	46.5	60	73.5	86.5	100
Adsorbed concentration ($\times 10^{-6}$ mol m^{-2})	2.98	2.97	2.72	2.37	2.31	2.33	2.21	2.31

Table A.5: Experiment 5: small footprint trough, large weir, 0.625 ml/min flow rate, 25 mL solution volume and a $\times 2$ volume exchange. Surfactant: 2 mM LAS-4.

Time (mins)	4	12	19.5	26	32.5	39.5	46
Adsorbed concentration ($\times 10^{-6}$ mol m^{-2})	2.23	2.28	2.43	2.41	2.355	2.18	2.39
Time (mins)	52.5	59	65.5	72	78.5	85	
Adsorbed concentration ($\times 10^{-6}$ mol m^{-2})	2.24	2.34	2.32	2.39	2.28	2.33	

Table A.6: Experiment 6: large footprint trough, small weir, 2.5 ml/min flow rate, 30 mL solution volume and a $\times 2$ volume exchange. Surfactant: 2 mM LAS-6.

Appendix B

Implementation of the kinetic monolayer dilution experiment using COMSOL Multiphysics

In Chapter 3 we present numerical simulations of the kinetic monolayer dilution experiment using COMSOL Multiphysics version 4.3 software. To use COMSOL's inbuilt fluid dynamics model we rescale the variables as follows

$$x, u \sim \epsilon, \qquad p \sim \epsilon^2. \tag{B.1}$$

For simplicity we assume that the solution is submicellar initially and so rescale the surfactant monomer concentration via

$$S \sim \frac{S_{\mathrm{CMC}}}{S_b}, \tag{B.2}$$

which corresponds to the dimensional monomer concentration being nondimensionalised with the bulk surfactant concentration, S_b. Under the rescalings (B.1) and (B.2) the model given by (3.46)–(3.48f) is now given by

$$\nabla \cdot \mathbf{u} = 0, \tag{B.3a}$$

$$Re^* \frac{D\mathbf{u}}{Dt} = -\nabla p + \nabla^2 \mathbf{u}, \tag{B.3b}$$

$$\frac{\partial S}{\partial t} + \mathbf{u}\cdot\nabla S = \frac{1}{Pe^*}\nabla^2 S, \tag{B.3c}$$

$$-\frac{1}{Pe^*}S_y\Big|_{y=1} = \frac{\lambda_D}{\beta+S}\left(\frac{\beta S_t}{\beta+S} + Su_{sx} + \frac{\beta u_s S_x}{\beta+S} - \beta\frac{D^*}{Pe^*}\left(\frac{S_{xx}}{\beta+S} - \frac{2S_x^2}{(\beta+S)^2}\right)\right)\Big|_{y=1}, \tag{B.3d}$$

and boundary conditions

$$y=0: \qquad u=v=S_y=0, \tag{B.3e}$$

$$y=1: \qquad (u_y+v_x) = -\frac{Ma}{\epsilon}\frac{S_x}{\beta+S}, \quad v=0, \tag{B.3f}$$

$$x=0: \qquad u=\frac{6}{\epsilon h_w}\frac{y}{h_w}\left(1-\frac{y}{h_w}\right), \quad v=S=0, \qquad 0<y<h_w, \tag{B.3g}$$

$$u=v=S_x=0, \qquad h_w<y<1, \tag{B.3h}$$

$$x=1/\epsilon: \qquad p=S_x=0, \qquad 0<y<h_w, \tag{B.3i}$$

$$u=v=S_x=0, \qquad h_w<y<1. \tag{B.3j}$$

The initial conditions are

$$\mathbf{u}=\mathbf{0} \qquad \text{and} \qquad S=1. \tag{B.3k}$$

The adsorbed concentration is given by the Langmuir isotherm

$$\Gamma = \frac{S}{\beta+S}. \tag{B.4}$$

Under this scaling the dimensionless time for the dilution to occur is given by

$$T = \frac{2}{\epsilon < u >}, \quad \text{where} \quad < u > = \int_0^{h_w} \frac{6}{\epsilon h_w}\frac{y}{h_w}\left(1-\frac{y}{h_w}\right)\,\mathrm{d}y = \frac{1}{\epsilon}, \tag{B.5}$$

i.e. $T=2$.

The definitions of the dimensionless parameters of the model and typical values are given in Table B.1.

Parameter	Expression	Description	Value
ϵ	H_f/L	aspect ratio	5.9×10^{-2}
Re^*	$\epsilon^2 \rho U L/\mu$	reduced Reynolds number	2.9×10^{-2}
Pe^*	$\epsilon^2 U L/D_s$	reduced Péclet number	8.9×10^{1}
Ma	$RT\Gamma_{\mathrm{sat}}/\mu U$	Marangoni number	$4.4{\times}10^{4}$
λ_D	$\Gamma_{\mathrm{sat}}/H_f S_b$	ratio of adsorbed to net surfactant conc.	6.6×10^{-4}
β	k/S_b	dimensionless Langmuir rate constant	1.2×10^{-1}
h_w	H_w/H_f	dimensionless weir height	3.7×10^{-1}
D	D_{s_m}/D_s	ratio of diffusion coefficients	2.7×10^{-1}
D^*	D_Γ/D_s	ratio of diffusion coefficients	1.8
N	–	aggregation number	53

Table B.1: Definitions of the relevant dimensionless parameters and corresponding typical values for the kinetic monolayer dilution Experiment 2.

B.1 Implementation in COMSOL

We want to solve (B.3a)–(B.3k) using COMSOL Multiphysics. To do this we use the 'Laminar Flow' node and the 'Transport of Diluted Species' node. Boundary conditions (B.3e) and (B.3g)–(B.3j) are straight forward to implement using the standard boundary condtions available. However, we note that to avoid discontinuities in the gradient of the velocity we 'ramp-up' the inlet boundary condition from $t = 0$ using a smooth step function, *e.g.* boundary condition (B.3g) is implemented as

$$u = \frac{6}{\epsilon h_w}\frac{y}{h_w}\left(1 - \frac{y}{h_w}\right)\mathrm{step}(t), \quad 0 < y < h_w, \tag{B.6}$$

where $\mathrm{step}(t)$ is a smooth step function from 0 to 1. To implement boundary condition (B.3f) we apply a 'Symmetry' boundary condition on $y = 1$ and then apply a 'Weak-Contribution' condition which contributes with the slip boundary condition. The weak expression used is

$$-\frac{Ma}{\epsilon}\frac{S_x}{\beta + S}\mathrm{test}(u), \tag{B.7}$$

where $\mathrm{test}(u)$ is some suitable test function. In addition to this we impose point constraints $u_y = 0$ at $(0, 1)$ and $(1/\epsilon, 1)$.

We note the following settings we apply in COMSOL, which differ to the default settings:

Discretisation

- We set the dicretisation of the concentration to quartic.

Mesh

We calibrate for fluid dynamics:

- in the bulk domain, we use Size = 'coarse';
- near the corners $(x, y) = (0, 1), (1/\epsilon, 1)$, we use Size1 = 'finer';
- on the fixed boundaries of the trough, we use Size2 = 'fine';
- on the free-surface $y = 1$, we implement 'boundary Layers' with no. = 12, scaling factor = 1.2.

Solver configurations

- We set the tolerances for the time-dependent solver to be: AbsTol = 0.002, RelTol = 0.001.
- Time stepping - we use backward differentiation formula (BDF) and the maximum BDF order is set to 5.
- In the 'Fully Coupled' feature we set the nonlinear method to 'automatic highly nonlinear (Newton)'.

Appendix C

Numerical methods for the model of self-assembly at interfaces

In Chapter 4 we consider a model for self-assembly at interfaces governed by the PDE

$$\frac{\partial B}{\partial t} = \frac{\partial}{\partial x}\left(\operatorname{sgn}(B_x)\left({B_x}^2 - BB_{xx}\right)\right), \quad 0 < x < 1, \quad 0 < t. \tag{C.1}$$

In this Appendix we summarise the numerical methods used to solve (C.1) for the two cases:

(i) one adsorbing surface, as described in §4.3;

(ii) two adsorbing surfaces, as described in §4.4.

C.1 One-adsorbing-surface problem

For the case of the single adsorbing surface we consider the boundary and initial conditions

$$B = \Gamma, \quad \text{on} \quad x = 0, \quad \text{and} \quad B_x^2 - BB_{xx} = 0, \quad \text{on} \quad x = 0, 1, \tag{C.2}$$

$$B(x, 0) = f(x), \tag{C.3}$$

where there are two possibilities for Γ:

(i) $\Gamma = 1$,

(ii) $\Gamma(t)$ satisfies the ODE

$$\frac{\mathrm{d}\Gamma}{\mathrm{d}t} = 2\bar{\alpha}_{\mathrm{m}}\Gamma(1-\Gamma)^2, \tag{C.4}$$

where $\Gamma(0) = \Gamma_0 < 1$.

For both cases we use method of lines and discretise in space only as follows:

$$B(x,t) \approx u_j(t), \quad x = j\triangle x, \quad j = 0 \ldots J, \tag{C.5}$$

where $\triangle x$ is the space step.

The numerical scheme used to solve used (C.1)–(C.3) numerically for $\Gamma = 1$ and space step $\triangle x = L/J$ is given below

$$u_j(0) = f(j\triangle x), \quad \text{for} \quad j = 1, \ldots, J, \tag{C.6a}$$

$$u_0 = 1, \tag{C.6b}$$

$$\frac{\mathrm{d}u_j}{\mathrm{d}t} = \mathrm{sgn}(u_j - u_{j-1})\Bigg(\left(\frac{u_j - u_{j-1}}{\triangle x}\right)\left(\frac{u_{j+1} - 2u_j + u_{j-1}}{\triangle x^2}\right) - u_j\left(\frac{u_{j+1} - 3u_j + 3u_{j-1} - u_{j-2}}{\triangle x^3}\right)\Bigg), \quad \text{for} \quad j = 1, \ldots J, \tag{C.6c}$$

where

$$u_{-1} = \frac{1}{u_1}, \quad \text{and} \quad u_{J+1} = \frac{u_J^2}{u_{J-1}}. \tag{C.7}$$

The truncation error for this scheme is $O(\triangle x)$.

To solve the problem for a time-dependent adsorbing surface where Γ is given by (C.4) we replace the expressions for u_{-1} and u_0 in the above scheme with

$$u_{-1} = \frac{u_0^2}{u_1} \quad \text{and} \quad \frac{\mathrm{d}u_0}{\mathrm{d}t} = 2\bar{\alpha}_{\mathrm{m}}u_0(1-u_0)^2. \tag{C.8}$$

C.2 Two-adsorbing-surfaces problem

We now consider two approaches to compute numerical solutions to the model of self-assembly between two adsorbing surfaces given by (4.111) in §4.4. In C.2.1 we reformulate the problem by fixing the moving boundary and discretise using the method of lines and in C.2.2 we consider the numerical solution to the regularised problem (4.120).

C.2.1 Numerical scheme that solves for the free boundary

We discretise the transformed problem (4.119) using the method of lines as follows. Let

$$U(X,t) \approx u_j(t), \quad V(X,t) \approx v_j(t), \quad X \approx j\triangle X \quad \text{for} \quad j = 0, \dots J, \tag{C.9}$$

where $\triangle X = 1/J$. The system of differential-algebraic equations for variables $u_1, \dots, u_{J-1}$, $v_1, \dots, v_{J-1}$ and s is given by

$$\begin{aligned}\frac{\mathrm{d}u_j}{\mathrm{d}t} = &-\frac{1}{\triangle X^3 s^3}\left((u_j - u_{j-1})(u_{j+1} - 2u_j + u_{j-1}) - u_j(u_{j+1} - 3u_j + 3u_{j-1} - u_{j-2})\right) \\ &+ \frac{j}{s}\frac{\mathrm{d}s}{\mathrm{d}t}(u_j - u_{j-1}), \qquad j = 1, \dots J-1, \end{aligned} \tag{C.10a}$$

$$\begin{aligned}\frac{\mathrm{d}v_j}{\mathrm{d}t} = &-\frac{1}{\triangle X^3 (s-1)^3}\left((v_j - v_{j-1})(v_{j+1} - 2v_j + v_{j-1}) - v_j(v_{j+1} - 3v_j + 3v_{j-1} - v_{j-2})\right) \\ &- \frac{j}{(1-s)}\frac{\mathrm{d}s}{\mathrm{d}t}(v_j - v_{j-1}), \qquad j = 1, \dots J-1, \end{aligned} \tag{C.10b}$$

$$(s-1)(u_J - u_{J-1}) + s(v_J - v_{J-1}) = 0, \tag{C.10c}$$

where

$$u_0 = \Gamma_L, \quad v_0 = \Gamma_R, \quad v_J = u_J, \tag{C.11}$$

and the ghost points are given by

$$u_{-1} = \frac{1}{2}\left(3u_0 - \sqrt{u_0(4u_1 - 3u_0)}\right), \tag{C.12a}$$

$$v_{-1} = \frac{1}{2}\left(3v_0 - \sqrt{v_0(4v_1 - 3v_0)}\right). \tag{C.12b}$$

We determine u_J by replacing (4.119e) with the conservation of mass equation

$$\int_0^1 s(t)U(X,t) - (s(t)-1)V(X,t)\ \mathrm{d}X = M \tag{C.13}$$

and discretise to obtain

$$u_J = \frac{1}{4}\Bigg[- \left(u_0 + v_0 - u_{J-1} - v_{J-1} - \frac{4M}{\triangle X} + 2\sum_{j=1}^{J-1} u_j + v_j \right) - \Bigg(\left(u_0 + v_0 - u_{J-1} - v_{J-1} - \frac{4M}{\triangle X} + 2\sum_{j=1}^{J-1} u_j + v_j \right)^2 - 4\left(u_{J-1}\left(\frac{2M}{\triangle X} - u_0 - 2\sum_{j=1}^{J-1} u_j \right) + v_{J-1}\left(\frac{2M}{\triangle X} - v_0 - 2\sum_{j=1}^{J-1} v_j \right) \right) \Bigg)^{1/2} \Bigg]. \tag{C.14}$$

The truncation error for this scheme is $O(\triangle X)$.

C.2.2 Numerical scheme for the regularized problem

We discretise the regularised problem (4.120) using the finite-volume method:

$$B(x,t) = u_j(t), \qquad x = j\triangle x, \qquad \text{for} \quad j = 0, \dots J, \tag{C.15a}$$

$$\frac{\mathrm{d}u_j}{\mathrm{d}t} = \frac{Q_{j+1/2} - Q_{j-1/2}}{2\triangle x}, \qquad \text{for} \quad j = 1, \dots J-1, \tag{C.15b}$$

where

$$Q_{j+1/2} = \operatorname{sgn}(u_{x,j+1/2})(u_{x,j+1/2}^2 - u_{j+1/2}u_{xx,j+1/2}) + \epsilon\left(u_{x,j+1/2}u_{xx,j+1/2} - u_{j+1/2}u_{xxx,j+1/2}\right), \quad \text{for} \quad j = 1, \dots J-1, \tag{C.15c}$$

$$Q_{j-1/2} = \operatorname{sgn}(u_{x,j-1/2})(u_{x,j-1/2}^2 - u_{j-1/2}u_{xx,j-1/2}) + \epsilon\left(u_{x,j-1/2}B_{xx,j-1/2} - u_{j-1/2}u_{xxx,j-1/2}\right), \quad \text{for} \quad j = 2, \dots J, \tag{C.15d}$$

$$Q_{1/2} = Q_{(J-1)+1/2} = 0, \quad u_0 = \Gamma_L, \quad u_J = \Gamma_R, \tag{C.15e}$$

and

$$u_{j+1/2} = \frac{u_j + u_{j+1}}{2}, \qquad u_{j-1/2} = \frac{u_j + u_{j-1}}{2}, \tag{C.15f}$$

$$u_{x,j+1/2} = \frac{u_{j+1} - u_j}{\triangle x}, \qquad u_{x,j-1/2} = \frac{u_j - u_{j-1}}{\triangle x}, \tag{C.15g}$$

$$u_{xx,j+1/2} = \frac{u_{j+2} - 2u_{j+1} + u_j}{\triangle x^2}, \qquad u_{xx,j-1/2} = \frac{u_{j+1} - 2u_j + u_{j-1}}{\triangle x^2}, \tag{C.15h}$$

$$u_{xxx,j+1/2} = \frac{u_{j+2} - 3u_{j+1} + 3u_j - u_{j-1}}{\triangle x^3}, \qquad u_{xxx,j-1/2} = \frac{u_{j+1} - 3u_j + 3u_{j-1} - u_{j-2}}{\triangle x^3}. \tag{C.15i}$$

The truncation error for this scheme is $O(\triangle x)$.

Appendix D

Derivation of models presented in Chapter 5

In this appendix we derive the dimensionless macroscopic models presented in Chapter 5 for the evolution of a multilayer with free surfactant monomers and calcium ions in the bulk. We follow the derivation presented in §4.3.1 for the multilayer-only model and so omit some of the details that have already been presented there.

D.1 Free-surfactant model

As in §4.3.1 we consider the one-dimensional domain $D := \{x : x \in [0, L]\}$, where the x-axis points downwards into the solution and the boundary $x = 0$ corresponds to the adsorbing surface. The domain D is divided into K compartments each of length h so that the ith compartment represents the ith bilayer in the multilayer structure for $i = 1, ..., K$. We denote the concentration of bilayer molecules and free surfactant monomers in the ith compartment by B_i and S_i, for $i = 1, ..., K$, which have units $\text{mol}\,\text{m}^{-2}$ and $\text{mol}\,\text{m}^{-3}$ respectively. We assume that surfactant must dissociate into free monomers before adsorbing at the surface $x = 0$ and we denote the concentration of adsorbed surfactant monomers by Γ, which has units $\text{mol}\,\text{m}^{-2}$. We assume the additional single-step reactions below, as discussed in §5.2, for the concentration of free surfactant monomers, bilayer molecules and adsorbed surfactant.

1. The formation of a monolayer from free surfactant is given by

$$S_1 + \text{adsorption site in monolayer} \underset{r_0^-}{\overset{r_0^+}{\rightleftharpoons}} \Gamma, \tag{D.1}$$

where r_0^+ and r_0^- are the adsorption and desorption rate constants, respectively.

2. Bilayer molecules form from free surfactant monomers according to

$$2S_i + \text{adsorption site} \underset{r_i^-}{\overset{r_i^+}{\rightleftharpoons}} B_i,$$

where r_i^+ and r_i^- are the formation and dissociation rate constants for a bilayer molecule, respectively.

3. Surfactant monomers move randomly throughout the domain according to the set of diffusion reactions

$$S_1 \underset{d}{\overset{d}{\rightleftharpoons}} S_2 \underset{d}{\overset{d}{\rightleftharpoons}} \dots \underset{d}{\overset{d}{\rightleftharpoons}} S_{K-1} \underset{d}{\overset{d}{\rightleftharpoons}} S_K, \tag{D.2}$$

where d is the diffusion reaction rate constant.

In addition, if we assume the reactions that describe the movement of bilayer molecules between layers given in §4.2.1 then by the law of mass action the concentrations Γ, S_i, and B_i satisfy the system of ordinary differential equations:

$$\frac{\mathrm{d}\Gamma}{\mathrm{d}t} = 2\left(Q_{\mathrm{m}}^a - Q_{\mathrm{m}}^b - Q_{\mathrm{m}}^d\right) + r_0^+ S_1(\Gamma_{\mathrm{sat}} - \Gamma) - r_0^-\Gamma, \tag{D.3a}$$

$$\frac{\mathrm{d}B_1}{\mathrm{d}t} = -\left(Q_{\mathrm{m}}^a - Q_{\mathrm{m}}^b - Q_{\mathrm{m}}^d\right) + Q_1^a - Q_2^b + Q_1^c - Q_2^d + r_1^+ S_1^2\left((\Gamma - B_1)^+ + (B_2 - B_1)^+\right) - r_1^- B_1, \tag{D.3b}$$

$$\frac{\mathrm{d}B_i}{\mathrm{d}t} = Q_i^a - Q_{i-1}^a + Q_i^b - Q_{i+1}^b + Q_i^c - Q_{i-1}^c + Q_i^d - Q_{i+1}^d + r_i^+ S_i^2\left((B_{i-1} - B_i)^+ + (B_{i+1} - B_i)^+\right) - r_i^- B_i, \quad \text{for} \quad i = 2, \dots, K-2, \tag{D.3c}$$

$$\frac{\mathrm{d}B_{K-1}}{\mathrm{d}t} = Q_{K-1}^a - Q_{K-2}^a + Q_{K-1}^b - Q_K^b + Q_{K-1}^c - Q_{K-2}^c + Q_{K-1}^d + r_{K-1}^+ S_{K-1}^2\left((B_{K-2} - B_{K-1})^+ + (B_K - B_{K-1})^+\right) - r_{K-1}^- B_{K-1}, \tag{D.3d}$$

$$\frac{\mathrm{d}B_K}{\mathrm{d}t} = -Q_{K-1}^a + Q_K^b - Q_{K-1}^c + r_K^+ S_K^2 (B_{K-1} - B_K)^+ - r_K^- B_K, \tag{D.3e}$$

$$\frac{\mathrm{d}S_1}{\mathrm{d}t} = d(S_2 - S_1) - \frac{1}{h}\left(r_0^+ S_1(1-\Gamma) - r_0^-\Gamma\right) - \frac{2}{h}\left(r_1^+ S_1^2\left((\Gamma - B_1)^+ + (B_2 - B_1)^+\right) - r_1^- B_1\right), \tag{D.3f}$$

$$\frac{\mathrm{d}S_i}{\mathrm{d}t} = d(S_{i+1} - 2S_i + S_{i-1}) - \frac{2}{h}(r_i^+ S_i^2\left((B_{i-1} - B_i)^+ + (B_{i+1} - B_i)^+\right) - r_i^- B_i), \quad \text{for} \quad i = 2, \ldots, K-1, \tag{D.3g}$$

$$\frac{\mathrm{d}S_K}{\mathrm{d}t} = d(-S_K + S_{K-1}) - \frac{2}{h}\left(r_K^+ S_K^2 (B_{K-1} - B_K)^+ - r_K^- B_K\right), \tag{D.3h}$$

where the fluxes are given by

$$Q_{\mathrm{m}}^a = a_{\mathrm{m}} V_{\mathrm{m}}^2 B_1 = a_{\mathrm{m}}(\Gamma_{\mathrm{sat}} - \Gamma)^2 B_1, \tag{D.4a}$$

$$Q_{\mathrm{m}}^b = b_{\mathrm{m}} V_1 \Gamma^2 = b_{\mathrm{m}}\left(\Gamma - B_1\right)^+ \Gamma^2, \tag{D.4b}$$

$$Q_{\mathrm{m}}^d = d_{\mathrm{m}} H_1 \Gamma^2 = d_{\mathrm{m}}\left(B_2 - B_1\right)^+ \Gamma^2, \tag{D.4c}$$

$$Q_1^a = a_1 V_1 B_2 = a_1(\Gamma - B_1)^+ B_2, \tag{D.4d}$$

$$Q_i^a = a_i V_i B_{i+1} = a_i\left(B_{i-1} - B_i\right)^+ B_{i+1}, \quad \text{for} \quad i = 2, \ldots, K-1, \tag{D.4e}$$

$$Q_i^b = a_i V_i B_{i-1} = a_i\left(B_{i-1} - B_i\right)^+ B_{i-1}, \quad \text{for} \quad i = 2, \ldots, K, \tag{D.4f}$$

$$Q_i^c = a_i H_i B_{i+1} = a_i\left(B_{i+1} - B_i\right)^+ B_{i+1}, \quad \text{for} \quad i = 1, \ldots, K-1, \tag{D.4g}$$

$$Q_i^d = a_i H_i B_{i-1} = a_i\left(B_{i+1} - B_i\right)^+ B_{i-1}, \quad \text{for} \quad i = 2, \ldots, K-1. \tag{D.4h}$$

Summing (D.8) leads to the conservation–of–mass equation

$$\Gamma + 2\sum_{i=1}^{K} B_i + hS_i = hS_b, \tag{D.5}$$

where S_b is the net concentration of surfactant which has units $\mathrm{mol\,m^{-3}}$.

D.1.1 Nondimensionalisation

We nondimensionalise the variables of the model as follows

$$t = \frac{1}{a_1 \Gamma_{\text{sat}} \epsilon^3} t', \qquad \Gamma = \Gamma_{\text{sat}} \Gamma', \qquad B_i = \Gamma_{\text{sat}} B_i', \qquad S_i = \sqrt{\frac{r^- hH}{k^+}} S_i', \tag{D.6}$$

where $\epsilon = h/H = 1/K$ and H is the characteristic depth of the multilayer given by

$$H = \left(\frac{\sqrt{r^+} a_1 \Gamma_{\text{sat}}^2}{\sqrt{r^-} hd} \right)^{2/3}. \tag{D.7}$$

Thus, for $H < x \leq L$ the concentration of bilayer molecules is assumed to be negligible.

Substituting the rescaled variables (D.6) into (D.8) and on dropping primes we obtain the system of dimensionless ODEs

$$\epsilon^3 \frac{\mathrm{d}\Gamma}{\mathrm{d}t} = 2\left(Q_{\text{m}}^a - Q_{\text{m}}^b - Q_{\text{m}}^d\right) + \kappa_0^+ S_1 (1 - \Gamma) - \kappa_0^- \Gamma, \tag{D.8a}$$

$$\begin{aligned} \epsilon^3 \frac{\mathrm{d}B_1}{\mathrm{d}t} = &- \left(Q_{\text{m}}^a - Q_{\text{m}}^b - Q_{\text{m}}^d\right) + Q_1^a - Q_2^b + Q_1^c - Q_2^d \\ &+ \epsilon^2 \kappa_1^+ {S_1}^2 \left((\Gamma - B_1)^+ + (B_2 - B_1)^+\right) - \epsilon^3 \kappa_1^- B_1, \end{aligned} \tag{D.8b}$$

$$\begin{aligned} \epsilon^3 \frac{\mathrm{d}B_i}{\mathrm{d}t} = &\, Q_i^a - Q_{i-1}^a + Q_i^b - Q_{i+1}^b + Q_i^c - Q_{i-1}^c + Q_i^d - Q_{i+1}^d \\ &+ \epsilon^2 \kappa_i^+ {S_i}^2 \left((B_{i-1} - B_i)^+ + (B_{i+1} - B_i)^+\right) - \epsilon^3 \kappa_i^- B_i, \\ &\qquad\qquad \text{for} \quad i = 2, \ldots, K-2, \end{aligned} \tag{D.8c}$$

$$\begin{aligned} \epsilon^3 \frac{\mathrm{d}B_{K-1}}{\mathrm{d}t} = &\, Q_{K-1}^a - Q_{K-2}^a + Q_{K-1}^b - Q_K^b + Q_{K-1}^c - Q_{K-2}^c + Q_{K-1}^d \\ &+ \epsilon^2 \kappa_{K-1}^+ {S_{K-1}}^2 \left((B_{K-2} - B_{K-1})^+ + (B_K - B_{K-1})^+\right) \\ &- \epsilon^3 \kappa_{K-1}^- B_{K-1}, \end{aligned} \tag{D.8d}$$

$$\epsilon^3 \frac{\mathrm{d}B_K}{\mathrm{d}t} = -Q_{K-1}^a + Q_K^b - Q_{K-1}^c + \epsilon^2 \kappa_K^+ {S_K}^2 (B_{K-1} - B_K)^+ - \epsilon^3 \kappa_K^- B_K, \tag{D.8e}$$

$$\epsilon^3 \frac{\mathrm{d}S_1}{\mathrm{d}t} = \epsilon D(S_2 - S_1) - \Gamma^* \left(\kappa_0^+ S_1(1-\Gamma) - \kappa_0^- \Gamma\right) - 2\Gamma^* \left(\epsilon^2 \kappa_1^+ {S_1}^2 \left((\Gamma - B_1)^+ + (B_2 - B_1)^+\right) - \epsilon^3 \kappa_1^- B_1\right), \tag{D.8f}$$

$$\epsilon^3 \frac{\mathrm{d}S_i}{\mathrm{d}t} = \epsilon D(S_{i+1} - 2S_i + S_{i-1}) - 2\Gamma^* \left(\epsilon^2 \kappa_i^+ {S_i}^2 \left((B_{i-1} - B_i)^+ + (B_{i+1} - B_i)^+\right) - \epsilon^3 \kappa_i^- B_i\right), \quad \text{for} \quad i = 2, \ldots, K-1, \tag{D.8g}$$

$$\epsilon^3 \frac{\mathrm{d}S_K}{\mathrm{d}t} = \epsilon D(-S_K + S_{K-1}) - 2\Gamma^* \left(\epsilon^2 \kappa_K^+ {S_K}^2 (B_{K-1} - B_K)^+ - \epsilon^3 \kappa_K^- B_K\right), \tag{D.8h}$$

where the fluxes are given in dimensionless form by

$$Q_{\mathrm{m}}^a = \alpha_{\mathrm{m}} V_{\mathrm{m}}^2 B_1 = \alpha_{\mathrm{m}} (1-\Gamma)^2 B_1, \tag{D.9a}$$

$$Q_{\mathrm{m}}^b = \beta_{\mathrm{m}} V_1 \Gamma^2 = \beta_{\mathrm{m}} \left(\Gamma - B_1\right)^+ \Gamma^2, \tag{D.9b}$$

$$Q_{\mathrm{m}}^d = \delta_{\mathrm{m}} H_1 \Gamma^2 = \delta_{\mathrm{m}} \left(B_2 - B_1\right)^+ \Gamma^2, \tag{D.9c}$$

$$Q_1^a = \alpha_1 V_1 B_2 = \alpha_1 (\Gamma - B_1)^+ B_2, \tag{D.9d}$$

$$Q_i^a = \alpha_i V_i B_{i+1} = \alpha_i \left(B_{i-1} - B_i\right)^+ B_{i+1}, \quad \text{for} \quad i = 2, \ldots, K-1, \tag{D.9e}$$

$$Q_i^b = \alpha_i V_i B_{i-1} = \alpha_i \left(B_{i-1} - B_i\right)^+ B_{i-1}, \quad \text{for} \quad i = 2, \ldots, K, \tag{D.9f}$$

$$Q_i^c = \alpha_i H_i B_{i+1} = \alpha_i \left(B_{i+1} - B_i\right)^+ B_{i+1}, \quad \text{for} \quad i = 1, \ldots, K-1, \tag{D.9g}$$

$$Q_i^d = \alpha_i H_i B_{i-1} = \alpha_i \left(B_{i+1} - B_i\right)^+ B_{i-1}, \quad \text{for} \quad i = 2, \ldots, K-1. \tag{D.9h}$$

The dimensionless conservation–of–mass equation is

$$\Gamma + 2\sum_{i=1}^{K} B_i + \frac{1}{\Gamma^*} S_i = S^*, \tag{D.10}$$

where S^* is the dimensionless net concentration of surfactant.

The dimensionless parameters of the model are defined as follows

$$\alpha_i = \frac{a_i}{a_1}, \qquad \alpha_{\mathrm{m}} = \frac{a_{\mathrm{m}}}{a_1}\Gamma_{\mathrm{sat}}, \qquad \beta_{\mathrm{m}} = \frac{b_{\mathrm{m}}}{a_1}\Gamma_{\mathrm{sat}}, \qquad \delta_{\mathrm{m}} = \frac{d_{\mathrm{m}}}{a_1}\Gamma_{\mathrm{sat}},$$

$$\kappa_0^+ = \frac{r_0^+\sqrt{r_1^- hH}}{a_1\sqrt{r_1^+}\Gamma_{\mathrm{sat}}}, \qquad \kappa_0^- = \frac{r_0^-}{a_1\Gamma_{\mathrm{sat}}}, \qquad \kappa_i^+ = \frac{r_i^+ r_1^- hH}{\epsilon^2 a_1 r_1^+ \Gamma_{\mathrm{sat}}}, \qquad \kappa_i^- = \frac{r_i^-}{\epsilon^3 a_i \Gamma_{\mathrm{sat}}},$$

$$D = \frac{d}{a_1\Gamma_{\mathrm{sat}}}, \qquad \Gamma^* = \frac{\Gamma_{\mathrm{sat}}\sqrt{r_1^+}}{h\sqrt{r_1^- hH}}, \qquad S^* = \frac{hS_b}{\Gamma_{\mathrm{sat}}}. \tag{D.11}$$

D.1.2 Derivation of macroscopic model

The continuous approximations to the concentration of bilayer and free monomer molecules in the ith compartment are given by

$$B(x,t) \approx B_i(t), \quad S(x,t) \approx S_i(t), \quad x = i\epsilon, \tag{D.12}$$

where $\epsilon = h/H$ and we assume that B_i, S_i, and the fluxes Q_i are all piecewise continuously differentiable. We also assume that the rate parameters $\kappa_i^{\pm}$ are all equal, *i.e.* we set $r_i^{\pm} = r^{\pm}$, which results in $\kappa^+ = \kappa^- = \kappa$. For convenience we define

$$J_{S_i} = \kappa\left(\epsilon^2 {S_i}^2\left((B_{i-1} - B_i)^+ + (B_{i+1} - B_i)^+\right) - \epsilon^3 B_i\right), \quad \text{for} \quad i = 2, \ldots, K-1. \tag{D.13}$$

Then the leading-order term in the Taylor expansion of J_{S_i} as $\epsilon \to 0$ is given by

$$J_{S_i} \approx \epsilon^3\kappa\left(S^2|B_x| - B\right) + \ldots, \tag{D.14}$$

Thus, to expand (D.8c) and (D.8g) in a Taylor series about $\epsilon = 0$ one can use the results of §4.3.1 and (D.14) to obtain the governing equations to leading order and noting that $D/\Gamma^* = 1$ gives

$$B_t = \left(\alpha(x)\mathrm{sgn}(B_x)({B_x}^2 - BB_{xx})\right)_x + \kappa(|B_x|S^2 - B), \tag{D.15a}$$

$$\frac{1}{\Gamma^*}S_t = S_{xx} - 2\kappa\left(|B_x|S^2 - B\right), \tag{D.15b}$$

for $t > 0$ and $0 < x < l$, where $l = L/H$ is the dimensionless depth of the solution.

To derive the boundary conditions on the adsorbing surface at $x = 0$ we consider the Taylor expansion of equations (D.8a), (D.8b), (D.8c) for $i = 2$, and (D.8f):

$$\epsilon^3\dot{\Gamma} = 2J_{\mathrm{m}} + J_{S_0} \qquad \text{at} \quad x = 0, \tag{D.16a}$$

$$\epsilon^3 B_t + \epsilon^4 B_{tx} + \ldots = J_1 - J_m + J_{S_1} \qquad \text{at} \quad x = 0, \tag{D.16b}$$

$$\epsilon^3 B_t + 2\epsilon^4 B_{tx} + \ldots = J_2 - J_1 + J_{S_2} \qquad \text{at} \quad x = 0, \tag{D.16c}$$

$$\epsilon^3 S_t + 2\epsilon^4 S_{tx} + \ldots = \epsilon^2 D S_x + \ldots + 2\Gamma^*(J_{S_0} + 2J_{S_1}) \qquad \text{at} \quad x = 0. \tag{D.16d}$$

In the limit $\epsilon \to 0$ the J's are given by

$$\begin{aligned} J_{\mathrm{m}} = \;& Q^a_{\mathrm{m}} - Q^b_{\mathrm{m}} - Q^d_{\mathrm{m}} \\ \approx \;& \alpha_{\mathrm{m}}(1-\Gamma)^2\left(B + \epsilon B_x + \frac{1}{2}\epsilon^2 B_{xx}\right) + \ldots \\ & - \beta_{\mathrm{m}}\Gamma^2 H[\Gamma - B]\left(\Gamma - B - \epsilon B_x - \frac{1}{2}\epsilon^2 B_{xx}\right) + \ldots \\ & - \delta_{\mathrm{m}}\Gamma^2 H[B_x]\left(\epsilon B_x + \frac{3}{2}\epsilon^2 B_{xx}\right) + \ldots \Bigg|_{x=0}, \end{aligned} \tag{D.17a}$$

$$\begin{aligned} J_1 = \;& Q^a_1 - Q^b_2 + Q^c_1 - Q^d_2 \\ \approx \;& (\alpha + \epsilon\alpha_x + \ldots)\, H[\Gamma - B]\big((\Gamma - B)B + \epsilon\,(2\Gamma - 3B)\, B_x \\ & + \frac{\epsilon^2}{2}\left(4(\Gamma - B)B_{xx} - 4{B_x}^2 - BB_{xx}\right) + \ldots\big) \\ & + (\alpha + \epsilon 2\alpha' + \ldots)\, H[-B_x]\left(\epsilon B B_x + \epsilon^2\left({B_x}^2 + \frac{3}{2}BB_{xx}\right) + \ldots\right) \\ & + (\alpha + \epsilon\alpha' + \ldots)\, H[B_x]\left(\epsilon B B_x + \epsilon^2\left(2{B_x}^2 + \frac{3}{2}BB_{xx}\right) + \ldots\right) \\ & - (\alpha + \epsilon\alpha' + \ldots)\, H[B_x]\left(\epsilon B B_x + \epsilon^2\left({B_x}^2 + \frac{5}{2}BB_{xx}\right) + \ldots\right)\Bigg|_{x=0}, \end{aligned} \tag{D.17b}$$

$$
\begin{aligned}
J_2 = \;& Q_2^q - Q_3^b + Q_2^c - Q_3^d \\
\approx & -(\alpha + \epsilon\alpha_x + \ldots)\, H[-B_x] \left(\epsilon B B_x + \epsilon^2 \left(3B_x^2 + \frac{3}{2} B B_{xx} \right) + \ldots \right) \\
& + (\alpha + 3\epsilon\alpha' + \ldots)\, H[-B_x] \left(\epsilon B B_x + \epsilon^2 \left(2{B_x}^2 + \frac{5}{2} B B_{xx} \right) + \ldots \right) \\
& + (\alpha + 2\epsilon\alpha' + \ldots)\, H[B_x] \left(\epsilon B B_x + \epsilon^2 \left(3{B_x}^2 + \frac{5}{2} B B_{xx} \right) + \ldots \right) \\
& - (\alpha + 3\epsilon\alpha' + \ldots)\, H[B_x] \left(\epsilon B B_x + \epsilon^2 \left(2{B_x}^2 + \frac{7}{2} B B_{xx} \right) + \ldots \right) \Bigg|_{x=0}, \qquad \text{(D.17c)}
\end{aligned}
$$

$$
J_{S_0} = \kappa_0^+ S_1 (1-\Gamma) - \kappa_0^- \Gamma \approx \kappa_0^+ (S + \epsilon S_x + \ldots)(1-\Gamma) - \kappa_0^- \Gamma \Big|_{x=0}, \qquad \text{(D.17d)}
$$

$$
\begin{aligned}
J_{S_1} &= \kappa(\epsilon^2 {S_1}^2 \left((\Gamma - B_1)^+ + (B_2 - B_1)^+ \right) - \epsilon^3 B_1) \\
&\approx \kappa(\epsilon^2 S^2 \left(H[\Gamma - B](\Gamma - B) + \epsilon(-H[\Gamma - B] B_x + H[B_x] B_x) + \ldots \right) - \epsilon^3 B) \Big|_{x=0},
\end{aligned} \qquad \text{(D.17e)}
$$

$$
\begin{aligned}
J_{S_2} &= \kappa(\epsilon^2 {S_2}^2 \left((B_1 - B_2)^+ + (B_3 - B_2)^+ \right) - \epsilon^3 B_2) \\
&\approx \kappa\epsilon^3 (S^2 \left(|B_x| + \ldots \right) - B) \Big|_{x=0},
\end{aligned} \qquad \text{(D.17f)}
$$

where $'$ denotes differentiation with respect to x.

Following the derivation of the flux boundary condition in §4.3.2.1 we sum equations (D.16):

$$
\epsilon^3 \left(\frac{\mathrm{d}\Gamma}{\mathrm{d}t} + 2B_t + \frac{1}{2\Gamma^*} S_t + \ldots \right) = J_2 + J_{S_2} + \frac{1}{2}\epsilon^2 S_x, \qquad \text{(D.18)}
$$

which to leading order gives the boundary condition

$$
S_x + 2\alpha(x)\mathrm{sgn}(B_x)(B_x^2 - B B_{xx}) = 0, \quad \text{on} \quad x = 0. \qquad \text{(D.19)}
$$

A range of possible scenarios can be derived for the remaining boundary conditions on the free surface by rescaling the rate parameters $\kappa_0^{\pm}$, α_{m}, β_{m}, and δ_{m} appropriately. We focus on the two most physically relevant scalings:

(i) $(\kappa_0^{\pm}, \alpha_{\rm m}, \beta_{\rm m}, \delta_{\rm m}) = \epsilon^2(\bar{\kappa}_0^{\pm}, \bar{\alpha}_{\rm m}, \bar{\beta}_{\rm m}, \bar{\delta}_{\rm m})$,
which corresponds to the adsorbed concentration, Γ, being in equilibrium with the sub-surface phases;

(ii) $(\kappa_0^{\pm}, \alpha_{\rm m}, \beta_{\rm m}, \delta_{\rm m}) = \epsilon^3(\bar{\kappa}_0^{\pm}, \bar{\alpha}_{\rm m}, \bar{\beta}_{\rm m}, \bar{\delta}_{\rm m})$,
which corresponds to the adsorbed concentration, Γ, being out of equilibrium with the sub-surface phases.

For case (i) equations (D.16a), (D.16b), (D.16d) to leading order are

$$0 = 2\bar{\alpha}_{\rm m}(1-\Gamma)^2 B - \bar{\beta}_{\rm m} H[\Gamma - B](\Gamma - B) + \bar{\kappa}_0^+(1-\Gamma)S - \bar{\kappa}_0^-\Gamma, \tag{D.20a}$$

$$0 = \alpha H[\Gamma - B](\Gamma - B), \tag{D.20b}$$

$$0 = DS_x - \Gamma^*(\bar{\kappa}_0^+(1-\Gamma)S - \bar{\kappa}_0^-\Gamma). \tag{D.20c}$$

Thus, the boundary conditions on the free surface are given by

$$B = \Gamma, \quad S_x = (\bar{\kappa}_0^+(1-\Gamma)S - \bar{\kappa}_0^-\Gamma), \qquad \text{on} \quad x = 0, \tag{D.21a}$$

$$\alpha(0)\mathrm{sgn}(B_x)(B_x^2 - BB_{xx}) = \bar{\alpha}_m(1-\Gamma)^2\Gamma, \qquad \text{on} \quad x = 0, \tag{D.21b}$$

where Γ is given by the isotherm

$$2\bar{\alpha}_{\rm m}(1-\Gamma)^2 B + \bar{\kappa}_0^+(1-\Gamma)S - \bar{\kappa}_0^-\Gamma = 0, \quad \text{on} \quad x = 0. \tag{D.21c}$$

For case (ii) equations (D.16a), (D.16b), (D.16d) to leading order are

$$\frac{\mathrm{d}\Gamma}{\mathrm{d}t} = 2\bar{\alpha}_{\rm m}(1-\Gamma)^2 B - \bar{\beta}_{\rm m} H[\Gamma - B](\Gamma - B) + \bar{\kappa}_0^+(1-\Gamma)S - \bar{\kappa}_0^-\Gamma, \tag{D.22a}$$

$$0 = \alpha H[\Gamma - B](\Gamma - B), \tag{D.22b}$$

$$0 = DS_x. \tag{D.22c}$$

Thus, the boundary conditions on the free surface are given by

$$B = \Gamma, \quad S_x = B_x^2 - BB_{xx} = 0, \quad \text{on} \quad x = 0, \tag{D.23a}$$

where Γ evolves according to

$$\frac{\mathrm{d}\Gamma}{\mathrm{d}t} = 2\bar{\alpha}_{\rm m}(1-\Gamma)^2 B + \bar{\kappa}_0^+(1-\Gamma)S - \bar{\kappa}_0^-\Gamma, \quad \text{on} \quad x = 0. \tag{D.23b}$$

In Chapter 5 we drop the over-bar notation on the parameters $\kappa_0^{\pm}$, $\alpha_{\rm m}$, $\beta_{\rm m}$, and $\delta_{\rm m}$.

Similarly, one can derive the leading–order boundary conditions at depth that are given by

$$B_x{}^2 - BB_{xx} = S_x = 0 \quad \text{on} \quad x = l. \tag{D.24}$$

We note that to close the problem initial conditions for Γ, B, and S must also be prescribed.

D.1.2.1 Dimensional model

The dimensional form of the continuum model can be written as

$$B_t = \left(a_0 a(x)\mathrm{sgn}(B_x)(B_x{}^2 - BB_{xx})\right)_x + k^+|B_x|S^2 - k^-B, \tag{D.25a}$$

$$S_t = D_S S_{xx} - \frac{2}{h}\left(k^+|B_x|S^2 - k^-B\right), \tag{D.25b}$$

$$S_x = B_x^2 - BB_{xx} = 0, \qquad \text{on} \quad x = L, \tag{D.25c}$$

$$B = \Gamma, \qquad \text{on} \quad x = 0, \tag{D.25d}$$

where $a(x) = \alpha(x')$ and x' the dimensionless depth variable. The possible additional surface boundary conditions are:

(i)

$$D_S S_x = k_0^+(\Gamma_{\rm sat} - \Gamma)S - k_0^-\Gamma, \qquad \text{on} \quad x = 0, \tag{D.26a}$$

$$a_0 a(0)\mathrm{sgn}(B_x)(B_x^2 - BB_{xx}) = k_{\rm m}(\Gamma_{\rm sat} - \Gamma)^2\Gamma, \qquad \text{on} \quad x = 0, \tag{D.26b}$$

where Γ is given by the isotherm

$$2k_{\rm m}(1-\Gamma)^2 B + k_0^+(\Gamma_{\rm sat} - \Gamma)S - k_0^-\Gamma = 0, \quad \text{on} \quad x = 0. \tag{D.26c}$$

(ii)

$$S_x = B_x^2 - BB_{xx} = 0, \quad \text{on} \quad x = 0, \tag{D.27a}$$

where Γ evolves according to

$$\frac{\mathrm{d}\Gamma}{\mathrm{d}t} = 2k_{\rm m}(\Gamma_{\rm sat} - \Gamma)^2 B + k_0^+(\Gamma_{\rm sat} - \Gamma)S - k_0^-\Gamma, \quad \text{on} \quad x = 0. \tag{D.27b}$$

The dimensional parameters of the model (D.25)–(D.27) are given in terms of the parameters of the mesoscopic model:

$$\begin{aligned} a_0 &= h^3 a_1, \qquad k^+ = \frac{r^+}{h}, \qquad k^- = r^-, \\ k_0^\pm &= \epsilon^\nu r_0^\pm, \qquad k_\mathrm{m} = \epsilon^\nu \alpha_\mathrm{m}^\pm, \qquad D_S = dh^2, \end{aligned} \tag{D.28}$$

where ν is an integer which is chosen to give either of the boundary conditions (D.26) or (D.27).

D.2 Free calcium-surfactant model

In §5.3 we extend the free-surfactant model of §5.2 to include free calcium ions that necessitate the formation of bilayer molecules. Therefore, we modify the microscopic reaction for the formation of bilayer molecules as follows

$$2S_i + C_i + \text{adsorption site} \underset{r_i^-}{\overset{r_i^+}{\rightleftharpoons}} B_i,$$

where C_i denotes the concentration of calcium ions in the ith bilayer and has units $\mathrm{mol\,m^{-3}}$. The derivation of the macroscopic model is analogous to that presented above so we omit the details but note that the calcium ion concentration takes the same scaling as the surfactant monomer in the nondimensionalisation of the mesoscopic model, namely

$$[S], [C] \sim \left(\frac{k^- H}{k^+}\right)^{1/3}, \tag{D.29}$$

where the characteristic lengthscale, H, is now given by

$$H = \left(\frac{k^+ a_0^3 \Gamma_\mathrm{sat}^6}{k^- h^3 D_s^3}\right)^{1/4}. \tag{D.30}$$

The dimensionless governing equations are given by

$$B_t = \left(\alpha(x)\mathrm{sgn}(B_x)({B_x}^2 - BB_{xx})\right)_x + \kappa(|B_x|CS^2 - B), \tag{D.31a}$$

$$\frac{1}{\Gamma^*}S_t = S_{xx} - 2\kappa\left(|B_x|CS^2 - B\right), \tag{D.31b}$$

$$\frac{1}{\Gamma^*}C_t = DC_{xx} - \kappa\left(|B_x|CS^2 - B\right), \tag{D.31c}$$

$$S_x = C_x = B_x^2 - BB_{xx} = 0, \qquad \text{on} \quad x = l, \tag{D.31d}$$

$$B = \Gamma, \qquad C_x = 0, \qquad \text{on} \quad x = 0, \tag{D.31e}$$

The possible additional surface boundary conditions are the same as those given in either (D.23) or (D.23). The dimensionless parameters of the model are defined below

$$\kappa = \frac{k^- H^3}{a_0\Gamma_{\mathrm{sat}}}, \qquad \Gamma^* = \frac{\Gamma_{\mathrm{sat}}}{h}\left(\frac{k^+}{k^- H}\right)^{1/3}, \qquad D = \frac{D_C}{D_S}, \qquad l = \frac{h}{H},$$
$$\alpha_{\mathrm{m}} = \frac{k_{\mathrm{m}}\Gamma_{\mathrm{sat}}H^3}{a_0}, \qquad \kappa_0^+ = \frac{k_0^+ H^3}{k^+ a_0\Gamma_{\mathrm{sat}}}\left(\frac{k^- H}{k^+}\right)^{1/3}, \qquad \kappa_0^- = \frac{k_0^- H^3}{a_0\Gamma_{\mathrm{sat}}}, \tag{D.32}$$

where D_C is the diffusivity for the calcium ions.

References

[1] A.W. Adamson. *Physical Chemistry of Surfaces.* Wiley, 1982.

[2] Alberts. *Molecular biology of the cell.* Garland Publ. NY, 1994.

[3] C.D. Bain. The overflowing cylinder sixty years on. *Adv. Coll. Interface Sci.*, 144:4–12, 2008.

[4] C.G. Bell. Mathematical modelling of polymer/surfactant systems. D.Phil thesis, Oxford, 2007.

[5] C.J.W. Breward, R.C. Darton, P.D. Howell, and J.R. Ockendon. The effect of surfactants on expanding free surfaces. *Chem. Eng. Sci.*, 56:2867–2878, 2001.

[6] C.J.W. Breward and P.D. Howell. Straining flow of a micellar surfactant solution. *Euro. Jnl of Applied Mathematics*, 15:511–531, 2004.

[7] B. Cabane and R. Duplessix. Neutron-scattering study of water-soluble polymers adsorbed on surfactant micelles. *Colloid Surfaces*, 13:19–33, 1985.

[8] C. Chang and E.I. Franses. Adsorption dynamics of surfactants at the air/water interface: a critical review of mathematical models, data, and mechanisms. *Colloid Surfaces*, 100:1–45, 1995.

[9] P. A. Clarkson, E. L. Mansfield, and T. J. Priestley. Symmetries of a class of nonlinear third-order partial differential equations. *Mathl. Comput. Modelling*, 25:195–212, 1997.

[10] R. Courant and D. Hilbert. *Methods of Mathematical Physics.* John Wiley and Sons, 1962.

[11] J. Crank. *Free and moving boundary problems.* Oxford University Press, 1984.

[12] R.V. Craster and O.K. Matar. Surfactant transport on mucus films. *J. Fluid Mech.*, 425:235–258, 2000.

[13] E.C. Crouch. Surfactant protein-d and pulmonary host defense. *Respiratory Research*, 1:2, 2000.

[14] D. Follows, F. Tiberg, R.K. Thomas, and M. Larsson. Multilayers at the surface of solutions of exogeneous lung surfactant: direct observation by neutron reflection. *Biochimica et Biophysica Acta*, 1768:228–235, 2007.

[15] I.M. Griffiths, C.D. Bain, C.J.W. Breward, D.M. Colgate, P.D. Howell, and S.L. Waters. On the predictions and limitations of the becker–döring model for reaction kinetics in micellar surfactant solutions. *J. Colloid Interface Sci.*, 360:662–671, 2011.

[16] P.D. Howell and C.J.W. Breward. Mathematical modelling of the overflowing cylinder experiment. *J. Fluid Mech.*, 474:275–298, 2003.

[17] O.E. Jensen and D. Halpern. The stress singularity in surfactant-driven thin-film flows. part 1. viscous effects. *J. Fluid Mech.*, 372:273–300, 1998.

[18] D. Kashchiev and Exerowa. Structure and surface energy of the surfactant layer on the alveolar surface. *Eur. Biophys. J.*, 30:34–41, 2001.

[19] T. Kawai, Y. Yamada, and T. Kondo. Adsorbed monolayers of mixed surfactant solutions of sodium dodecylsulfate and cetylpyridinium chloride studied by infrared external reflection spectroscopy. *J. Phys. Chem*, 112:2040–2044, 2008.

[20] Z.X. Li, J.R. Lu, R.K. Thomas, and A. Weller. Conformal roughness in the adsorbed lamellar phase of aerosol-ot at the air-water and liquid-solid interfaces. *Langmuir*, 17:5858–5864, 2001.

[21] M. Lósche, J. Schmitt, G. Decher, W.G. Bouwman, and K. Kjaer. Detailed structure of molecularly thin polyelectrolyte multilayer films on solid substrates as revealed by neutron reflectometry. *Macromolecules*, 31:8893–8906, 1998.

[22] J.R. Lu, R.K. Thomas, and J. Penfold. Surfactant layers at the air/water interface: structure and composition. *Adv. Coll. Interface Sci.*, 84:143–304, 2000.

[23] S. Manning-Benson, C.D. Bain, and R.C. Darton. Measurement of dynamic interfacial properties in an overflowing cylinder by ellipsometry. *J. Colloid Interface Sci.*, 189:109–116, 1997.

[24] S. Manning-Benson, S.W.R. Parker, C.D. Bain, and J. Penfold. Measurement of the dynamic surface excess in an overflowing cylinder by neutron reflection. *Langmuir*, 14:990–996, 1998.

[25] C.E. Morgan, I.M. Griffiths, C.J.W. Breward, P.D. Howell, J. Penfold, R.K. Thomas, I. Tucker, J.T. Petkov, and J.R.P. Webster. The kinetics of surfactant desorption at the air-solution interface. *Langmuir (in press)*, 2012.

[26] J. Ockendon, S. Howison, A. Lacey, and A. Movchan. *Applied Partial Differential Equations.* Oxford University Press, 1999.

[27] J. Penfold. Private communication. 2012.

[28] J. Penfold, D.S. Sivia, E. Staples, I. Tucker, and R.K. Thomas. Surface ordering in dilute dihexadecyl dimethyl ammonium bromide solutions at the air-water interface. *Langmuir*, 20:2265–2269, 2004.

[29] J. Penfold, E. Staples, S. Ugazio, I. Tucker, L. Soubiran, J. Hubbard, M. Noro, B. O'Malley, A. Ferrante, G. Ford, and H. Buron. The microstructure of di-alkyl chain cationic/nonionic surfactant mixtures: observation of coexisting lamellar and micellar phases and depletion induced phase separation. *J. Phys. Chem. B*, 109:18107–18116, 2005.

[30] J. Penfold, R.K. Thomas, C.C. Dong, I. Tucker, K. Metcalfe, S. Golding, and I. Grillo. Equilibrium surface adsorption behaviour in complex anionic/nonionic surfactant mixtures. *Langmuir*, 23:10140–10149, 2007.

[31] J.T. Petkov, I.M. Tucker, J. Penfold, R.K. Thomas, D.N. Petsev, C.C. Dong, S. Golding, and I. Grillo. The impact of multivalent conterions Al^{3+}, on the surface adsorption and self-assembly of the anionic surfactant alkyloxyethylene sulfate and anionic/nonionic surfactant mixtures. *Langmuir*, 26:16699–16709, 2010.

[32] C.M. Phan, A.V. Nguyen, and G.M. Evans. Dynamic adsorption of sodium dodecylbenzene sulphonate and dowfroth 250 onto the air-water interface. *Minerals Engineering*, 18:599–603, 2005.

[33] I.P. Purcell, J.R. Lu, R.K. Thomas, A.M. Howe, and J. Penfold. Adsorption of sodium dodecyl sulfate at the surface of aqueous solutions of poly(vinylpyrrolidone) studied by neutron reflection. *Langmuir*, 14:1637–1645, 1998.

[34] D.J. Shaw. *Introduction to Colloid and Surface Chemistry.* Butterworth-Heinmann, 1992.

[35] T.P. Stevens, M. Blannow, E.H. Myers, and R. Soll. Early surfactant administration with brief ventilation vs. selective surfactant and continued mechanical ventilation for preterm infants with or at risk for respiratory distress syndrome. *Cochrane Database of Systematic Reviews*, 4, 2007.

[36] D.J.F. Taylor, R. K. Thomas, and J. Penfold. Adsorption of oppositely charged polyelectrolyte/surfactant mixtures. neutron reflection from alkyl trimethylammonium bromides and sodium poly(styrenesulfonate) at the air/water interface: The effect of surfactant charge. *Langmuir*, 19:3712, 2003.

[37] D.J.F. Taylor, R. K. Thomas, and J. Penfold. Polymer/surfactant interactions at the air/water interface. *Adv. Coll. Interface Sci.*, 132:69–110, 2007.

[38] R. C. Tolman. The principle of microscopic reversibility. *Proc. of the National Academy of Science of the USA*, page 436, 1925.

[39] I. Tucker, J. Penfold, R.K. Thomas, C.C. Dong, S. Golding, C. Gibson, and I. Grillo. The adsorption and self-assembly of mixtures of alkylbenzene sulfonate isomers and the role of divalent electrolyte. *Langmuir*, 27:6674–6682, 2011.

[40] Unilever. Sustainable development overview, 'creating a better future everyday', 2009.

[41] D.S. Valkovska, G.C. Shearmand, C.D. Bain, R.C. Darton, and J. Eastoe. Adsorption of ionic surfactants at an expanding air-water interface. *Langmuir*, 20:4436–4445, 2004.

[42] M. Van Dyke. *Perturbation Methods in Fluid Mechanics*. Academic Press, 1964.

[43] X.L. Zhang, D.J.F. Taylor, R.K. Thomas, and J. Penfold. The role of electrolyte and polyelectrolyte on the adsorption of the anionic surfactant, sodium dodecylbenzenesulfonate, at the air-water interface. *J. Colloid Interface Sci.*, 356:656–664, 2011.

[44] Y. Zhu and S. Granick. Biolubrication: hyaluronic acid and the influence on its interfacial viscosity of an antiinflammatory drug. *Macromolecules*, 36:973–976, 2003.